Technical Document 2932
October 1996

Proceedings of the 8th Matched-Field Processing Workshop 12–14 June 1996

Workshop coordinated by Dr. John Ozard
Esquimalt Defence Research Detachment (EDRD)
Victoria, BC, Canada

Proceedings compiled and produced by Dr. B. Sotirin and Ms. S. Hall
Naval Command, Control and Ocean Surveillance Center (NCCOSC)
RDT&E Division (NRaD), Code D881

19961216 052

Naval Command, Control and
Ocean Surveillance Center
RDT&E Division

San Diego, CA
92152–5001

Sponsored by EDRD and NRaD

DISCLAIMER NOTICE

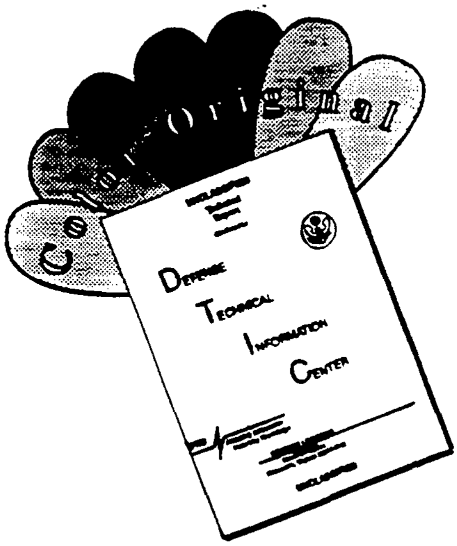

Technical Document 2932
October 1996

Proceedings of the 8th Matched-Field Processing Workshop
12–14 June 1996

Workshop coordinated by Dr. John Ozard
Esquimalt Defence Research Detachment (EDRD)
Victoria, BC, Canada

Proceedings compiled and produced by Dr. B. Sotirin and Ms. S. Hall
Naval Command, Control and Ocean Surveillance Center (NCCOSC)
RDT&E Division (NRaD), Code D881

Sponsored by Esquimalt Defence Research Detachment (EDRD)
Victoria, BC, Canada
and
Naval Command, Control and Ocean Surveillance Center (NCCOSC)
RDT&E Division (NRaD)

NAVAL COMMAND, CONTROL AND
OCEAN SURVEILLANCE CENTER
RDT&E DIVISION
San Diego, California 92152-5001

H. A. WILLIAMS, CAPT, USN
Commanding Officer

R. C. KOLB
Executive Director

ADMINISTRATIVE INFORMATION

This document is a compilation of work presented at the 8th Matched-Field Processing Workshop, 12–14 June 1996, Victoria, BC, Canada. The workshop was coordinated by Dr. John Ozard at the Esquimalt Defence Research Detachment (EDRD) and cosponsored by EDRD and the Naval Command, Control and Ocean Surveillance Center RDT&E Division, San Diego, CA.

Released by
C. D. Rees, Head
Acoustic Branch

Under authority of
J. H. Richter, Head
Propagation Division

JA

CONTENTS

Matched Field Processing - What Next?

John A. Tague
Undersea Surveillance Signal Processing Team
Office of Naval Research
800 N. Quincy St.
Arlington, VA 22217-5660, USA

12 June 1996

Abstract

Matched field processing is an intellectually fascinating blend of statistics and underwater acoustics. Furthermore, it works! Many experiments have demonstrated its viability - in both shallow water and deep ocean environments. Where do we go next? What challenging problems remain to be solved, and what options can we offer the U.S. Navy for practical arrays capable of supporting this advanced processing technique? The Office of Naval Research is interested in developing matched field processing that can provide a new and vital fleet capability.

Active Matched Field Processing

Z.–H. Michalopoulou and M. B. Porter

Center for Applied Mathematics and Statistics
New Jersey Institute of Technology
Newark, NJ 07102

Proceedings of the 8th Matched–Field Processing Workshop,
Victoria, Canada

Active MFP

two–way active processing:
transmitter – target – receiver
it involves two–way modeling of sound propagation and requires knowledge of the scattering function of the target

one–way active processing:
transmitter – receiver (decide whether the source is present by monitoring the receiver)

Gulf of Mexico experiment: example of a one – way active problem

limiting factors: noise, reverberation

one way **$r(t) = h(t) * s(t) + n(t)$**

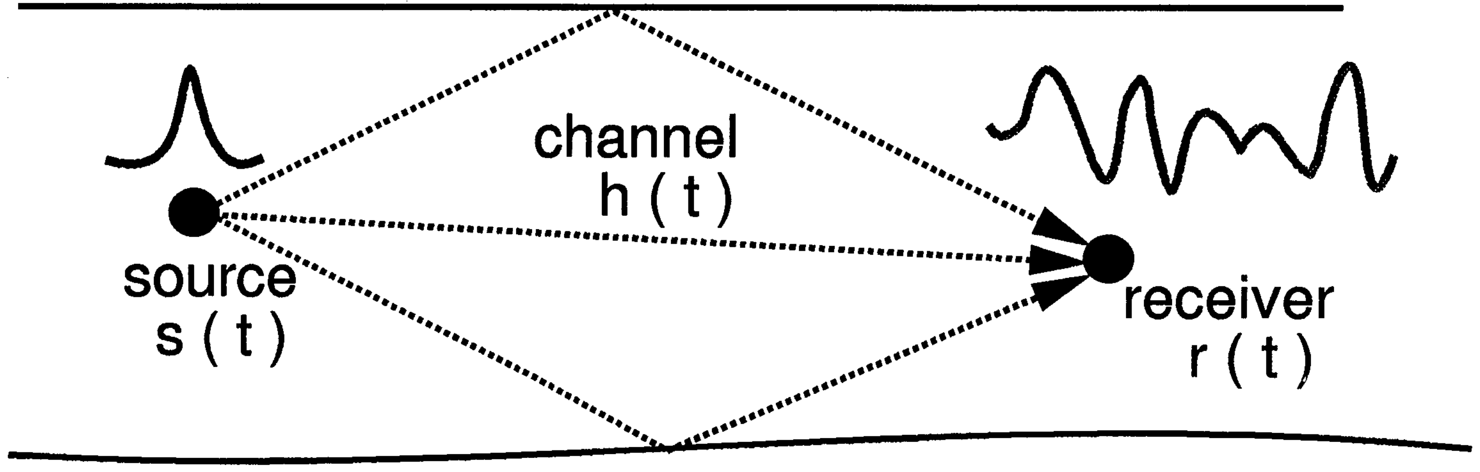

two way **$r(t) = h(t) * h(t) * g(t) * s(t) + n(t)$**

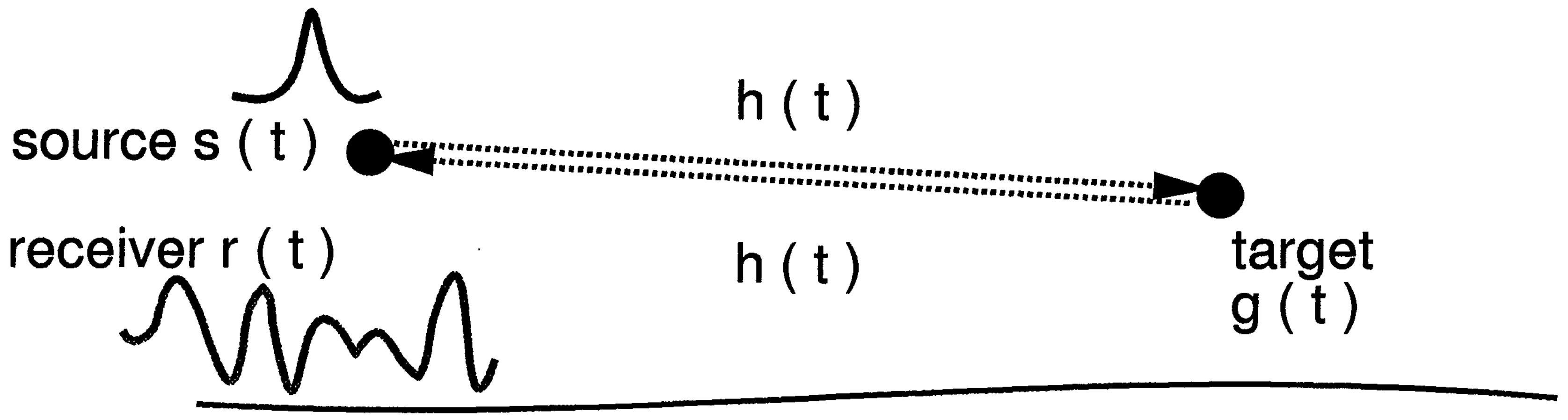

Signal Detection

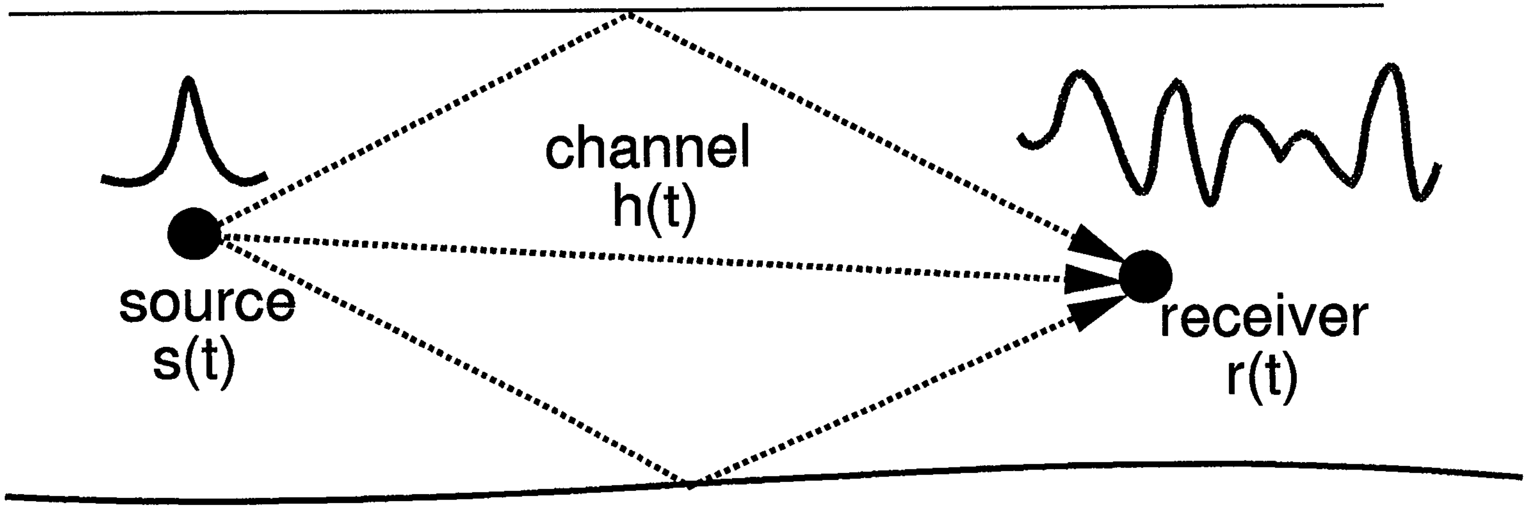

$$r = h * s + n$$

standard *signal detection* technique:

1. correlate **s**, **r** (*matched–filter*) for all lags
2. obtain the maximum of the envelope of the correlation

Signal Detection

signal known exactly in white Gaussian noise:
$\mathbf{r} = \mathbf{s} + \mathbf{n}$

optimum detector: $\lambda = \mathbf{r} \cdot \mathbf{s} \gtrless$ threshold
(*matched–filter* or *correlation detector*)

unknown time of arrival: obtain maximum of $\mathbf{r} \cdot \mathbf{s}$ for all lags (approximately optimum)

unknown amplitude: obtain envelope of correlation

Whalen, *Detection of Signals in Noise*
Johnson and Dudgeon, *Array Signal Processing*

Signal Detection

Optimum detection in the ocean:
correlation between **r** and **h** * **s**

model based matched filter *(Hermand and Roderick, IEEE JOE 1993)*

<u>Detection Study:</u>

- Dispersion effects on detection
- ROC (receiver operating characteristic) curves for performance comparison between three detectors:
  (a) model based matched filter
  (b) model based matched filter with uncertain amplitude
  (c) standard matched filter

Model Based Detector

correlation of **h** * **s** and **r** (**MBMF**) is an **optimum** detector when **h** is *known exactly* (that is, environment and geometry of source and receiver are *known exactly*)

Questions:

1. How does mismatch affect the **MBMF** performance?

2. What is the optimum processor in the presence of uncertainty?

3. Is the pay off from the computation of the optimum processor significant?

Simulations Scenario

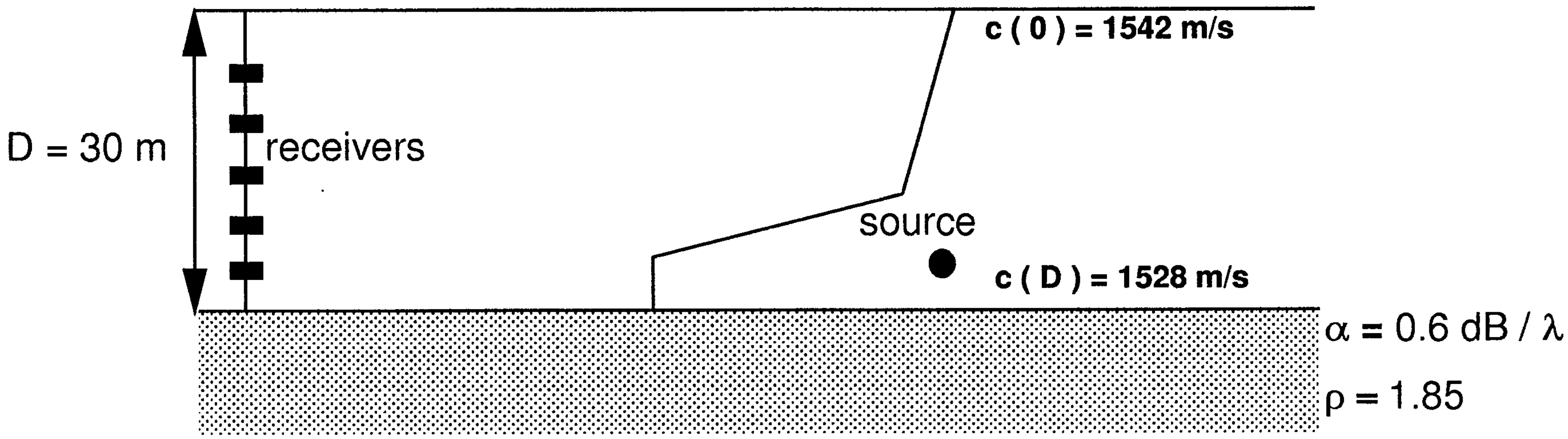

(Ferris, Ingenito, Faber)

Frequency: 300 – 900 Hz
Background: white Gaussian noise

Dispersion Curves of Waveguide

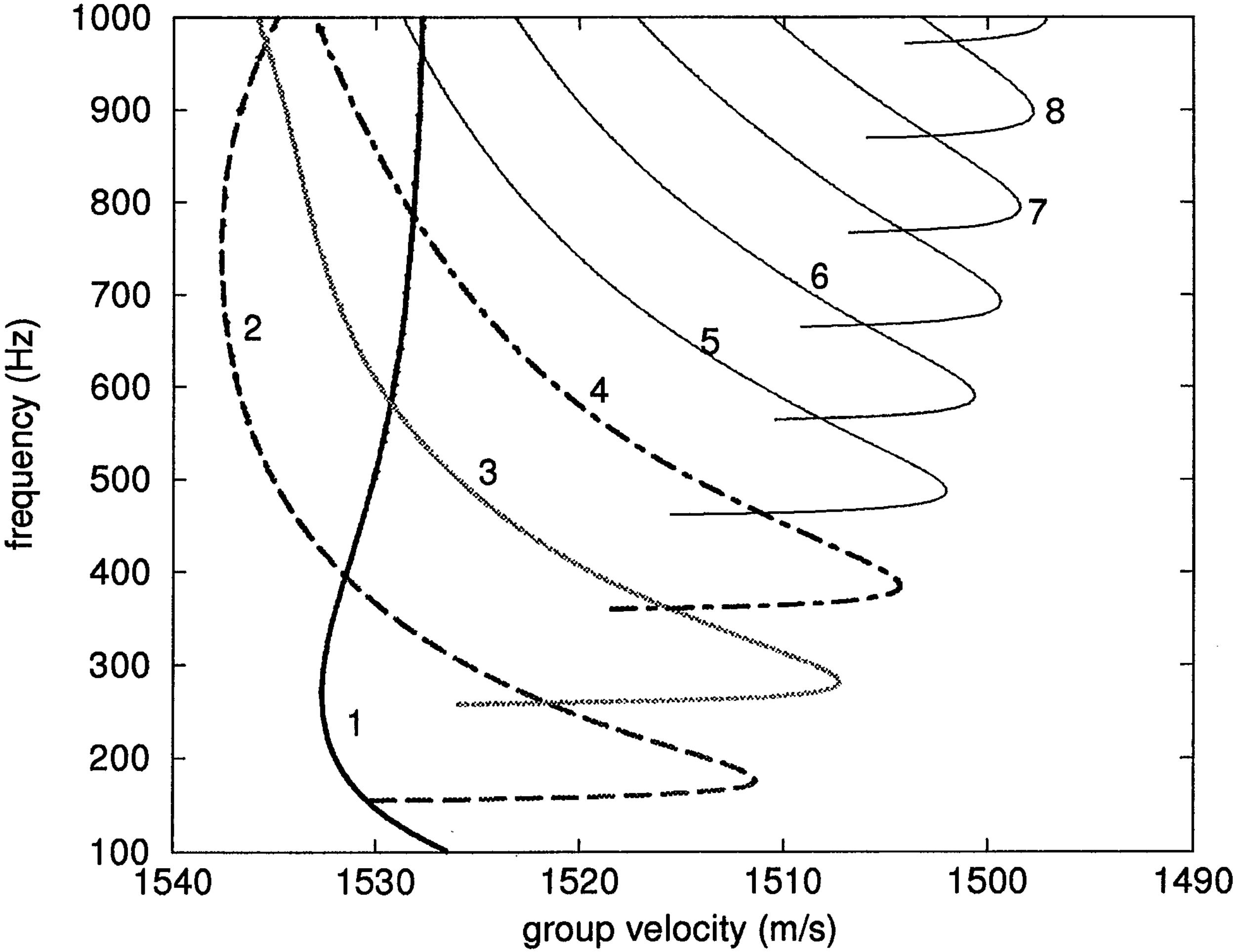

Dispersion

time–series for 12 km range

sinc pulse (500 - 900 Hz)

We can identify pulses carried through distinct modes.

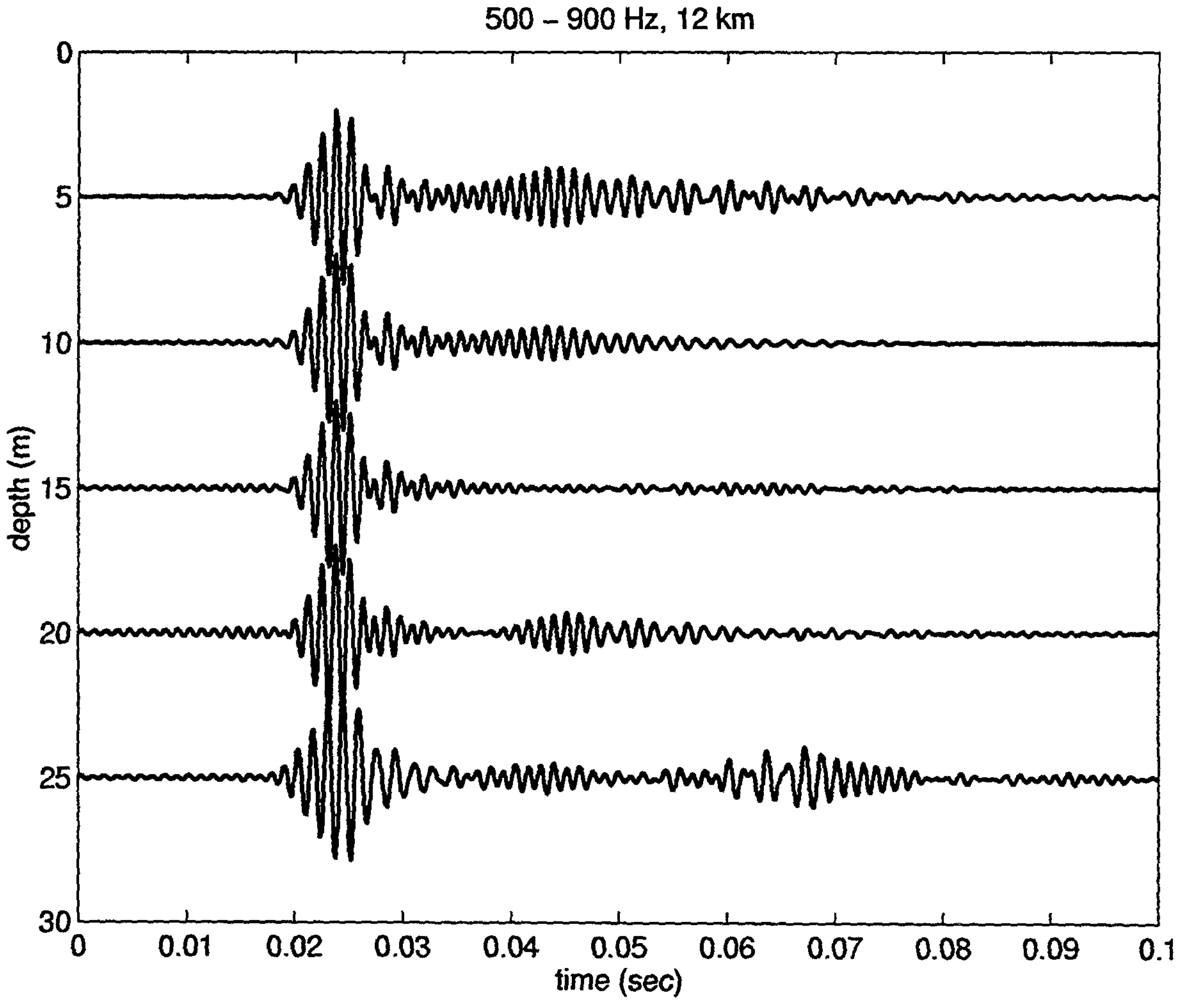

Dispersion – Distortion

pulses corresponding to different modes are identified

- dispersion within a mode

- dispersion between different modes

variations with receiver depth, range, frequency content, geoacoustic parameters

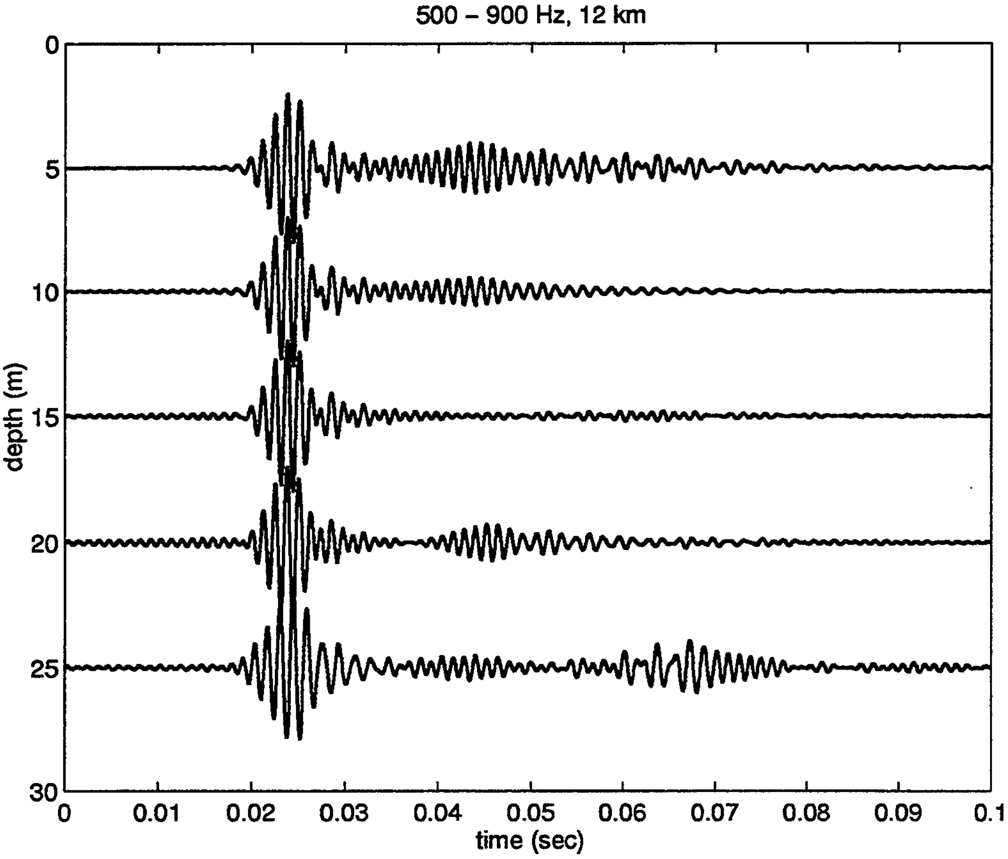

sr = 12 km, mode 2 arrives first , followed by modes 3 and 1

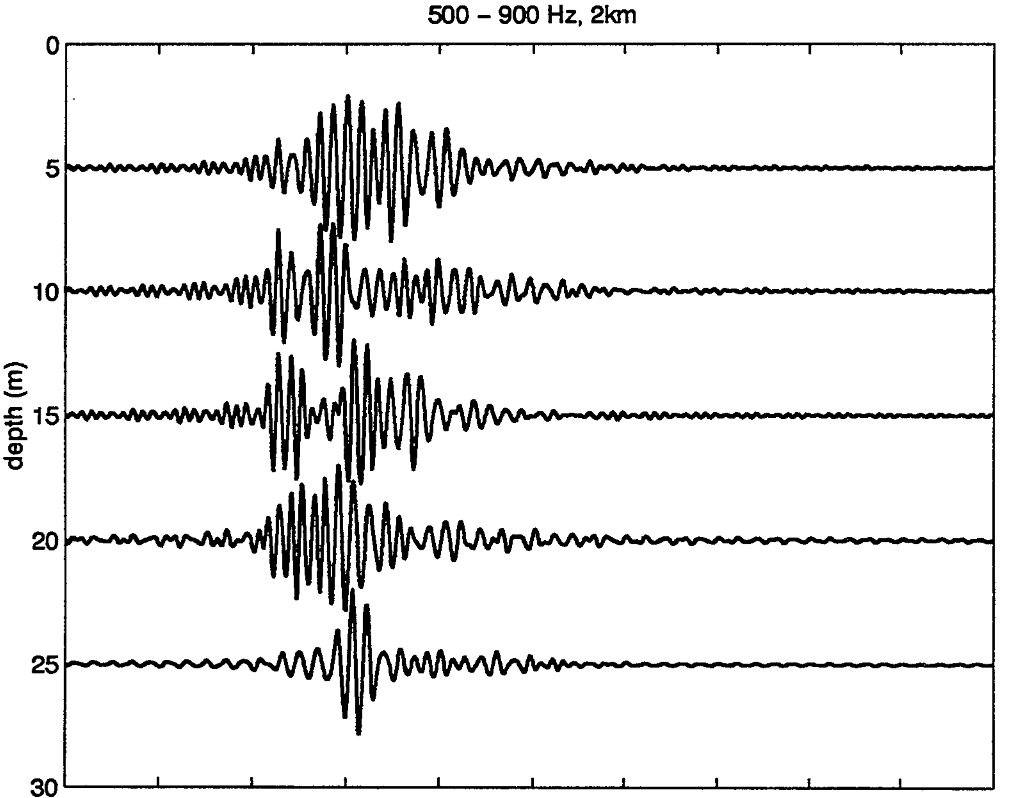

sr = 2 km, modes have not separated yet.

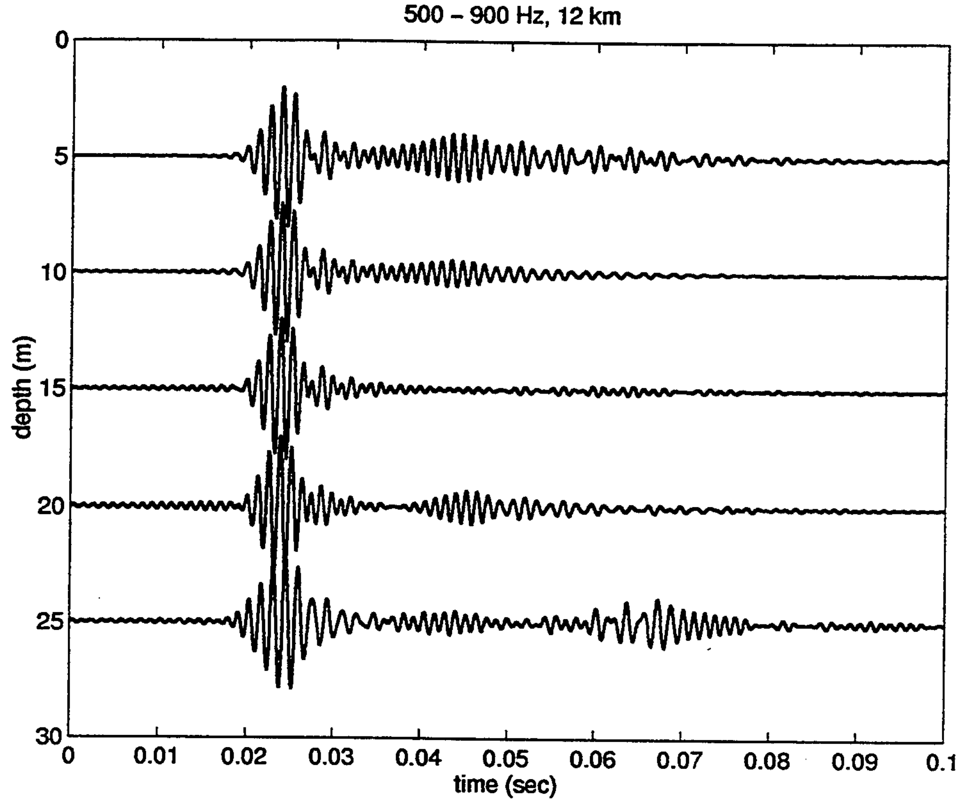

sr = 12 km

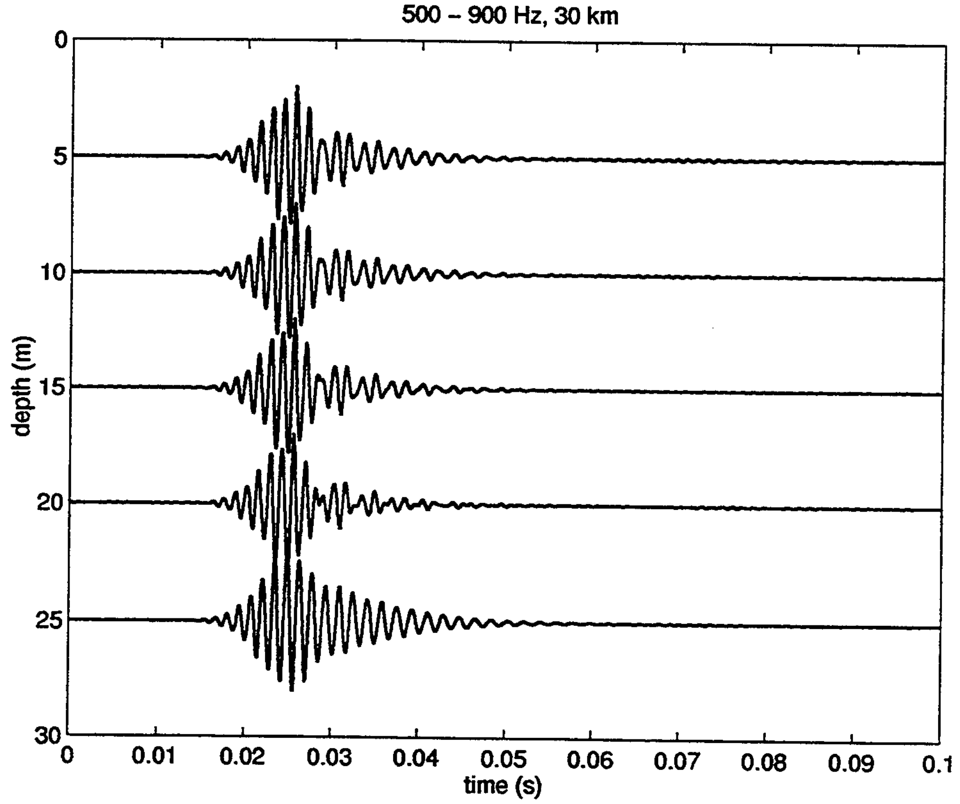

sr = 30 km, modes 1 and 3 have attenuated, mode 2 shows intramodal dispersion

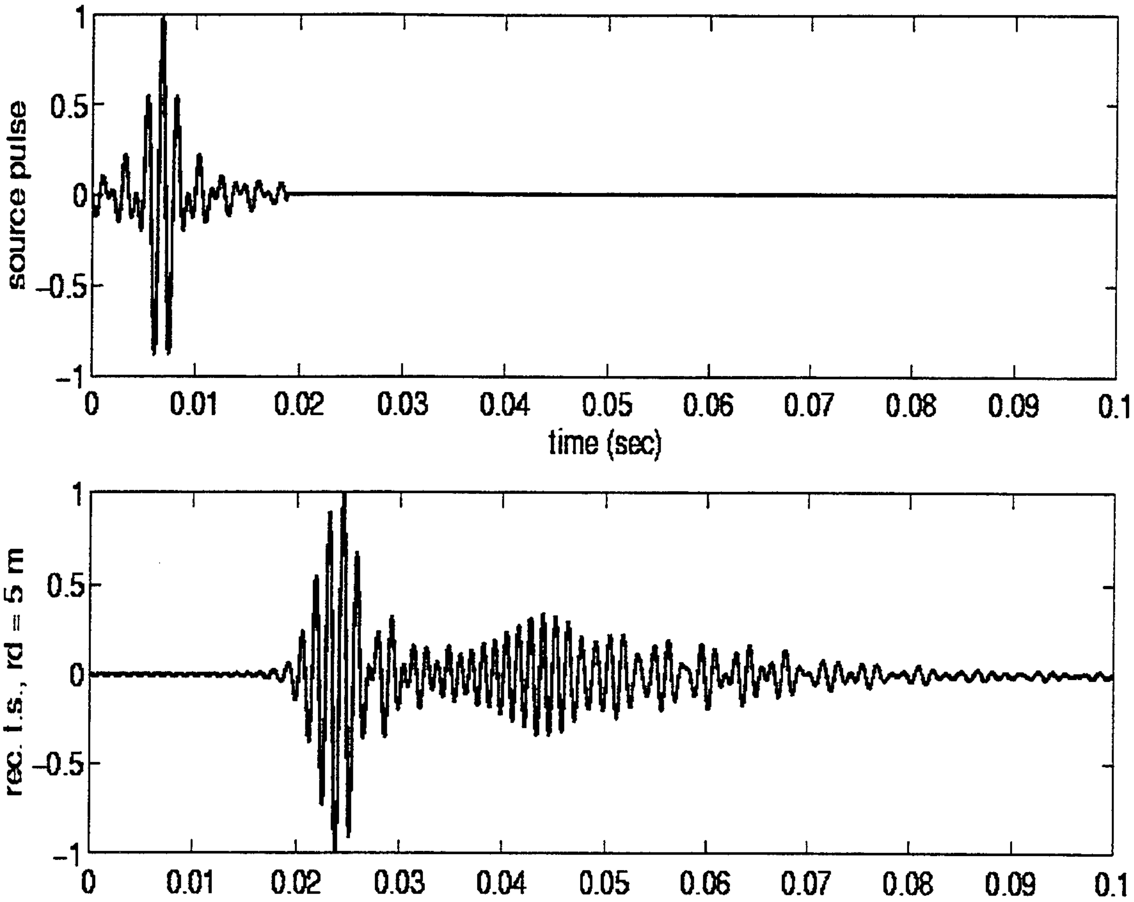

cross-correlation (standard matched-filter)

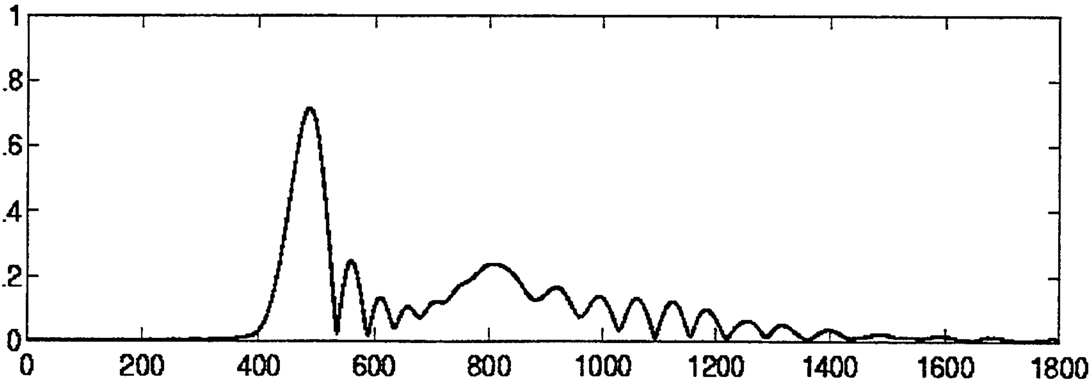

auto-correlation (model-based matched-filter)

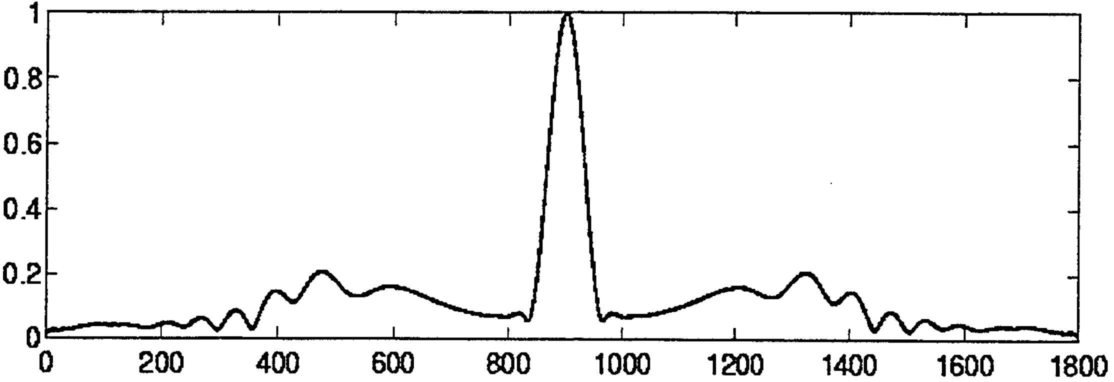

high frequency , less dispersion

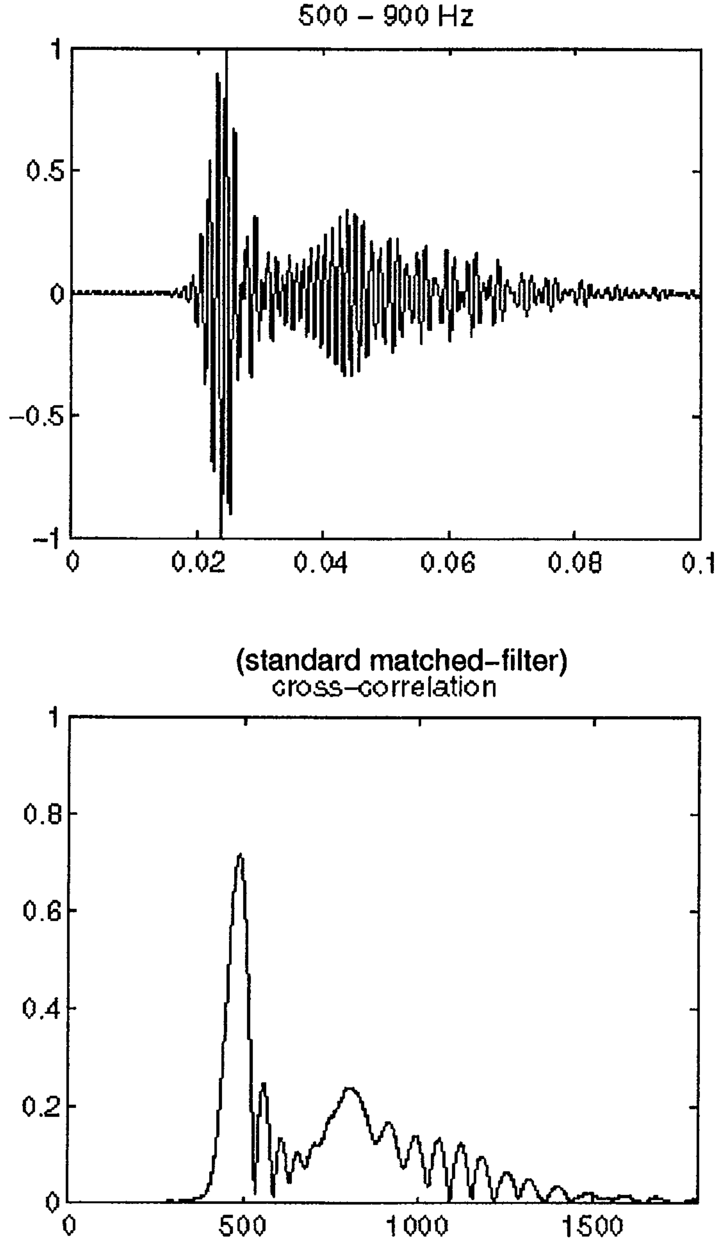
500 - 900 Hz

(standard matched-filter) cross-correlation

low frequency , more dispersion

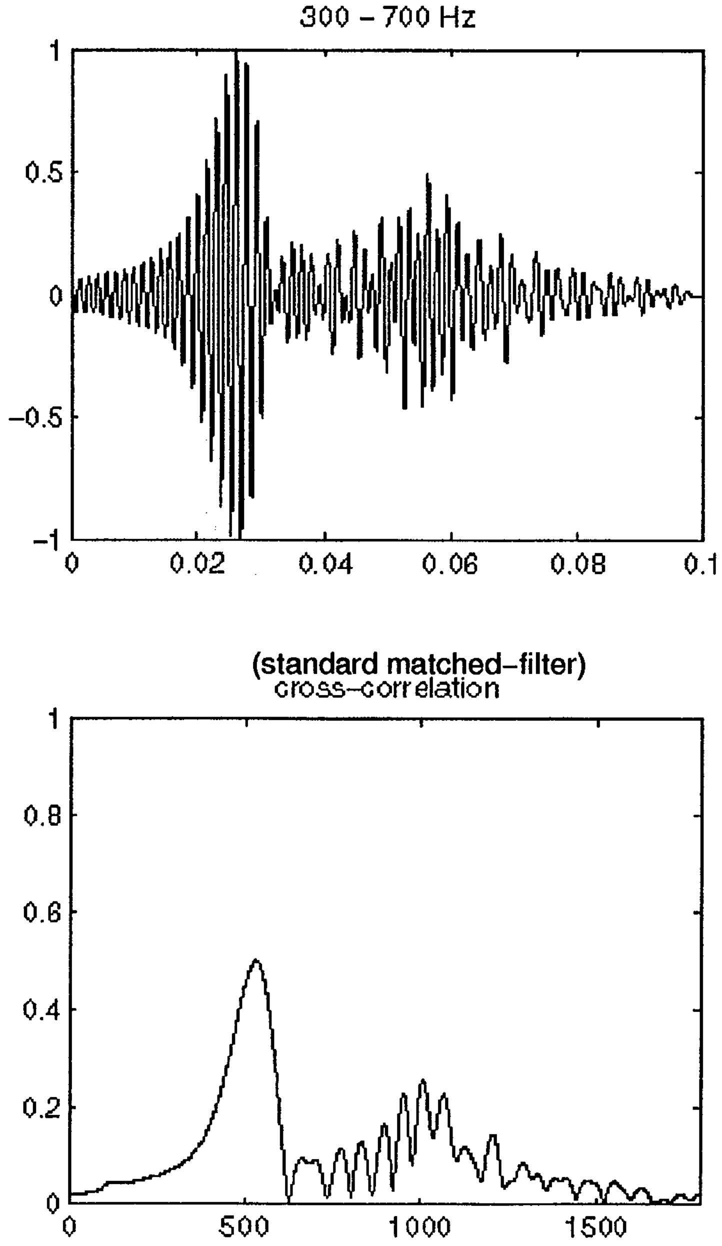
300 - 700 Hz

(standard matched-filter) cross-correlation

Correlation vs. Frequency
(standard matched–filter)

500 – 900 Hz

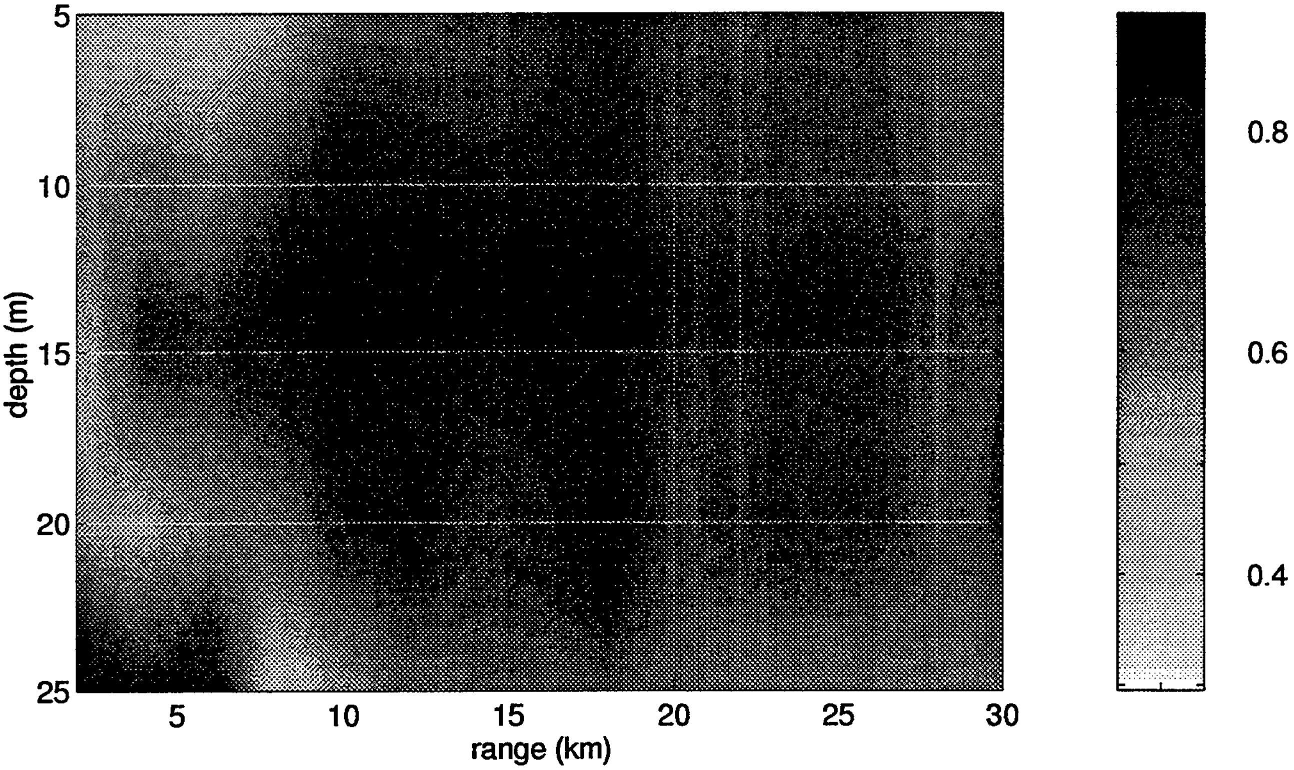

300 – 700 Hz

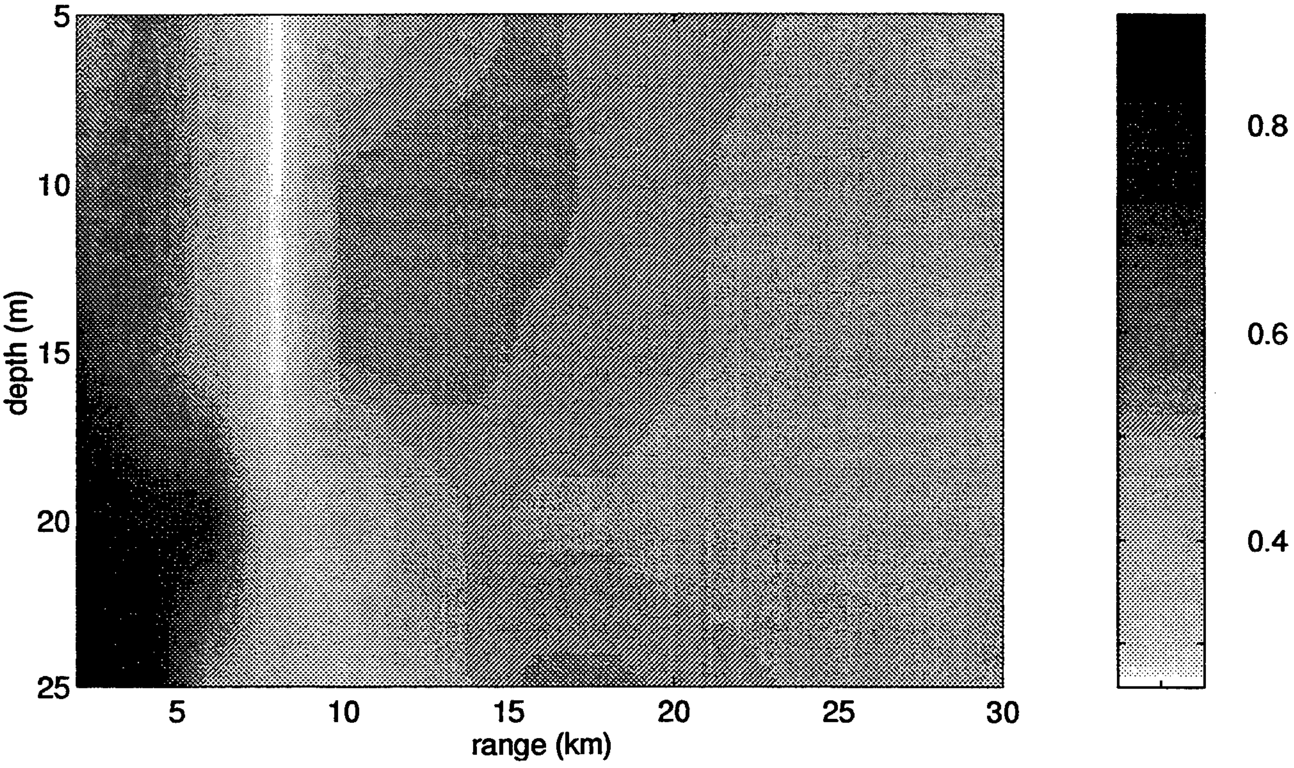

Ambiguity Surfaces of Standard Matched–Filter

high frequency (500 – 900 Hz) ambiguity surface shows higher correlations overall than the low frequency ambiguity surface (300 – 700 Hz)

correlation varies with range, depth, frequency

ROC Performance Evaluation

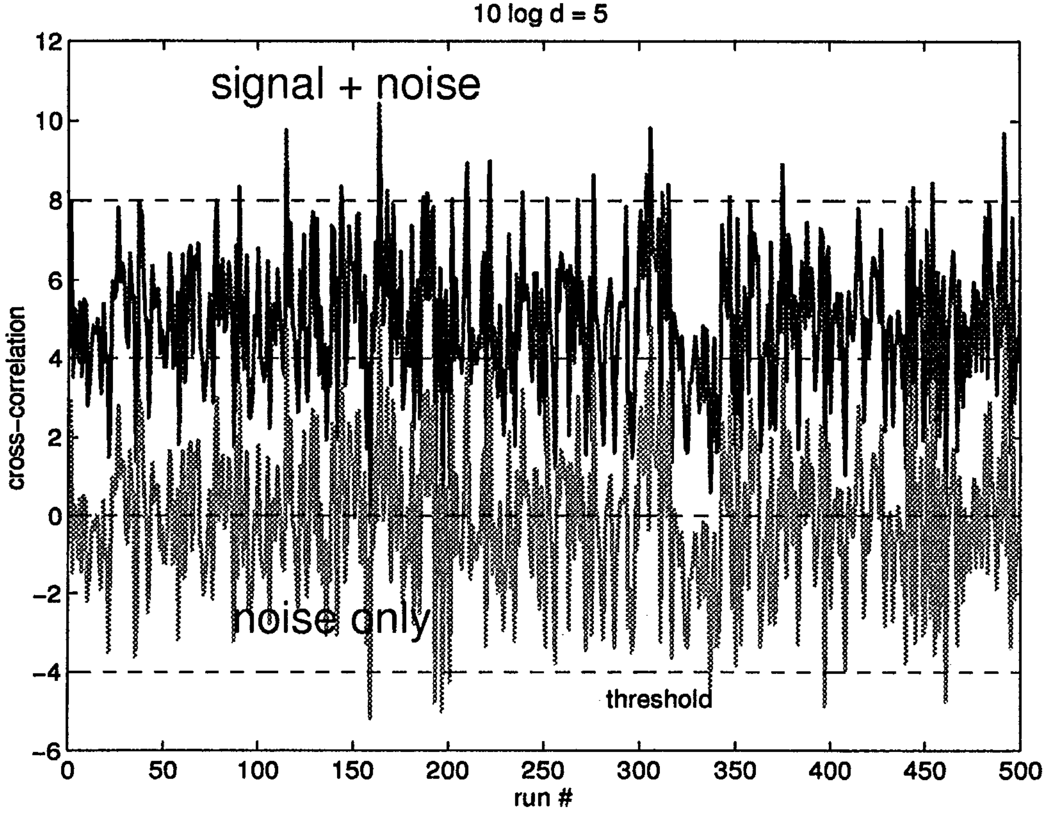

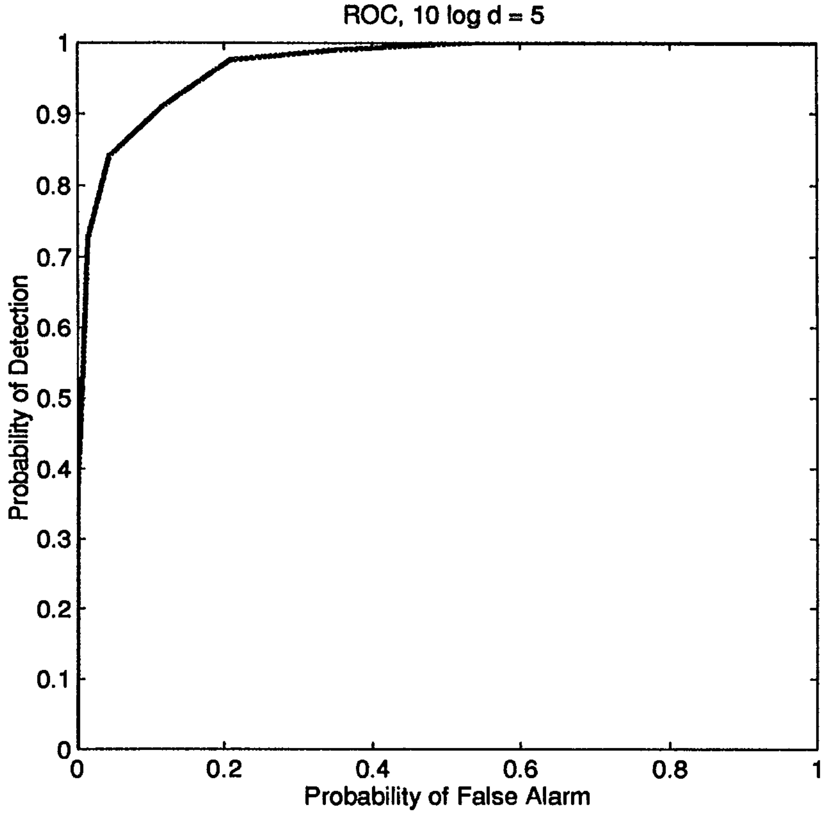

$$d = E_s / \sigma^2$$

E_s: signal energy, σ^2=noise variance

ROC Performance Evaluation

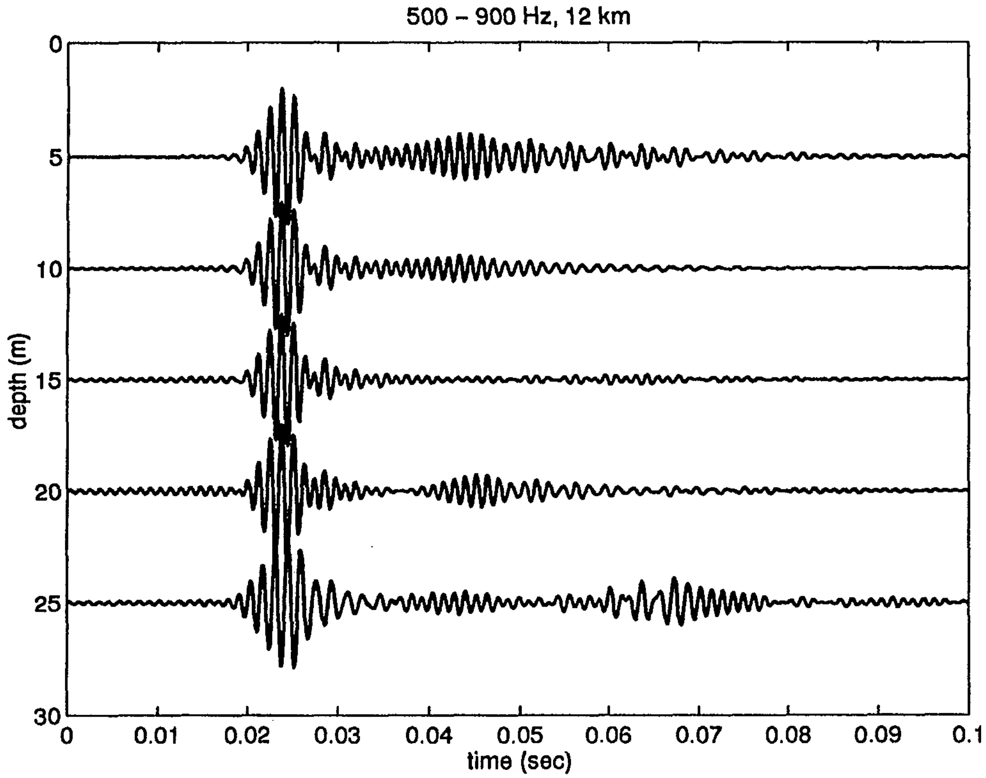

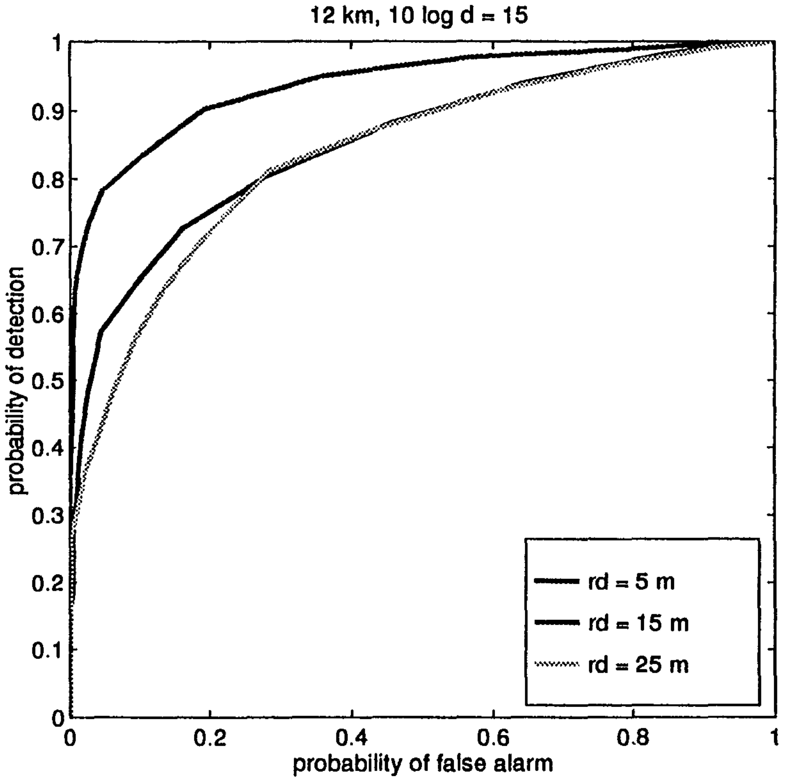

standard matched-filter

Detection Performance

12 km, rd=15 m

12 km, rd= 5 m

15 dB

10 dB

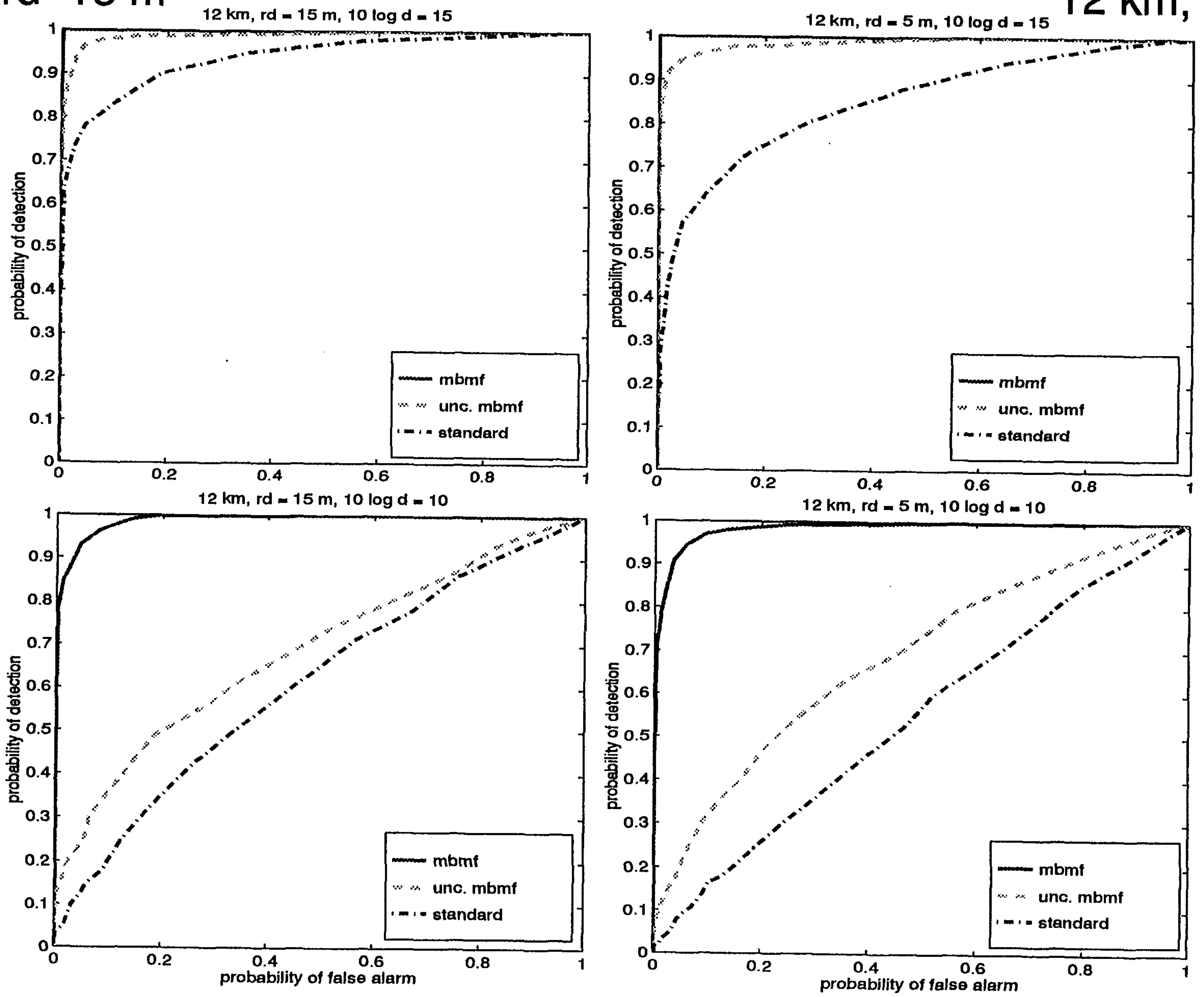

Detection Performance

12 km

30 km

15 dB

10 dB

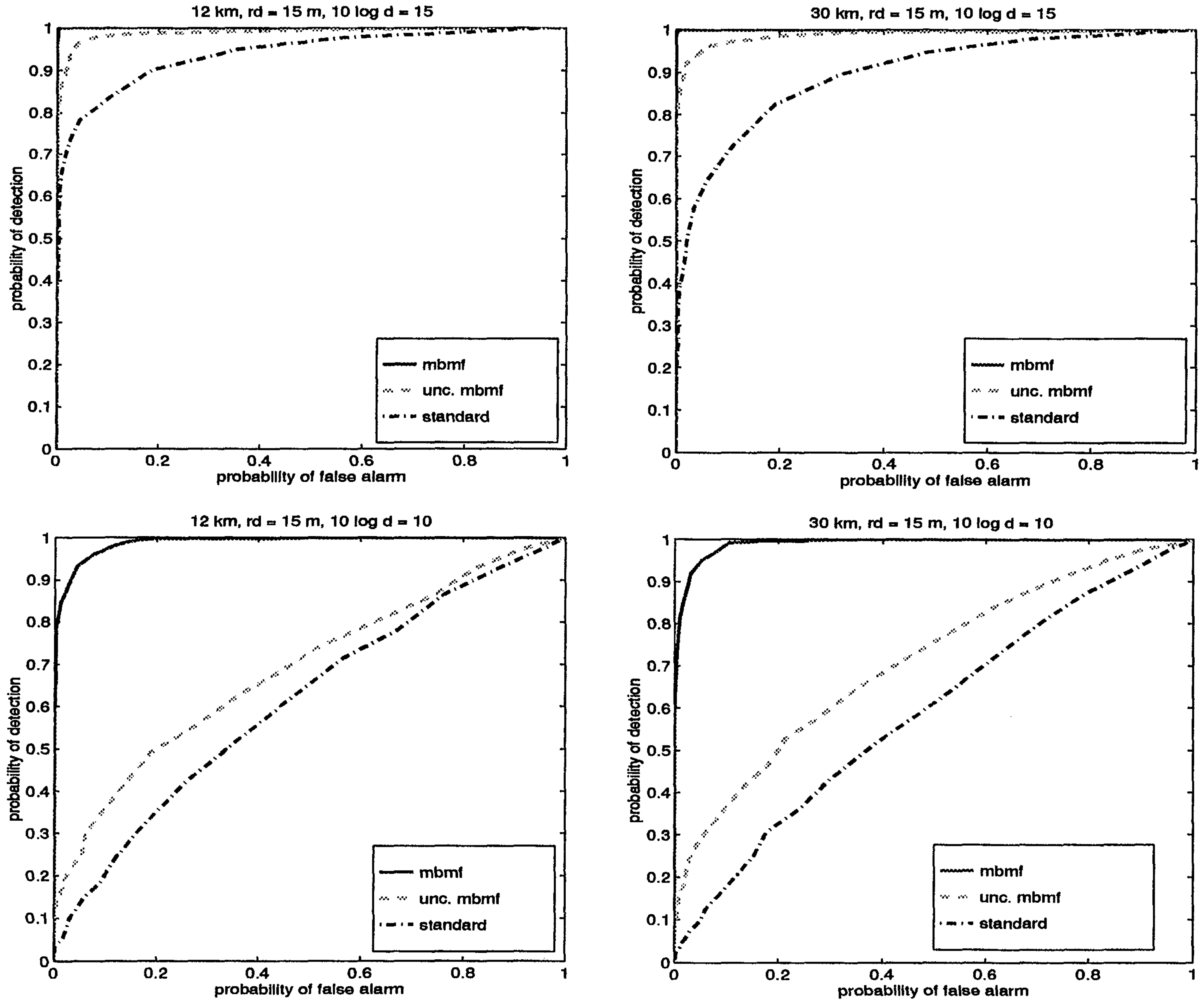

Depth Mismatch

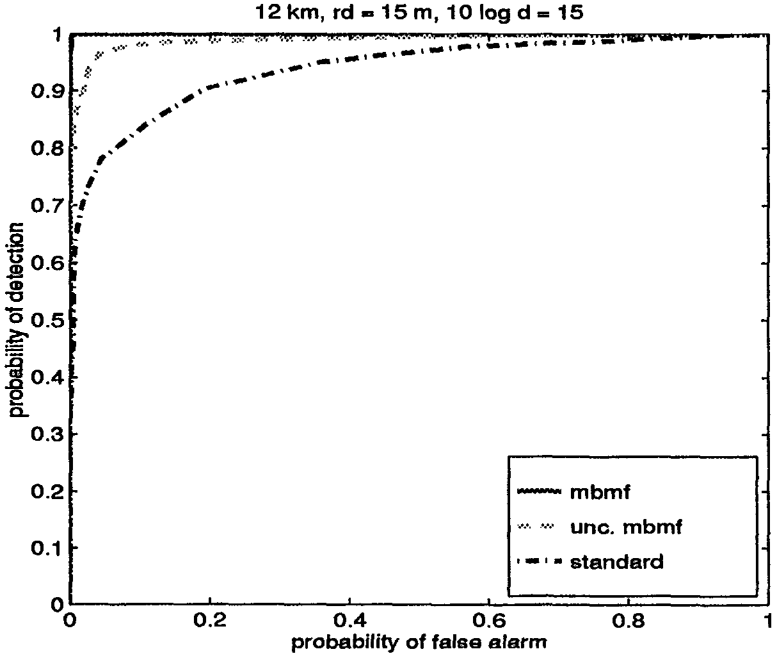

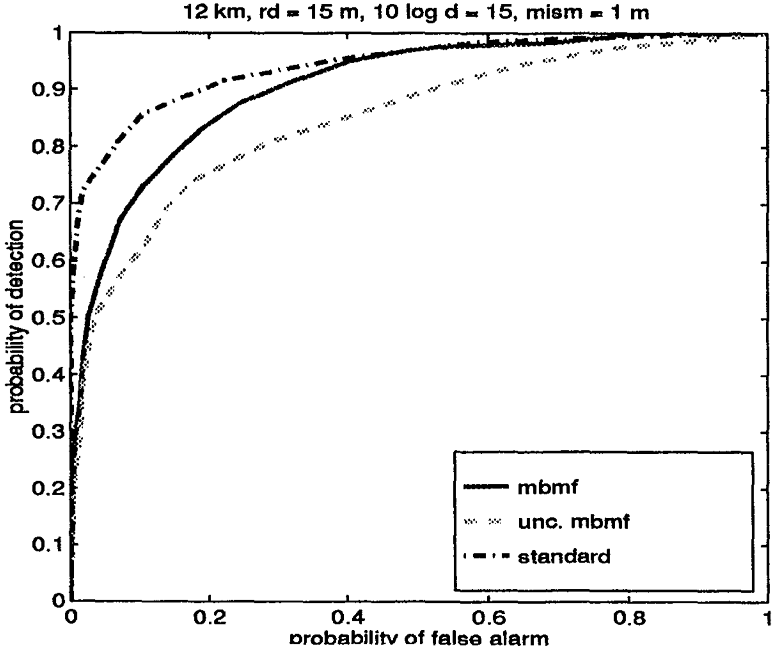

mismatch =
1 m

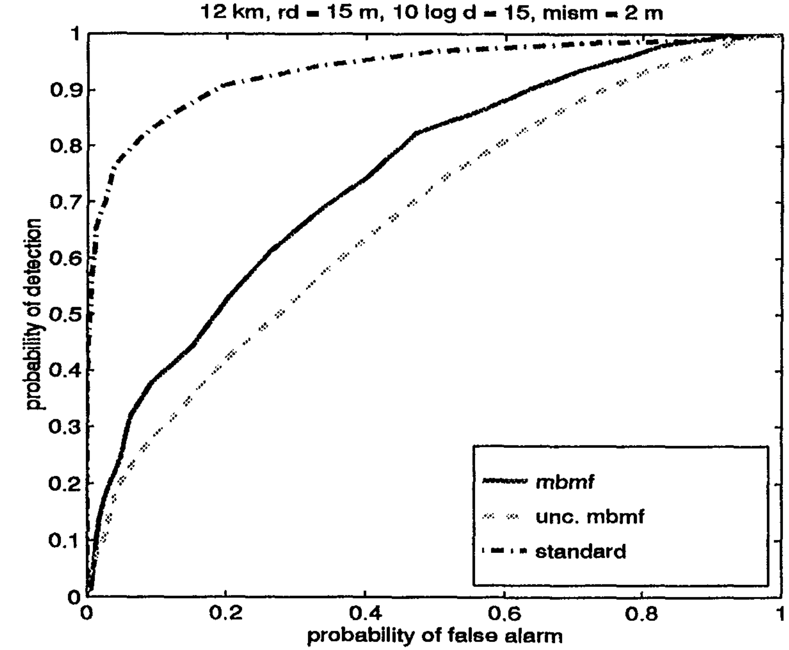

mismatch =
2 m

Optimum MBMF Detection

likelihood ratio detector:

$\lambda = \left(\int p_1(\mathbf{r} / \theta)\ w(\theta)\, d\theta\ /\ p_0(\mathbf{r}) \right) \gtrless$ threshold

θ: unknown parameters (environment, location)
$w(\theta)$: prior information on θ

OUFP (Richardson and Nolte, Shorey and Nolte)

optimization: Monte Carlo methods
OUFP *(Shorey, Nolte, Krolik)*
Genetic Algorithms *(P. Gerstoft)*
Simulated Annealing *(Collins, Kuperman – N. Frazer – Michalopoulou, Porter)*

Summary

–the detection performances of the *standard* matched filter and the model based matched filter were compared

–the *standard* matched filter is environment– and frequency–dependent

intermodal dispersion
intramodal dispersion
absorption
center frequency of source pulse

– the *model based* matched filter is preferable to the standard detector but is computationally intensive and requires accurate modeling of the involved uncertainty

Acknowledgments

This work was sponsored by the Office of Naval Research (Ocean Acoustics), and Defence Research Establishment Atlantic.

ACTIVE MATCHED-FIELD TRACKING (AMFT)

Homer Bucker, NRaD, San Diego CA

A primary objective of a shallow water ASW system is to develop tracks of an underwater submarine. In matched-field tracking (J. Acoust. Soc. Amer. 96, 3809-, 1994) outputs of a set of passive sensors are processed to find the best match, i.e. highest correlation, between elements of the measured covariance matrix and those calculated for possible tracks. The processing is straight-forward but computer intensive because all data collected over a time window of several minutes and a frequency band of several hundred Hz must be carefully examined.

In the active case, similar methods can be used. However, the definition of a covariance matrix needs to be extended (J. Acoust. Soc. Amer. 99, 1784-, 1996). Fortunately, only a small fraction of the data collected need be compared to calculated values. This is because with a given set of pulses and a postulated track, only a few received values are compared with those calculated.

The matched-field tracking algorithm was tested with a simulation of an ASW system operating in a 200 m shallow water channel with a sloping bottom. As shown in the figure, three surface ships and a submarine at 100 m depth were pinged upon (160 pings) for a period of 5 minutes. The source was a vertical string of 10 transducers emitting 500 ms CW pings at a frequency of 250 Hz and was located at the origin of the coordinate system. When transmitting, each transducer radiated 10 w of power so that the average radiated power in the water is less that 3 watts. The receiving array consisted of 7 sensors collocated with the transducer string. There were 7 hydrophones, with 5 sensors located along the X axis and 2 sensors along the Y axis. The ambient noise level was 65 dB/μPa.

The results of the simulation are shown in the figure where the best track for an under-water target is shown as the curve of dots that closely follows the submarine track (the solid curve). The estimated track is a composite of 16 associated segments. Each segment is defined by six coordinates, the x and y values of the end points, a constant depth, and a measure of the curvature. This track has a correlation value of 0.178 and the estimated target depth varied between 98 and 107 m. The simulated depth was 100 m.

In the current example, 10 multi-paths were used to calculate the simulated signals received at the array and 2 multi-paths were used to calculate the sound pressures for the covariance elements associated with possible tracks While the results seem promising, at sea experiments are needed to validate the AMFT concept.

Submarine & 3 Surface Ships in Shallow Channel with Sloping Botom

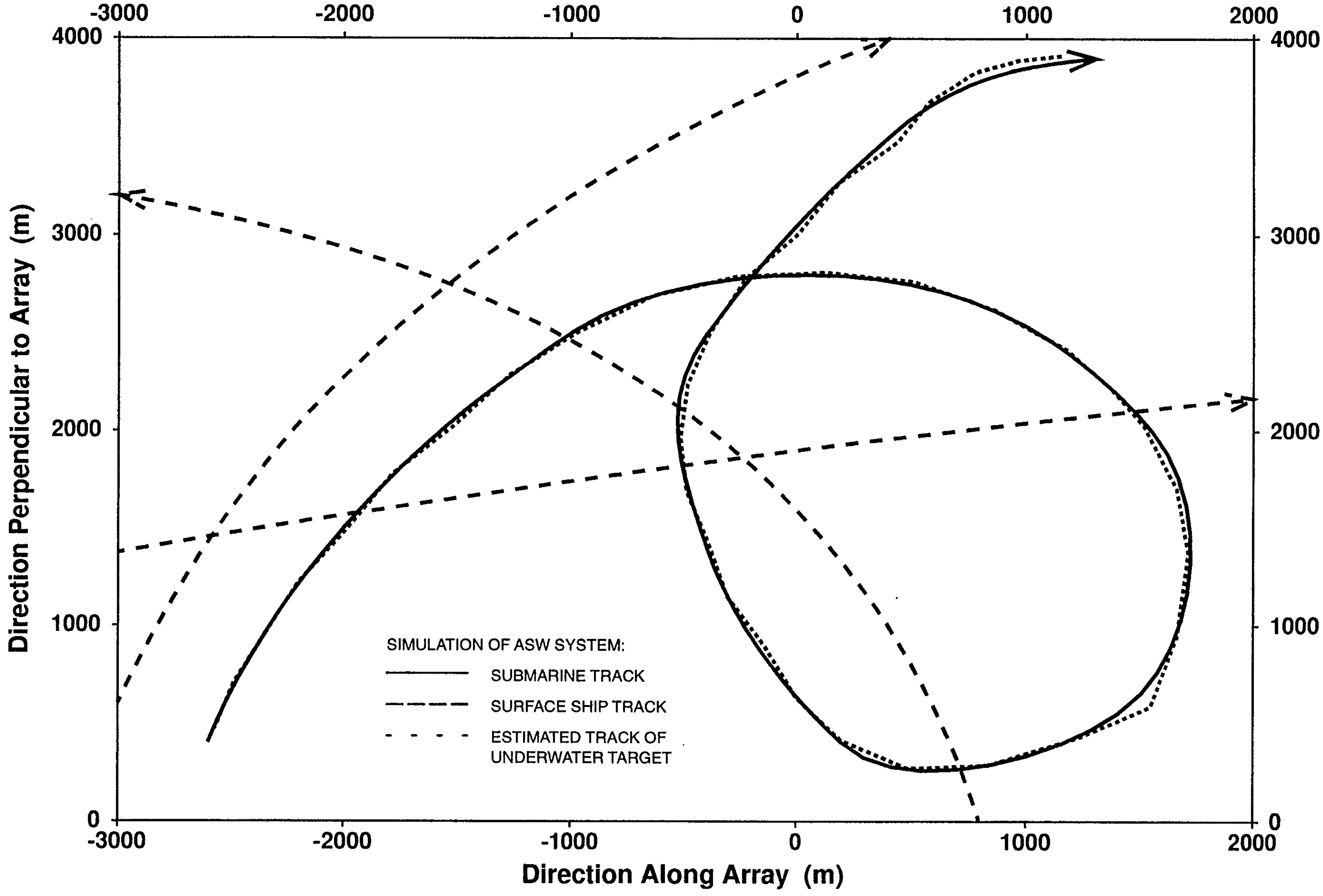

Matched-Field Track-Before-Detect (TBD) Processing using SWellEX Data

Paul A. Baxley
Naval Command Control and Ocean Surveillance Center
Research, Development, Test and Evaluation Division
San Diego, CA 91935 USA

12 June 1996

Abstract

Matched-field tracking is a generalization of matched-field processing in which the time evolution of matched-field ambiguity surfaces are used in a source-track search. Track-before-detect (TBD) processing makes use of this technique to extract source track information so that the source signal function can be reconstructed, rendering it more detectable. The detection enhancement produced by a shift-then-average TBD algorithm is investigated for multitone source-tow data recorded near San Diego during the first and third shallow water evaluation cell experiment (SWellEX-1 and 3). The source-tow (approximately 3 knots in SWellEX-1 and 5 knots in SWellEX-3) traversed a range-independent radial from a FLIP-mounted vertical line array (VLA). Previously masked sources were rendered detectable in ambient noise (SWellEX-3) and in the presence of a single loud interferer (SWellEX-1). Frequency averaging appears to improve TBD performance primarily for cases in which the source peak is masked by strong sidelobes of noise sources, as occurs when an interferer passes nearby.

Introduction

Matched-field tracking [1] is a generalization of matched-field processing in which the time evolution of matched-field ambiguity surfaces are used in a source-track search. Matched-field track-before-detect (TBD) processing [2],[3] makes use of this technique to extract source track information so that the source signal function can be reconstructed, rendering it more detectable. For a vertical line array in a range-independent environment and a constant range-rate source, this may be accomplished via a simple shift-then-average approach, which yields the track parameters corresponding to the optimal source track. The objective of this work is to experimentally demonstrate the feasibility of this approach and to evaluate the performance gains which may be achieved. This was accomplished via the analysis of multitone source-tow data recorded near San Diego during the first and third shallow water evaluation cell experiment (SWellEX-1 and 3).

I Scenario assumptions

For the most general case of an asymmetric environment or array, matched-field trackers must search for optimal tracks from a set of those defined by curves connecting all combinations of potential start and end points. If an assumption of constant speed is assumed, these curves collapse to straight lines. A maximum correlation between measured and predicted pressures arriving at the array sensors over a given time interval yields the optimal track, characterized by 6 track parameters; namely, the three cartesian coordinates of the start and end points of the track. A full search for this case is obviously a formidable problem and will often be computationally restrictive.

A significant reduction of the search space occurs for the case of VLA processing in a symmetric (range-independent) environment. For such a scenario, the array cannot distinguish the azimuthal direction of incoming energy. Consequently the search is transformed into a search for a family of tracks, which may occur at any azimuth. The search space for this case is reduced to four parameters: the range and depth at either the start or end of the track, the speed, and the range at the closest point of approach (CPA). If the search is further restricted to tracks along a radial line connecting the source and VLA, which is equivalent to a constant range-rate assumption, then the range at CPA is zero and the track parameters are reduced to three: the range and depth at either the start and end of the track, and the range-rate. This last scenario was selected for this analysis for several reasons. First, the computational load is greatly reduced allowing for more efficient evaluation of the TBD techniques. Second, good quality SWellEX data with such scenarios is readily available. In addition, the SWellEX tracks analysed in this study are along nearly constant bathymetry lines, so that range-dependent or three-dimensional effects need not be considered. Third, this scenario allows for the use of a simple shift-then-average TBD technique, to be discussed shortly. And lastly, while this shift-then-average technique implies on-radial tracks, it can still be applied approximately to off-radial tracks at long range, since the range-rate varies slowly in this case.

II Processing Technique

Given the above track scenario assumption, the optimal track can be obtained by a simple shift-then-average process applied to consecutive matched-field ambiguity-surface time samples. Assume that over a given time interval M samples of acoustic pressure are measured at each phone of the VLA. A measure of the match between the observed pressure p_n^o at each phone of an N-phone array and the predicted pressure $p_n(\mathbf{x})$ at the same phones for an assumed source location vector $\mathbf{x}$ is given by the Bartlett estimator, defined as

$$\hat{B}_{BART}(\mathbf{x}) = \frac{\sum_{n=1}^{N} \sum_{m=1}^{N} p_m^*(\mathbf{x}) R_{mn} p_n(\mathbf{x})}{\sum_{n=1}^{N} |p_n(\mathbf{x})|^2 \, E\left[\sum_{n=1}^{N} |p_n^o|^2\right]}. \tag{1}$$

where $E[\,]$ denotes the time average (expected value), and $R_{mn} = E[p_m^o p_n^{o*}]$, the time-averaged cross-spectral matrix of the observed pressures. Application of (1) to each measured time sample yields a range-depth ambiguity surface for each sample. For a source moving at a constant depth, the range of the source peak will change, according to its motion trajectory, for each sample. Averaging the surfaces without taking into account this motion will therefore cause a degradation in the correlation level of the source peak. If however, the surfaces are shifted in the range direction by the amount the source has moved for each time interval, the source peaks in each surface will be aligned and the source peak will experience no degradation upon averaging. By searching through different range rates, which defines the shift between surfaces, the range-rate at which a maximum average correlation occurs can be determined. In this way the gain in detectability achievable by averaging for a stationary source ($5logM$) can be regained for the case of the moving source.

III SWellEX 1 and 3 environment

SWellEX 1 and 3 took place near the southern California coast in approximately 50-200 m water southwest of Point Loma, the entrance to San Diego Harbour. The data analyzed in this work is that measured on Marine Physical Laboratory (MPL) SRP VLAs during mutlitone source tows along tracks of nearly constant water depth (198 m) and flat bathymetry. Figure 1 shows the experimental area along with the VLA location and source tracks performed on a single day (August 17, 1993) during SWellEX-1. The VLA location during SWellEX-3 was nearly identical to that in SWellEX-1. Only the track northward from the VLA in Fig.1, and a similar northward track during SWellEX-3, are considered in this work. For each data set, 80 minutes of data was processed using 8192-point FFT's with 50% overlap, resulting in a total of 1775 FFT samples.

Depth (m)	Compressional Wave Speed (m/s)	Shear Wave Speed (m/s)	Density (g/cm^3)	Compressional Wave Attenuation (dB/(kmHz))	Shear Wave Attenuation (dB/(kmHz))	Bottom Type
198.0	1572.368	0.0	1.76	0.20	0.0	sediment
228.0	1593.016	0.0	1.76	0.20	0.0	
228.0	1881.000	0.0	2.06	0.06	0.0	mudstone
1028.0	3245.800	0.0	2.06	0.06	0.0	
1028.0	5200.000	0.0	2.66	0.02	0.0	basement

Table 1: Geoacoustic Model for SWellEX1,3.

With a sampling rate of 1500 sample/sec, the FFT binwidth was 0.1831 Hz, the FFT length was 5.46 sec, and the time between consecutive samples was 2.73 sec.

The SRP VLA contained 48 elements with a 88.125-m aperture for SWellEX-1 and 63 elements with a 116.25-m aperture for SWellEX-3. The element spacing was 1.875 m in both cases. The SWellEX-1 analysis considered the full 48-element VLA, whereas the SWellEX-3 analysis used only a subset of 8 elements, spaced by 11.25 m, with a total aperture of 90 m. The reason for using the sparser array in the latter case was the discovery in previous SWellEX-1 analyses [4] that there are only about 17 propagating modes present in the data at the highest frequency (195 Hz), thus requiring a sparser vertical sampling of the field. While a number of tonals were transmitted in each experiment, only a strong 95-Hz tonal in SWellEX-1 and a weak 125-Hz tonal in SWellEX-3 are considered in this analysis.

Superimposed on Fig. 1 is the sound speed profile measured near the VLA site. Measurements at other sites and times varied little from this profile. The geoacoustic model in Table 1 is thought to adequately represent the bottom properties for this region and was used in the generation of all replicas. This model is close to that determined by inversion studies to be optimal [4].

IV Experimental results

The 95-Hz tonal in the SWellEX-1 data was selected for analysis primarily because the occurrence of periods of very high signal-to-noise ratio, which facilitate an assessment of the gain in detectibility obtainable via the TBD technique. However, the presence of a strong unknown interferer during a portion of the track also allowed for a performance analysis of the practical case of a low signal-to-interferer-ratio scenario. The 125-Hz tonal in the SWellEX-3 data was one of the quietest tonals of that experiment, providing for a practical analysis of the TBD technique at low signal-to-noise ratios (between -2 and -12 dB). The shift-then-average TBD technique was applied to these 80-min range-independent data sets using averaging times of 0.32 min (8 samples), 0.68 min (16 samples), 1.41 min (32 samples), 2.87 min (64 samples), 5.78 min (128 samples). Averaging intervals were overlapped by 75% in all cases. The SWellEX-1 results will be presented first, followed by the SWellEX-3 results.

IV.1 SWellEX-1 results

The TBD technique searches through potential range-rates, via the shift-then-average process, to obtain the range-rate and source range and depth at the start or end of the optimal track corresponding to the maximum correlation in the set of averaged surfaces. The results of the range-rate search for the SWellEX-1 data are summarized in Fig. 2, which plots maximum correlation in an averaged surface (corresponding to a particular range rate) versus the number of ambiguity surface samples included in the average for the full duration of the source-tow track. Figure 2a corresponds to 16 samples (0.68 min), Fig. 2b to 32 samples

(1.41 min), Fig. 2c to 64 samples (2.87 min), and Fig. 2d to 128 samples (5.78 min). The first column is for the 95-Hz tonal, while the second column is for a noise-only bin centered at 96 Hz, included to facilitate an understanding of tracker in this noise environment. Each point in these plots has a maximum correlation level, range-rate, and source range and depth (at the end of potential track) associated with it. It is first observed for the 95-Hz tonal that with a low number of samples (8 to 32) a track is clearly discernible for times less than 25 min and greater than about 45 min. This gap in track detection is caused by the presence of an interferer during this period. The noise-only plots (second column) clearly indicate the presence of a high-speed ($>$ 10 m/s) track in the noise, which masks the source-tow track in the signal+noise plots (first column). In addition, even though the track is detectable for the low number of averages, the range-rate resolution is poor. Increasing the averaging time (number of samples) however, simultaneously increases the range-rate resolution and renders the track more detectable during the time of the interferer. These effects are more clearly observed in the maximum correlation versus range-rate curves obtained at specific times in Fig. 3. Figure 3a plots the results for the case in which the averaging time begins at 30 min from the start of the track, during the period in which the interferer is present, while Fig. 3b plots the results for the case in which the averaging time begins at 52 min from the start of track, when the interferer is absent and signal-to-noise level is high. When the interferer is present and the averaging time is small, peaks in the maximum correlation versus range-rate curves tend toward the higher range rates, under the influence of the interferer, as observed in the noise-only curves. However, when the number of samples exceeds 32 (1.41 min), the source peaks along the true track have reinforced each other to the point of being detectable above the interferer's track, resulting in a peak at the true range rate of 1.6 m/s. The maximum correlation versus range rate curves for the high signal-to-noise period following the period of the interferer demonstrates nicely the improved range-rate resolution with increased averaging time. The noise-only results during this period indicate no preferential range rate, except at the higher averaging times when the peaks tend toward a zero range rate. This tendency towards a zero range rate in the noise is also observed in Fig. 2, for periods before and after the interferer. This effect is probably caused by the fact that source of noise during these periods is long-range shipping, whose range-rates vary slowly over the averaging times considered. However, as a ship moves into short range, as with the interferer, peaks move away from the zero range-rate position.

In practice, the tracker could be automated to report the maximum correlation from among the set of averaged surfaces (corresponding to candidate range-rates) and the range-rate, source range, and source depth associated with that maximum. Figure 4 presents such automated results, as a function of number of samples, over the source-tow period. Each dot in this figure represents the result for an averaging interval, while the solid curves in the range and depth versus time plots represent the known values. Note that for the small averaging times, while there is considerable scatter, there is a definite congregating of data near the true values, except when the interferer is present (between 25 and 45 min). Also, note that the speed (or range rate) data is, on average, offset from the zero range-rate position when the interferer is absent, but is scattered over a wide range of values when it is present. As averaging time is increased, the estimated range rate is observed to coalesce into the true range rate (approximately 1.6 m/s on average), even when the interferer is present. This is accompanied by a more frequent determination of the correct range and depth at of the source over time.

It is common practice to average ambiguity surfaces without regard to source motion in an effort to enhance the signal-induced features of the ambiguity surface relative to the noise-induced features. Because of the broadness of the peaks in Figs. 2 and 3 in the range-rate direction for the smaller averaging times, it is evident that some track detection enhancement may be realized even for a zero range-rate assumption. This is because for small averaging times the peaks have not moved enough, relative to each other, to cause significant degradation upon averaging. For the higher averaging times (e.g. 128 samples), however, the consecutive peaks become separated enough to cause degradation upon averaging. In Figs. 2 and 3, this is manifested as a higher resolution in range-rate, so that the zero-range rate line no longer intersects the peaks. These effects are illustrated in the automated results in Fig. 5, which plots the optimal peak data versus times for a zero range rate (no TBD) assumption for 64 and 128 samples. It is observed that the 64-sample case is nearly as good as that obtained with TBD in Fig. 4d. This is because the source peaks have not moved much relative to each other and the zero range-rate line in Figs. 2 and 3 intersect the maximum peak.

For 128 samples, however, the track performance without TBD in Fig. 5b has been destroyed, because the source peaks are separated enough in time to destroy the average peak, and the zero range-rate line in Figs. 2 and 3 no longer intersect the maximum peak. When track motion is taken in account using this averaging time (Fig. 4e), however, the good tracking performance is maintained. The maximum correlation versus time plots in Fig. 4 include a dashed curve representing the value obtained without TBD (zero range rate). Note the significant enhancement in correlation for the 128-sample case.

Little is known from data logs or other sources regarding the true location and speed of the interferer disrupting the signal between 25 and 45 min into the track. It is interesting, therefore, to let the tracker estimate these parameters for the interferer. This was done by applying the TBD technique to data in a noise-only bin centered at 96 Hz. Figure 6 plots the automated optimal peak results versus time and averaging time. For low averaging times, it is difficult to distinguish any clear track; the data is largely scattered over all values of range rate, range, and depth. As averaging time is increased, however, the range rate is seen to coalesce toward the zero range rate, except during the period of the interferer, in agreement with the behavior observed in Figs. 2 and 3. Range and depth, however, do not appear to follow any preferential pattern when the interferer is absent, suggesting again that the noise during these periods in probably caused by long-range shipping. A close observation of the 128-sample case reveals a track estimate for the interferer has been successfully obtained. For a period beginning roughly at 25 min from the start of the track, source range for consecutive times steadily increases from about 1 to 6 km, source depth remains constant at about 30 m, and range-rate congregates around 10 m/s. It is impossible to ascertain the accuracy of these estimates, since the true values for the interferer are not known, and since the interferer was most likely in a range-dependent environment away from the source track. In addition, the peaks tracked may actually be sidelobes of the true interferer peak. Nevertheless, these results demonstrate the feasibility of this approach for practical scenarios.

It is well known that if a single source is transmitting a signal with a frequency content in some band of frequencies, then ambiguity surface sidelobes can be reduced by averaging single-frequency ambiguity surfaces across the band [5],[6],[7]. To investigate how this technique effects the TBD results, the shift-then-average technique was applied to four-tone (70, 95, 145, and 195 Hz) frequency-averaged signal+noise surfaces and to four-noise-only-bin (71, 96, 146, and 196 Hz) frequency-averaged noise-only surfaces. Results are presented in Figs. 7 and 8, in the same format as Figs. 2 and 3. Comparing these two sets of figures, it is observed that the range-rate resolution has been increased for the frequency-averaged surfaces, since a stricter requirement of obtaining a match for all four frequencies has been instituted. In addition, it is observed that the track is now much more detectable during the period when the interferer is present for all averaging times. This is particularly striking for the comparison between Fig. 3a and Fig. 8a. This track detection enhancement may be attributable to two possible influences. First, the signal-to-interferer ratios may be higher for the additional tonals, resulting in less interference upon averaging. Second, the frequency-averaging has greatly reduced the sidelobes of the interferer, allowing the source to be more detectable. A comparison of the noise-only plots in Figs. 2 and 3 with those in Figs. 7 and 8 reveals that the responses at high range rate disappear when frequency averaging is used, suggesting that the tracker is actually tracking the interferer's sidelobes in the single-frequency case. The observed track enhancement is most likely of combination of these effects.

Figure 9 presents the automated optimal track-parameter estimates for the frequency-averaged case, in the same format as Fig. 4. It is observed that extremely good track detection and parameter estimation are obtained by the combination of TBD and frequency-averaging techniques, for the reasons discussed above. But in addition to a reduction of the interferer's sidelobes, the source's sidelobes have also been reduced, decreasing the possibility that a source sidelobe will be mistaken for the true source location. It is particularly striking that very good track estimates can be obtained with small averaging times. It should be noted, however, that these results are for high signal-to-noise ratios, at least when the interferer is absent. The analysis of the SWellEX-3 data will demonstrate that these results are difficult to achieve at low signal-to-noise ratios.

IV.2 SWellEX-3 results

The SWellEX-3 data analysed here was characterized by a low signal-to-noise ratio over the entire extent of the track. During the first 30 min of the 80-min data set, the tow ship loitered near a constant position awaiting commencement of the source-tow. As the source moved away from the VLA (with a speed between 2.4 and 2.9 m/s) along a near-radial track, the signal-to-noise ratio decreased further, providing a good test on the limits of TBD detection performance. Figures 10 and 11 present maximum correlation in averaged surfaces versus range rate and time for this data, using the same format in Figs. 2 and 3. Results for three periods, (a) 35 min, (b) 45 min, and (c) 55 min from the beginning of the data set, are included in Fig. 11 so that the performance as the source moves away from the VLA can be observed. Figure 10 indicates that the nearly constant position of the source during the loitering period is clearly detected. However, during the period of the source tow, the track is difficult to detect at the lower averaging times. The track at a range-rate of about 2.5 m/s (at times greater than 30 min) clearly becomes more detectable as averaging time is increased, and is accompanied by an increase in range-rate resolution. Note also the tendency of noise-only results toward a zero range rate over the entire time period, suggesting that the noise in this data set is caused primarily by long-range shipping. These results are particularly striking in Figs. 11a and 11b. Note in both Figs. 10 and 11, however, that as the source moves further away from the VLA, the averaging times considered here become inadequate for track detection. For example, Figure 11c fails to detect a track at 55 min from the start of the data set using 128 samples.

Figure 12 presents automated track-parameter estimates for optimal tracks, in the same format used in Fig. 4. As with the SWellEX-1 data, track detection and parameter estimation improves with increasing averaging time. While the true data values are not plotted in this figure, it should be stated that the detected tracks agree well with the known positions of the source during this period. The loitering period, extending out to about 30 min, is clearly detected, characterized by a near-zero range rate, a nearly-constant source range (between 2 and 2.5 km), and a nearly-constant source depth of about 50 m. Beyond the loitering period, the 2.5-m/s source tow track is detected out to a time of about 50 min when 128 samples (5.87-min averaging time) are used. Note that the source-tow track is not detected using less than 32 samples. Beyond 50 min, the tracker is operating on the ambient noise, with range-rate tending toward zero, and source range and depth possessing considerable scatter.

Results for the case in which TBD techniques are not implemented and the surfaces are averaged without searching for range rate (zero range-rate assumed) are presented for 64 and 128 samples in Fig. 13. Track detection performance is seen to be seriously degraded, failing to detect the source tow after 30 min. The reason this failure occurs for a smaller number of samples than observed for the SWellEX-1 data in Fig. 5 (64 instead of 128) is the fact the source speed was larger in the SWellEX-3 data (2.5 m/s instead of 1.6 m/s). This greater speed produces a greater separation between consecutive source peaks, resulting in greater degradation upon averaging without shifting. Alternatively, the peak in the maximum correlation versus range rate plots of Figs. 10 and 11 have moved further to the right, decreasing the tendency of the zero range-rate line to intersect that peak.

The effect of frequency averaging on the TBD results for SWellEX-3 data is demonstrated in the maximum correlation versus range rate curves of Fig. 14, for which four low level tonals (77, 125, 157, and 205 Hz) were averaged. The curves are seen to be sharper and cleaner, as a result of the added requirement that a match for all tonals be obtained. The lower correlations for small averaging times in Figs. 14b and 14c, compared to the 125-Hz results in Fig. 11b and 11c, suggest that sidelobes from noise sources are being reduced by the frequency averaging process at these times. Nevertheless, the failure to detect the track at 55 min from the start of the data set (Fig. 14c) implies that a single large sidelobe of a noise source is not responsible for the masking the of source, as was the case for the interferer in SWellEX-1. Instead, the low level of the source has caused its correlation peak to lie below many noise sidelobes, of varying level, and frequency-averaging is unable to reduce all of these sidelobes sufficiently to render the track detectable.

Finally, the automated optimal track-parameter estimates for the frequency-averaged case are presented in Fig. 15. The decreased variability of the estimates, particularly during the first 50 min of the data set, is a result of source sidelobe reduction, which decreases the possibility that a source sidelobe will be mistaken for the true source location. But once again, it is observed that frequency-averaging fails to detect the track past the 50-min limit.

V Detectibility

A measure of the matched-field detection performance is provided by the detectability (or deflection ratio), defined as

$$D = 10\, log\, \frac{P_{signal+noise} - \mu_{noise}}{\sigma_{noise}} \tag{2}$$

where $P_{signal+noise}$ is the peak level in a range-depth ambiguity surface (averaged or not) containing signal and noise, and μ_{noise} and σ_{noise} are the mean and standard deviation, respectively, of a range-depth ambiguity surface containing only noise, but at the same time and frequency (or close to that frequency) as the signal+noise surface. Detectability is best measured experimentally at high signal-to-noise ratio, when $P_{signal+noise}$ is known to be signal-induced. When noise masks the signal to the point in which the maximum peak in the signal+noise surface is noise-induced, the expression above no longer measures the detectability of the signal. The detectability of the signal in low signal-to-noise ratio environments can be measured if the exact source location is known and $P_{signal+noise}$ above is replaced by the correlation at that location. In this paper, however, only detectability measurements at high signal-to-noise ratio will be considered.

A high signal-to-noise-ratio case suitable for calculating detectability is that following the period of the interferer in the SWellEX-1 data. Figure 16 plots the measured detectability, with and without TBD, versus the number of samples used in averages beginning 52 min from the start of the track. Also shown is the $5logM$ theoretical gain expected from incoherently averaging the surfaces; on the log_2 scale used, theory predicts a gain of 1.5 dB per doubling of the sample size. First it is observed that when source motion is not taken into account (zero range-rate assumption), the detectability first rises gradually according to theory and then drops sharply as the number of samples is increased. The drop is caused by the source peaks for a moving source not being aligned when averaging over time, as already discussed. When shift-then-average TBD technique is used, however, the theoretical gain is retained because the TBD technique seeks to realign the source peaks for the optimal range-rate. The gain in detectability for the TBD case is about 8 dB above that obtained without TBD when 128 samples are used. The higher-than-theoretical gain obtained using TBD at the larger averaging times is most likely caused by changes in source or noise levels over the averaging time.

Conclusion

The feasibility of using a shift-then-average TBD technique to improve detection and obtain source track parameters has been experimentally demonstrated using SWellEX-1 and 3 source-tow data. A track originally masked by a strong interferer was successfully detected, and its source parameters accurately estimated, using this technique in the SWellEX-1 data. When the interferer was absent, the gains in detectability were shown to agree well with the theoretical value expected for incoherently averaging the surfaces. Gains in detectability of 8 dB over a that obtained by averaging without regard for the source motion were realized. Previously masked tracks were also detected in the low signal-to-noise SWellEX-3 data set, which was characterized by long-range shipping noise. The gain with TBD over that without TBD was greater for the SWellEX-3 data because of the greater speed of the source-tow. Frequency averaging appears to improve TBD performance primarily in cases in which the source peaks are masked by strong sidelobes of noise sources, as occurs when a strong interferer passes nearby.

An extension of this technique to the problem of detecting short-range off-radial tracks is currently underway.

Acknowledgements

This work was supported by the Office of Naval Research, ONR-321US.

References

[1] BUCKER, H. P. Matched-field tracking in shallow water. *Journal of the Acoustical Society of America 96* (1994), 3809-3811.

[2] BAXLEY, P. A., WILLIAMS, R. B., HODGKISS, W. S. Track-before-detect matched-field processing. *Journal of the Acoustical Society of America 94* (1993), 1844-1845.

[3] BAXLEY, P. A. Experimental evaluation of matched-field track-before-detect (TBD) processing in shallow water. *Journal of the Acoustical Society of America 98* (1995), 2931.

[4] BAXLEY, P. A., AND BOOTH, N. O. Matched-field replica model optimization and bottom property inversion using multitone signals in shallow water *Journal of the Acoustical Society of America 97* (1995), 3290-3291.

[5] BAGGEROER, A. B., KUPERMAN, W. A., AND SCHMIDT, H. Matched field processing: Source localization in correlated noise as an optimum parameter estimation problem *Journal of the Acoustical Society of America 83* (1988), 571-587.

[6] BACHMAN, R. T., SCHEY, P. W., BOOTH, N. O., AND RYAN, F. J. Geoacoustic databases for matched-field processing: preliminary results in shallow water off San Diego, California *Journal of the Acoustical Society of America 99* (1996), 2077-2085.

[7] BOOTH, N. O., BAXLEY, P. A., RICE, J. A., SCHEY, P. W., HODGKISS, W. S., D'SPAIN, G. L., AND MURRAY, J. J Source localization with broadband matched-field processing in shallow water *IEEE Journal of Oceanic Engineering 21* (1996), page numbers to be determined.

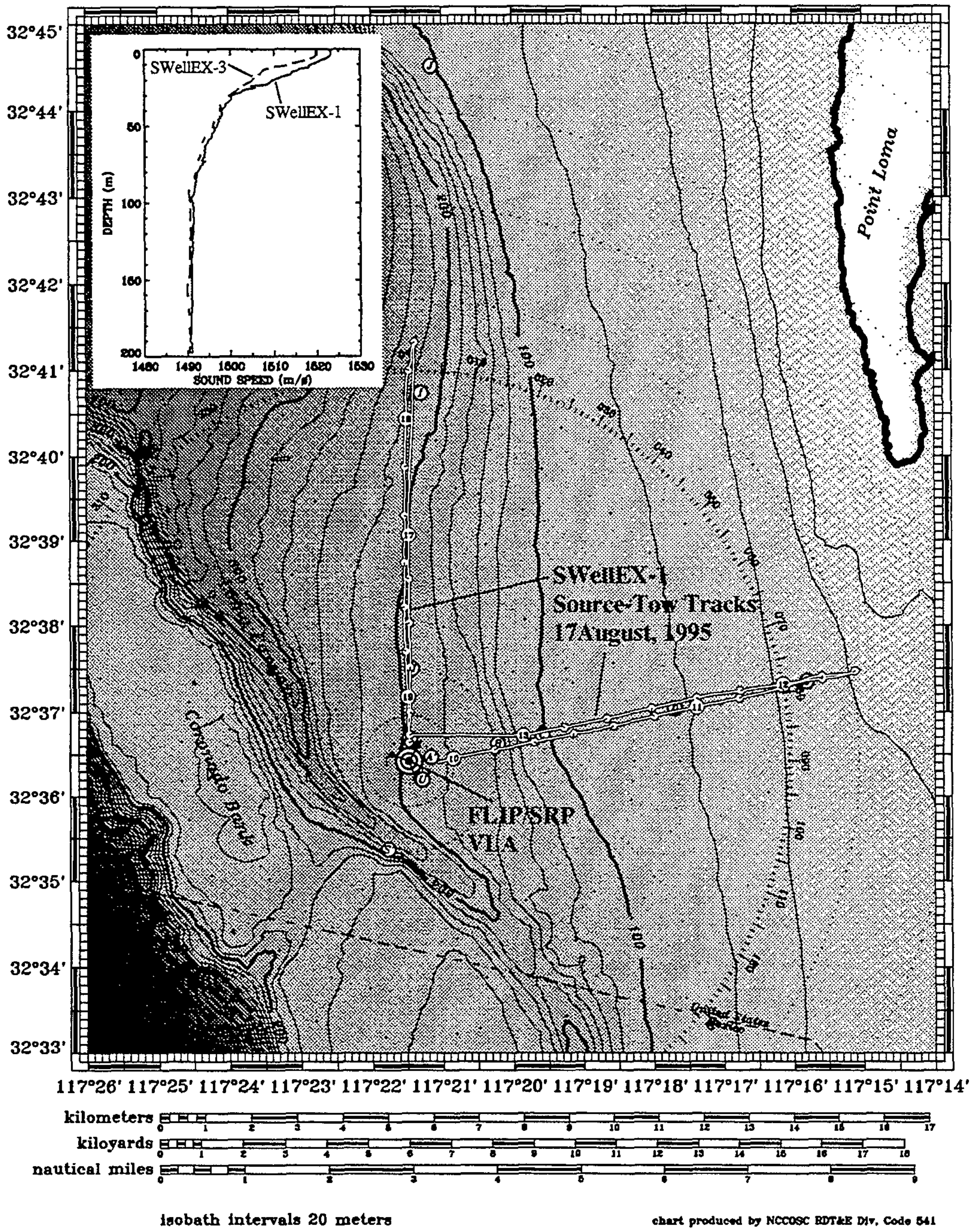

Figure 1. Location of SWellEX-1 and SWellEX-3. Concentric rings mark location of FLIP/SRP VLA. Source-tow tracks shown are those for SWellEX-1 on 17 August, 1995. *Insert:* Sound speed profiles measured at FLIP location in SWellEX-1 (solid) and SWellEX-3 (dashed).

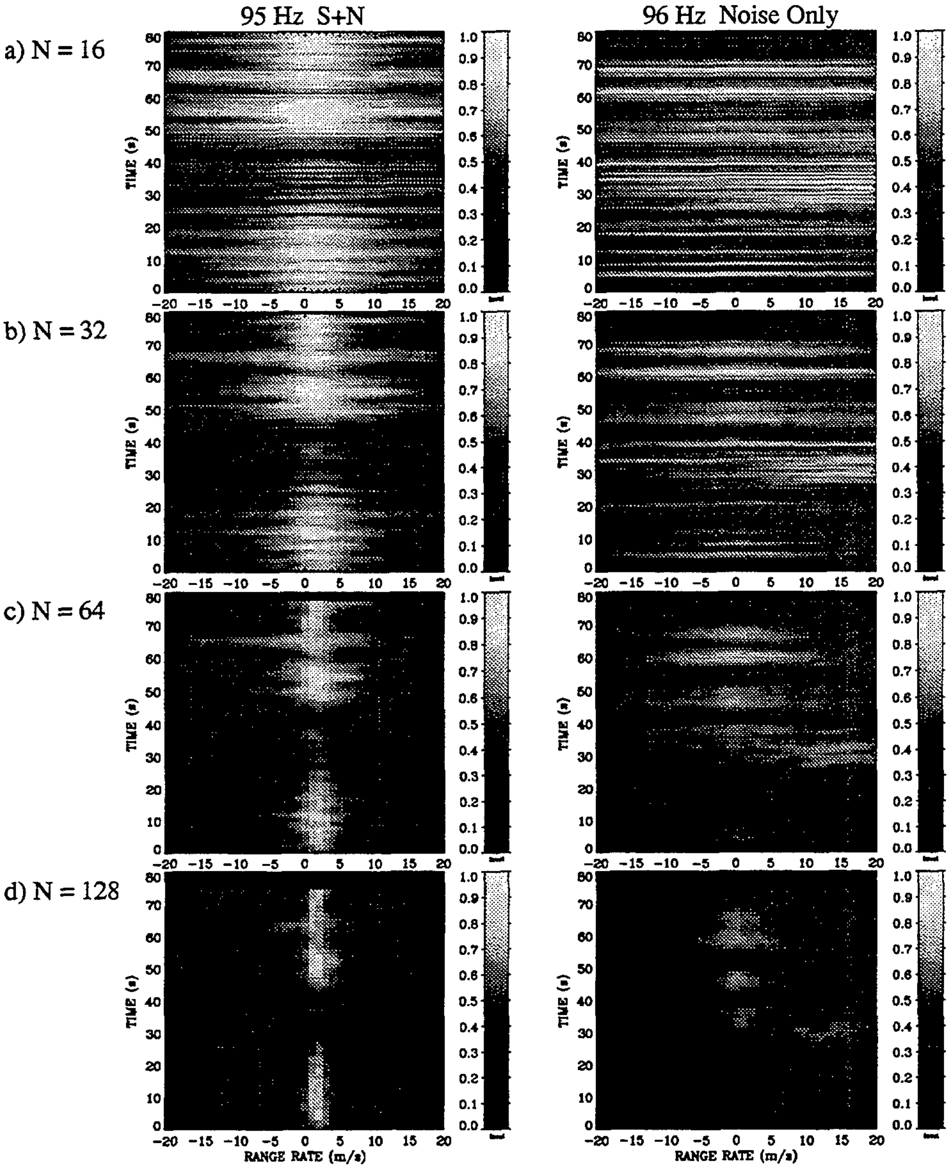

Figure 2. Maximum correlation in shifted-then-averaged range-depth ambiguity surfaces versus candidate range rate, time, and number of samples in average for SWellEX-1 source-tow track. Number of samples in average = (a) 16 (0.68 min), (b) 32 (1.41 min), (c) 64 (2.87 min), and (d) 128 (5.78 min). First column is for the 95-Hz tonal while second column is for a noise-only bin centered at 96 Hz.

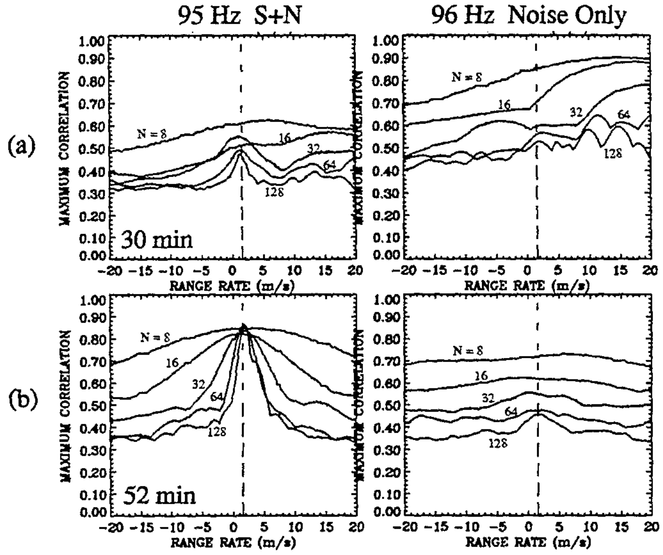

Figure 3. Maximum correlation in shifted-then-averaged range-depth ambiguity surfaces versus candidate range rate and number of samples in average at two periods of SWellEX-1 source-tow track. Averaging begins at (a) 30 min, and (b) 52 min, from the start of the track, In each row, the first column is for the 95-Hz tonal (S+N) while the second column is for a noise-only bin centered at 96 Hz. The vertical dashed lines mark the true range rate of the source-tow during each period.

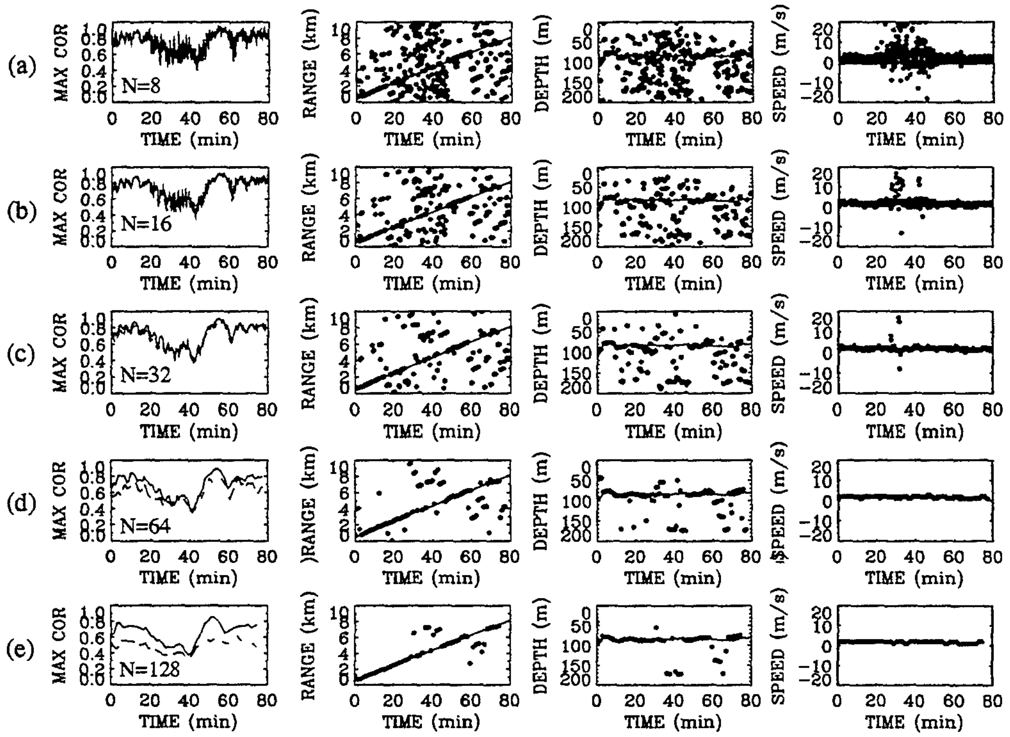

Figure 4. TBD (shift-then-average) automated detection results for 95-Hz tonal in SWellEX-1 source-tow track. Maximum correlation and range, depth, and speed (range rate) at maximum are plotted versus time for (a) 8 samples (0.32 min), (b) 16 samples (0.68 min), (c) 32 samples (1.41 min), (d) 64 samples (2.87 min), and (e) 128 samples (5.78 min) in average. The dashed curves in the maximum correlation versus time plots are those obtained without TBD, as in Fig. 5.

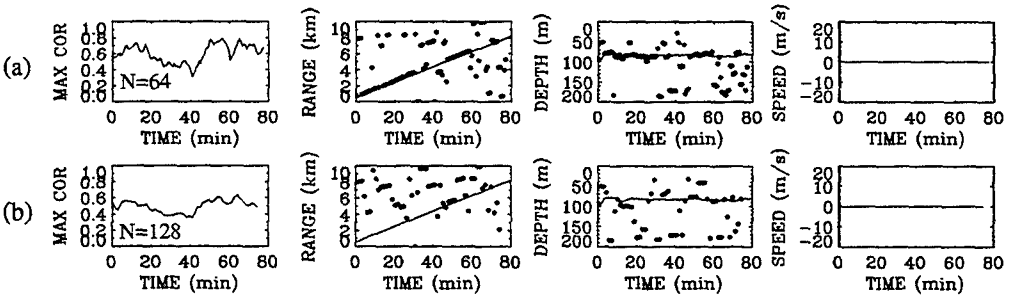

Figure 5. Automated detection results obtained without TBD (averaging ambiguity surfaces without searching for range rate) for the 95-Hz tonal in SWellEX-1 source-tow track. Maximum correlation, range at maximum correlation, and depth at maximum correlation are plotted versus time for (a) 64 samples and (b) 128 samples in average. The speed (or range rate) in the last column is always zero for this case.

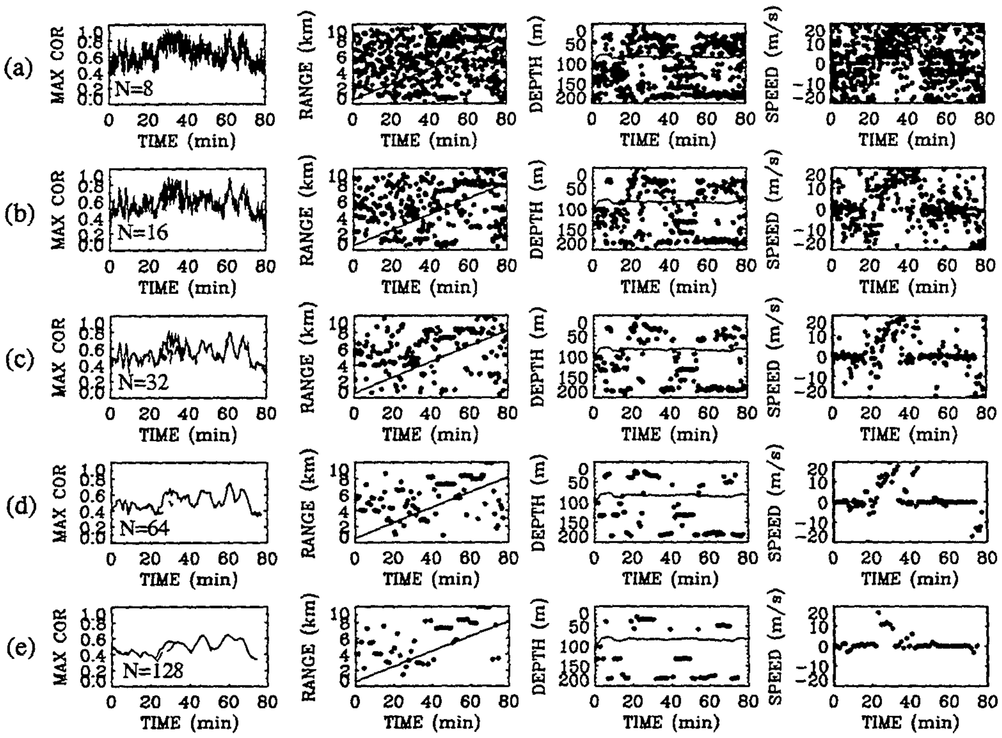

Figure 6. TBD (shift-then-average) automated detection results for 96-Hz noise-only bin in SWellEX-1 source-tow track. Maximum correlation and range, depth, and speed (range rate) at maximum are plotted versus time for (a) 8 samples (0.32 min), (b) 16 samples (0.68 min), (c) 32 samples (1.41 min), (d) 64 samples (2.87 min), and (e) 128 samples (5.78 min) in average. The dashed curves in the maximum correlation versus time plots are those obtained without TBD.

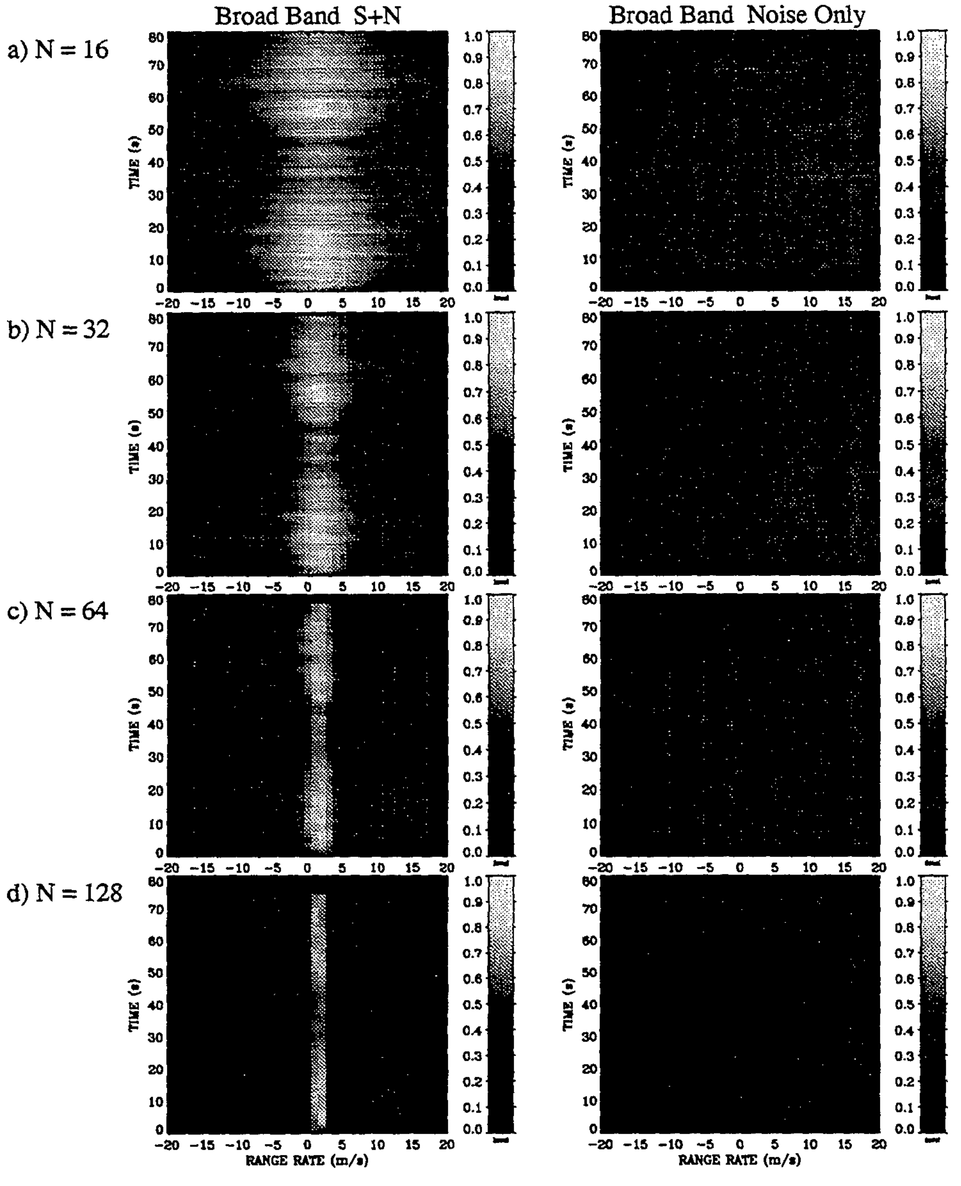

Figure 7. Maximum correlation in frequency-averaged shifted-then-averaged range-depth ambiguity surfaces versus candidate range rate, time, and number of samples in average for SWellEX-1 source-tow track. Number of samples in average = (a) 16 (0.68 min), (b) 32 (1.41 min), (c) 64 (2.87 min), and (d) 128 (5.78 min). First column is for a four-tone (70, 95, 145, and 195 Hz) frequency average, while second column is for a four noise-only-bin (71, 96, 146, and 196 Hz) frequency average.

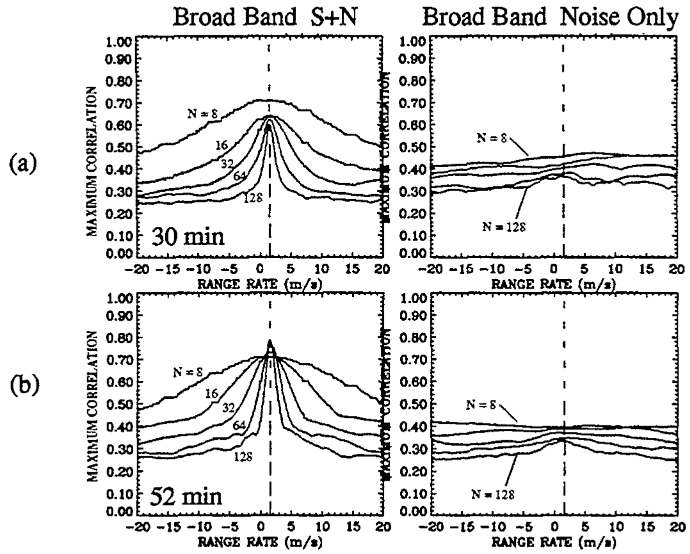

Figure 8. Maximum correlation in frequency-averaged shifted-then-averaged range-depth ambiguity surfaces versus candidate range rate and number of samples in average at two periods of SWellEX-1source-tow track. Averaging begins at (a) 30 min and (b) 52 min from the start of the track. In each row, the first column is for a four-tone (70, 95, 145, and 195 Hz) frequency average while second column is for a four noise-only-bin (71, 96, 146, and 196 Hz) frequency average. The vertical dashed lines mark the true range rate of the source-tow during each period.

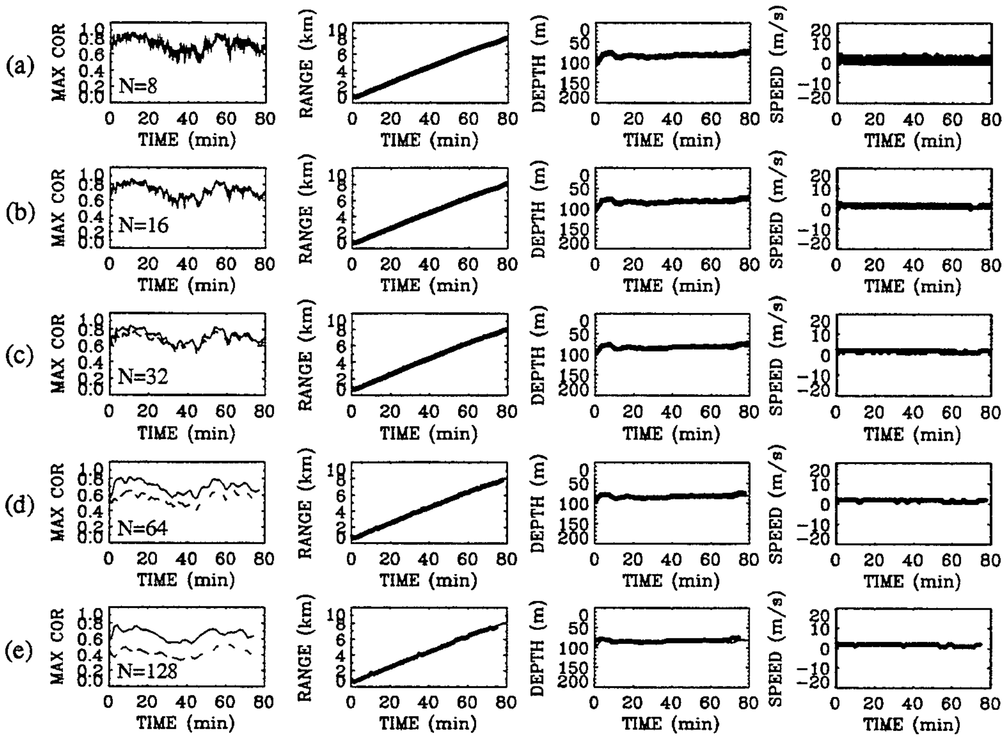

Figure 9. TBD (shift-then-average) automated detection results for four-tone frequency average in SWellEX-1 source-tow track. Maximum correlation and range, depth, and speed (range rate) at maximum are plotted versus time for (a) 8 samples (0.32 min), (b) 16 samples (0.68 min), (c) 32 samples (1.41 min), (d) 64 samples (2.87 min), and (e) 128 samples (5.78 min) in average. The dashed curves in the maximum correlation versus time plots are those obtained without TBD.

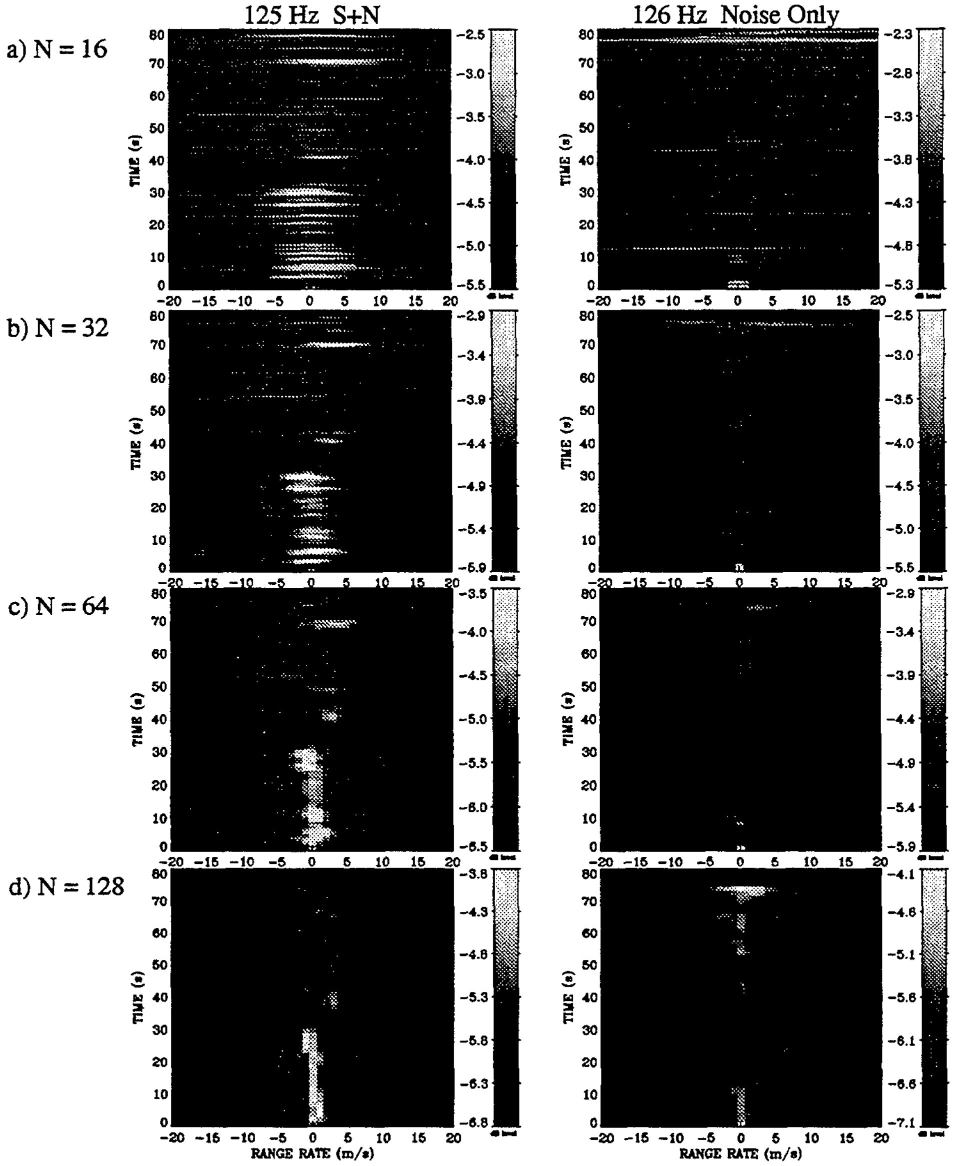

Figure 10. Maximum correlation in shifted-then-averaged range-depth ambiguity surfaces versus candidate range rate, time, and number of samples in average for SWellEX-3 source-tow track. Number of samples in average = (a) 16 (0.68 min), (b) 32 (1.41 min), (c) 64 (2.87 min), and (d) 128 (5.78 min). First column is for the 125-Hz tonal while second column is for a noise-only bin centered at 126 Hz.

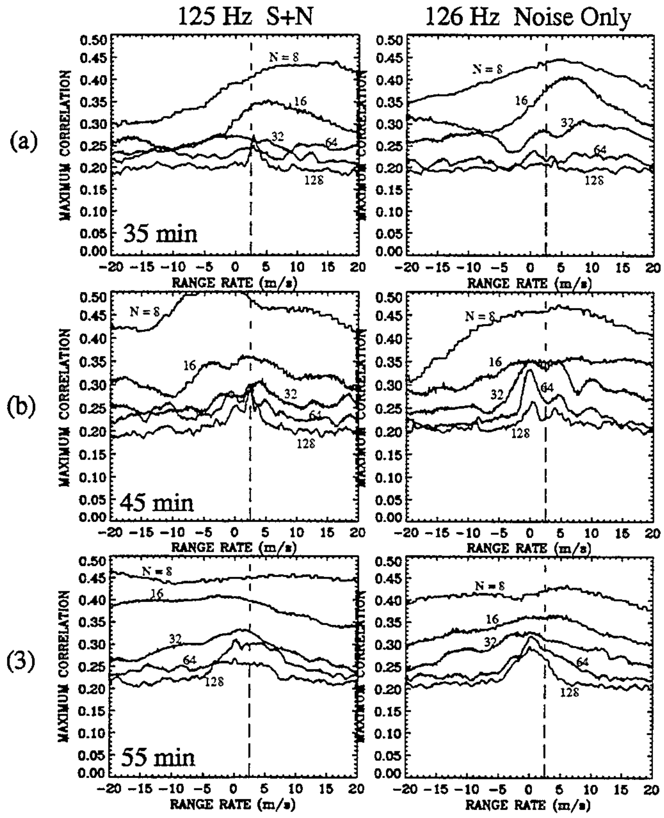

Figure 11. Maximum correlation in shifted-then-averaged range-depth ambiguity surfaces versus candidate range rate and number of samples in average at three periods of SWellEX-3 source-tow track. Averaging begins at (a) 35 min, (b) 45 min, and (c) 55 min, from the start of the track,. In each row, the first column is for the 125-Hz tonal (S+N) while the second column is for a noise-only bin centered at 126 Hz. The vertical dashed lines mark the true range rate of the source-tow during each period.

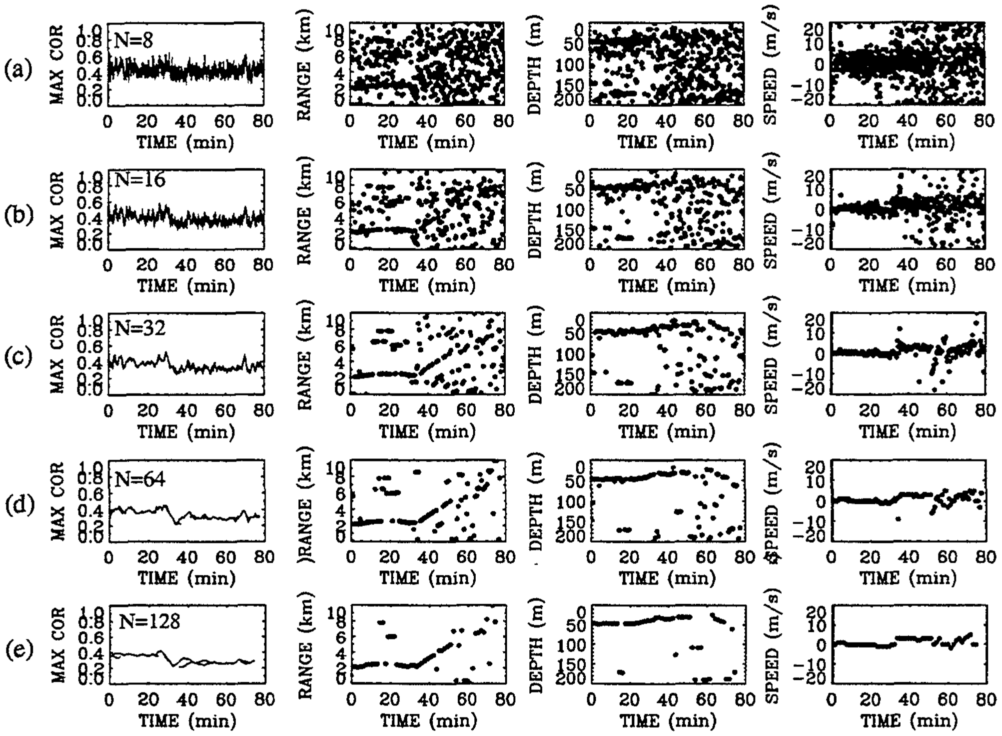

Figure 12. TBD (shift-then-average) automated detection results for 125-Hz tonal in SWellEX-3 source-tow track. Maximum correlation and range, depth, and speed (range rate) at maximum are plotted versus time for (a) 8 samples (0.32 min), (b) 16 samples (0.68 min), (c) 32 samples (1.41 min), (d) 64 samples (2.87 min), and (e) 128 samples (5.78 min) in average. The dashed curves in the maximum correlation versus time plots are those obtained without TBD, as in Fig. 13.

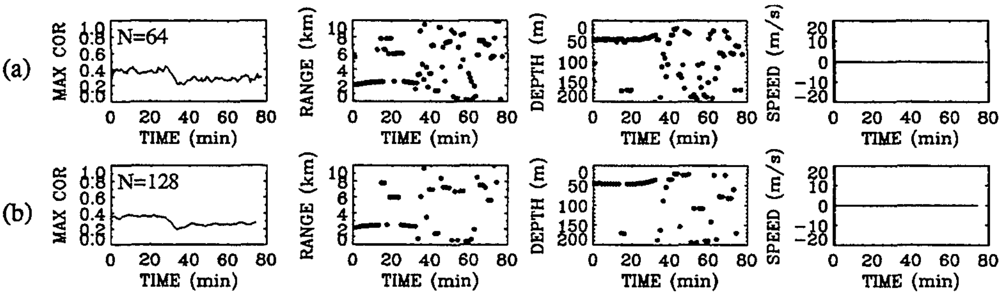

Figure 13. Automated detection results obtained without TBD (averaging ambiguity surfaces without searching for range rate) for the 125-Hz tonal in SWellEX-3 source-tow track. Maximum correlation, range at maximum correlation, and depth at maximum correlation are plotted versus time for (a) 64 samples and (b) 128 samples in average. The speed (or range rate) in the last column is always zero for this case.

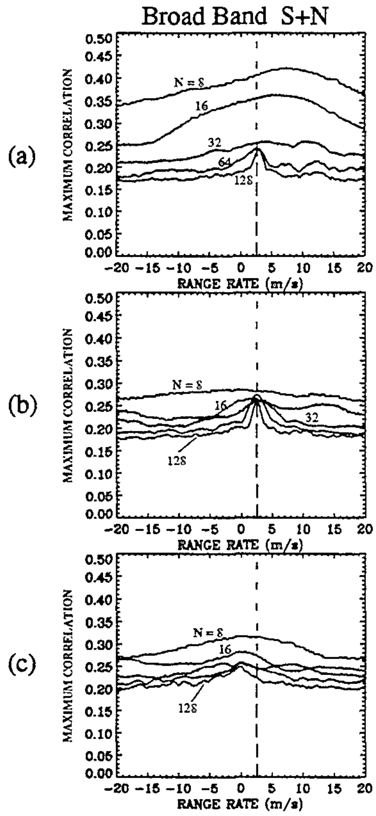

Figure 14. Maximum correlation in frequency-averaged shifted-then-averaged range-depth ambiguity surfaces versus candidate range rate and number of samples in average at three periods of SWellEX-3 source-tow track. Averaging begins at (a) 35 min, (b) 45 min, and (c) 55 min, from start of track. Frequency average is over four tones (77, 125, 157, and 205 Hz). The vertical dashed lines mark the true range rate of the source-tow during each period.

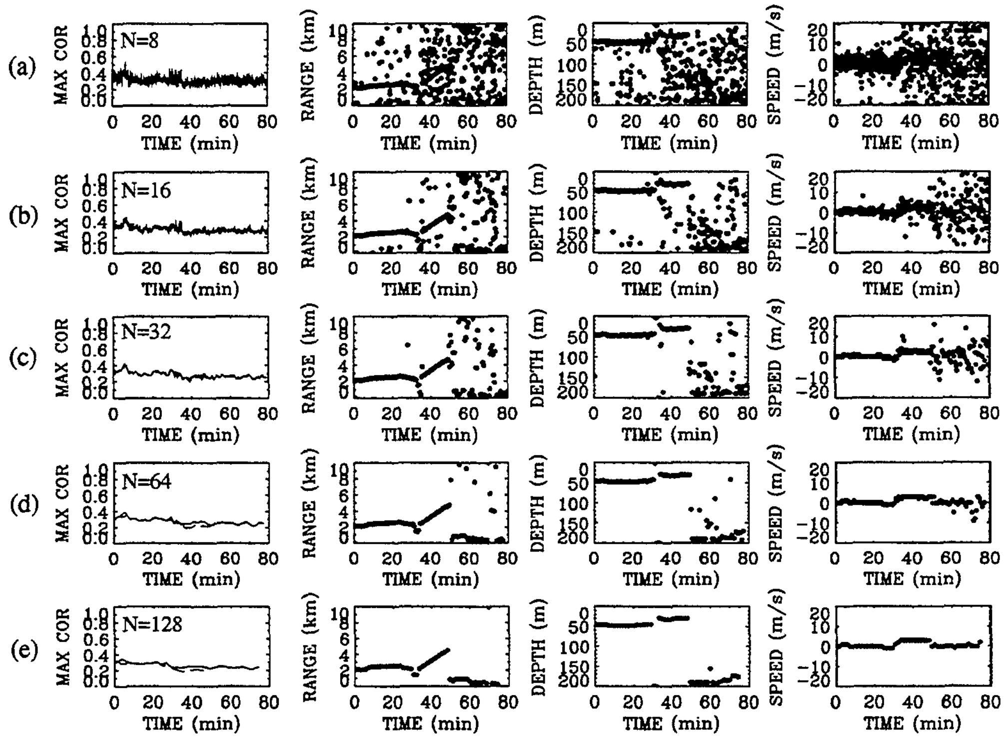

Figure 15. TBD (shift-then-average) automated detection results for four-tone (77, 125, 157, and 205 Hz) frequency average in SWellEX-3 source-tow track. Maximum correlation and range, depth, and speed (range rate) at maximum are plotted versus time for (a) 8 samples (0.32 min), (b) 16 samples (0.68 min), (c) 32 samples (1.41 min), (d) 64 samples (2.87 min), and (e) 128 samples (5.78 min) in average. The dashed curves in the maximum correlation versus time plots are those obtained without TBD.

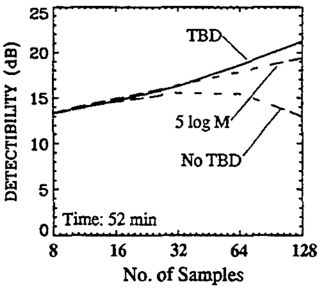

Figure 16. Detectibility versus number of samples (averaging time) for averages beginning at 52 min from start of track in SWellEX-1. *Solid line:* TBD (shift-then-average) result. *Top dashed line:* 5 log M theoretical gain curve, where M = number of samples. *Bottom dashed line:* No TBD (averaging without range-rate search) result.

Matched-Field Processing in a Range-Dependent Shallow Water Environment in the North-East Ocean: Array Tilt Considerations

M.L. Yeremy, J.M. Ozard,
Defence Research Establishment Atlantic
Esquimalt Defence Research Detachment
FMO Victoria, B.C., Canada V0S 1B0

N.R. Chapman
University of Victoria
Victoria, B.C., Canada, V8W 2Y2

and
M.J. Wilmut
Royal Military College
Kingston, Ontario, Canada K7K 5L0

3 SEPTEMBER 1996

Introduction

A series of ocean acoustic experiments referred to as the PACIFIC SHELF Sea Trial was completed in September, 1993 by the Defence Research Establishment Pacific (DREP), Victoria, B.C. and the Applied Research Laboratory (ARL), University of Texas at Austin. The purpose of these experiments was primarily to evaluate Matched-Field Processing (MFP) techniques in a Pacific shallow water environment. Efficient Linear Tracker (ELT) results from this trial are shown in this paper, for data collected from a Vertical Line Array (VLA) during an experiment where a Continuous Wave (CW), multi-frequency source was towed from a shallow-water position on the shelf towards the VLA, further downslope. In particular, the effect that array tilt has on these results is investigated.

I Environment, Data and Processing

The towed source's track, shown in Figure 1, began 11.9 km from the array, on the continental shelf where the water column depth was $\sim$ 150 m and proceeded down the continental slope towards the VLA at a source depth of $\sim$ 30 m. The VLA consisted of 16 phones which were equispaced at 15 m and spanned the depths from 90 m to 315 m at a water column depth of $\sim$ 375 m. Both the source and receiver positions were recorded from GPS (Global Positioning System) and Radar which each have range errors of $\sim$ 200 m. The experiment was conducted during a time when there was considerable shipping traffic.

The multi-frequency, CW source emitted three tones, 45, 70 and 72 Hz, each of a different and specified Source Level (SL). The source levels at 45 Hz and 70 Hz were typical of a strong line on a merchant vessel

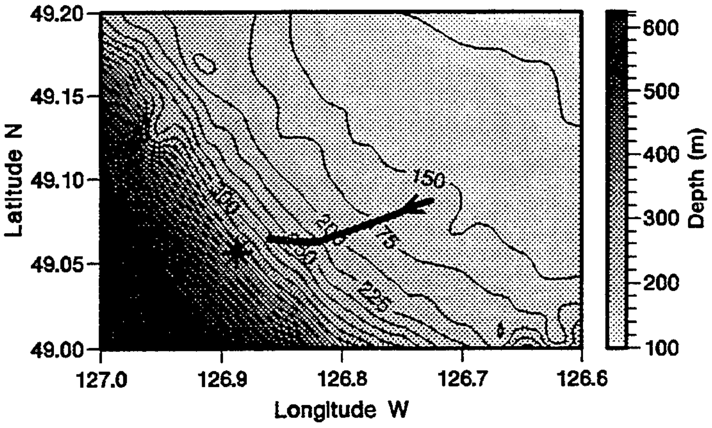

Figure 1: The line overlaying the region's bathymetry, represents the towed source's track with the tow direction shown by the arrow. The star shows where the VLA was located at the beginning of the experiment.

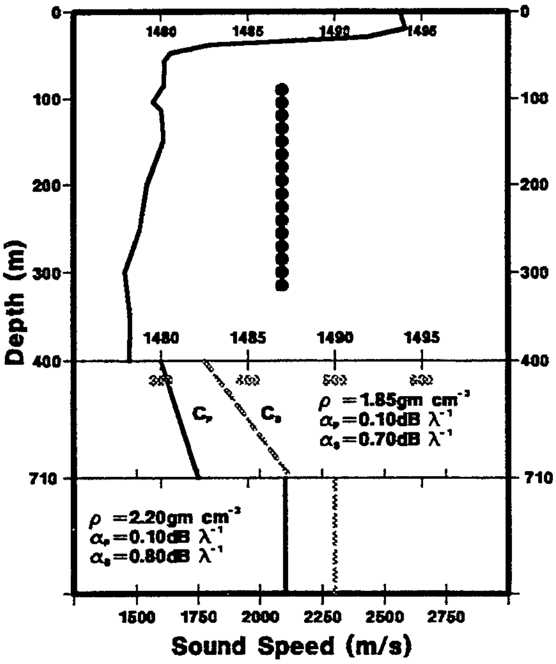

Figure 2: The sound-speed profiles used in the environmental model are shown as well as the hydrophone depths. The shear speed (shaded and dashed) and the compressional speed (dark and solid) are shown on the two lower abscissa scales.

while the 72 Hz line was 20 dB lower. The results obtained for a strong (45 Hz) and a weak (72 Hz) line are presented here.

The environment model used here is shown in Figure 2. It was based on an XSV (Expendable Sound Velocimeter) measurement which was cast eighty minutes prior to the experiment's start time, and typical bottom acoustic values (e.g. Ref. [1] and [2]) for the vicinity of the array.

Recent, seismo-acoustic results from another PACIFIC SHELF experiment [3] indicate that the sediment thickness and compressional speed of the bottom half-space in the location of the VLA are similar to the values used for this analysis. It is likely that these bottom parameters vary from the continental shelf to the slope regions. However, in this study, we did not have sufficient knowledge of the environment to model the range-dependent acoustic parameters. Therefore, with the exception of the bathymetry shown in Figure 1, the environment model used here was the same at all ranges. More detailed information of the environment model and the data are given in [4].

The results presented here are from an ELT [5] which finds constant depth linear tracks and estimates their track Signal-to-Noise Ratios (SNR) from a collection of MFP ambiguity surfaces which are sampled in time. The ELT operated on a Bartlett ambiguity surface and is described further in [4].

The adiabatic normal mode approximation was the method used to calculate the range-dependent replica fields required for MFP. One advantage of using this method is that field calculations are fast and efficient if the acoustic modal data are precomputed. This approach does not include effects due to mode-coupling, and inaccuracies commonly associated with these effects for a range-dependent environment were addressed in [4] for this experiment. It was found that mode-coupling inaccuracies were negligible except at the steepest slopes of the environment. Nevertheless, the MFP results had very high correlations with average values of about 0.85 and 0.70 for the respective 45 and 72 Hz data and with correlations as high as ~ 0.95 for the stronger received signals at 45 and 70 Hz. This indicates that mismatch from the replica field does not substantially debilitate the MFP results despite the mode-coupling inaccuracies introduced with the adiabatic normal-mode method.

ORCA [6], [7], [8] was the normal mode program used for modelling the environment's modal data. It was used primarily because the data were collected in a shallow water environment which likely had low sea floor shear speed properties.

In Figure 1, it can be seen that the ship track was not along a radial path relative to the VLA but consisted of two segments with path directions on different headings. For this study, the replica field was approximated as a radial instead of modelling and tracking in 3-dimensions. Because a linear tracker assumes a constant velocity source, the data were analysed separately for the two segments which are distinguished by the heading of the towed source. The far and near-range segments refer to the furthest and nearest segment relative to the VLA.

II Results

II.1 Performance Assuming No Array Tilt

The two segments were processed with the ELT algorithm assuming source depths between 10 and 100 m in 10 m-depth increments. The maximum track SNR at both frequencies for both segments is plotted in Figures 3 and 4 respectively. The SNR threshold for a Probability of False Alarm of $\sim 10^{-4}$ at any specific depth is found to have a linear-scale SNR level of 8 (i.e., 9 dB) when the noise is spatially white [9], [5]. A signal of 9 dB SNR would have a probability of detection of 0.75. In this analysis, the source track is identified by the largest track SNR over all depths which is also greater than this threshold. The source track SNR levels for the 72 and 45 Hz far-range segment were respectively 34 and 107 (15.3 and 20.3 dB), and for the near-range segment these were 98 and 661 (19.9 and 28.2 dB). The information presented in Figures 3 and 4 indicates that the tracks from both frequencies are well above the threshold SNR level and that they accurately identify the source depth except for the 45 Hz far-range segment for which a depth 10 m too shallow was indicated. For this array design, spatial leakage causes the track SNR to be above the threshold at non-source depths. However the maximum SNR occurs within 10 m of the known source depth.

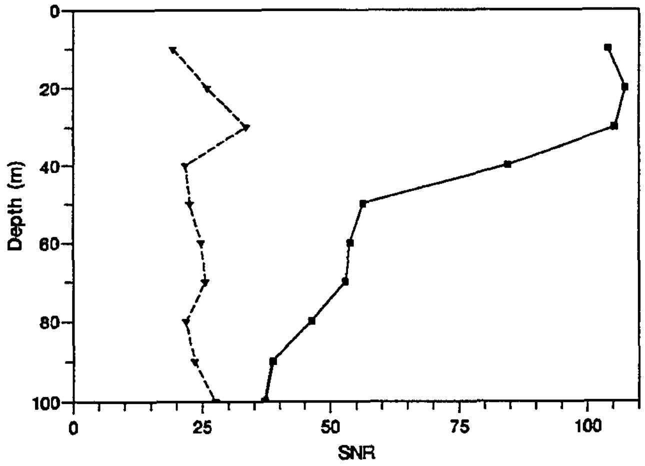

Figure 3: The maximum track SNR (linear scale) at each depth, for the far-range segment at 45 Hz (solid) and 72 Hz (dashed).

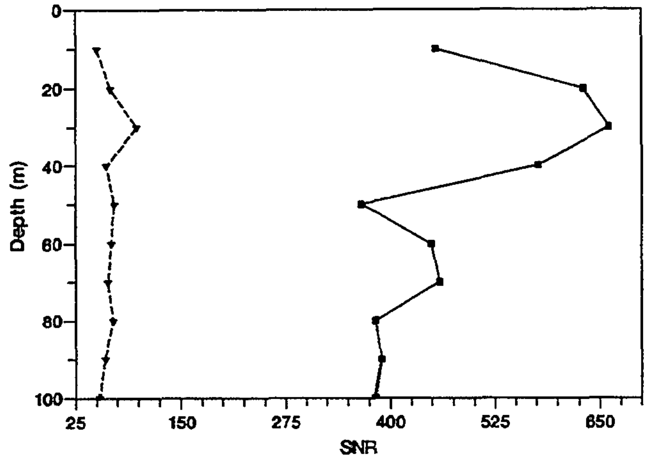

Figure 4: The maximum track SNR (linear scale) at each depth, for the near-range segment at 45 Hz (solid) and 72 Hz (dashed).

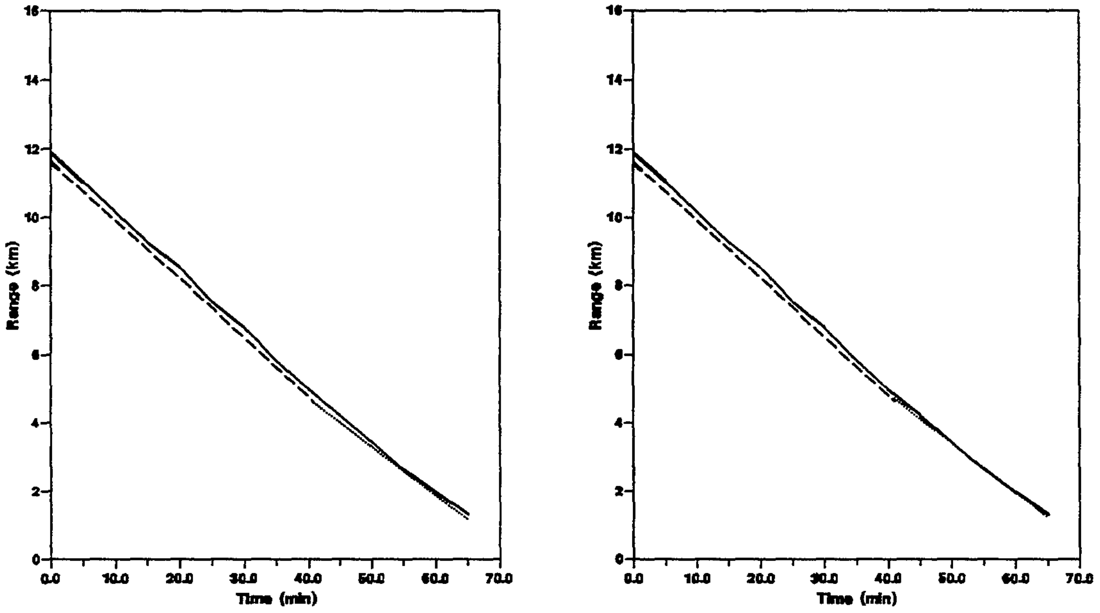

Figure 5: The 45 and 72 Hz track results are shown in the respective left and right-hand side plots. The dashed and dotted lines are the top acoustic tracks from the respective far and near-range segments and the solid line is the GPS track.

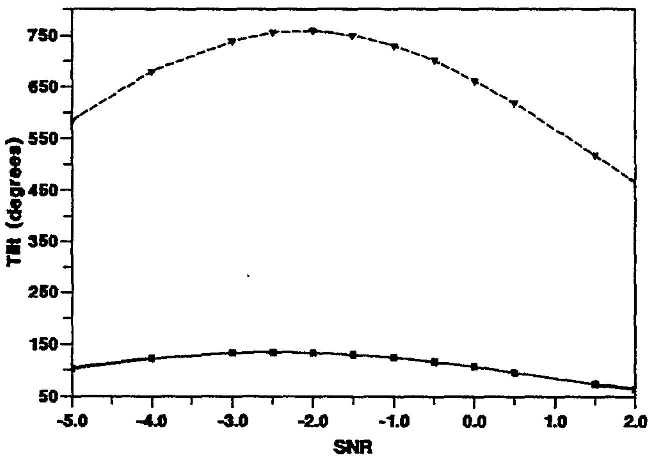

Figure 6: Maximum track SNR at 45 Hz, for the far (solid line) and near-range (dashed line) segments as a function of array tilt.

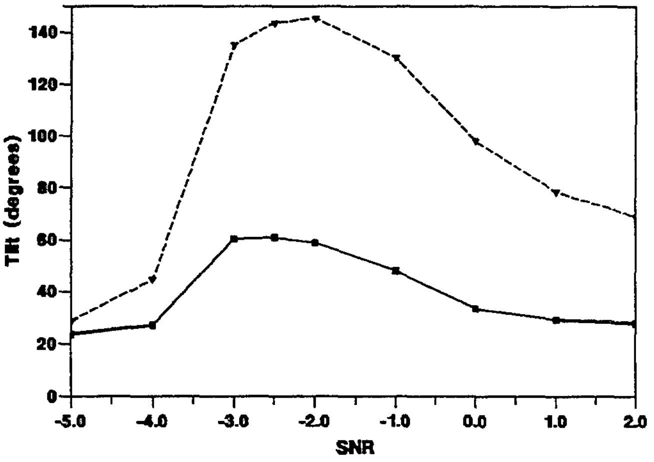

Figure 7: Maximum track SNR at 72 Hz, for the far (solid line) and near-range (dashed line) segments as a function of array tilt.

Figure 5 shows the range-time tracks for the 45 Hz and 72 Hz signals. The most significant track estimates for both data segments (at the depth of the maximum SNR in Figures 3 and 4), are plotted as dashed and dotted lines while the target track, which is based on GPS measurements, is represented as a solid line. The most significant tracks for both the 45 and 72 Hz signal are essentially coincident with the GPS track. Variations between the GPS and acoustic tracking are at most 300 m and the maximum difference between the 72 and 45 Hz estimated tracks was 130 m. The agreement between GPS and acoustic tracks at both frequencies is remarkably good considering that many other sources were present in the region. In this respect, it should also be noted that the SNR at 72 Hz is low.

It should be noted that at the depths with the largest track SNRs the top 25 track-positions and SNR are very similar to each other. At depths with lower track SNR the most significant track positions are much more ambiguous since noise and depth mismatch affect these weaker sidelobe tracks to a greater extent.

II.2 Performance for Different Array Tilts

A MFP mismatch study [10], [11] found that array tilt was a significant source of mismatch. In this study, tracking was performed for different array tilts in the plane of the radial. The results are shown in Figures 6 and 7 for the respective 45 and 72 Hz data. The track SNR is consistent with an array tilt of $\sim -2.5^\circ \pm 0.5^\circ$ as the SNR improved by as much as ~ 2.5 dB for the 72 Hz data and ~ 1.0 dB for the 45 Hz data compared to no array tilt. Here, a positive tilt implies that the bottom array element is closest to the source. The 72 Hz track estimates were nearer to the GPS ranges by as much as 120 m while the 45 Hz results improved by 30 m over the whole track for a -2.5° tilt. Higher correlations were also observed. Similar array tilts (2.6°) were measured near the time of the experiment. However, the orientation of the array tilt was unknown.

III Conclusions

MFP with tracking was applied to data from a north-east Pacific shallow water environment. Despite incomplete environmental knowledge of the geoacoustic bottom profile, high MFP correlations were obtained. The average of the largest correlations for high SNR data at 45 Hz and low SNR data at 72 Hz were about 0.85 and 0.70 respectively. These results are very encouraging since they imply that detailed environmental knowledge may not be a prerequisite for source localization with MFP. Better environmental information would likely enable higher track SNRs and result in improved source tracking. This has been demonstrated here, to an extent, for the case where array tilt considerations improved the SNR.

An Efficient Linear Tracker which finds the most significant tracks (over the set of ambiguity surfaces) was found to agree with the GPS source range within 300 m and known source depth within 10 m at both frequencies. The accuracy of these track ranges was comparable to the GPS source range error of 200 m. The track SNRs for the 72 and 45 Hz far-range segment were respectively 12.7 and 19.2 dB while for the near-range segment these were respectively 17.7 and 28 dB. The SNR and track estimates were improved by as much as 2.5 dB and 120 m respectively, when array tilt was taken into account. The highest SNR levels attained occurred for a modelled array tilt which was very near recorded array tilt values. When this tilt was modelled, the estimated track was even closer to the GPS track. In all cases the tracker contributed to system gain due to the integration of MFP ambiguity surfaces over time, despite the presence of mismatch. These encouraging results may be improved by a better knowledge of the environment, 3D modelling and the use of multiple frequencies in the analysis.

References

[1] STOLL, R. D., *Sediment Acoustics,* Springer-Verlag Berlin Heidelberg, 1989.

[2] HAMILTON, E. L., Sound velocity as a function of depth in marine sediments. *J. Acoust.,Soc. Am., 78, 1348–1355, 1985.*

[3] CHAPMAN, N. R., Geoacoustic profile estimation by inversion of head wave data. *J. Acoust.,Soc. Am., 98, No. 5, Pt. 2, 2971, 1995.*

[4] OZARD, J. M., YEREMY, M. L., WILMUT, M. J., AND CHAPMAN, N. R., Matched-Field Processing in a range-dependent shallow water environment in the north-east Pacific Ocean. *Submitted to IEEE, J. Oc. Eng.*

[5] WILMUT, M. J. AND OZARD, J. M., Detection performance of two efficient source tracking algorithms for matched-field processing. *Submitted to J. Acoust. Soc. Am.*

[6] WESTWOOD, E. K., TINDLE C. T., AND CHAPMAN, N. R., A normal mode model for multilayered acoustoelastic ocean environments based on an analytic reflection coefficient method. *J. Acoust. Soc. Am., 95, (1994), 2908.*

[7] WESTWOOD, E. K., An efficient broadband normal-mode model for acoustoelastic ocean environments. *J. Acoust. Soc. Am. 96, (1994) 3352.*

[8] WESTWOOD, E. K., TINDLE C. T., AND CHAPMAN, N. R., A normal-mode model for acoustoelastic ocean environments. *Submitted to J. Acoust. Soc. Am.*

[9] WILMUT, M. J., OZARD, J. M. AND BROUWER, P., Evaluation of Two Efficient Target Tracking Algorithms for Matched-Field Processing with Horizontal Arrays. *J. Comp. Acoust., 3, No. 4, (1995), 311–326.*

[10] OZARD, J. M. AND YEREMY, M. L., Effects of Mismatch on Matched-Field Processing for Arctic and Pacific Shallow Water. *Presented at the Matched Field Processing Workshop, NRL, Washington, D. C. May 24–26, 1993.*

[11] OZARD, J. M. AND YEREMY, M. L., Effects of Mismatch on Matched-Field Processing for Arctic and Pacific Shallow Water. *Proceedings of the* 22^{nd} *meeting TTCP Technical Panel GTP-9, DREA, Dartmouth, N. S., Oct 18–22, 1993.*

EFFICIENT ARRAY PERFORMANCE ESTIMATION WITH EXAMPLES

C. A. Zala
Barrodale Computing Services Ltd., Box 1700,
Victoria, B.C., Canada V8W 2Y2

J. M. Ozard
Esquimalt Defence Research Detachment, Defence Research Establishment Atlantic
FMO Victoria, B.C., Canada V0S 1B0

and
M. J. Wilmut
Royal Military College
Kingston, Ontario, Canada K7K 5L0

August 1 1996

Abstract

An efficient technique for determining the performance of Matched Field Processing (MFP) with tracking is summarized and illustrated with examples. In this algorithm the candidate source tracks are the linear tracks passing through the strongest peaks in ambiguity surfaces from MFP at different times. The candidate track with the largest Bartlett sum, over the sequence of ambiguity surfaces in time, is declared a source track, provided it is above a preassigned threshold. Simulation and an analytic approximation are used to determine the probability the source track is examined. Furthermore, the probability the source track is detected, if examined, is given. The above probabilities are used to illustrate the tracking performance of slanted and horizontal arrays operating in an Arctic environment.

Linear Tracking Algorithm

Matched Field Processing (MFP) is an advanced signal processing method for the localization and detection of acoustic sources.[1] In this paper the problem of detection of sources of low signal-to-noise ratio (SNR) is considered. Signals from such sources are matched against predictions of the received signal for all possible positions to form ambiguity 'surfaces'. A Bartlett beamformer was chosen for the matching in this study. The SNR is so low that the Bartlett statistic at the source position is often not the largest value. Tracking, combining the information on a set of contiguous surfaces is used to determine the source's track, if one is present. In this study we assumed a source, if present, is moving linearly at constant speed, depth and heading and that *NS* contiguous ambiguity surfaces are available for analysis. The unweighted Linear Tracking Algorithm (LTA) [2,3] consists of five sets of computations performed for each possible depth:
(1) for each of the *NS* surfaces the positions of the NPK largest peaks are determined;
(2) all possible linear tracks joining pairs of peaks on different surfaces are found. These are called combinatoric tracks;
(3) a constraint to realistic maximum speeds for the source is imposed to reduce the combinatoric tracks to

the physically possible tracks;
(4) the unweighted track statistic is calculated for each physically possible track:

$$T_u = \frac{1}{NS}\sum_{i=1}^{NS} B(\mathbf{r}_i) \tag{1}$$

where $B(\mathbf{r}_i)$ is the Bartlett output for the unit norm replica vector $\mathbf{r}_i$ on the i^{th} surface along the track;
(5) the unweighted estimated track SNR outputs are calculated:

$$SNR = \frac{T_u - \overline{x}}{s}\sqrt{NS} \tag{2}$$

where $\overline{x}$ is the average value and s is the standard deviation of the Barlettt statistic for all points on all ambiguity surfaces in noise alone.

To be detected a source track must be examined (i.e. be one of the tracks found at step 2), and if examined have the largest estimated track SNR and exceed a threshold. As the Bartlett statistics on a surface are correlated the probabilities for the above two events are difficult to determine. A technique employing some simulation and an analytic approximation will be described below to determine the Probability the source Track is Examined (PTE). Reference[5] contains results needed to calculate the Probability the source Track is Detected, if Examined (PTDE).

Simulation Scenario

A range-independent upward-refracting channel with a 650 m water depth and a 22-m thick attenuating sediment layer, representative of an Arctic scenario, was chosen.[4] A normal mode propagation model was used to model the 25 Hz sound source. The sound source was at a depth of 100 m and spatially white noise was added to the signal. Data was simulated for a 20 element slanted array (vertically spacing spanning the water column and with half wavelength horizontal spacing), a 10 element slanted array (spanning the top half of the water column and with half wavelength horizontal spacing), and a 20 element horizontal array (located on the bottom with half wavelength spacing). The arrays were oriented so their horizontal extent was along the x axis. The search region was two dimensional, 5 to 30 km in range and -45° to 45° in bearing. K averages were used in the formation of the data covariance matrix used in the Bartlett processing.

Probability Source Track Examined

The probability the source track is examined is

$$PTE = 1 - [\prod_{i=1}^{NS}(1-p_i) + \sum_{i=1}^{NS}(p_i)\prod_{j=1,j\neq i}^{NS}(1-p_j)] \tag{3}$$

where p_i is the probability that the Bartlett statistic for a region about the source forms one of the top NPK peaks on the i^{th} surface. This region must be sufficiently large to include source peaks that have been displaced by noise effects and yet not too large so as to include neighbouring non source peaks.The p_i are dependent on many factors and can be found by simulation. In Reference 4 it is shown that if the region about the source is 0.15-0.20 of the signal half width (a source position dependent quantity) then p_i may be approximated by $P_{T,R(\mathbf{s})}$:

$$P_{T,R(s)} = \frac{1}{\sqrt{2\pi}}\int_{T-R(\mathbf{s})}^{\infty} e^{-\frac{t^2}{2}}dt \tag{4}$$

$P_{T,R(\mathbf{s})}$ is the probability that the Bartlett output for source position vector s is greater than the threshold T. $R(\mathbf{s})$ is the source SNR in the ambiguity surface. T is the threshold above which there will be NPK peaks in the noise-only standarized Bartlett ambiguity surface. The threshold is a function of the scenario, the number of peaks ranked and the number of averages K. The per sensor SNR is assumed to be small and K is assumed to be large. The threshold values for NPK peaks are found by simulation. For any track PTE was found from Equation 3 using the approximation to the p_i's along the track from Equation 4.

Array comparison

The performance of the above arrays was found for a source sequentially positioned at each of five equispaced locations along a linear track. The initial position was 10000 m range at a -30° bearing and the final position was 25000 m range at a 30° bearing. The source level was 105 dB re 1 μPa at 1 m and the noise level was 50 dB re 1 μPa at all sensors. Figure 1 shows the threshold T versus the number of peaks NPK and the number of averages K for the three arrays. PTE and PTDE are tabulated in Table I for the three arrays for an NPK of 20 and a K of 60.

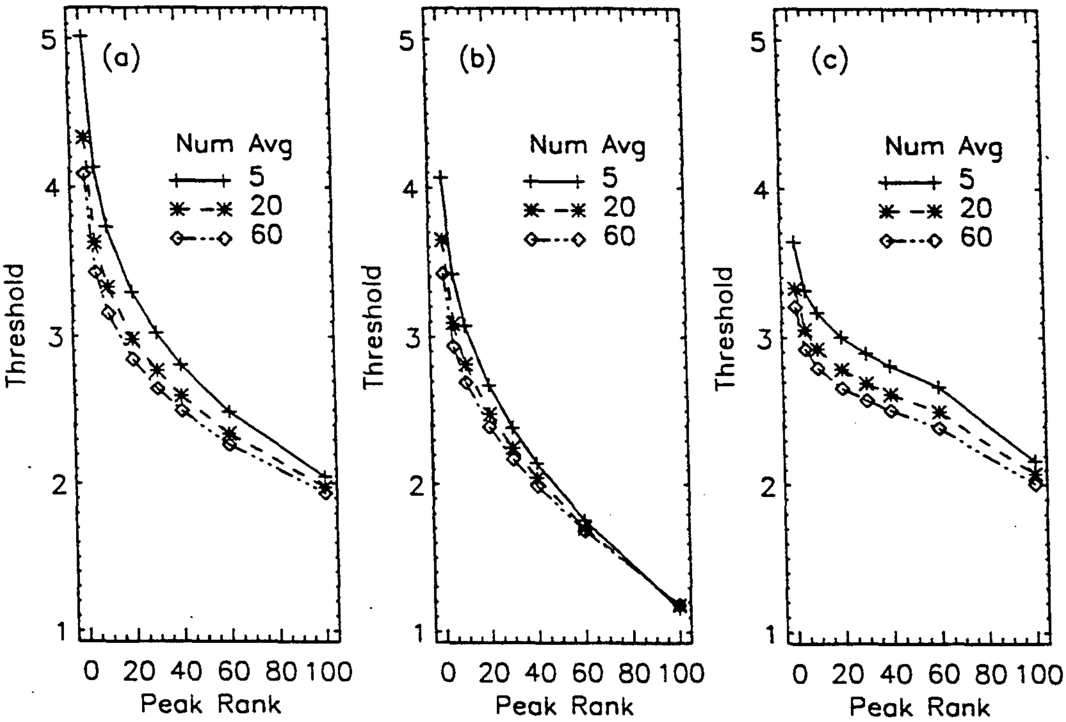

Figure 1: Estimated thresholds for peaks in the noise-only standarized ambiguity surface as a function of number of peaks ranked, for the number of averages indicated: (a) slanted 20-element array; (b) slanted 10-element array; (c) horizontal 20-element array. The threshold scale is linear in terms of the standard deviation of the noise.

Not suprisingly PTE is high when PTDE is high and visa-versa. As can be seen the 20 element slanted array would very likely detect the track, the 10 element slanted array might detect the source track while the horizontal array would almost never detect the source. The difference in performnce between the arrays stems from the difference in SNR received at the arrays through the term $R(s)$ in Equation 4. This study does not adjust the noise level, which would probably be significantly lower for the bottom horizontal array, and thus dramatically underestimates the horizontal arrays performance. This could be taken into account in future work.

Table 1: Tracking performance of the three arrays for the above scenario. The probability the track was examined (PTE) and the probability the source track is detected, if examined (PTDE). The threshold for PTDE corresponds to a false alarm probability of 10^{-4}.[5]

Array Type	PTE	PTDE
Slanted 20 element	0.974	0.90
Slanted 10 element	0.892	0.60
Horizontal 20 element	0.005	0.01

Concluding Remarks

The probability a source track is examined in a particular scenario using the Linear Tracking Algorithm may be found with minimal computer simulation and an analytic approximation. The probability a source track, if examined, is detected may also be determined analytically. This approach may be applied to any array configuration to estimate array detection performance.

References

[1] A Tolstoy, *Matched Field Processing for Underwater Acoustics*, World Scientific,Singapore, 1993.

[2] M.J. Wilmut, J.M. Ozard and B. Woods, "An Efficient Target Tracking Algorithm for Matched Field Processing", OCEANS 93, Vol III, 81–85, 1993.

[3] M.J. Wilmut, J.M. Ozard and P. Brouwer, "Evaluation of Two Efficient Target Tracking Algorithms for Matched-Field Processing with Horizontal Arrays", J. Comp. Acoust. **3**, 311-326 (1995).

[4] C.A. Zala J.M. Ozard, and M.J. Wilmut "Efficient performance estimation for matched-field processing with tracking", submitted to J. Acoust. Soc. Am.

[5] M.J. Wilmut and J.M. Ozard, "Detection Performance of Two Efficient Source Tracking Algorithms for Matched-Field Processing", submitted to J. Acoust. Soc. Am.

Broad-band Shallow Water Detection Experiments: Adaptive Matched-Field Processing on VLA's and Adaptive Plane-Wave Beamforming on HLA's

Newell Booth and Phil Schey, NRaD
William Hodgkiss, SIO/MPL

Abstract

Quantitative measurements of multi-tone detection performance are presented for two broadband adaptively processed array systems:

1) vertical line arrays with matched field replicas, and
2) horizontal line arrays with plane wave beamforming replicas.

The issues of measuring minimum detectable level, array gain, and deflection ratios are discussed and compared. Clutter rejection and target classification by depth are illustrated for the matched field processed VLA. Remaining critical issues for use of matched field processing in undersea surveillance are summarized.

The results presented were obtained in the third Shallow Water Evaluation Cell Experiment (SWellEX-3) was conducted 12 km off the coast of San Diego, CA, in July 1994[1,2]. The conditions of the experiment are shown in Fig. 1. Data were recorded on a vertical line array (VLA) suspended from the research platform FLIP and on a bottom mounted horizontal line array (HLA) at the positions shown.

SWellEX-3 Experiment, ArcMFP-5 Event

On 30 July between 13:10 and 13:30 GMT, an acoustic source (J-13) was towed at 30 m depth along the track shown in Fig. 1. Propagation from the source was along the 200 m isobath. The sound speed profile measured at FLIP is also shown. The acoustic source, towed at 30 m depth, transmitted a continuous 50-tone comb signal, illustrated on the right side of Fig. 1.

This multi-tone Minimum Detectable Level (MDL) signal consisted of ten pilot tones spread between 53 and 197 Hz. Each pilot tone at frequency f_i was accompanied be a set of four tones at frequencies f_i+2, f_i+4, f_i+6, and f_i+8 Hz, at levels -10, -14, -18 and -22 dB below the pilot tone, respectively. The results reported in this paper use the pilot tones to estimate the input signal to noise ratio (ISNR) from which the ISNR of the lower level tones is inferred by subtracting the appropriate difference in source level. The ISNRs for the pilot tones and the "-22 dB" set of tones is shown in the lower left of Fig. 1 for event ArcMFP-5. This signal enables calibrated measurement of the performance of the adaptive algorithms at low signal to noise ratio, where the algorithms are less sensitive to replica mismatch.

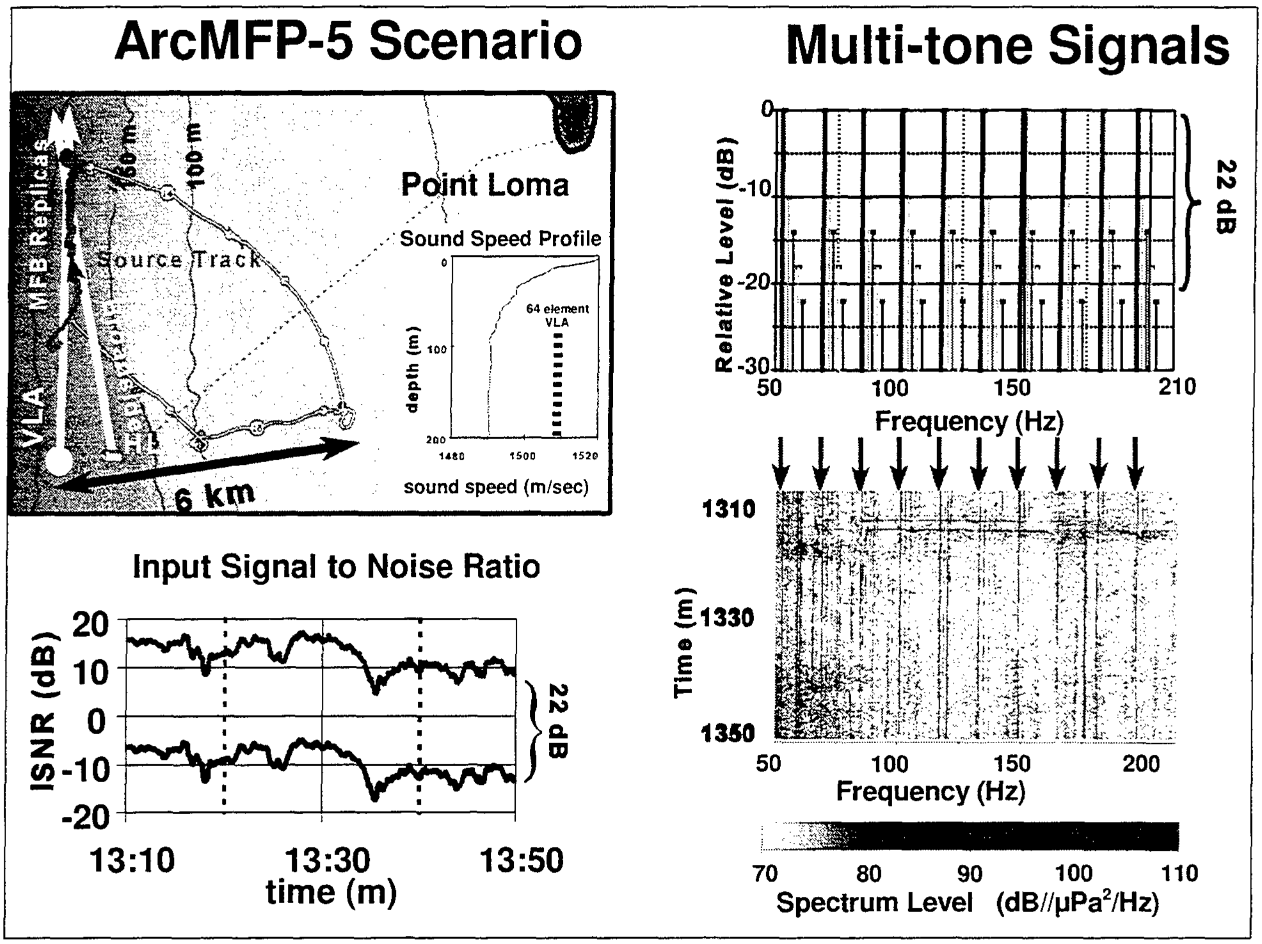

Figure 1: Event ArcMFP-5 of SWellEX-3

Beamforming and Adaptive Processing Methods

Processing was done using the ten pilot tone frequencies, the "-22 dB" set and a noise only set of ten frequencies at f_i+9 Hz, 1 Hz above the "-22 dB" set. Adaptive Matched-Field Processing (MFP) was done on a 78.5 m, N_e =8 element subset of the 64 available array elements of the VLA (λ/2 @ 67 Hz). Adaptive Plane-Wave Beamforming (PWB) was also done on a 52 m, N_e =14 element subset of the HLA (λ/2 @ 187.5 Hz). Each six seconds of element data was Fourier analyzed with a 50% overlapped Kaiser-Bessel window to form a N_e element data vector, $\mathbf{X}(f_i, t_j)$, for each pilot frequency, f_i, and time, t_j. The frequencies of the pilot tones were tracked and used to derive the low level and noise only frequencies that were used in the processing. The covariance matrix was estimated by averaging N_t outer products of the data vectors

$$\mathbf{K}(f_i, t) = \frac{1}{N_t} \sum_{j=1}^{N_t} \mathbf{X}(f_i, t_j)\mathbf{X}^*(f_i, t_j) \qquad (1)$$

for T seconds, where * indicates complex conjugate transpose. The processing and array parameters are summarized in TABLES I and II for the VLA and HLA respectively.

TABLE I: VERTICAL ARRAY AND PROCESSING PARAMETERS

Name	Value	Comments
Number of elements, N_e	8	Spacing 11.25 m ($\lambda/2$ at 67 Hz)
Array Aperture	78.5 m	starting 6 m from bottom at 198 m depth
Array Tilt (α)	<2 deg	Toward North during both events
Sampling rate	1,500 Hz	
FFT length	8192	50 % overlapped
FFT binwidth	0.18 Hz	Kaiser-Bessel weighting with $\alpha = 2.5$
Covariance Integration Time, T	60 sec	$N_t = 20$ samples

TABLE II: HORIZONTAL ARRAY AND PROCESSING PARAMETERS

Name	Value	Comments
Number of elements, N_e	14	Spacing 4 m ($\lambda/2$ at 187.5 Hz)
Array Aperture	52 m	
Sampling rate	1,562.5 Hz	
FFT length	8192	50 % overlapped
FFT binwidth	0.19 Hz	Kaiser-Bessel weighting with $\alpha = 2.5$
Covariance Integration Time, T	73 sec	$N_t = 28$ samples

The narrowband beamforming (matched-field or plane-wave) process used was an estimate of the normalized cross-correlation of the received data with weight vectors, **w**. For each time, t, and pilot frequency, f_i, the "correlation" was calculated using

$$C(f_i,\mathbf{r},t) = \frac{\mathbf{w}^*(f_i,\mathbf{r})\ \mathbf{K}(f_i,t)\ \mathbf{w}(f_i,\mathbf{r})}{\frac{1}{N_e}\ \mathrm{Tr}\big(\mathbf{K}(f_i,t)\big)}\ , \tag{2}$$

where Tr(**K**) is the trace of the covariance matrix, **K**. Since $\mathrm{Tr}\big(\mathbf{K}(f_i,t)\big) = N_e \cdot \hat{P}_{s+n}(f_i)$, the correlation is the output power normalized by the total signal power plus noise power in all of the elements. The weight vector, $\mathbf{w}(f_i,\mathbf{r})$, was calculated for each position in the search space, $\mathbf{r}$ (assumed range r, depth d, and azimuth θ, for MFP and assumed azimuth θ for PWB). The correlations were averaged over the N_f = 10 frequencies to generate the multi-tone correlation estimate

$$\overline{C(r,d,\theta,\alpha,t)} = \frac{1}{N_f}\sum_{i=1}^{N_f} C(f_i,r,d,\theta,\alpha,t)\ . \tag{3}$$

The adaptive process used in the analysis was the Minimum Variance Distortionless Response (MVDR) with white noise constraint[3]. The MVDR weight vectors are calculated using

$$\mathbf{w} = \frac{(\mathbf{K}+\varepsilon\mathbf{I})^{-1}\mathbf{s}}{\mathbf{s}^*(\mathbf{K}+\varepsilon\mathbf{I})^{-1}\mathbf{s}}\ , \tag{4}$$

where $\mathbf{K}$ is the covariance matrix, $\mathbf{I}$ is the identity matrix, and ε is the white noise that is added to reduce the sensitivity to replica mismatch[4] at high SNR. The steering vector $\mathbf{s}$ is given by

$$\mathbf{s} = \frac{\mathbf{g}\sqrt{N_e}}{|\mathbf{g}|} \tag{5}$$

The replicas, $\mathbf{g}(f_i,\mathbf{r})$, are calculated using a model of the acoustic field. For PWB, the model is a plane wave at frequency, f_i, and azimuthal arrival angle, θ. Targets are located in the PWB search space given by $\mathbf{r}_{PWB} = (\theta)$. For MFP, the replicas are calculated using Collins' Finite Element Parabolic Equation (FEPE) propagation model[5] for the bathymetry of azimuth, θ, for each frequency, f_i, and for each range, r, and depth, d. Targets are located in the MFP search space given by $\mathbf{r}_{MFP} = (r,d,\theta)$.

The element positions of the bottom mounted HLA were measured prior to the source tows. Independent Array Element Location (AEL) measurements of the VLA were made during the events[6] but were not yet available for this analysis. Instead the array was assumed to be straight and the array tilt, α, was included in the search parameters. The MFP results presented here are for array tilts corresponding to the tilt with maximum $\overline{C(r,d,\alpha_{\max},t)}$ obtained using the pilot tones and linear (Bartlett) MFP, $\mathbf{w} = \frac{\mathbf{s}}{N_e}$. Array shapes derived by the two methods are compared in ref. 6.

The loss from replica mismatch was measured using the pilot tones for both PWB and MFP replicas with the methods described in ref. 2. In both cases, the loss was less than 1 dB for the ranges, frequencies and arrays used in the experiment.

Adaptive MFP Results using VLA

The adaptive MFP beamforming described above was done on the ArcMFP-5 VLA data set using replicas generated with the bathymetry along the azimuth of the track shown in Fig. 1. Displays of output correlation vs range and time were generated at several search depths. Processing was done using the ten pilot tone frequencies, the "-22 dB" set and a noise only set of ten frequencies at f_i+9 Hz, 1 Hz above the "-22 dB" set. Fig. 2 shows range-time ambiguity surfaces for the target depth of 30 m.

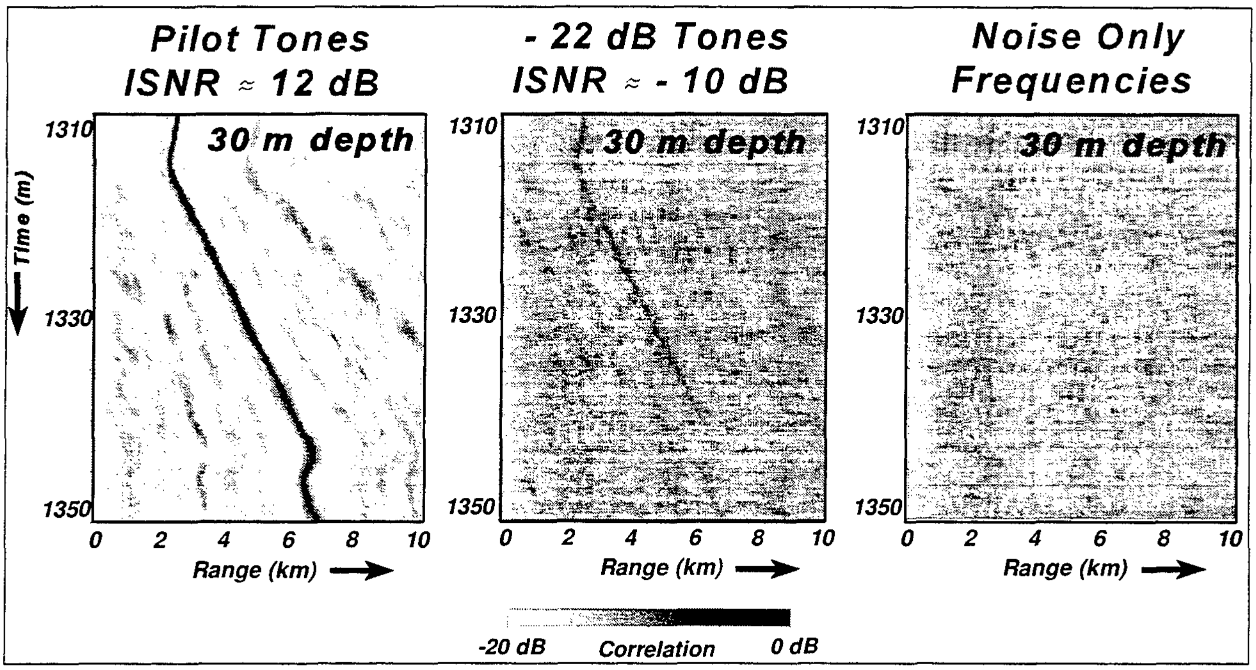

Figure 2: Range-Time ambiguity surfaces from VLA for the pilot tones, the "-22 dB" tones and the noise only frequencies at the target depth of 30 m. MFP using MVDR algorithm with white noise constraint with white noise gain = 6 dB. The VLA consisted of 8 elements spaced at $\lambda/2$ @ 67 Hz.

The pilot tone surface (far left) shows the track of the target. The ISNR, seen in Fig 1, was approximately 12 dB for the first 35 minutes of the track. Sidelobes of the signal are also seen. These sidelobes were not reduced by the adaptive processing because of the white noise constraint. The "-22 dB" tone surface (center) illustrates the detection and track of the low level signal at - 10 dB ISNR. The noise only frequencies surface is shown at the right. The array gain for the low level signal vs time can be calculated by

$$AG = 10\log\left(\frac{C_T(t,r_T)}{\overline{C_N(t)}}\right) - ISNR \qquad (6)$$

where $10\log\left(\dfrac{C_T(t,r_T,d_T)}{\overline{C_N(t)}}\right)$ is the output signal to noise ratio (OSNR), $C_T(t,r_T,d_T)$ is the output correlation at the target range and depth, and $\overline{C_N(t)}$ is the average of the output correlation of the noise only surface over range at the target depth. For the case of Fig 2, the array gain was the order of 10 dB. This is consistent with the "-22 dB" track disappearing when the ISNR dropped below -10 dB.

Examining the "-22 dB" surface, it can be seen that the source track is discernable in a low clutter background. The low clutter results from the depth resolution of MFP combined with the sidelobe reduction from frequency averaging and MVDR processing.

Adaptive PWB Results using HLA

The adaptive PWB beamforming described above was done on the ArcMFP-5 HLA data. The HLA was oriented so that the broadside direction was pointing -10° re: true North. The PWB replicas provided a search space from -90°T to +90°T. Displays of output correlation vs azimuth (re: true North) and time were generated. Processing was done using the ten pilot tone frequencies, the "-22 dB" set and a noise only set of ten frequencies at f_i+9 Hz, 1 Hz above the "-22 dB" set. Fig. 3 shows azimuth-time ambiguity surfaces (bearing time records) for the ArcMFP-5 data set. The target track is between the two dark lines in the pilot tone surface.

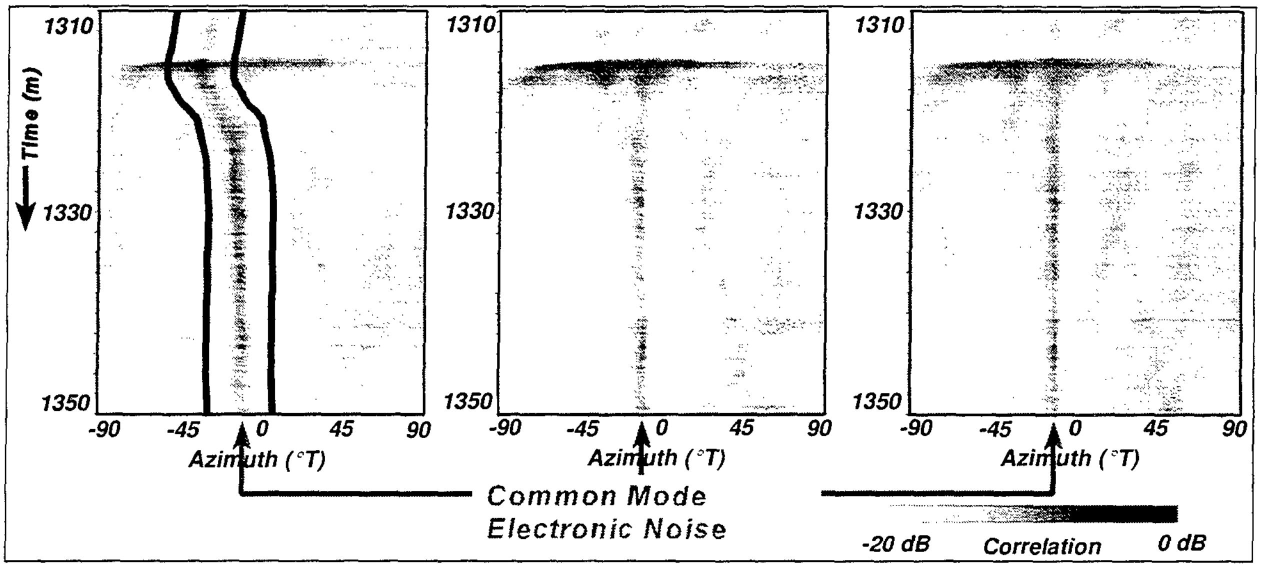

Figure 3: Azimuth-Time ambiguity surfaces from HLA for the pilot tones, the "-22 dB" tones and the noise only frequencies at the target depth of 30 m. PWB using MVDR algorithm with white noise constraint with white noise gain = 6 dB. The HLA consisted of 14 elements spaced at $\lambda/2$ @ 187.5 Hz. The track of the towed source is between the dark lines which were drawn on the pilot tone surface.

The ISNR was measured separately on the HLA and was within 1 dB of that shown in Fig 1 for the VLA, ~ 12 dB for the first 35 minutes of the track. The "-22 dB" tone surface is in the center with an ISNR of ~ -10 dB. The noise only frequencies surface is shown at the right.

The most prominent feature of all surfaces is common-mode electronic noise in the broadside direction (-10°T). The common-mode noise was in the same direction as the signal at the end of the track. This noise combined with other effects discussed in the next paragraph made quantitative comparison with the VLA MFP result using this data fruitless.

Several interfering ships can be seen in the noise only surface. The noise only surface also shows a detection track when the source is. These effects illustrate several issues of importance in experimentally evaluating the detection and classification performance of an HLA with PWB on submerged signals.

- With the HLA, additional means of submerged target identification and classification must be used to distinguish the target from the clutter.
- The output SNR for array gain estimates should be taken locally to exclude interferences. The noise estimate should exclude any tow ship signal.
- The variance in the "noise only" search space relates to the detection threshold of the display. If a target is well separated from the clutter it can be detected, so the variance should also be measured locally.

As a result of these difficulties, quantitative comparison is not definitive. However, it can be said that the low level signals were detected with about the same array gain (~10 dB) as the VLA with MFP.

Issues for SWellEX-96

The SWellEX-96 experiment was conducted at the same site in May of 1996 to address new issues and to incorporate the lessons learned in SWellEX-3. It was planned and conducted by NRaD in conjunction with the following projects:

• Environmentally Enhanced Signal Processing (EESP)	NRL-7100
• All Optical Deployable System (AODS)	PMW-183
• USS Dolphin Project	PMS-395

The MFP objectives of SWellEX-96 are listed below:

- Demonstrate Matched Field Processing (MFP) techniques on extended targets whose size is on the order of the resolution cell.
- Determine the feasibility of MFP at frequencies up to 700 Hz.
- Compare broadband and multi-tone MFP detection performance between a tilted vertical line array (TVLA) and a vertical line array (VLA). The TVLA has range, depth and azimuthal resolution providing the potential for adaptive processing to resolve and null interferences in azimuth.
- Compare broadband and multi-tone minimum detectable level of HLA plane wave beamforming with VLA and TVLA MFP using the diesel-electric submarine USS DOLPHIN with augmentation.

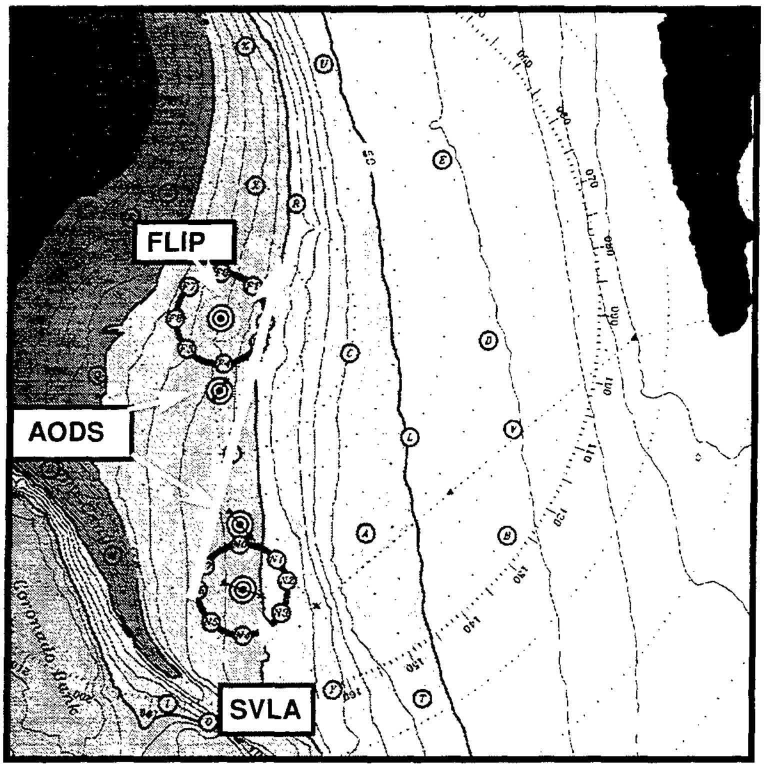

Figure 4: SWellEX-96 Experiment Geometry

The SWellEX-96 geometry is shown in Fig. 5. The acoustic sensors deployed included:

- A vertical line array (VLA) and a tilted vertical line array (TVLA) were deployed by FLIP, shown in Fig 6.
- The All Optical Deployable System (AODS) consisting of two horizontal line arrays (HLAs) was installed on the sea floor.
- The Satellite linked Vertical Line Array (SVLA), also shown in Fig. 6, was brought to the experiment by the NRL EESP project. SVLA is a remotely controlled, self recording VLA system which extends 165 m up from the sea floor.

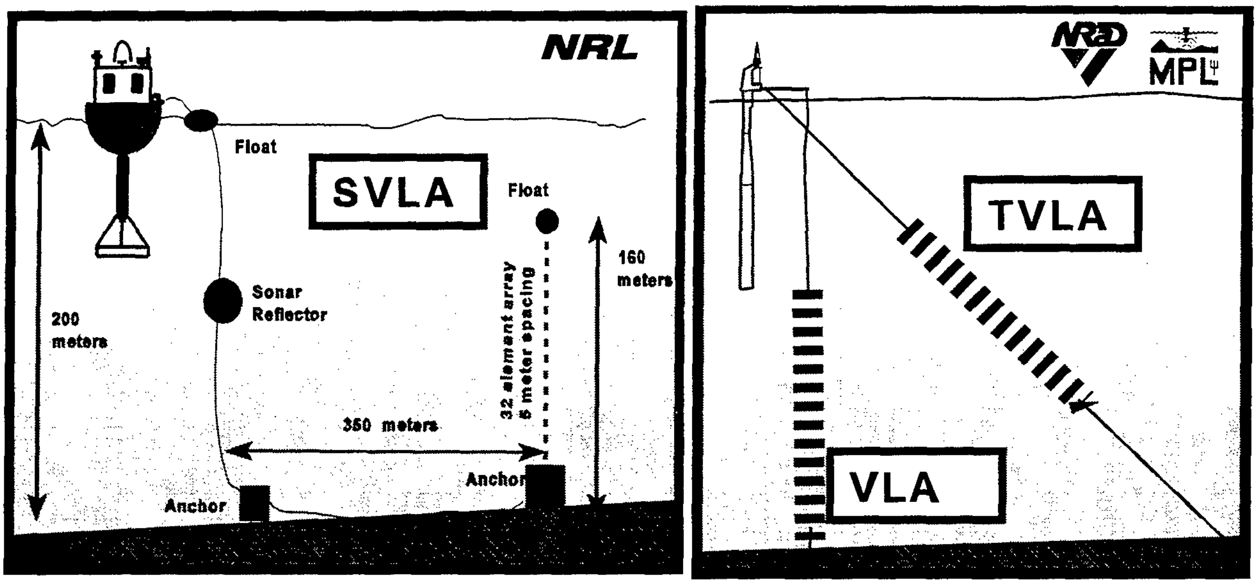

Figure 5: SWellEX-96 Vertical Arrays for Matched Field Processing

The environment was sampled to support control and interpretation of the various experimental events. The full details of SWellEX-96 events are published in the test plans and preliminary data report, which may be obtained from the author. Processing onboard FLIP and at the onshore SVLA site during the experiment detected, localized and tracked multi-tone signals with time-late of 3 hours, compared to the 3 days achieved ashore during SWellEX-3.

The difficulties experienced in SWellEX-3 should have been alleviated in the following ways:

- The augmented quiet diesel-electric research submarine, USS DOLPHIN, carried the source transmitting multi-tone MDL signals which spanned frequencies between 50 and 680 Hz. If DOLPHIN's signature appears in the noise only surfaces, it will appear in both the VLA and HLA surfaces with the same source level.
- The AODS HLA array had no common-mode electrical noise at broadside because of its all optical design. The HLAs were oriented such that source tracks were not in the broadside direction, so that any common-mode noise, should it appear, will not appear on the source azimuths.

Summary and Conclusions

The results of the SWellEX-3 experiment have demonstrated the potential of using vertical line arrays with adaptive MFP for the detection and tracking of submerged signals. Broad-band adaptive processing coupled with the depth resolution of MFP shows a low-variance clutter free search space at depth for signal detection. The array gain of the VLA was comparable to the HLA with adaptive PWB.

The SWellEX-96 experiment was designed to overcome many of the difficulties in comparing VLA and HLA array detection performance which were experienced in SWellEX-3. Several issues remain to be addressed to accomplish a quantitative and objective comparison including:

- Determining the probability of false alarm in the large MFP search space.
- Determining the mean and variance of the noise in the cluttered search space of the HLA.

The hypothesis will be tested that the range, depth and azimuthal resolution of the tilted vertical array will improve the detection performance.

References

1. R. T. Bachman, P. W. Schey, N. O. Booth and F. J. Ryan, "Geoacoustic data bases for matched-field processing: preliminary results in shallow water off San Diego, California", *J. of the Acoustical Soc. of Amer.*, vol. 99(4), Pt. 1, p 2077-2085, April 1996.

2. N. O. Booth, P. A. Baxley, J, A. Rice, P. W. Schey, W. S. Hodgkiss, G. L. D'Spain, and J. J. Murray, "Source Localization with Broadband Matched Field Processing in Shallow Water", *IEEE J. Oceanic Eng.,* vol. 21(4), October 1996.

3. A. B. Baggeroer, W. A. Kuperman, and P. N. Mikhalevsky, "An Overview of Matched Field Methods in Ocean Acoustics", *IEEE J. of Oceanic Engineering*, vol. OE-18(4), pp. 401-424, 1993.

4. R. A. Gramann, "ABF Algorithms Implemented at ARL:UT", Applied Research Laboratories, University of Texas at Austin, ARL/UT Technical Report 92-7, 12 May 1992.

5. M. D. Collins and E. K. Westwood, "A higher-order energy-conserving parabolic equation for range-dependent ocean depth, sound speed, and density", *J. of the Acoustical Soc. of Amer.*, vol. 89(3), pp. 1068-1075, 1991.

6. W. S. Hodgkiss, D. E. Ensberg, J. J. Murray, G. L. D'Spain, N. O. Booth and P. W. Schey, “Direct Measurement and Matched Field Inversion Approaches to Array Shape Estimation”, *IEEE J. Oceanic Eng.,* vol. 21(4), October 1996.

Robust MFP Processor Performance with SWellEx Data

W.S. Hodgkiss, K.H. Kim, and J.J. Murray

Marine Physical Laboratory
Scripps Institution of Oceanography
La Jolla, CA 92093-0701

J.L. Krolik

Dept. of Electrical Engineering
Duke University
Durham, NC 27708-0291

Abstract

SWellEx-1 (Shallow Water evaluation cell Experiment #1) and SWellEx-3 were carried out in August 1993 and July 1994 west of Point Loma in approximately 200 m water. During SWellEx-1, a MPL 48-element vertical array was deployed from the R/P FLIP. Similarly, during SWellEx-3, a MPL 64-element vertical array was deployed from the R/P FLIP. Source tow events were carried out throughout the region and included both range-independent radial tracks as well as tracks over a variable bathymetry. In SWellEx-1, a set of 4 tonals were transmitted in the 50-200 Hz band while in SWellEx-3, 10 tonals were transmitted. Shipping noise varied substantially during these experiments due to fluctuations in traffic patterns.

The focus of this paper is on the performance of the MV-EPC (Minimum Variance - Environmental Perturbation Constraint) matched field processor with SWellEx-1 and SWellEx-3 data. For selected data segments, a comparison is made between the broadband averaged range-depth ambiguity surfaces at the output of the following processors: (1) conventional (Bartlett) matched field processor given a measured speed profile at the vertical array and good estimates of geoacoustic parameters, (2) unconstrained MVDR (Minimum Variance Distortionless Response) processor using the same environmental information as (1), and (3) MV-EPC processor given the measured sound speed profile at the vertical array and a statistical description of the geoacoustic environment. Also, range-time ambiguity surfaces (at the depth of the source) are shown to illustrate the time-evolving structure of the surfaces at the output of these processors.

[Work supported by ONR, Code 321US.]

Robust MFP Processor Performance with SWellEx Data

W.S. Hodgkiss

K.H. Kim

J.J. Murray

Marine Physical Laboratory
Scripps Institution of Oceanography
La Jolla, CA 92093-0701

J.L. Krolik

Dept. of Electrical Engr.
Duke University
Durham, NC 27708-0291

13 June 1996

Processors

- Bartlett
- MVDR (Minimum Variance Distortionless Response)
- MVDR - NLC (Neighborhood Location Constraints)
- MVDR - WNC (White Noise Constraint)
- MVDR - EPC (Environmental Perturbation Constraints)

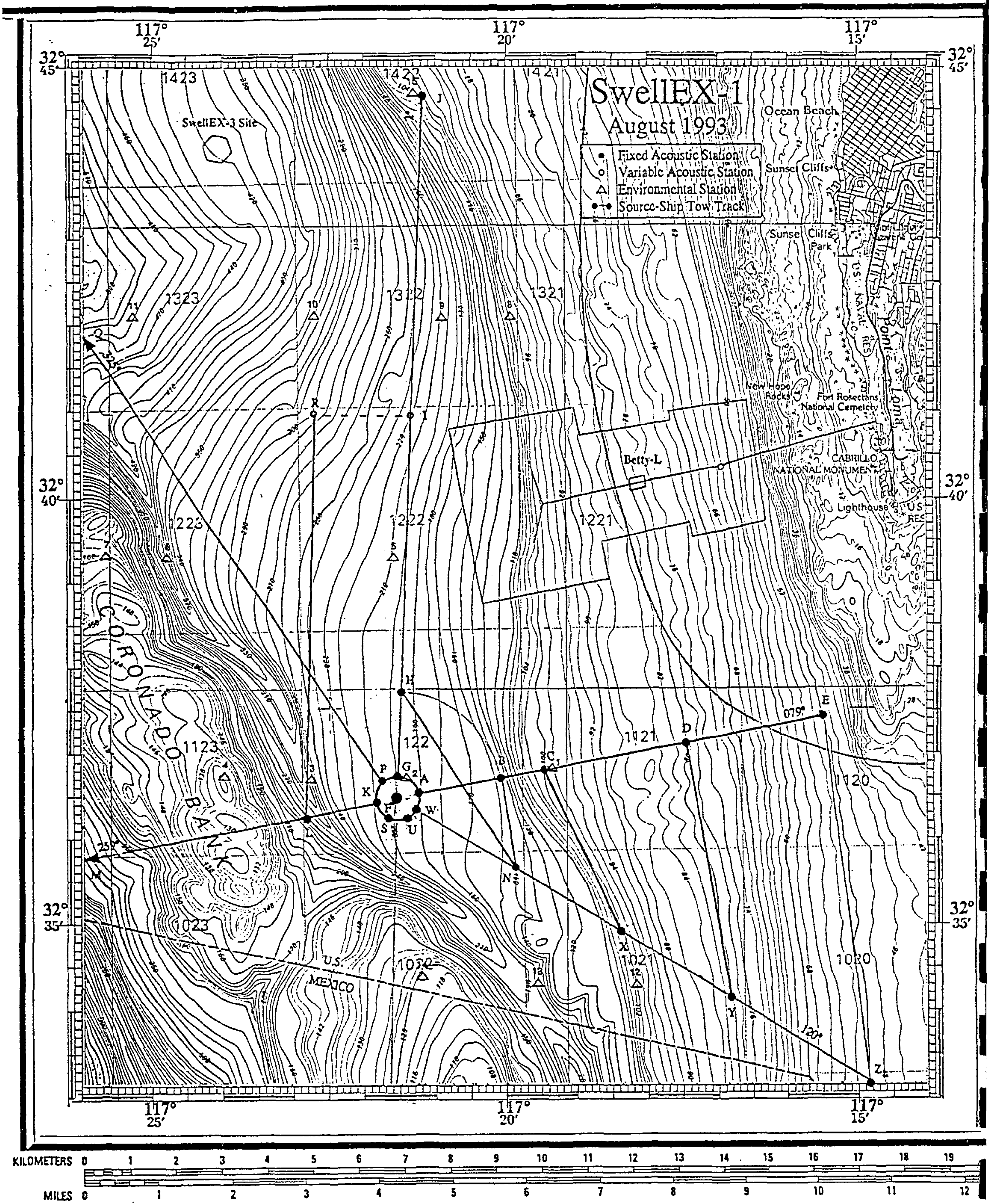
SwellEX-1
August 1993
● Fixed Acoustic Station
○ Variable Acoustic Station
△ Environmental Station
●-● Source-Ship Tow Track
117° 25′
117° 20′
117° 15′
32° 45′
32° 40′
32° 35′
SwellEX-3 Site
Ocean Beach
Sunset Cliffs
Sunset Cliffs Park
New Hope Rocks
Fort Rosecrans National Cemetery
Point Loma
CABRILLO NATIONAL MONUMENT
Lighthouse
Betty-L
CORONADO BANK
U.S.
MEXICO
1423
1422
1421
1323
1322
1321
1223
1222
1221
1123
122
1121
1120
1023
1022
1021
1020
J
R
I
H
E
D
C1
B
A
G2
P
K
F
S
U
W
L
M
N
X
Y
Z
079°
120°
250°
325°
1
2
3
4
5
6
7
8
9
10
11
12
13
KILOMETERS 0 1 2 3 4 5 6 7 8 9 10 11 12 13 14 15 16 17 18 19
MILES 0 1 2 3 4 5 6 7 8 9 10 11 12

SWellEx - 1 Arrays

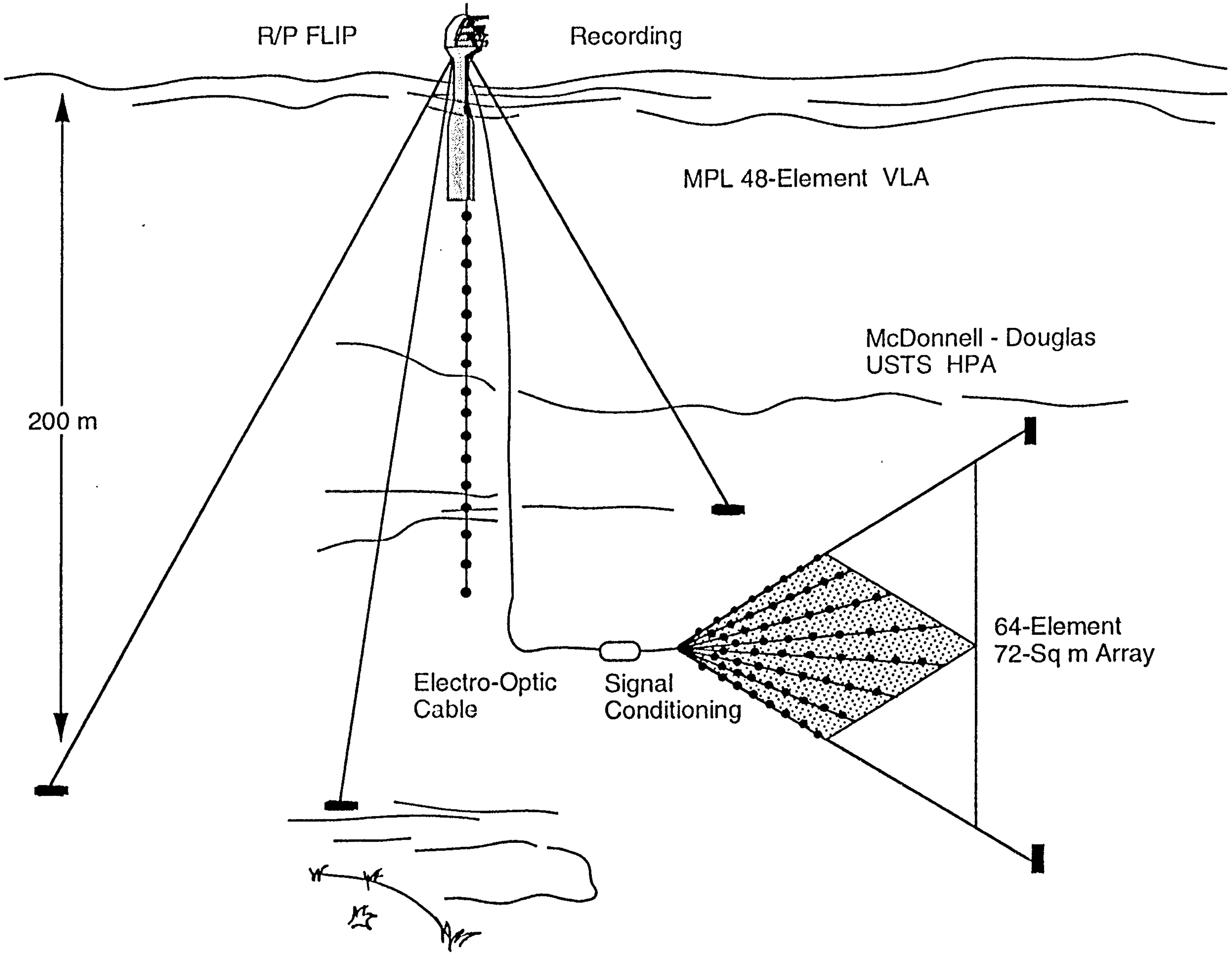

SWellEx-1

Track G to I

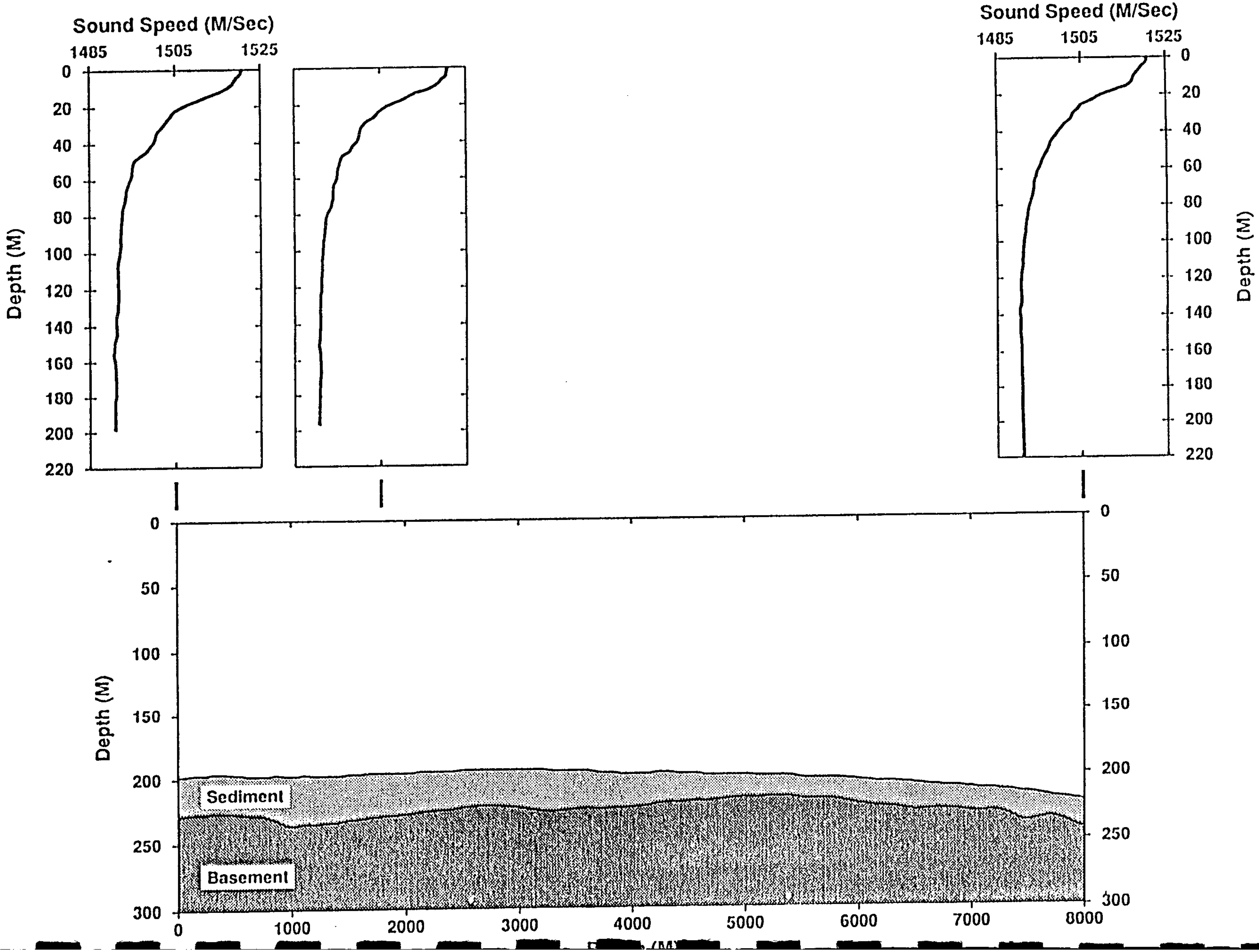

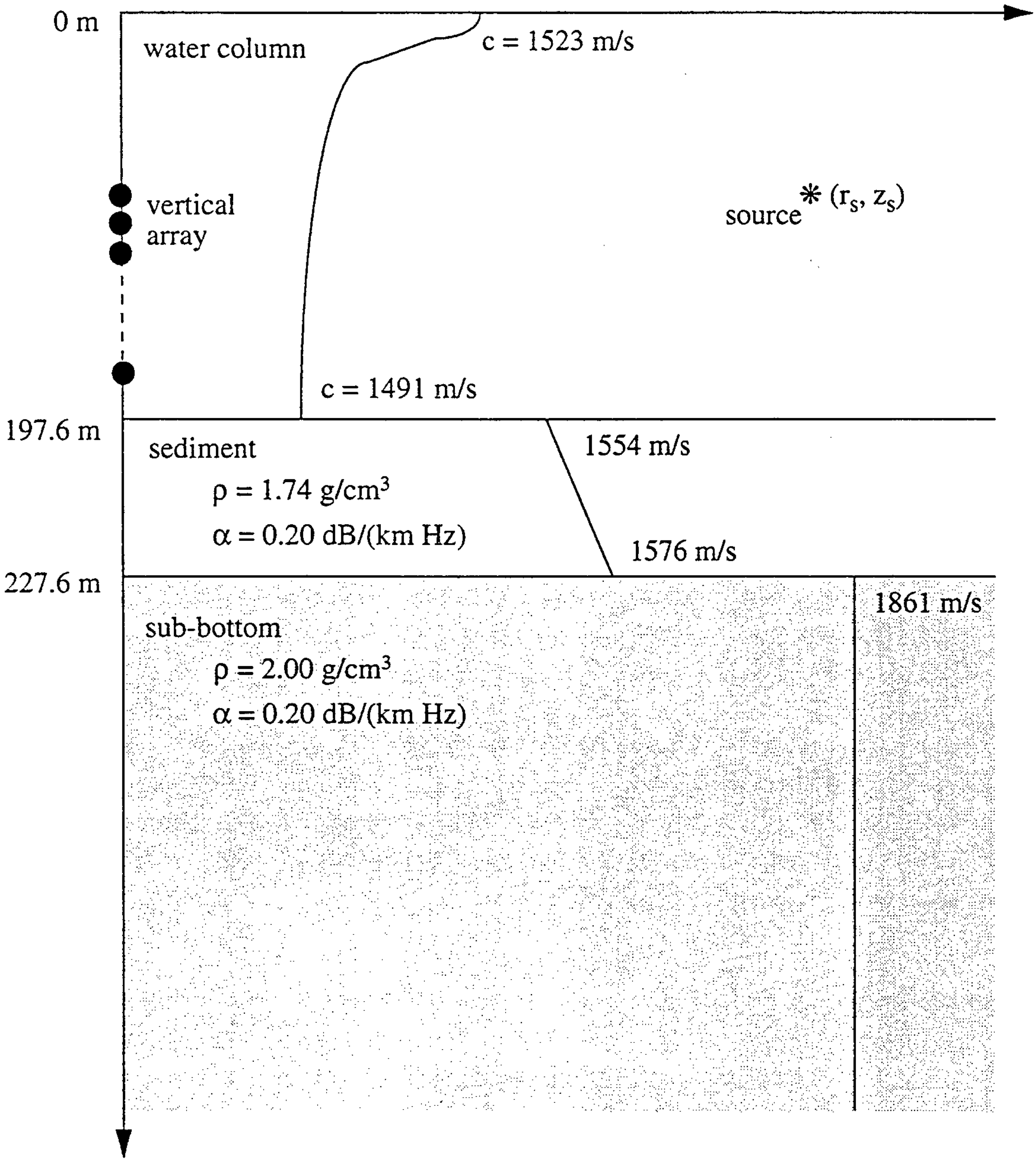

The SWellEx-1 environment.

Environmental Parameter	Lower Bound	Baseline Value	Upper Bound	Units
Bottom depth	195.0	197.6	200.0	m
Sediment velocity (top)	1545.0	1554	1565.0	m/s
Sediment velocity (bottom)	1565.0	1576	1585.0	m/s
Sediment density	1.65	1.74	1.85	g/cm^3
Sediment attenuation	0.1	0.2	0.3	dB/(km Hz)
Sediment thickness	28.5	30.0	32.5	m
Bottom velocity	1850.0	1861.0	1870.0	m/s
Bottom density	1.9	2.0	2.1	g/cm^3
Bottom attenuation	0.1	0.20	0.3	dB/(km Hz)

SWellEx-1 Environmental Parameters.

SWellEx-1 - Source Parameters

- Depth = 82 m
- Speed = 3 knots
- Frequencies = 70, 95, 145, and 195 Hz

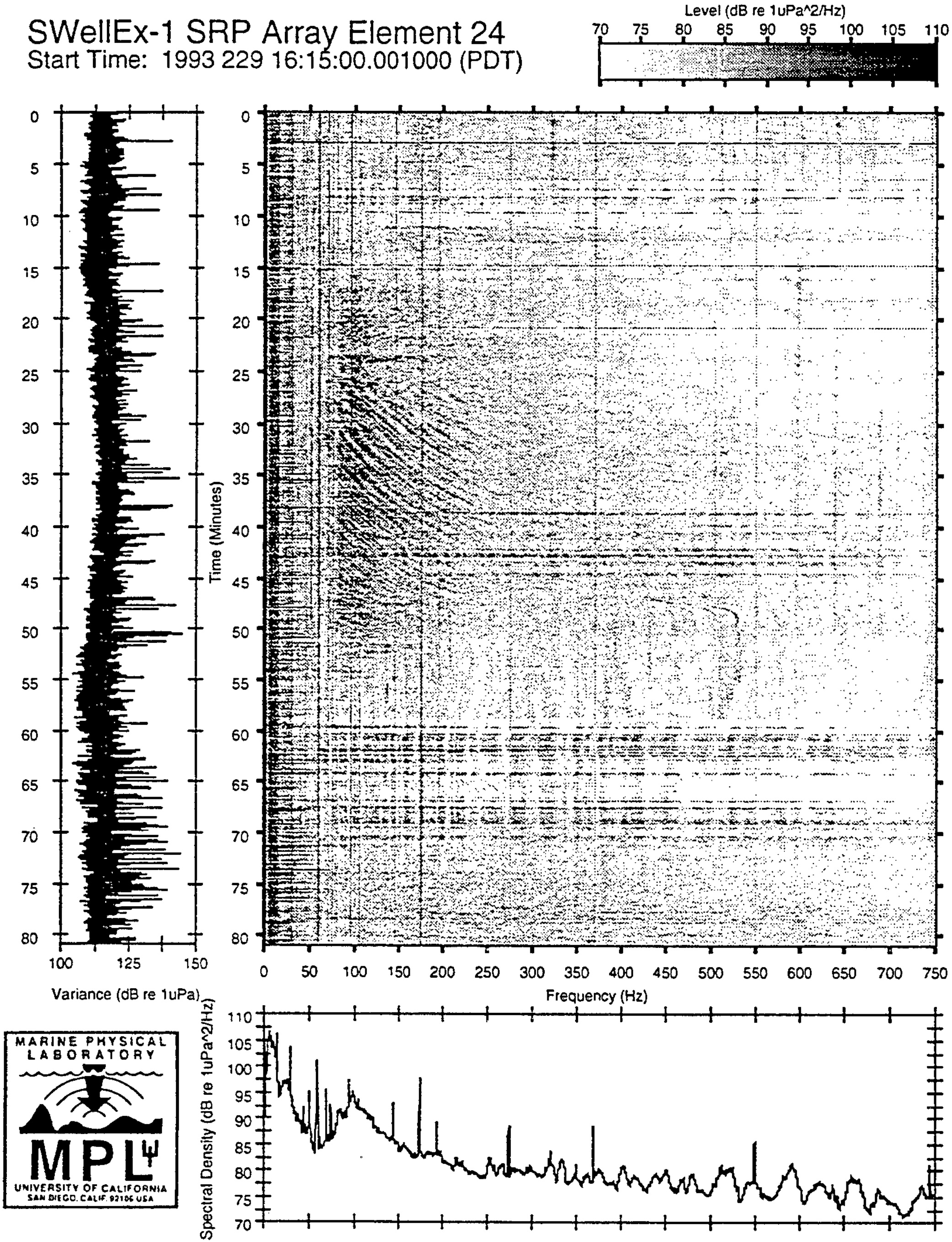

Lofargram of the G-I Track event

(source frequencies of 70, 95, 145, and 195 Hz).

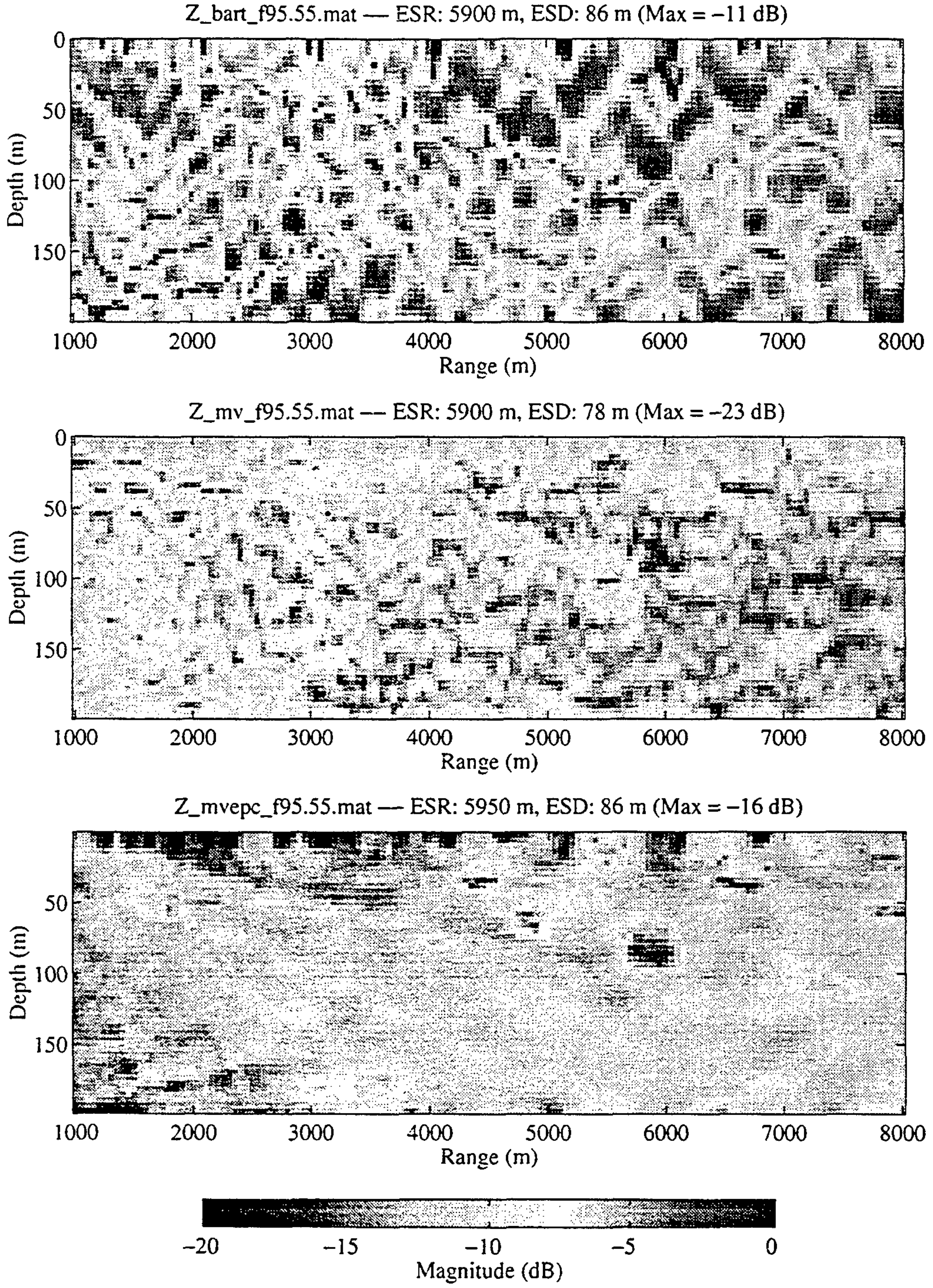

Depth-range ambiguity surfaces for the Bartlett, MV, and MV-EPC methods (f = 95 Hz).

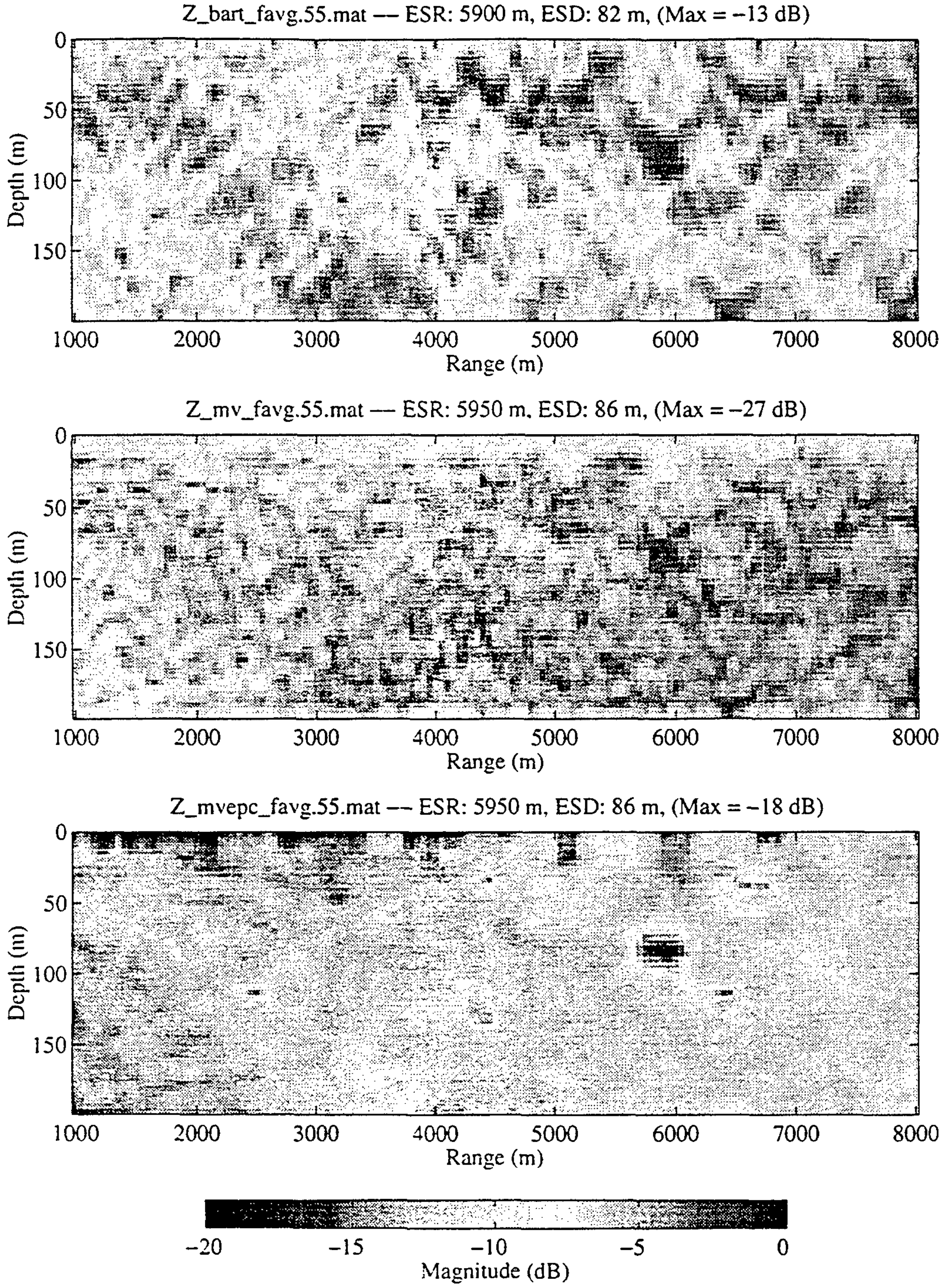
Z_bart_favg.55.mat — ESR: 5900 m, ESD: 82 m, (Max = −13 dB)

Z_mv_favg.55.mat — ESR: 5950 m, ESD: 86 m, (Max = −27 dB)

Z_mvepc_favg.55.mat — ESR: 5950 m, ESD: 86 m, (Max = −18 dB)

Depth-range ambiguity surfaces for the Bartlett, MV, and MV-EPC methods (frequency-averaged).

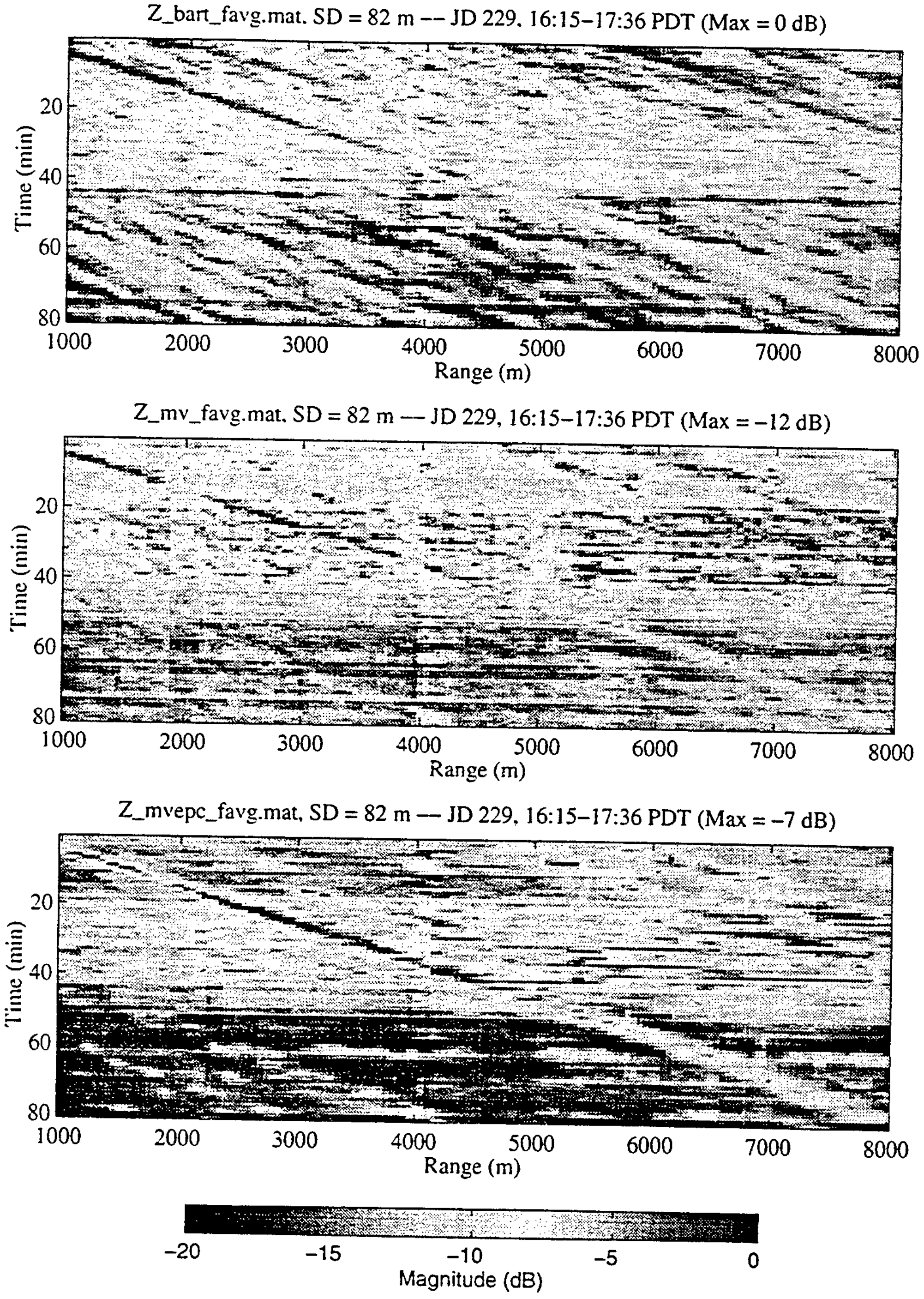

Time-range ambiguity surfaces for the Bartlett, MV, and MV-EPC methods (frequency-averaged).

SWellEX-3 ArcMFP-5 Event, 94.Jul.30

DGPS track of R/V Acoustic Explorer, 211.1300Z–211.1540Z

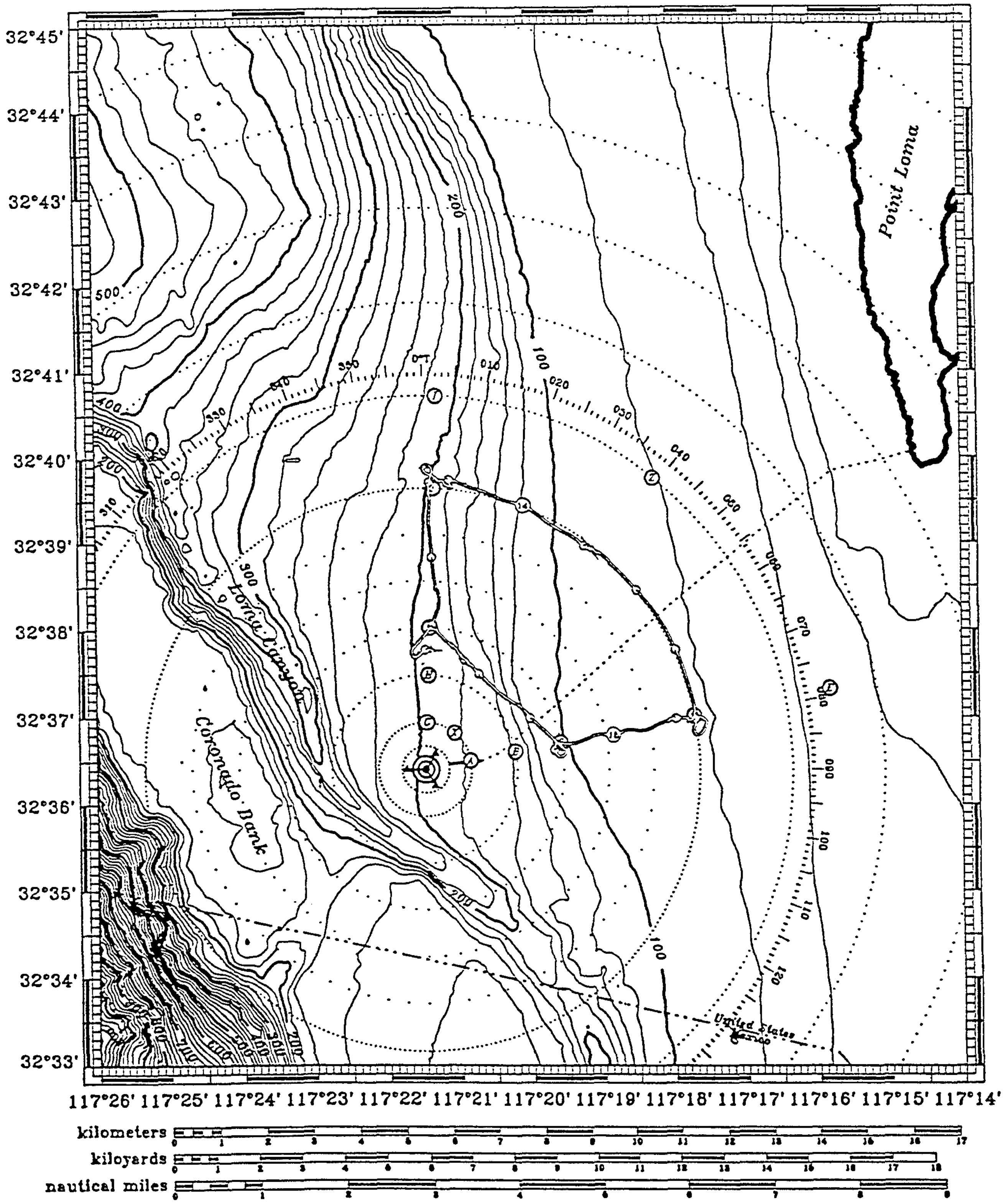

isobath intervals 20 meters

chart produced by NCCOSC RDT&E Div. Code 541

SWellEx - 3 Vertical Array

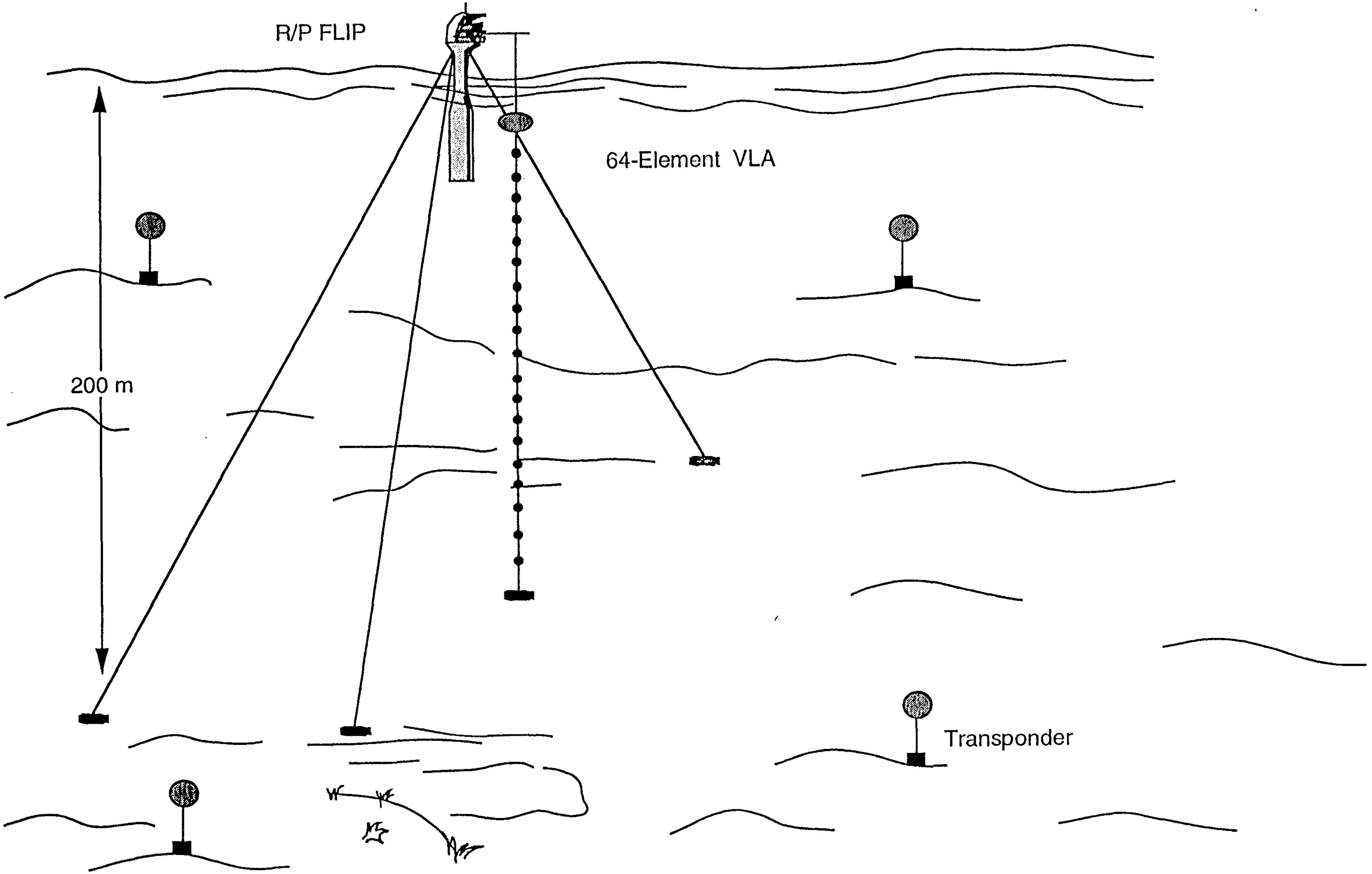

rev. 2/96

SWellEX-3 CTD Sound Speed Profile No. 151, Site G, 30 July 1994, 1319 ZULU

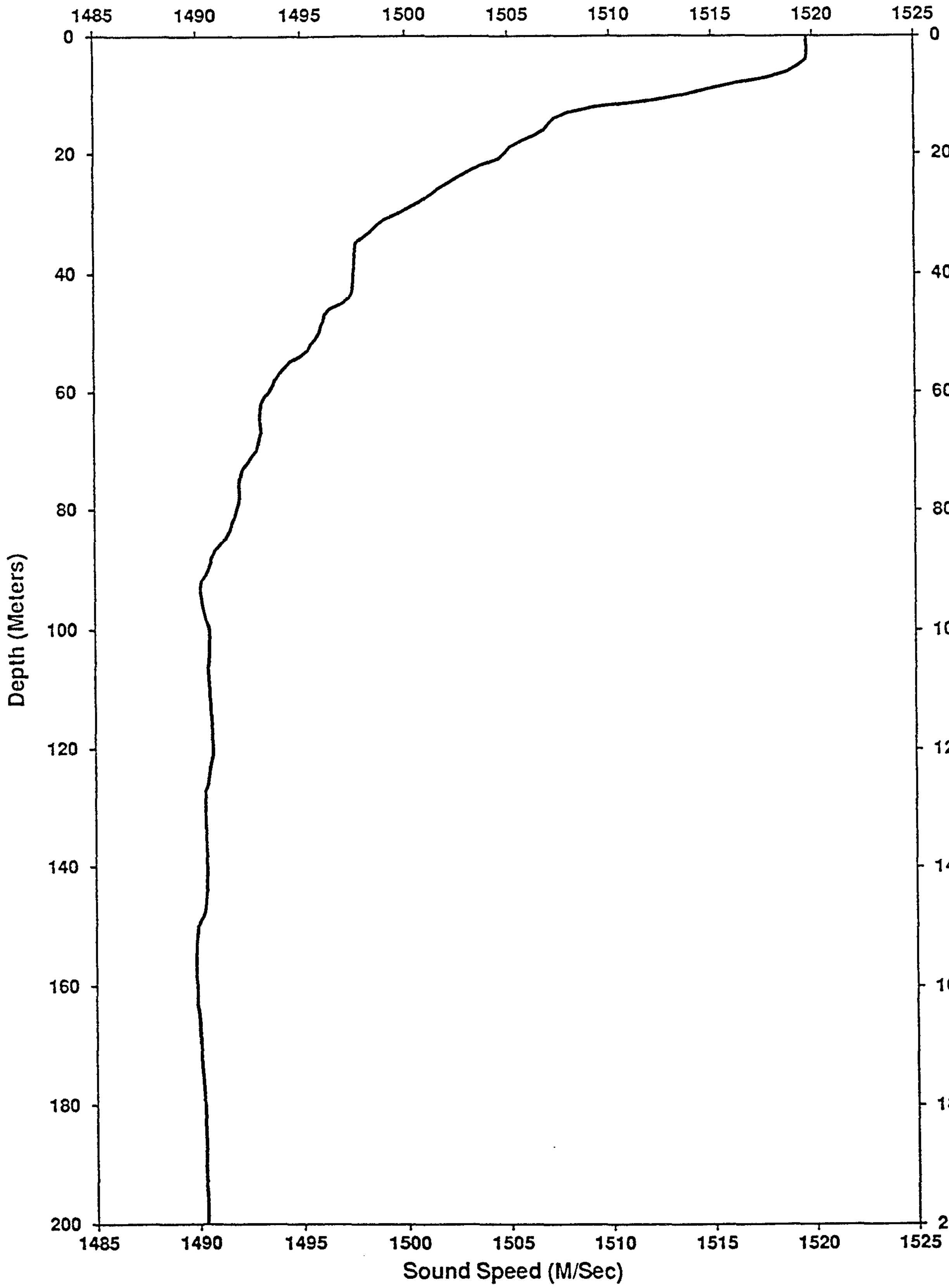

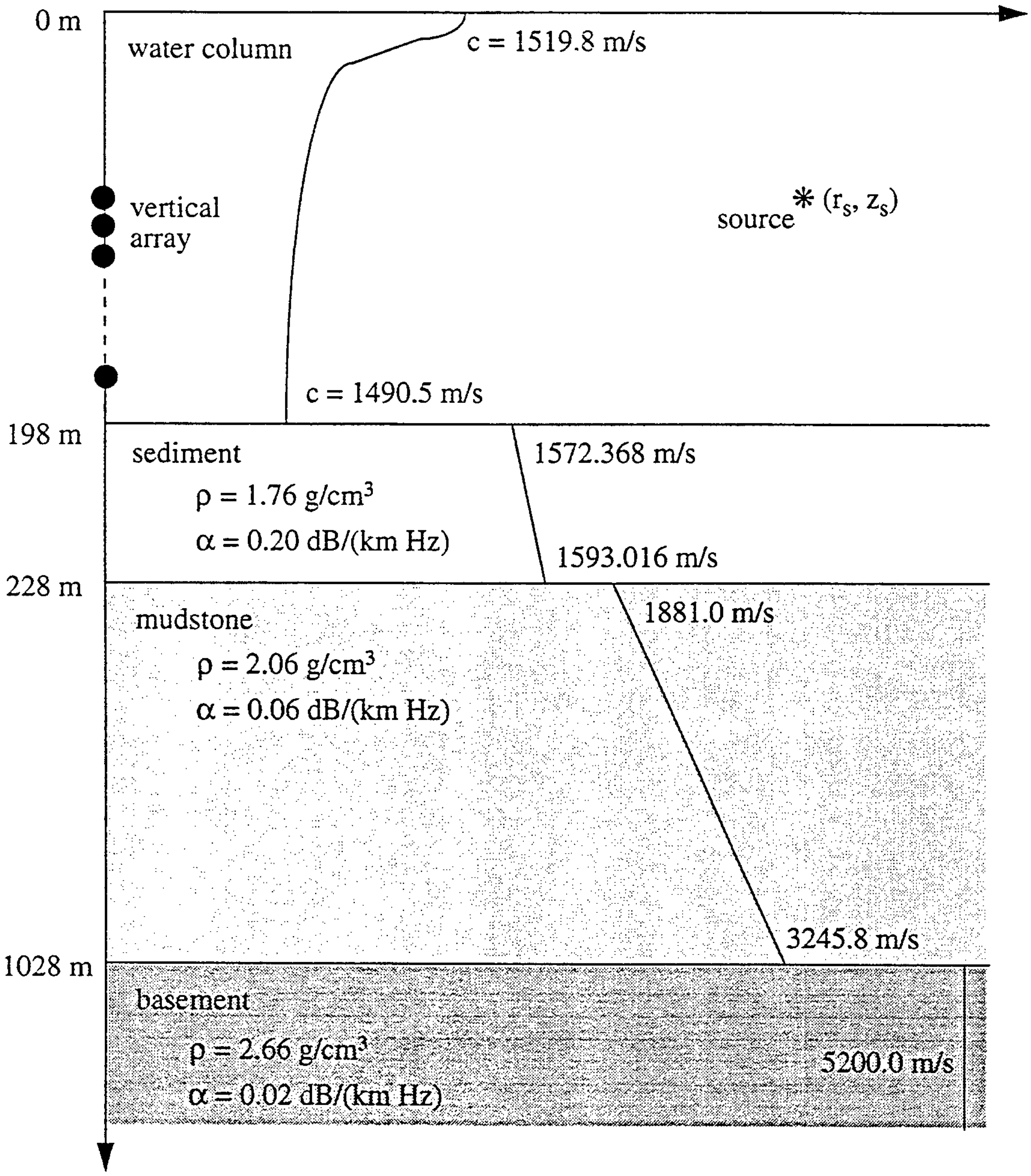

The SWellEx-3 environment.

Environmental Parameter	Lower Bound	Baseline Value	Upper Bound	Units
Bottom depth	195.0	198.0	200.0	m
Sediment velocity (top)	1560.0	1572.368	1580.0	m/s
Sediment velocity (bottom)	1585.0	1593.016	1605.0	m/s
Sediment density	1.65	1.76	1.85	g/cm^3
Sediment attenuation	0.1	0.2	0.3	dB/(km Hz)
Sediment thickness	28.5	30.0	32.5	m
Mudstone velocity (top)	1870.0	1881.0	1890.0	m/s
Mudstone velocity (bottom)	3235.0	3245.8	3255.0	m/s
Mudstone density	1.95	2.06	2.15	g/cm^3
Mudstone attenuation	0.01	0.06	0.11	dB/(km Hz)
Mudstone thickness	798.0	800.0	802.0	m
Basement velocity	5200.0	5200.0	5200.0	m/s
Basement density	2.66	2.66	2.66	g/cm^3
Basement attenuation	0.02	0.02	0.02	dB/(km Hz)

SWellEx-3 Environmental Parameters.

SWellEx-3 - Source Parameters

- Depth = 30 m
- Speed = 5 knots
- Frequencies = 53, 69, 85, 101, 117, 133, 149, 165, 181, and 197 Hz

SWellEx-3 SRP Array Element 22

Start Time: 1994 211 13:20:00.001000 (GMT)

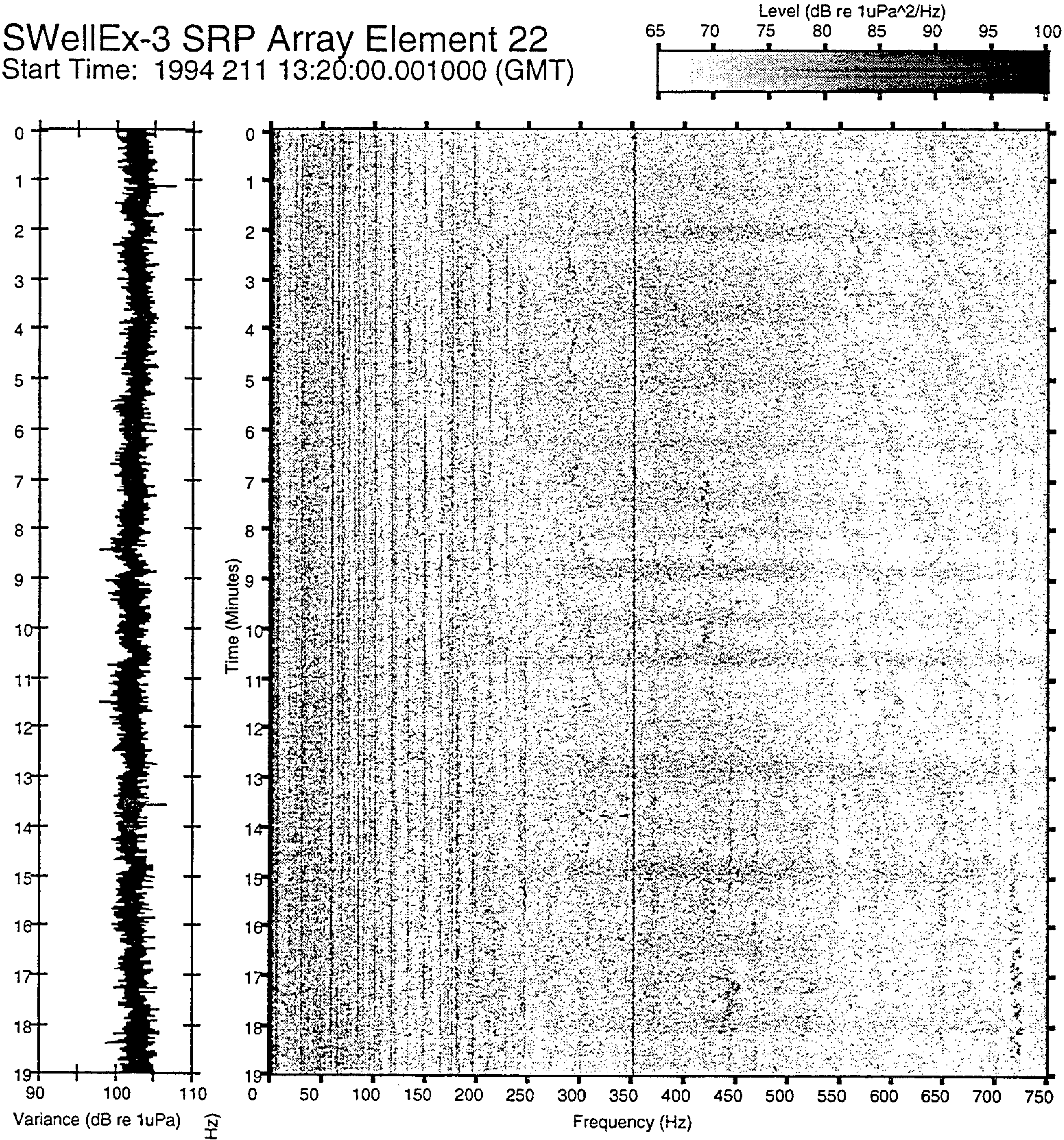

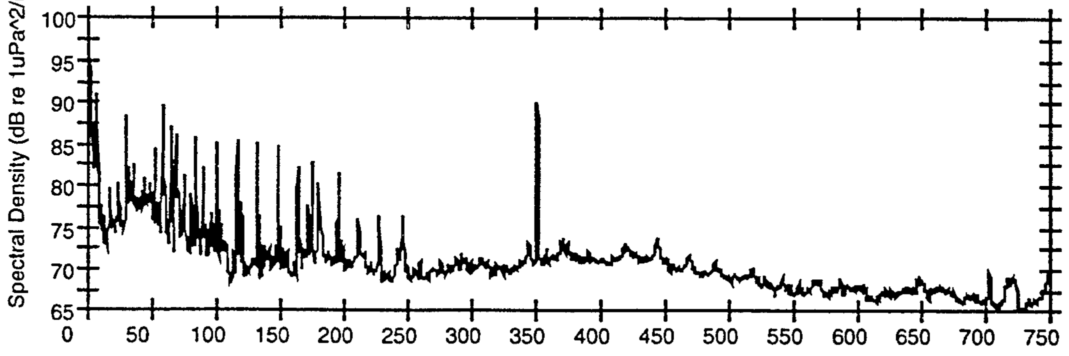

MARINE PHYSICAL LABORATORY

MPL

UNIVERSITY OF CALIFORNIA
SAN DIEGO, CALIF. 92186 USA

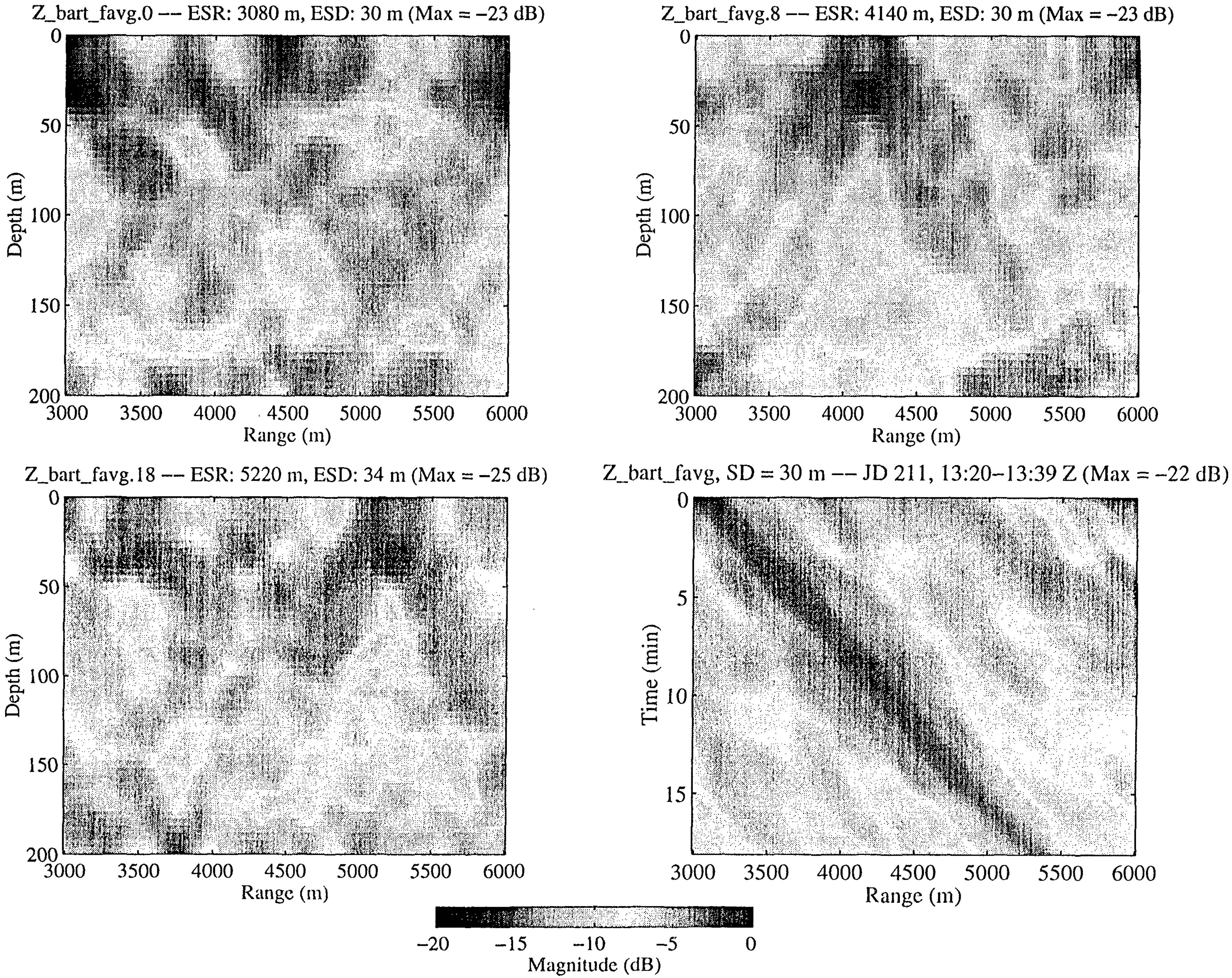
Z_bart_favg.0 –– ESR: 3080 m, ESD: 30 m (Max = –23 dB)
Z_bart_favg.8 –– ESR: 4140 m, ESD: 30 m (Max = –23 dB)
Z_bart_favg.18 –– ESR: 5220 m, ESD: 34 m (Max = –25 dB)
Z_bart_favg, SD = 30 m –– JD 211, 13:20–13:39 Z (Max = –22 dB)
Depth (m)
Time (min)
Range (m)
0
50
100
150
200
5
10
15
3000
3500
4000
4500
5000
5500
6000
–20
–15
–10
–5
0
Magnitude (dB)

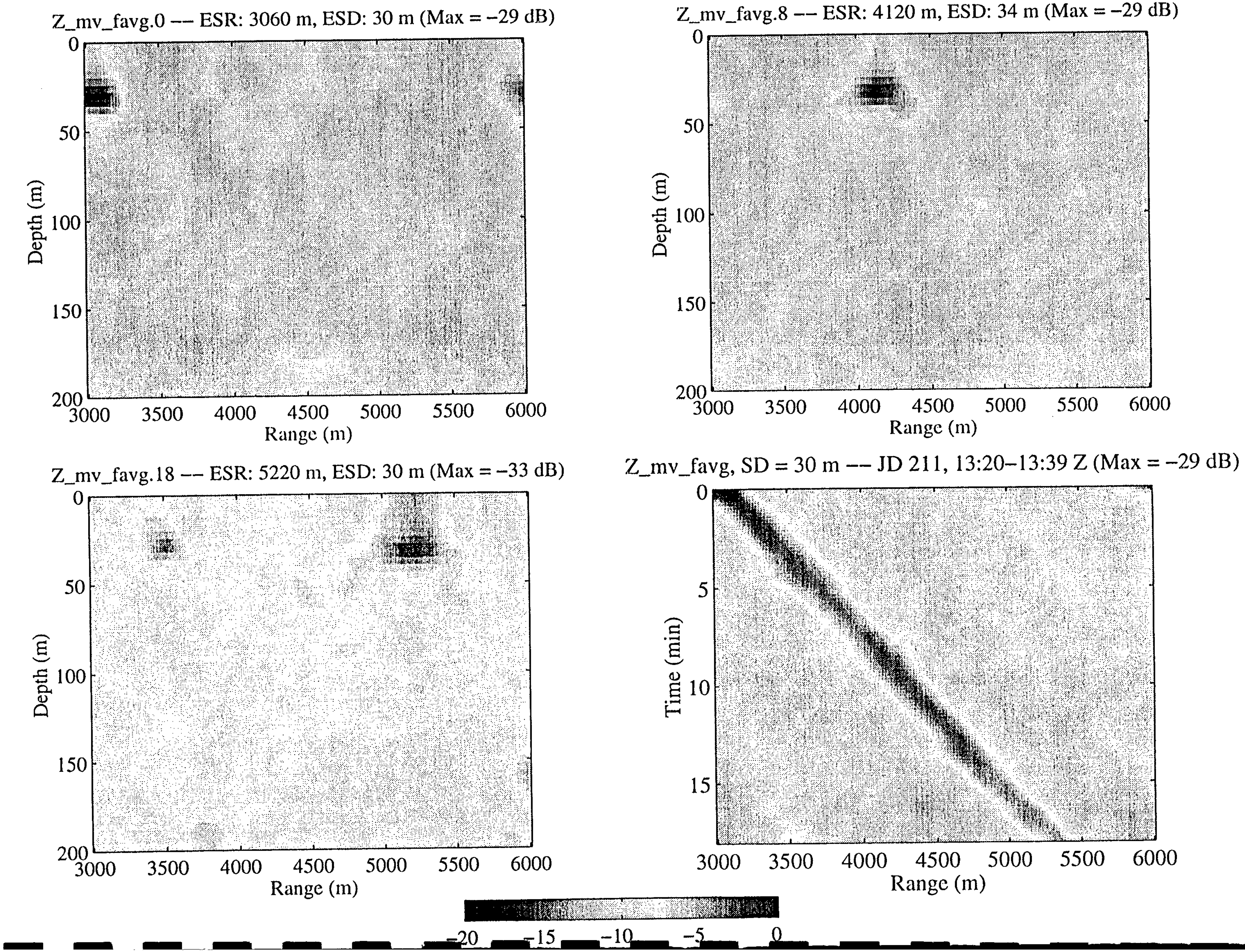

Z_mv_favg.0 -- ESR: 3060 m, ESD: 30 m (Max = −29 dB)

Z_mv_favg.8 -- ESR: 4120 m, ESD: 34 m (Max = −29 dB)

Z_mv_favg.18 -- ESR: 5220 m, ESD: 30 m (Max = −33 dB)

Z_mv_favg, SD = 30 m -- JD 211, 13:20–13:39 Z (Max = −29 dB)

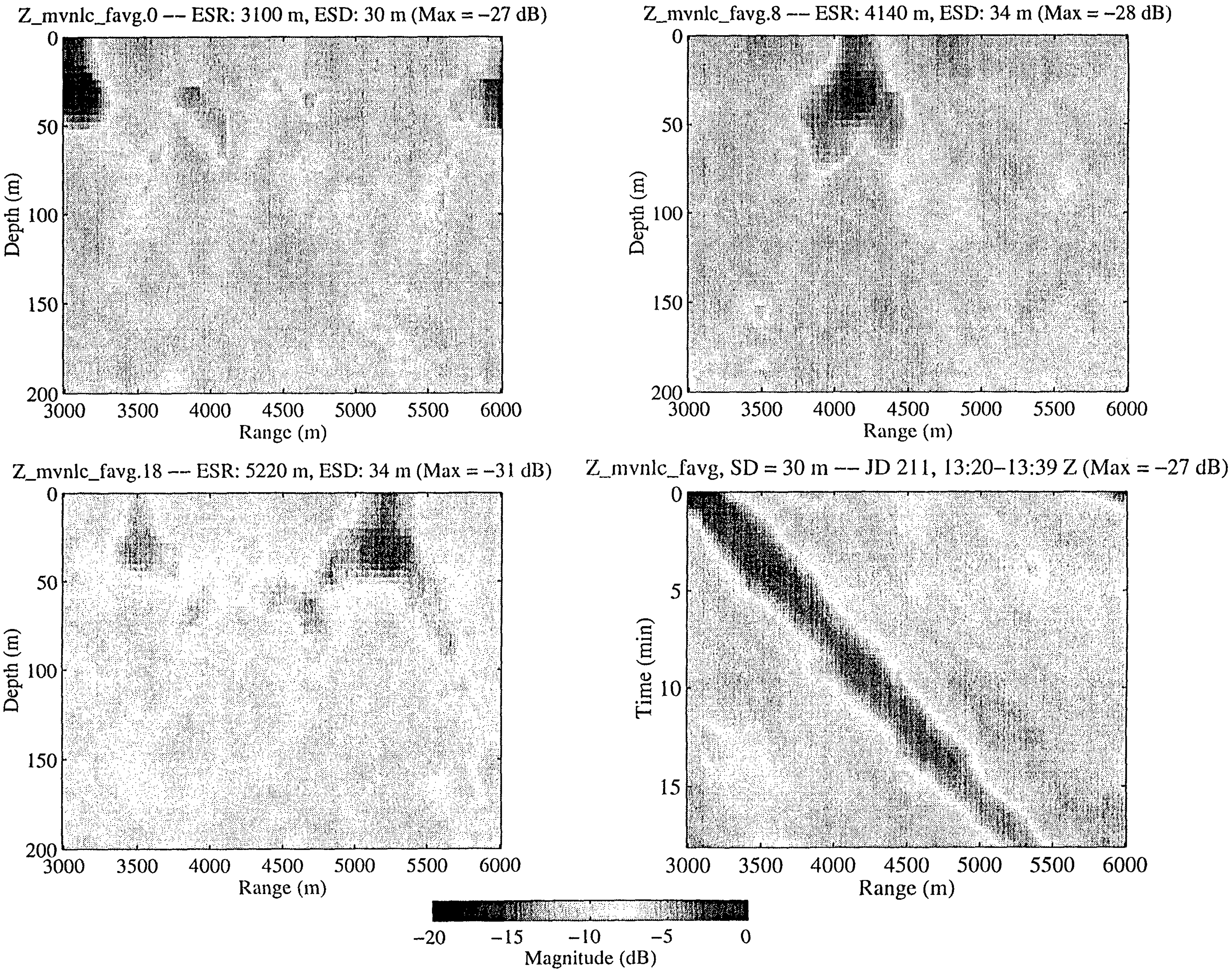
Z_mvnlc_favg.0 –– ESR: 3100 m, ESD: 30 m (Max = −27 dB)

Z_mvnlc_favg.8 –– ESR: 4140 m, ESD: 34 m (Max = −28 dB)

Z_mvnlc_favg.18 –– ESR: 5220 m, ESD: 34 m (Max = −31 dB)

Z_mvnlc_favg, SD = 30 m –– JD 211, 13:20–13:39 Z (Max = −27 dB)

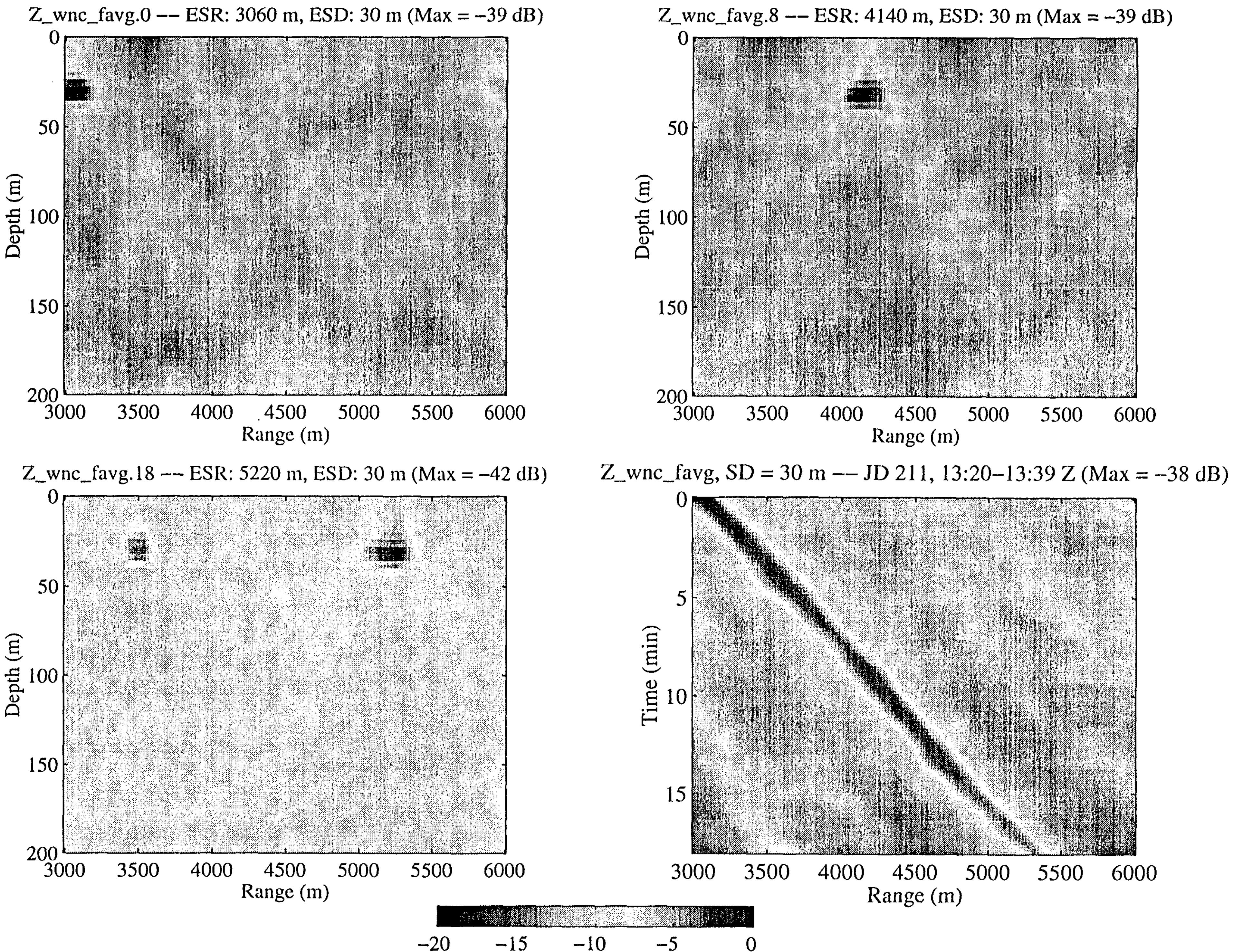
Z_wnc_favg.0 –– ESR: 3060 m, ESD: 30 m (Max = –39 dB)

Z_wnc_favg.8 –– ESR: 4140 m, ESD: 30 m (Max = –39 dB)

Z_wnc_favg.18 –– ESR: 5220 m, ESD: 30 m (Max = –42 dB)

Z_wnc_favg, SD = 30 m –– JD 211, 13:20–13:39 Z (Max = –38 dB)

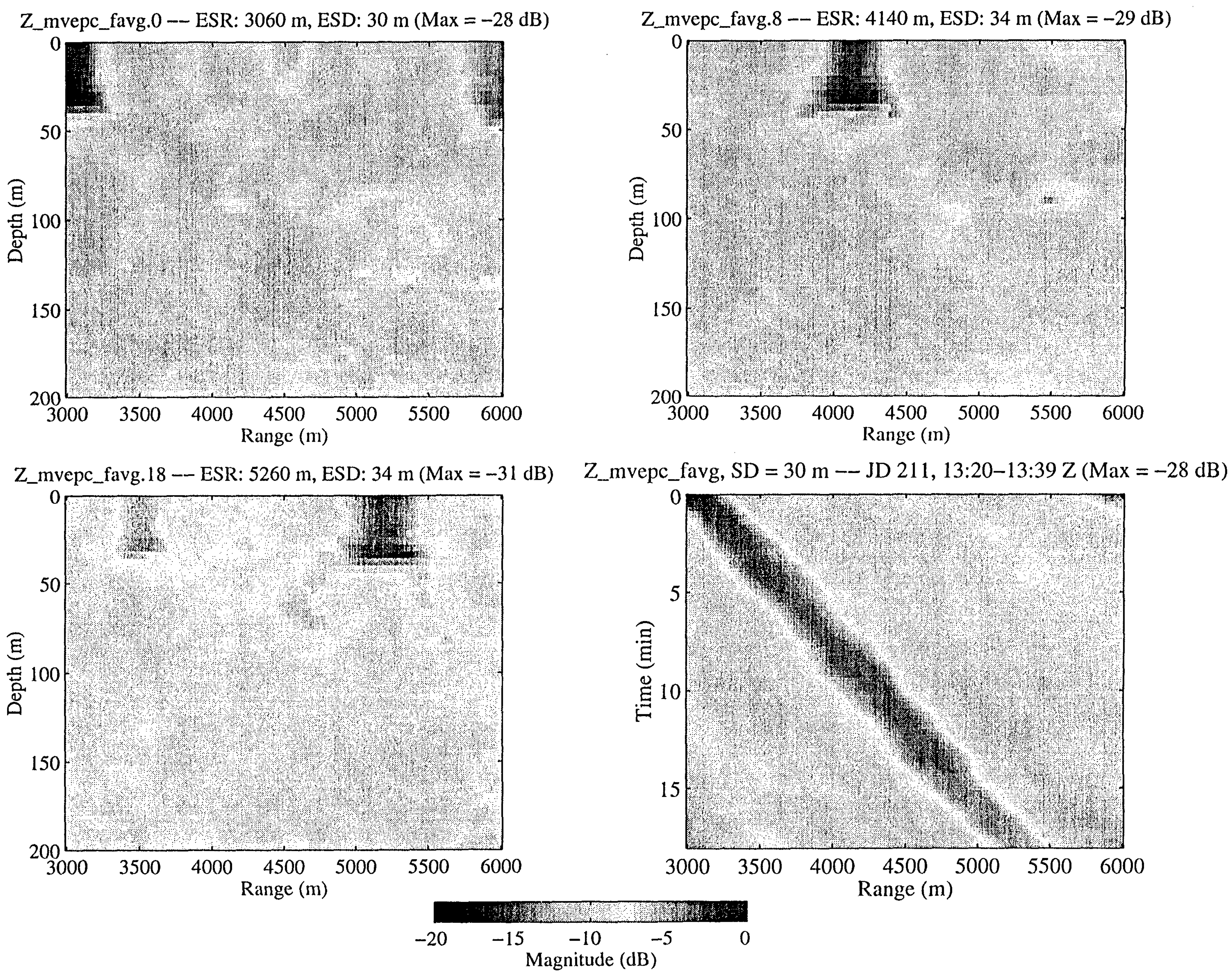

Z_mvepc_favg.0 –– ESR: 3060 m, ESD: 30 m (Max = −28 dB)

Z_mvepc_favg.8 –– ESR: 4140 m, ESD: 34 m (Max = −29 dB)

Z_mvepc_favg.18 –– ESR: 5260 m, ESD: 34 m (Max = −31 dB)

Z_mvepc_favg, SD = 30 m –– JD 211, 13:20–13:39 Z (Max = −28 dB)

Matched Field Inversion of Real Acoustic Data Using Simulated Annealing and Genetic Algorithms

Dick G. Simons and Mirjam Snellen
Underwater Acoustics Group
TNO-Physics and Electronics Laboratory
Oude Waalsdorperweg 63
P.O.Box 96864
2509 JG The Hague
The Netherlands

Abstract

Localization of underwater acoustic sources by matched field processing requires very accurate knowledge of the ocean environment. This stringent requirement is circumvented in the focalization approach, in which environmental parameters are included in the parameter search space. Due to the extremely large number of parameter combinations, this inverse problem requires modern global optimization methods.

Experimental results on the simultaneous estimation of source position, geo-acoustic parameters and other parameters (such as water depth and array geometry) are presented for a shallow water environment. The stationary source at a range of about 5.4 km from the vertical array is succesfully localized in range and depth.

For the forward propagation model we used a normal-mode code developed at TNO-FEL. For the global optimization both simulated annealing algorithms and genetic algorithms have been employed. The performance of these algorithms with regard to efficiency and robustness have been investigated. Further, different parametrizations of the ocean environment (with different degrees of complexity) have been employed.

The inversion is followed by a statistical analysis of the parameter values obtained. When simulated annealing is used for the optimization this has been accomplished by running the algorithm a large number of times. Both the uncertainty in the inverted parameters (which is related to their acoustical importance) and the correlation between the inverted parameters have been investigated.

1 Introduction

During the last decade Matched field processing (MFP) has become an important research topic in underwater acoustics. The main application of MFP is localization of underwater acoustic sources.

The basic principle of MFP is simple: The acoustic field measured with a (vertical) hydrophone array is correlated with the acoustic field computed by an appropriate propagation model for candidate values of the range and depth of the source. This yields the so-called range/depth ambiguity surface. The candidate range and depth showing the highest correlation between measured and modelled field should correspond to the true range and depth of the source.

In MFP it is assumed that all environmental (and other) input parameters for the model are accurately known. However, these parameters are generally not known or at least not sufficiently accurate for a successful source localization. This situation is referred to as mismatch.

Under practical conditions, i.e. when using real experimental acoustic data obtained at sea, one always encounters mismatch. A very promising method for solving this problem and for making MFP more robust (a requirement for practical applications) is the so-called focalization approach [1]. In this case both the source position and the environmental parameters are candidate parameters, i.e. a range, depth *and* environment are sought for which the acoustic field focuses into a source point. Then, environmental parameters and other (geometrical) parameters such as array position, are being estimated as part of the localization process. Due to the extremely large number of possible parameter combinations, such an inverse problem requires modern global optimization methods such as simulated annealing [1] or genetic algorithms [4].

Hereafter focalization is referred to as matched field inversion.

The success of MFP stems also from the availability of highly accurate propagation models. At present, normal-mode models are the most appropriate for MFP calculations [7].

In this paper results are presented for real experimental data obtained in shallow water. For the propagation model we have used a normal-mode model developed at TNO-FEL [6], whereas both simulated annealing and genetic algorithms have been used as a global optimization method.

Section 2 provides a brief description of the experimental setup, i.e. the environmental conditions of the trial area and the characteristics of the transmitting and receiving equipment.

Section 3 discusses the basic principle of simulated annealing (SA) and the results obtained for the parameter inversion, whereas section 4 discusses the basic principle of genetic algorithms (GA) and the results obtained with this technique.

In section 5 the conclusions of this work are given.

2 Experimental setup

The experimental data we used were obtained from SACLANTCEN. In October 1993 SACLANTCEN has performed an MFP experiment in a shallow water area north of the island of Elba (position $43°02.86'N, 10°10.01'E$). In this area the geoacoustic properties were reasonably well known from previous experiments, i.e. a priori knowledge of the acoustic bottom parameters (hereafter denoted by historical parameters) was available. The experiment is described in great detail in [5] and is briefly summarized here.

The experiment has been carried out in a virtually range-independent area. The water depth H_w amounts to $\sim$ 127 m and the flat bottom is covered with a thin clay/sand-clay sediment of a few meters thickness. The propagation conditions are typical for the summer conditions encountered in the area around Elba (isothermal upper layer of $\sim$ 60 m). For the part of the data we selected, the wind speed amounts to $\sim$ 8 m/s corresponding to a rms surface roughness of about 0.5 m.

The complete sound speed profile of the ocean environment is given in figure 1. The sound speed profile in the water column has been measured at the site of the receiving array.

Here we have assumed that the bottom below the sediment (denoted as subbottom) is a semi-infinite homogeneous medium. This is in accordance with the usual normal-mode modelling of the sea floor: the ocean bottom is assumed to consist of a sediment layer over a semi-infinite homogeneous subbottom. In the sediment layer the sound speed is allowed to vary with depth, whereas in the subbottom the sound speed c_b is assumed to be constant. The density ρ_s and attenuation coefficient α_s of the sediment are also assumed to be constant. The same holds for ρ_b and α_b, the subbottom density and attenuation coefficient, respectively.

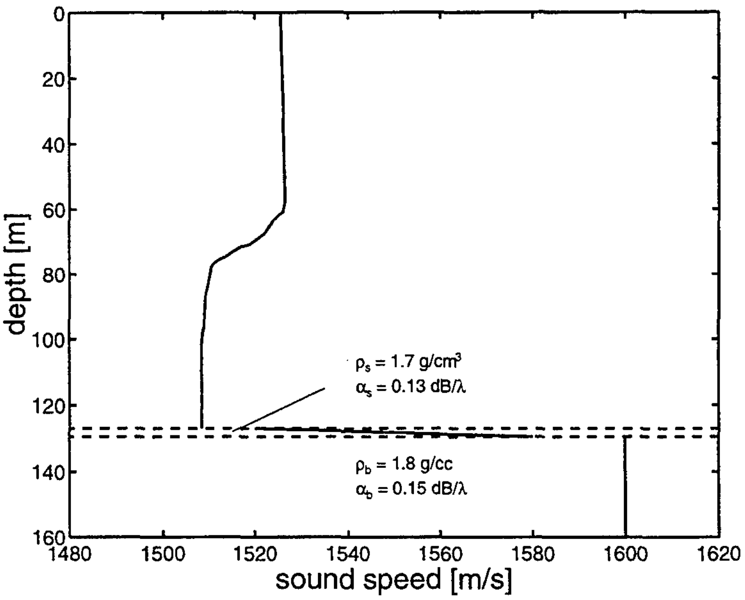

Figure 1: *The ocean environment discussed in this paper.*

Previous measurements carried out in this area have indicated that the sound speed in the sediment increases linearly with depth. Hence, the sound speed profile in the sediment can be characterized by three parameters: the upper sediment speed c_{su}, the lower sediment speed c_{sl} and the sediment thickness H_s. Historical values for the geo-acoustic parameters are taken from [5] and are given in table I below. These values were also used in figure 1.

TABLE I: Historical geo-acoustic parameters and nominal geometrical parameters

Parameter	symbol	unit	numerical value
upper sediment speed	c_{su}	m/s	1520
lower sediment speed	c_{lu}	m/s	1580
sediment thickness	H_s	m	2.5
sediment density	ρ_s	g/cc	1.7
subbottom density	ρ_b	g/cc	1.8
sediment attenuation	α_s	dB/λ	0.13
subbottom attenuation	α_b	dB/λ	0.15
subbottom speed	c_b	m/s	1600
source range	r_s	km	5.4
source depth	z_s	m	75
water depth	H_w	m	127
array depth	d_R	m	112.7

The receiving system is a vertical array consisting of 48 hydrophones with 2 m spacing. The nominal depth of the deepest hydrophone, hereafter denoted as receiving array depth d_R, is 112.7 m. Due to array tilt and/or imprecise measurement of the water depth the actual array depth can be different.

An acoustic source was deployed at a range r_s of $\sim$ 5.4 km north of the receiving array at a depth z_s of $\sim$ 75 m. Two broadband signals were transmitted by the source, not simultaneously. The frequency bands of these signals were 160 - 180 Hz and 320 - 350 Hz, respectively. For the analysis reported hereafter we have selected a single frequency in the centre of the 160 - 180 Hz band, i.e. the Fourier coefficients at 168.95 Hz obtained after a Fourier transformation of 8 seconds of the data received at each hydrophone (sample frequency of the data acquisition system is 1 kHz). This measured complex pressure vector has been inverted using simulated annealing (section 3) and genetic algorithms (section 4).

3 Inversion by simulated annealing

Matched field inversion has been applied to the measured complex pressure field described in the former section. Both source range and depth and other geometrical and environmental model input parameters are considered unknown parameters, which have to be determined through an optimization procedure. This involves finding a set of parameter values which minimizes the discrepancy between the modelled and measured acoustic field.
As a start the optimization was carried out for all 12 model input parameters given in table I. There was no optimization for the sound speed profile in the water column: the profile measured at the array site was used.
The determination of this relatively large number of unknown input parameters is a real inverse problem. The number of parameter value combinations is extremely large. In addition, the parameter search space can have a large number of local minima. Such a problem requires modern global optimization methods.
The application of simulated annealing as a global optimization method for solving the inverse problem is discussed in this section, whereas the application of a genetic algorithm is dicussed in the section thereafter. Both techniques are efficient methods for finding the global minimum of a cost or energy function that depends on many parameters.

3.1 Basic principle

In the SA algorithm the unknown parameters have been determined by minimizing the energy function (or cost function)

$$E = 1 - P_{lin}^2 \tag{1}$$

with P_{lin} the linear processor power given by

$$P_{lin} = |\vec{p}_{cal}(\vec{m}) \cdot \vec{p}_{obs}^{\,*}|^2 \tag{2}$$

i.e. the inner product of the calculated pressure field $\vec{p}_{cal}$ and the observed pressure field $\vec{p}_{obs}$, both in the frequency domain. Both column vectors are normalized to unity and are of length 48 (being the number of hydrophones)

$$\vec{p}_{cal}^{\,\dagger}\, \vec{p}_{cal} = 1 \tag{3}$$

$\vec{p}_{cal}$ has been computed by a normal-mode model [6] and depends on $\vec{m}$, the input parameter vector given by

$$\vec{m} = (c_{su}, c_{sl}, H_s, \rho_s, \rho_b, \alpha_s, \alpha_b, c_b, r_s, z_s, H_w, d_R)^T \tag{4}$$

The search is initiated with random values for the parameters m_i within the imposed bounds $[B_{l,i}, B_{u,i}]$. The search bounds for each model input parameter, i.e. the priori knowledge, are given in table II below.

TABLE II: Model input parameters, historical values, search bounds and SA results

m_i	Hist.	B_l	B_u	SA (log)	SA (lin)
c_{su} (m/s)	1520	1450	1550	1487 ±25	1492±24
c_{sl} (m/s)	1580	1500	1600	1535 ±25	1541±21
H_s (m)	2.5	1.5	6.0	3.9 ±1.2	4.0±1.3
ρ_s (g/cc)	1.7	1.2	2.2	1.9 ±0.3	1.9±0.2
ρ_b (g/cc)	1.8	1.2	2.2	1.6 ±0.3	1.8±0.3
α_s (dB/λ)	0.13	0.0	0.4	0.04 ±0.05	0.04±0.04
α_b (dB/λ)	0.15	0.0	0.4	0.13 ±0.11	0.19±0.11
c_b (m/s)	1600	1550	1650	1577 ±5	1577±6
r_s (m)	5400	1000	11000	5362 ±99	5361±65
z_s (m)	75	10	110	75.5 ±0.7	75.5±0.8
H_w (m)	127.0	125	130	127.5±1.6	127.3±1.3
d_R (m)	112.7	110	114	111.9±0.7	111.7±0.5

The energy function is evaluated for the initial parameter combination.
Then the individual parameters are randomly perturbed one at a time according to

$$m_i' = m_i + \xi \, \Delta_i \tag{5}$$

with ξ a random number drawn from a uniform distribution on $[-1, 1]$.
The maximum perturbation Δ_i allowed for parameter m_i has been taken half the corresponding search interval

$$\Delta_i = \frac{1}{2}(B_{u,i} - B_{l,i}) \tag{6}$$

When the new parameter value m_i' falls outside the interval $[B_{l,i}, B_{u,i}]$ a new value for m_i' is drawn again.
After each perturbation the energy function is evaluated. A decrease in E ($\Delta E < 0$) is accepted unconditionally, whereas an increase in E ($\Delta E > 0$) is accepted with a probability P given by the Boltzmann distribution

$$P = e^{-\Delta E/T_j} \tag{7}$$

with T_j a control parameter analogous to the temperature.
When all parameters have been perturbed a certain number of times (twice in this work [2]), the temperature is slightly reduced according to a cooling schedule. Two different sequences of decreasing temperatures have been employed, i.e. the logarithmic schedule

$$T_{j+1} = c_f \, T_j \tag{8}$$

and the linear schedule

$$T_j = T_1 + a \, (j-1) \, (T_{end} - T_1) \tag{9}$$

The cooling factor c_f for logarithmic cooling is a constant < 1, but close to 1. For linear cooling T_1 and T_{end} are the starting temperature and end temperature, respectively, and a is another constant.
Hence, the probability of accepting an increase in E decreases as T is lowered (see equation 7). The concept of accepting perturbations that increase E allows the algorithm to escape from local minima in the parameter search space.

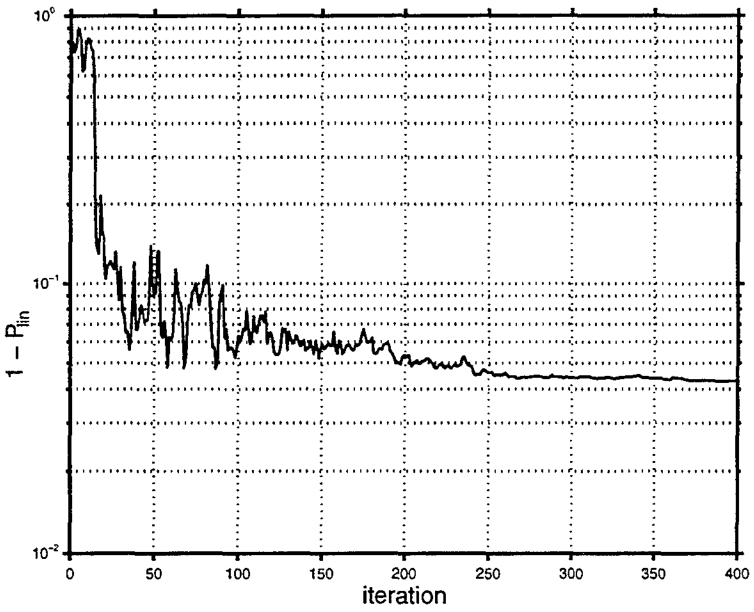

Figure 2: *Convergence of one of the SA runs.*

SA is problem-specific: appropriate values for T_1 and c_f (in the case of logarithmic cooling) and for T_1, T_{end} and a (for linear cooling) have to be determined by trial and error. The cooling must be sufficiently slow in order to reach the global minimum, thereby avoiding sub-optimal solutions (local minima).

3.2 Results

The SA algorithm has been run 25 times for both cooling laws mentioned above. For each run the same 8 seconds of experimental data was used.

For logarithmic cooling the SA parameters c_f and T_1 were 0.97 and 0.06, respectively. For linear cooling the SA parameters T_1, T_{end} and a were 0.06, 0.0003 and 0.00503, respectively. With 400 iterations (see below) then the start and end temperatures of both cooling sequences are equal.

The starting temperature has been determined such that about 85 % of the perturbations are accepted at the first iteration, see [2]. About 200 temperature steps turned out to be sufficient for converging of the algorithm. Since each parameter is changed twice at each temperature, this corresponds to 400 iterations. (After all parameters have been changed once, an iteration is completed).

The convergence of the SA algorithm is illustrated in figure 2. In this figure the mean energy averaged over all accepted model runs at a single temperature is plotted as a function of iteration for one of the SA runs (logarithmic cooling). Note that in this figure $1 - P_{lin}$ has been plotted instead of the (mean) energy $1 - P_{lin}^2$ (see equation 1).

The convergence of the model input parameters is given in figure 3. One observes that both the source range and source depth converge rapidly to correct values.

Employing the logarithmic cooling schedule (with $c_f = 0.97$) the SA algorithm has been successful 15 times, i.e. 10 times the algorithm converged to a local minimum. In the latter 10 cases correct values for source range and depth were not found. Employing the linear cooling schedule the number of successful runs amounts to 23 (out of 25). Since the start and end temperature of the cooling schedules are

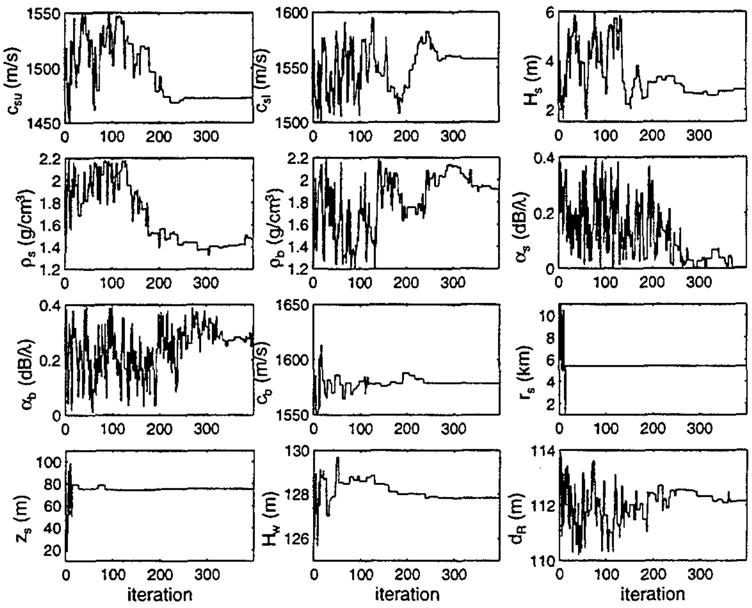

Figure 3: *Convergence of the model input parameters for the SA run of figure 2.*

equal, the much better performance of the linear cooling schedule must be due to the slower cooling in the first part of the linear cooling schedule.

In this way 15 estimates for each model input parameter are produced in the case of the logarithmic cooling schedule and 23 estimates for each parameter are produced in the case of the linear cooling schedule. The a posteriori probability distributions of the parameter estimates are given in figure 4 (using the linear cooling schedule results). In this way information is provided about the uncertainty in the final results obtained. Table II provides the mean and standard deviation of the parameter estimates.

It is seen that the source range r_s, the source depth z_s and the subbottom sound speed c_b are quite well determined. For these parameters the a posteriori probability distributions are unambigously peaked and the standard deviation (see table II) is small compared to the corresponding search intervals (the a priori information). The parameters r_s, z_s and c_b turn out to be the acoustically most important parameters. The other parameters are less well determined. Since the sediment thickness is less than half a wavelength at the selected frequency, propagation is less sensitive to the sediment parameters. The corresponding probability distributions are not unambigously peaked (see figure 4) and the standard deviations turn out to be a substantial fraction of the corresponding search intervals (see table II). Consequently, the sediment parameters are not well determined at the test frequency. The same holds for the subbottom density and attenuation constant. However, the subbottom sound speed c_b turns out to be a very important acoustic parameter. This is not surprising, since the number of normal modes is highly dependent on c_b.

It is also worthwhile examining the correlation between the model input parameter estimates. It is observed that the geometrical parameters (r_s, z_s, H_w and d_R) are highly correlated. For instance, the highest correlation is observed between source range r_s and water depth H_w. A plot of the source range estimates against water depth estimates, see figure 5, indeed reveals the high correlation between these parameters. This means that there exists a long valley in the parameter search

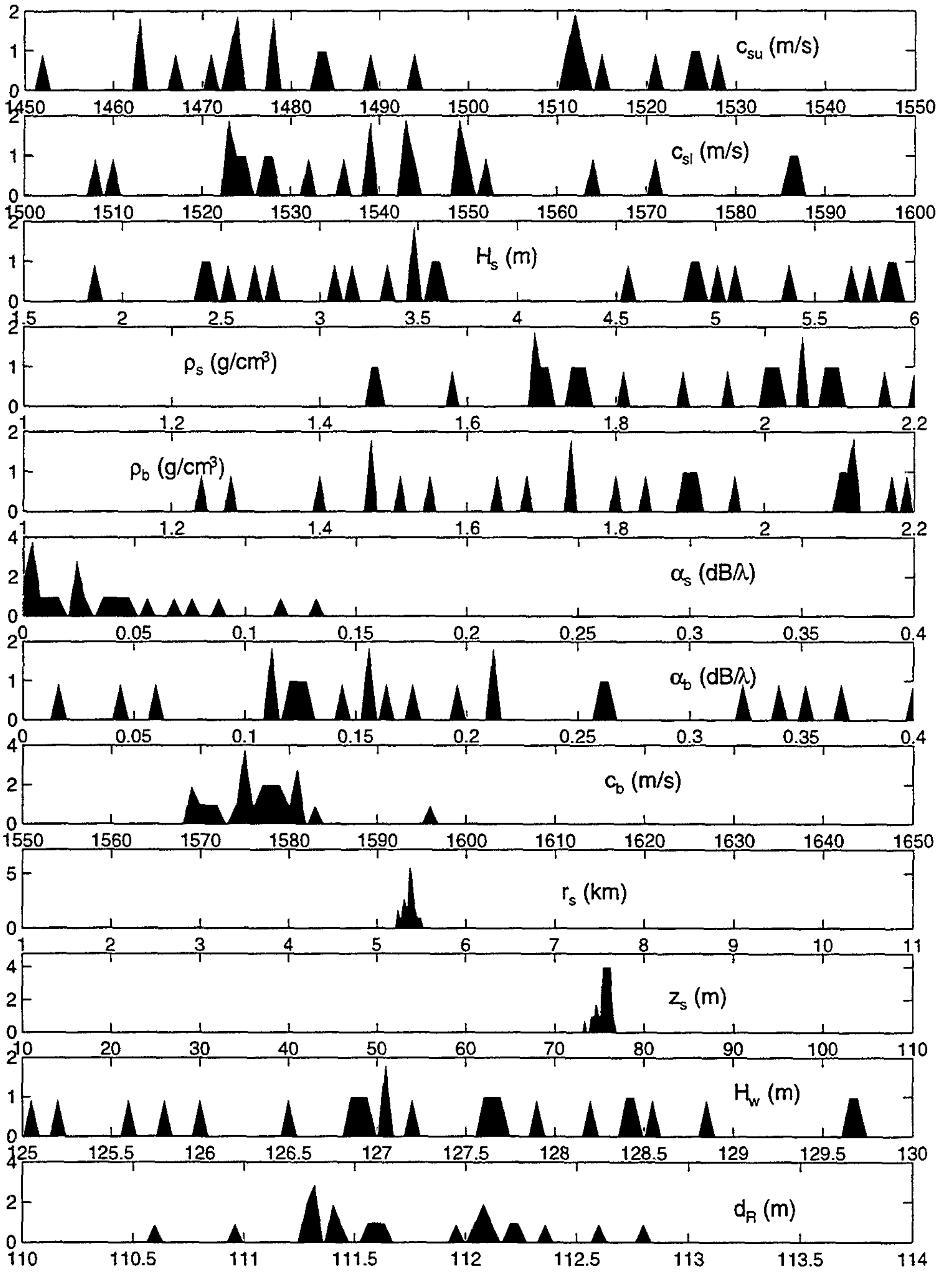

Figure 4: *Probability distributions of the parameter estimates of the SA runs with linear cooling.*

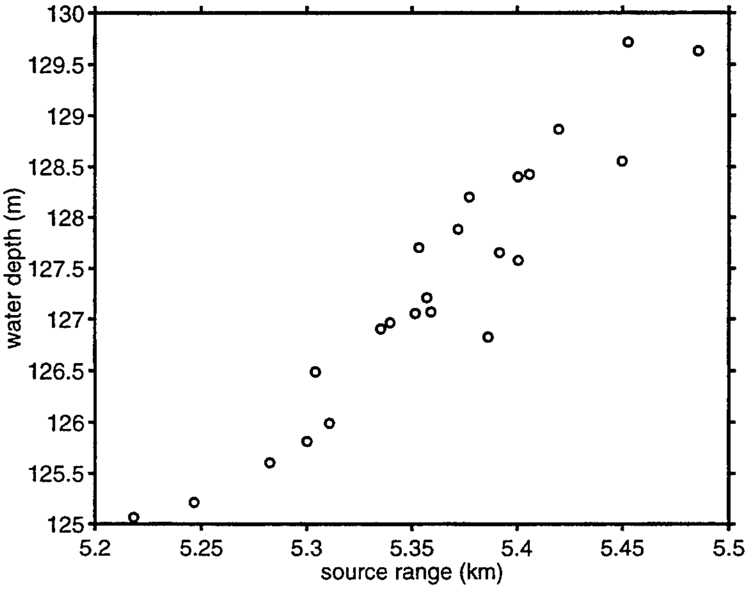

Figure 5: *Source range estimates ploted against water depth estimates obtained from the SA runs with linear cooling.*

space that is oriented obliquely to the parameter axes. Such a feature is difficult to navigate. However, rotating the the coordinate system such that the valley aligns with one of the axes can improve the efficiency of the SA algorithm [3].

As mentioned above, propagation cannot be very sensitive to the sediment parameters at the present test frequency. Therefore, the SA algorithm has also been run using only 7 input parameters. In this case the sediment parameters are omitted, thereby decreasing the complexity. At the same time the parameter search intervals were enlarged.

Using the logarithmic cooling law (with $c_f = 0.97$) the algorithms has been sucessful for 25 times out of 45 runs (success rate 62 %). In these cases both source range and source depth converge rapidly to correct values, whereas the third most important parameter, subbottom sound speed, converges to a value in agreement with that obtained for the SA runs with 12 parameters.

The 7 model input parameters, the corresponding search bounds imposed and the means and standard deviations of the estimated parameter values obtained after the 25 successful SA runs are given in table III below.

TABLE III: Model input parameters, search bounds and estimates resulting from the SA runs with only 7 parameters

m_i	B_l	B_u	SA estimates
ρ_b (g/cc)	1.2	2.6	2.3±0.3
α_b (dB/λ)	0.0	1.0	0.21±0.11
c_b (m/s)	1550	1750	1575±5
r_s (m)	0	11000	5435±75
z_s (m)	0	120	75.9±0.7
H_w (m)	125	135	129.6±1.3
d_R (m)	110	114	112.2±0.9

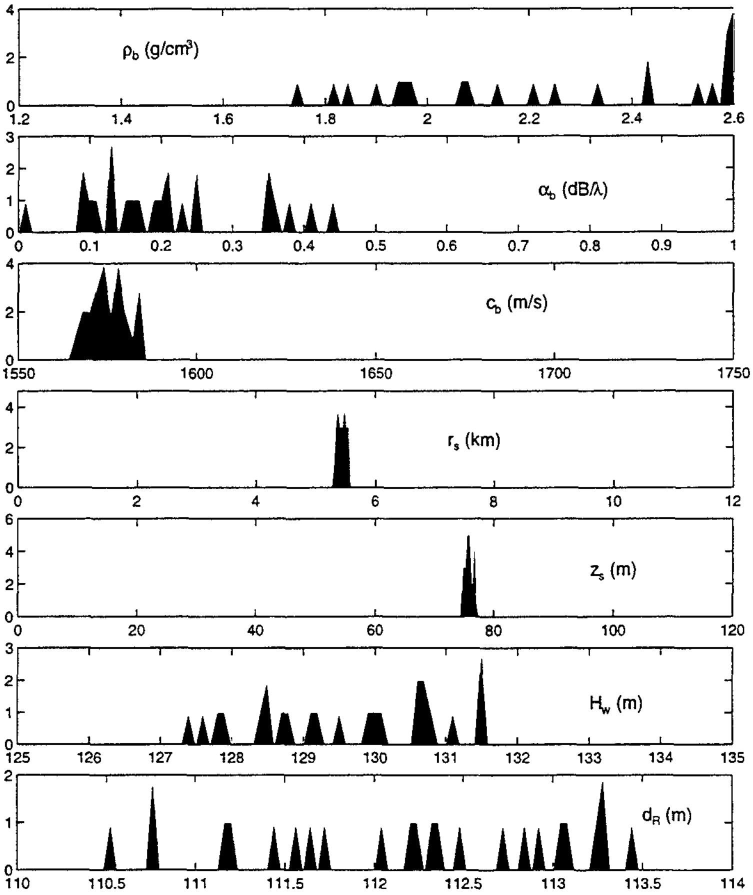

Figure 6: *Probability distributions of the parameter estimates of the SA runs with only 7 parameters.*

The a posteriori probability distributions of the parameter estimates are given in figure 6. These results are in accordance with the results obtained from the SA runs with 12 parameters (see table II).
It is interesting to note that now all parameters are highly correlated with each other (except for the bottom attenuation constant).

4 Inversion by a Genetic Algorithm

4.1 Basic principle

The genetic Algorithm (GA) [4] starts with a, randomly generated, initial population of q members, each representing a possible parameter value combination $\vec{m}$. Depending on the usefulness of the solution represented, all members of the population are assigned a fitness score. Based on these fitness scores, a parental distribution is selected from the initial population. The parents are combined in pairs, and operators are applied to them to produce children, i.e. a new set of possible solutions. Traditionally, the operators are crossover and mutation. In order to apply these operators the parents are coded in binary format. The parents in binary form are called chromosomes, consisting of genes, with each gene representing one parameter. If now a fraction of the current population is replaced by the children, a new population is created that contains a higher proportion of the characteristics possessed by the good members of the previous generation.

By continuing this process over many generations, good characteristics are spread throughout the population, meanwhile being mixed and exchanged with other good characteristics.

For each of the members of the population the cost or energy function

$$E = \sqrt{1 - P_{lin}} \tag{10}$$

is calculated (the fitness equals $(1 - E)$). P_{lin} is given by equation 2. The parental distribution is selected by assigning a selection probability to each of the members according to

$$p_l = \frac{exp(-\frac{E(\vec{m_l})}{T})}{\sum_{k=1}^{q} exp(-\frac{E(\vec{m_k})}{T})} \tag{11}$$

The temperature T is decreased as the evolution continues.

In the reproduction part q children are produced. The first part of the reproduction is crossover. For each pair of parents crossover points at each of the genes in a chromosome are randomly selected, and the gene parts of both parents are exchanged. Crossover occurs with a probability p_c. Following crossover each bit of the chromosome is perturbed with a mutation probability p_m.

Out of the set of q children, $(1 - f)q$ children are randomly selected to replace the $(1 - f)q$ least fit members of the initial population. Hence, the fq most fit members of the initial population are retained.

This process of producing a new generation is continued until a specified amount of generations is reached.

4.2 Results

The GA has been applied to the inversion process using the same data as used in SA. Following [4] the GA has been set as follows:

- The population size q should be large enough that the model parameter vectors can represent sufficient points in the parameter search space, but it should be small enough that several iterations can be performed. A population size of 64 members is used;
- The reproduction size f should be large enough such that the fittest members remain in the population, but it should also be small enough in order to avoid local minima. Here two different values for f have been examined, i.e. $f = 0.5$ [4] and $f = 0.2$;
- In each generation the temperature is taken equal to the lowest of the energy function values found (i.e. highest fitness). Hence, the temperature decreases as the evolution continues, which results in a stricter reproduction selection criterion (i.e. a p_i vs. E distribution more peaked towards higher E, see equation 11);
- For the crossover probability p_c a value of 0.8 is used;
- A value of 0.05 is taken for the mutation probability p_m;
- The number of generations used is 80, which is sufficient for converging of the algorithm;

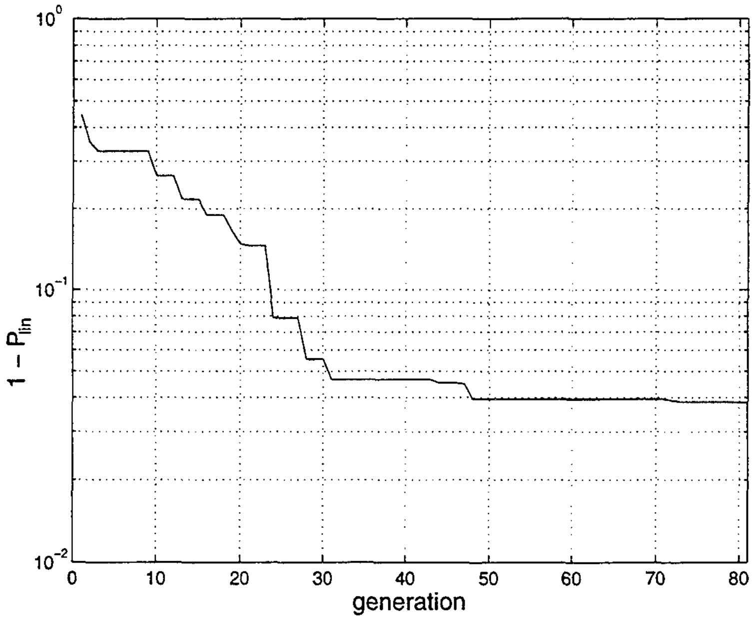

Figure 7: *Convergence of one of the GA inversions.*

- All parameters are represented by an 8 bit binary string.

The genetic algorithm has been run 15 times for $f = 0.5$. Only 40 % of these runs converged to the correct values for source range and the depth. For $f = 0.2$, however, 75% of the runs were successful. Therefore, this situation has been investigated more elaborately (55 runs). The better performance of the algorithm with the lower f is due to the fact that it allows a more extensive exploration of the parameter search space (thereby avoiding local minima).

The convergence of the GA algorithm is illustrated in figure 7. In this figure the energy of the most fit member of the population is plotted as a function of generation. Note that $1 - P_{lin}$ is plotted instead of energy $\sqrt{1 - P_{lin}}$.

The corresponding convergence of the model input parameters of this GA run is given in figure 8.

In the final population about 30 % of the members have converged (i.e. $(1 - P_{lin}) < 0.07$). The probability distributions of these most fit members are given in figure 9. This result cannot be compared directly to that obtained with the SA runs, see figure 6, since the results of several GA runs are required in order to obtain convergence to other optimum parameter combinations. Still, a single GA run provides information about the uncertainty (acoustical importance) of the inverted parameters.

5 Conclusions

It has been demonstrated that both simulated annealing and genetic algorithms are capable of inverting shallow water acoustic data. In particular the robustness of the algorithms, i.e. the relative number of successful inversions, has been investigated. The parameters of the algorithms have been established such that the success rate is, more or less, maximized without losing too much speed of convergence.

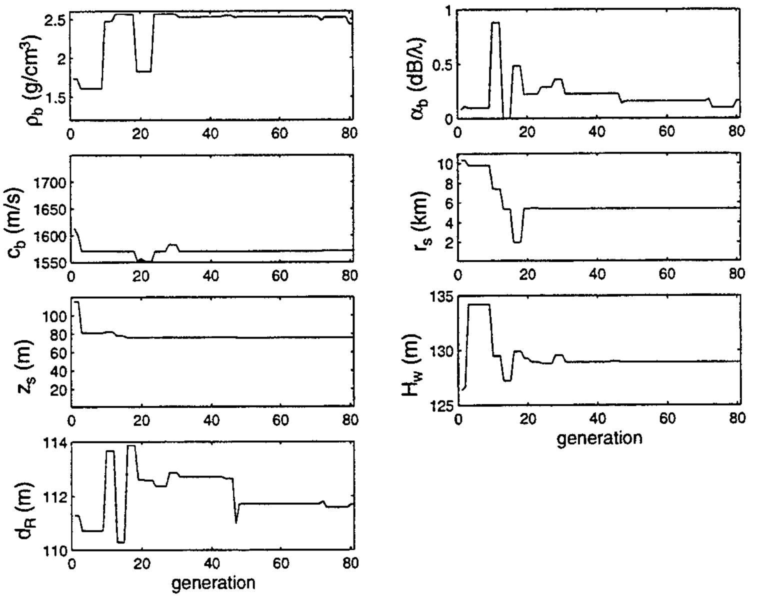

Figure 8: *Convergence of the model input parameters for the GA run shown in figure 7.*

It has been emphasized that an inversion is incomplete if not followed by a statistical analysis of the model input parameter estimates. Such an a posteriori analysis provides information about the uniqueness and uncertainty (i.e. acoustical importance) of the parameter estimates. It is also useful to investigate parameter coupling, i.e. correlation between the inverted parameters.

References

[1] M.D. Collins and W.A. Kuperman, *Focalization: environmental focussing and source localization*, J. Acoust. Soc. Am. **90**, 1410-1422 (1991)

[2] S.E. Dosso, M.L. Yeremy, J.M. Ozard and N.R. Chapman, *Estimation of Ocean-Bottom Properties by Matched-field Inversion of Acoustic Field Data*, IEEE J. Oceanic Eng. **18(3)**, 232 - 239 (1993)

[3] M.D. Collins and L. Fishman, *Efficient navigation of parameter landscapes*, J. Acoust. Soc. Am. **98**, 1637 - 1644 (1995)

[4] P. Gerstoft, *Inversion of seismoacoustic data using genetic algoritms and a posteriori probability distributions*, J. Acoust. Soc. Am. **95**, 770-782 (1994)

[5] D.F. Gingras and P. Gerstoft, *Inversion for geometric and geoacoustic parameters in shallow water: Experimental results*, SACLANTCEN REPORT SR-229

[6] D.G. Simons and R. Laterveer, *Normal-mode Sound Propagation Modelling for Matched Field Processing*, TNO-report FEL-95-A084, April 1995

[7] A. Tolstoy, *Matched field processing for Underwater Acoustics*, World Scientific Publishing Co. Pte. Ltd., 1993

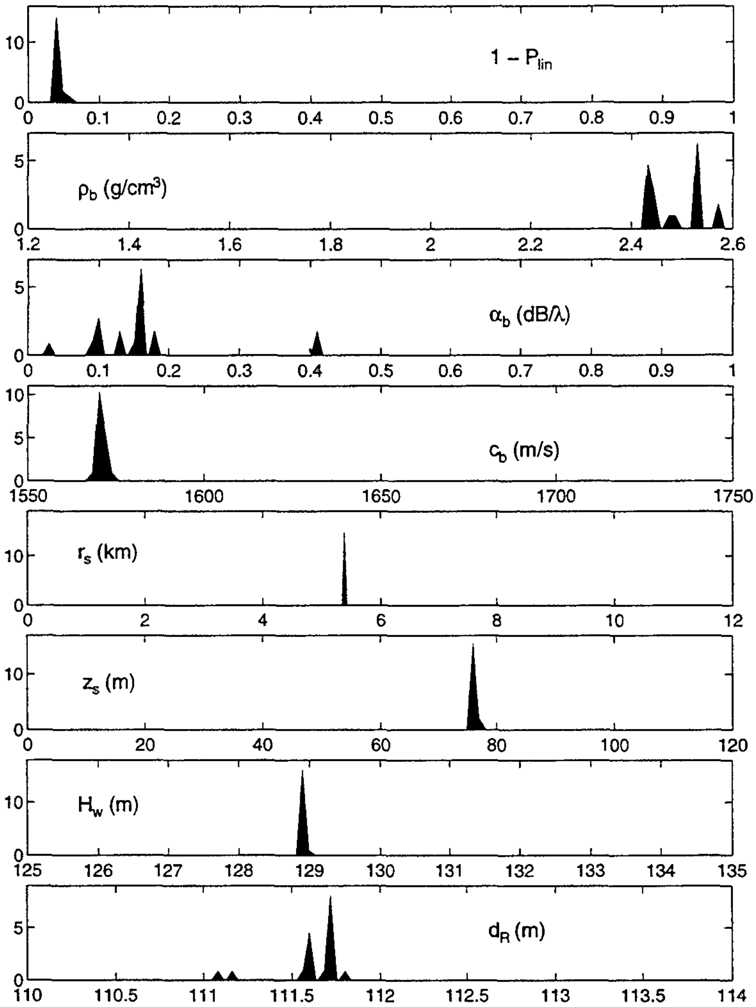

Figure 9: *Probability distributions of the most fit members of the final population (GA run of figure 7)*

Robust, Computationally Efficient Matched-Field Localization

Brian F. Harrison
Naval Undersea Warfare Center
Newport, RI 02841, USA

Donald W. Tufts and Richard J. Vaccaro
Department of Electrical Engineering
The University of Rhode Island
Kingston, RI 02881, USA

31 July 1996

Abstract

In many estimation problems, the set of unknown parameters can be divided into a subset of desired parameters and a subset of nuisance parameters. Using a maximum *a posteriori* (MAP) approach to parameter estimation, these nuisance parameters are integrated out in the estimation process. This can result in an extremely computationally-intensive estimator. In this paper, we present the fast, approximate MAP parameter estimator, FASTMAP. As an example, we apply the fast algorithm to matched-field source localization in an uncertain environment.

Introduction

In many estimation problems, the set of unknown parameters can be divided into two subsets. The parameters of major interest comprise one subset and the remaining parameters comprise the second subset. The remaining parameters only serve to complicate the problem and are referred to as nuisance parameters. In the maximum *a posteriori* (MAP) approach to parameter estimation, these nuisance parameters are treated as random variables with assumed prior probability density functions and integrated out in the process of estimating the desired parameters [1], [2]. Depending on the number of nuisance parameters, practical implementation of the MAP estimator can be extremely computationally-intensive. In the next section, we will show that under certain conditions a computationally-efficient approximation to the MAP estimator can be obtained. Efficiency is achieved by approximately performing the integration off-line prior to the processing of data observations.

Now let us describe the MAP estimator following the development of Richardson and Nolte [3]. Consider the following data model

$$\mathbf{y} = s\mathbf{a}(\Theta, \Psi) + \mathbf{n}, \tag{1}$$

where $\mathbf{y}$ is a $N \times 1$ vector of observed data, s is a Gaussian distributed complex random variable, $\mathbf{a}(\Theta, \Psi)$ is a $N \times 1$ vector parameterized by the vectors Θ and Ψ, and $\mathbf{n}$ is a $N \times 1$ vector of Gaussian random variables. This model is applicable to array processing and time-series analysis problems. We will assume that the parameters of interest are contained in Θ, while Ψ contains the nuisance parameters. Each of the nuisance parameters is assumed to be a random variable with a known uniform probability distribution. We can then express the *a posteriori* probability density function (pdf) of Θ as

$$p(\Theta|\mathbf{y}) = \frac{p(\Theta)}{p(\mathbf{y})} p(\mathbf{y}|\Theta). \tag{2}$$

The data vector $\mathbf{y}$ is considered to be a deterministic function of s, Θ, and Ψ. Therefore, the conditional pdf of the data is related to the pdf of $\mathbf{n}$ by

$$p(\mathbf{y}|\Theta, \Psi, s) = p_{\mathbf{n}}\left(\mathbf{y} - s\mathbf{a}(\Theta, \Psi)\right). \tag{3}$$

The pdf $p(\mathbf{y}|\Theta)$ is obtained by removing variables from (3) using the rule for conditional pdf's [4]

$$p(\mathbf{y}|\Theta) = \int\limits_{\Psi} \int\limits_{s} p_{\mathbf{n}}\left(\mathbf{y} - s\mathbf{a}(\Theta, \Psi)\right) p(s, \Psi|\Theta)\ ds\ d\Psi. \tag{4}$$

Substituting (4) into (2) yields the *a posteriori* pdf of Θ

$$p(\Theta|\mathbf{y}) = \frac{p(\Theta)}{p(\mathbf{y})} \int\limits_{\Psi} \int\limits_{s} p_{\mathbf{n}}\left(\mathbf{y} - s\mathbf{a}(\Theta, \Psi)\right) p(s, \Psi|\Theta)\ ds\ d\Psi. \tag{5}$$

We can simplify (5) by applying the previous assumptions and further assuming that s, Ψ, and Θ are all independent of each other. This results in [3]

$$p(\Theta|\mathbf{y}) = C(\mathbf{y}) p(\Theta) \int\limits_{\Psi} \frac{\exp\left\{\frac{H(\Theta,\Psi)}{G(\Theta,\Psi)}\right\}}{G(\Theta, \Psi)} p(\Psi)\ d\Psi, \tag{6}$$

where $C(\mathbf{y})$ is a normalization constant, $p(\Theta)$ is assumed uniform over the parameter space of interest, and

$$\begin{aligned} H(\Theta, \Psi) &= \left|F\mathbf{a}^H(\Theta, \Psi)\mathbf{R}_{\mathbf{n}}^{-1}\mathbf{y}\right|^2, \\ G(\Theta, \Psi) &= F\mathbf{a}^H(\Theta, \Psi)\mathbf{R}_{\mathbf{n}}^{-1}\mathbf{a}(\Theta, \Psi) + 1, \end{aligned} \tag{7}$$

where F is a constant and $\mathbf{R}_{\mathbf{n}} = E\{\mathbf{n}\mathbf{n}^H\}$. The maximum *a posteriori* (MAP) estimate of Θ is obtained by maximizing (6) over Θ, i.e.,

$$\hat{\Theta} = \arg\max_{\Theta} p(\Theta|\mathbf{y}) = \arg\max_{\Theta} \int\limits_{\Psi} \frac{\exp\left\{\frac{H(\Theta,\Psi)}{G(\Theta,\Psi)}\right\}}{G(\Theta, \Psi)} p(\Psi)\ d\Psi. \tag{8}$$

If the vectors $\mathbf{a}(\Theta, \Psi)$ are normalized to have unit norm and $\mathbf{R}_{\mathbf{n}}$ equals the identity matrix, equation (8) can be written as

$$\hat{\Theta} = \arg\max_{\Theta} \int\limits_{\Psi} \exp\left\{\frac{F^2\left|\mathbf{a}^H(\Theta, \Psi)\mathbf{y}\right|^2}{F+1}\right\} p(\Psi)\ d\Psi. \tag{9}$$

For numerical implementation of this estimator, we assume that $p(\Psi)$ is a uniformly distributed pdf and approximate the integral by a summation

$$\hat{\Theta} = \arg\max_{\Theta} \sum_{j=1}^{M} \exp\left\{\frac{F^2\left|\mathbf{a}^H(\Theta, \Psi_j)\mathbf{y}\right|^2}{F+1}\right\}, \tag{10}$$

where the Ψ_j are vectors of the nuisance parameters sampled from their probability distributions. A Monte Carlo approach to computing (10) was proposed in [5]. Thus M inner products between the vectors $\mathbf{a}(\Theta, \Psi_j)$, $j = 1, \ldots, M$ and $\mathbf{y}$ are computed for each point in parameter space Θ.

I Computationally-Efficient Maximum *A Posteriori* Parameter Estimation

The exponential in (10) can be approximated over a finite interval by a linear approximation of the form

$$\exp\left\{\frac{F^2\left|\mathbf{a}^H(\Theta,\Psi_j)\mathbf{y}\right|^2}{F+1}\right\} \approx a\left\{\frac{F^2\left|\mathbf{a}^H(\Theta,\Psi_j)\mathbf{y}\right|^2}{F+1}\right\} + b. \tag{11}$$

for some constants $a > 0$ and b. Substituting this approximation into (10) gives

$$\hat{\Theta} = \arg\max_{\Theta}\; Mb + \frac{aF^2}{F+1}\sum_{j=1}^{M}\left|\mathbf{a}^H(\Theta,\Psi_j)\mathbf{y}\right|^2, \tag{12}$$

or equivalently

$$\hat{\Theta} = \arg\max_{\Theta}\sum_{j=1}^{M}\left|\mathbf{a}^H(\Theta,\Psi_j)\mathbf{y}\right|^2. \tag{13}$$

Notice that if the perturbations of the $\mathbf{a}(\Theta,\Psi_j)$ vectors for each Θ over the realizations Ψ_j are small, then the variability of the values of $\left|\mathbf{a}^H(\Theta,\Psi_j)\mathbf{y}\right|^2$ will also be small. Under this condition, (13) will be a close approximation to (10). Rewriting (13) as

$$\hat{\Theta} = \arg\max_{\Theta}\mathbf{y}^H\mathbf{R}_{\mathbf{a}}(\Theta)\mathbf{y}, \tag{14}$$

where

$$\mathbf{R}_{\mathbf{a}}(\Theta) = \sum_{j=1}^{M}\mathbf{a}(\Theta,\Psi_j)\mathbf{a}^H(\Theta,\Psi_j), \tag{15}$$

reveals that the assumption of small $\mathbf{a}(\Theta,\Psi_j)$ vector perturbations over Ψ_j implies that the matrix $\mathbf{R}_{\mathbf{a}}(\Theta)$ is approximately low-rank. Therefore, we can make a low-rank approximation to $\mathbf{R}_{\mathbf{a}}(\Theta)$ by using its eigen decomposition $\mathbf{R}_{\mathbf{a}}(\Theta) = \mathbf{U}\mathbf{\Sigma}\mathbf{U}^H$ and setting the small eigenvalues in $\mathbf{\Sigma}$ to zero [6]. Defining $\mathbf{\Sigma}_1$ as a diagonal matrix of the non-zero eigenvalues and $\mathbf{U}_1$ as a matrix of the corresponding eigenvectors, a low-rank approximation to $\mathbf{R}_{\mathbf{a}}(\Theta)$ is given by $\widetilde{\mathbf{R}}_{\mathbf{a}}(\Theta) = \mathbf{U}_1\mathbf{\Sigma}_1\mathbf{U}_1^H$. Substituting this approximation into (14) and rewriting the expression as the norm-squared of a matrix-vector product gives

$$\hat{\Theta} = \arg\max_{\Theta}\left\|\mathbf{B}_{\mathbf{a}}(\Theta)\mathbf{y}\right\|^2, \tag{16}$$

where $\mathbf{B}_{\mathbf{a}}(\Theta) = \mathbf{\Sigma}_1^{\frac{1}{2}}\mathbf{U}_1^H$.

The advantage to using the approximate MAP estimator of (16) over the MAP estimator of (10) is that the computation of $\mathbf{B}_{\mathbf{a}}(\Theta)$ can be done off-line before the processing of data. The number of on-line inner product computations over each point in the desired parameter space Θ is reduced and equal to the rank of $\mathbf{B}_{\mathbf{a}}(\Theta)$. In contrast, (10) must compute M inner products over each point Θ on-line. Thus, (16) is a computationally-efficient approximation to the MAP estimator and will be called the *fast, approximate* MAP estimator or FASTMAP.

II Simulation Example from Matched-Field Processing

In this section we will demonstrate the utility of the FASTMAP estimator using the array processing technique known as matched-field processing (MFP) [7]. MFP is a model-based source localization method which is a function of the ocean environmental parameters. Precise knowledge of the environmental parameters are required. When the environmental parameters are uncertain, a MAP approach to MFP can be used. Using the model of (1) for this case, $\mathbf{\Theta}$ would contain the source location parameters of interest and the uncertain environmental parameters would be contained in $\mathbf{\Psi}$. The vector $\mathbf{a}(\mathbf{\Theta}, \mathbf{\Psi})$ is called a *replica vector* in the matched-field literature.

We will now compare the outputs of the MAP estimator and the FASTMAP estimator, through a simple simulation, for increasing levels of environmental uncertainty. As the environmental uncertainty level increases, the perturbations of the replica vectors at each $\mathbf{\Theta}$ over environment also increase. This will illustrate the performance decrease of the FASTMAP estimator when the small perturbation assumption is no longer valid.

We simulated a typical shallow water environment. All of the environmental parameters were assumed known except one. A linear sound velocity profile was used which had a sound speed at the surface of 1500 m/s and a sound speed at the bottom of 1480 m/s. We introduced uncertainty by allowing the sound speed at the bottom to be uncertain. A 20-element vertical array, which spanned the water column, was used. The data vector $\mathbf{y}$ was generated using the nominal value of the sound speed at the bottom 1480 m/s, while the estimators assumed its value could lie anywhere in its specified uncertainty interval of $1480 \pm \Delta s$ m/s. The source was located at a range of 9000 m and a depth of 24 m. For convenience, it was assumed that the source depth was known *a priori* by both processors. Therefore, range was the only source location parameter each had to search over. Figures 1 and 2 show the outputs of both estimators for $\Delta s = 1, 7.5$ m/s, respectively. For these levels of uncertainty, both estimators are able to correctly estimate the source range. Figure 3 shows the outputs as Δs was increased to 25 m/s. At this point, the small perturbation assumption no longer holds. With this large degree of uncertainty, the FASTMAP estimator produces a peak at an incorrect range estimate, while the MAP estimator displays a peak at the correct estimate.

This simple simulation provides an example of the computational savings of using the FASTMAP estimator over the MAP estimator. With $\Delta s = 7.5$ m/s, the uncertainty interval of the sound speed at the bottom ranged from 1472.5 m/s to 1487.5 m/s. This interval was sampled at 0.5 m/s resulting in 30 sample points, i.e., $M = 30$. However, the rank of $\mathbf{B_a}(\mathbf{\Theta})$ was equal to 5. Therefore, only 5 inner products per $\mathbf{\Theta}$ were required for the FASTMAP estimator, while the MAP estimator required 30.

A more complex MFP example in which seven environmental parameters were uncertain is shown in [8]. Using a smoothed version of the FASTMAP estimator, it is shown that the FASTMAP estimator provides a computational savings of 75:1 over the MAP estimator.

III Conclusion

The maximum *a posteriori* (MAP) parameter estimator was derived for a data model applicable to array processing and time-series analysis. It was then shown that a computationally-efficient approximate MAP estimator, called the FASTMAP estimator, could be obtained if the perturbations of the model vectors $\mathbf{a}(\mathbf{\Theta}, \mathbf{\Psi}_j)$ at each point in parameter space $\mathbf{\Theta}$ over the nuisance parameter space $\mathbf{\Psi}_j$ were small. Simulation results from matched-field processing were shown to illustrate the effects on the FASTMAP estimator when the small perturbation assumptions are violated.

References

[1] Van Trees, H. L., *Detection, Estimation, and Modulation Theory*, Part I, J. Wiley, 1968.

[2] Kay, S., *Fundamentals of Statistical Signal Processing: Estimation Theory*, Prentice-Hall, 1993.

[3] Richardson, A. M. and Nolte, L. W., "*A posteriori* probability source localization in an uncertain sound speed, deep ocean environment," *J. Acoust. Soc. Amer.*, vol. 89, 2280-2284, 1991.

[4] Papoulis, A., *Probability, Random Variables, and Stochastic Processes*, McGraw-Hill, 1984.

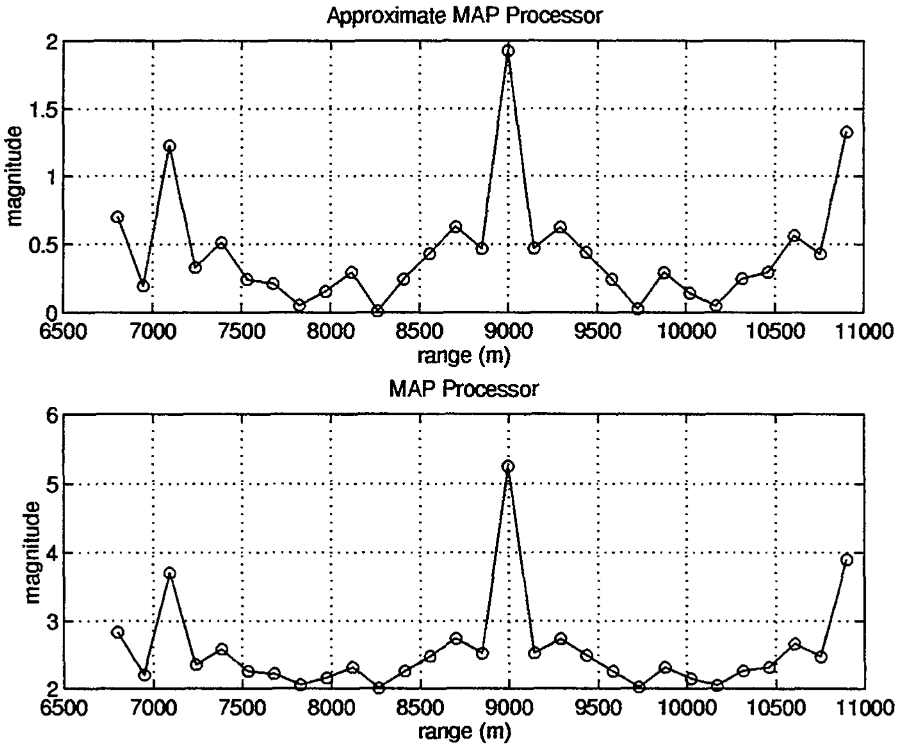

Figure 1: Outputs of FASTMAP and MAP processors in the presence of 2 m/s sound-speed uncertainty.

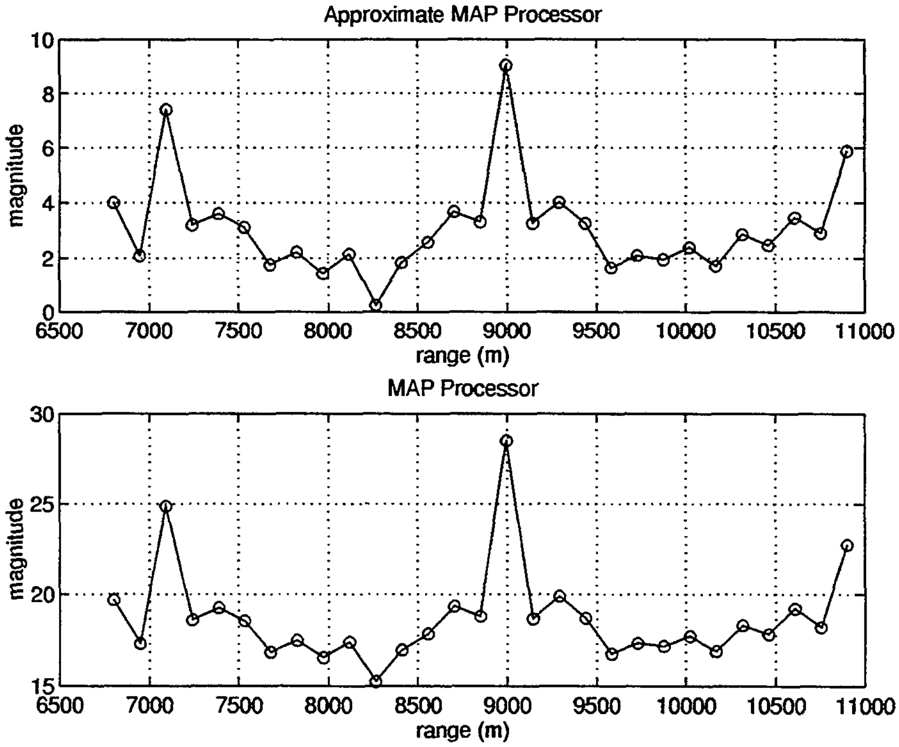

Figure 2: Outputs of FASTMAP and MAP processors in the presence of 15 m/s sound-speed uncertainty.

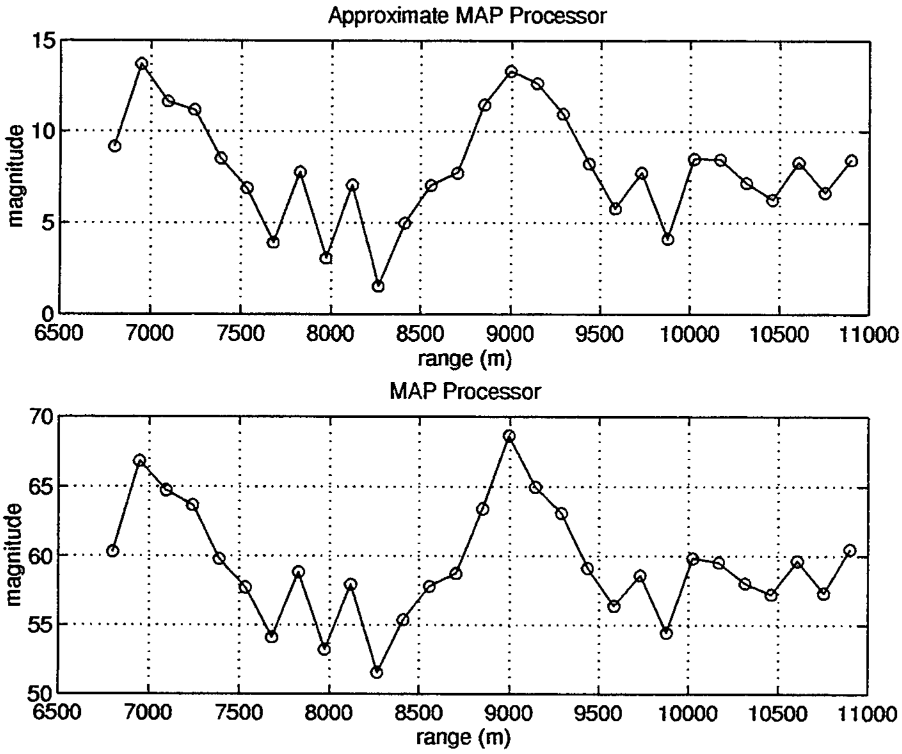
Approximate MAP Processor

MAP Processor

Figure 3: Outputs of FASTMAP and MAP processors in the presence of 50 m/s sound-speed uncertainty.

[5] Shorey, J. A., Nolte, L. W., and Krolik, J. L., "Computationally efficient monte carlo estimation algorithms for matched field processing in uncertain ocean environments," *J. Computational Acoust.*, vol. 2, pp. 285-314, 1994.

[6] Noble, B. and Daniel, J. W., *Applied Linear Algebra*, Prentice-Hall, 1988.

[7] Baggeroer, A. B., Kuperman, W. A., and Mikhalevsky, P. N., "An overview of matched field methods in ocean acoustics," *IEEE Journal of Oceanic Engr.*, vol. 18, pp. 401-424, 1993.

[8] Harrison, B. F., ***Robust Matched-Field Processing: A Subspace Approach***, PhD thesis, The University of Rhode Island, 1996.

Multiple-Frequency Matched-Field Source Localization in Shallow Water

Yung P. Lee
Science Applications International Corporation
1710 Goodridge Drive
McLean, VA 22102
yung@osg.saic.com

ABSTRACT

Multiple-frequency robust adaptive matched-field processing (MFP) has been applied to data from both the Hudson Canyon Experiment[1] and the Elba Sea Experiment[2]. The Hudson Canyon data set consisted of 20 snapshots of multiple-cw transmissions and was distributed in the 5th MFP workshop. The Elba Sea data set consisted of a period of broadband M-sequence transmissions and was distributed in the 6th MFP workshop. The MFP results from both data sets demonstrate excellent source localization up to about 5 km in range in shallow water. In a November 1995 experiment in the Gulf of Mexico, a vertical array was deployed in water 188 m deep . During a TL run, a projector transmitting multiple-cw tones was towed along the isobath line between 5.5 km and 15.5 km away from the array. The MFP results show that multiple-frequency robust adaptive processing provides excellent source localization up to 15 km in this shallow water environment.

1. INTRODUCTION

MFP refers to array processing algorithms which exploit the full field structure of signals propagating in an ocean waveguide. In it an acoustic model is used to calculate replica vectors in a search space. The measured signal plus noise data vectors are then matched with the replica vectors and an ambiguity surface is computed. The locations of peaks in the ambiguity surface are estimates of the source location. An excellent overview of MFP can be found in the paper by Baggeroer, et. al. [3].

Adaptive matched field processing (MFP) is an optimal method for source localization and detection in the ocean. It uses the measured signal-plus-noise (data) vectors to minimize the contributions from those components that do not match with the steering vector to a given search cell. When there is a mismatch between the actual signal vector and the calculated or replica vector, there is a degradation in the performance of the adaptive processor which can be severe when the signal-to-noise ratio (SNR) is high.

A review of several traditional approaches as well as some newer algorithms to make adaptive MFP robust to mismatch has been discussed by Lee, et.al.[4]. Applications of robust adaptive algorithms to multiple-frequency signals has been shown by Lee[5] using the data set from the Hudson Canyon Experiment. Comparing with arithmetic mean (averaging the amplitudes), taking the geometric-mean (averaging dB's) or the harmonic-mean (averaging the reciprocal of the amplitudes) of the discrete frequency output of the robust adaptive algorithms for multiple-frequency signals have demonstrated excellent source localization results.

In this study, two robust adaptive algorithms, namely the Feedback-Loop White-Noise-Constrained (FLWNC) method and the Signal-Coherence-Constrained Reduce-Rank (SCCRR) method have been applied. Section 2 will review both FLWNC and SCCRR algorithms. In section 3 we will describe the setup of a recent shallow water experiment off Gulf of Mexico, in section 4 we will show MFP results, and in section 5 we will present a discussion of the results.

2. MULTIPLE-FREQUENCY ROBUST ADAPTIVE ALGORITHMS

Adaptive processing uses the measured signal plus noise data vectors to minimize the sidelobe contributions from those components that do not match with the replica vector for a given search cell. Most adaptive techniques used today had their genesis in the Minimum Variance Distortionless Filter (MVDF) algorithm, or Capon's Maximum Likelihood Method (MLM). Let **K** be the measured covariance matrix; from singular value decomposition, it can be decomposed into a set of eigenvectors $\mathbf{V}_i$ associated with a set of eigenvalues $\boldsymbol{\lambda}_i$. Let **A** be a replica vector for a given search cell (look direction). The MVDF minimizes the variance at the output of a linear weighing of the sensors subject to the distortionless constraint that signals in the "look direction" have unity gain. Its output is given by

$$S_{MV} = \left(\sum_{i=1}^{N} \frac{1}{\lambda_i} |V_i^+ A|^2\right)^{-1} \tag{1}$$

Without mismatch, the steering vector **A** is perfectly matched with signal eigenvectors in the "look direction", the rest of eigenvectors are orthogonal to the steering vector and have no effect on the signal output. But, when there is mismatch present, the steering vector is no longer orthogonal to the rest of eigenvectors. The noise vectors associated with the least significant eigenvalues then dominate the inverse processing in Eq.(1) and degrade the signal estimation.

In MFP, there are several forms of mismatch, including mismatch due to environmental uncertainties and fluctuation and mismatch due to system errors. All forms of mismatch are either deterministic or random. Deterministic mismatch degrades the signal estimation and causes localization bias, but it can be minimized if more ground truth is provided. Random mismatch degrades the signal estimation but will not bias the localization. Random mismatch cannot be minimized so that robust algorithms were developed to tolerate a certain level of random mismatch.

The FLWNC method reduces sensitivity to mismatch by adding white noise (ϵ) to the diagonal elements of the covariance matrix **K**. Adding white noise (ϵ) to the diagonal elements of the covariance matrix **K** is the same as adding ϵ to each eigenvalue without modifying the eigenvectors. The white-noise-constrained output that results is
For each search location, the MVDF white-noise processing gain and spectral output are calculated. The white-noise processing gain, defined as the amplitude squared of the weight

$$S_{WNC} = \left(\sum_{i=1}^{N} \frac{\lambda_i}{(\lambda_i+\epsilon)^2}|V_i^+A|^2\right)\left(\sum_{i=1}^{N} \frac{1}{(\lambda_i+\epsilon)}|V_i^+A|^2\right)^{-1} \tag{2}$$

vector, is directly proportional to the SNR. If the white-noise processing gain falls below a constraining value, a "noise-cell" is defined and the FLWNC spectral output is set equal to the MVDF spectral output. If the white-noise processing gain is above the constraining value, a "signal-cell" is defined and an amount of white noise that equals the MVDF spectral output is added in the processing and a new white-noise processing gain and a new spectral output are calculated. The process is repeated until the white-noise processing gain falls below the constraining value. The feedback-loop approach insures that the amount of white noise added in each iteration is adequate so that the iteration procedure converges rapidly without overshooting.

For each search location, the coherence between an eigenvector and the steering vector, defined as the dot product of these two unit vectors, is calculated. Consider an environment in which the signal coherence is bounded within a constraining value α. In the SCCRR method, the coherence is compared with the constraining value α. If it is greater than α the eigenvector falls in a signal space for this search location otherwise the eigenvector falls in a noise space. The SCCRR method excludes eigenvectors in the noise space and uses those in signal space for the processing. The SCCRR output is then

$$S_{SCCRR} = \left(\sum_{|V_i^+A|^2>\alpha} \frac{1}{\lambda_i}|V_i^+A|^2\right)^{-1} \tag{3}$$

Broadband MFP is calculated in general by taking the weighted or unweighted arithmetic-mean of ambiguity surfaces resulting from each narrowband component across the frequency band of interest. Instead of taking the arithmetic mean, taking the geometric-mean or the harmonic-mean has proven to be a more effective way to control the ambiguous sidelobes. Let $y(f_i)$ be the narrowband MFP output at frequency f_i, and Y_a, Y_g, Y_h be the arithmetic-mean, geometric-mean, and harmonic-mean over frequency, respectively. Mathematically, $Y_a \geq Y_g \geq Y_h$; they become equal when $y(f_i)$ are the same. The narrowband responses line up at the target location and all three means have the same result. Because sidelobe distributions are different (misaligned) among the narrowband responses, the geometric-mean and the harmonic-mean have lower sidelobes than the arithmetic-mean.

3. EXPERIMENTAL SETUP

A shallow water experiment was conducted in November 1995 in Gulf of Mexico approximately 100 miles directly south of Panama City. A vertical array was deployed at 28°23.063' N 85°17.857' W. The water depth was measured to be approximately 188 m at the array site. The vertical array had 32 hydrophones and a total aperture of 153. The upper 13 hydrophones were uniformly spaced at 8 m, and the lower 19 hydrophones were uniformly spaced at 3 m. It was deployed in a bottom moored configuration and the deepest hydrophone was 3 m above the bottom. Few hydrophones were not functional and were excluded in MFP processing. Although array navigation data were collected during the experiment, they were not available at the time of data processing. So the array was assumed to be perfectly vertical for all MFP processing.

During the experiment, a HLF-6 source was towed at a speed of approximately 5 knots for a transmission loss measurement. The HLF-6 source broadcasted 5 CW tones at 47 Hz, 97 Hz, 147 Hz, 197 Hz, and 247 Hz at a nominal source level of 195 dB per line. Figure 1 shows the track where the source was towed starting from deep to shallow and then towed along an isobath line. In this study we concentrate on the source localization along the isobath line.

4. EXPERIMENTAL RESULTS

Figure 2 shows the average XBT profile taken close in time for this measurement. The sediment properties were modified from the Nobles parameters(6) to provide the best results for all frequencies at all ranges. A range-independent normal mode code was used for matched-field processing. Only the 97 Hz, 147 Hz, and 197 Hz signals were processed and the geometric-mean results of these three frequencies are presented.

Figure 3 shows the range-depth responses of the conventional MFP for the source at ten different ranges from 5.63 km to 14.45 km. Each range-depth response contour is normalized to its peak and has a 6 dB dynamic range. Sidelobes appear at about 3 to 4 dB below the peak. Figure 4 shows the range-depth responses of the FLWNC processor and Figure 5 shows the range-depth responses of the SCCRR processor. A 40 dB dynamic range is used for these response contours. Sidelobes appear at about 20 dB below the peak for the FLWNC processor and at more than 30 dB below the peak for the SCCRR processor. These results show excellent source localization at all ranges.

Figure 6 shows signal mismatch. Signal mismatch is defined as the difference between the array received energy and the peak output in the conventional MFP. Along the isobath line, from 5 km to 15 km, the signal mismatch is almost independent of range and is about 1 dB for 97 Hz, 1.3 dB for 147 Hz, and 2 dB for 197 Hz. When the source moved from deep to shallow water, at ranges from 20 km to 15 km, signal mismatch increased. Figure 7 shows the localization performance for different frequencies at different ranges. The source localization is consistent for all three frequencies along the isobath line up to 15 km. The consistency degrades when the distance is greater than 15 km because the water depth changed which is not included in our range-independent MFP processing. A consistent bias in depth estimation indicates that the source may not have been towed at the planned depth.

5. CONCLUSIONS

Multiple-frequency robust adaptive matched-field processing has been applied to data collected from a shallow water test in Gulf of Mexico. Using the average profile collected close in time to the measurement, the range-independent MFP provides an excellent source localization up to 15 km along an isobath line.

REFERENCES:

1. W. Carey, L. M. Dillman, and J. A. Doutt, "Shallow-water transmission measurements taken on the New Jersey continental shelf," Naval Undersea Warfare Center Tech. Doc. 10,025 (1992).

2. D. F. Gingras and P. Gerstoft, "Inversion for geometric and geoacoustic parameters in shallow water: Experimental results," J. Acoust. Soc. Am., Vol. 97, No. 6, pp. 3589-3598, June 1995.

3. A. B. Baggeroer, W. A. Kuperman, and P. N. Mikhalevsky, "An Overview of Matched Field Methods in Ocean Acoustics," IEEE J. of Oceanic Eng., vol. 18. no.4, pp. 401-424, Oct, 1993.

4. Y. Lee, P. Mikhalevsky, H. Freese, and J. Hanna, "Adaptive Matched-Field Processing," The 15th International Congress for Acoustics, Trondheim, Norway, June, 1995.

5. Y. P. Lee, "Multiple-frequency robust adaptive matched-field processing in shallow water," J. Acoust. Soc. Am., Vol. 97, No. 5, Pt. 2, pp 3290, May, 1995.

6. D. P. Knobles and R. A. Koch, "A Time Series Analysis of Sound Propagation in a Strongly Multipath Shallow Water Environment with an Adiabatic Normal Mode Approach," IEEE J. Oceanic Eng., vol 21, pp 1-13, 1996.

D e p t h m
-160.0
-162.5
-165.0
-167.5
-170.0
-172.5
-175.0
-177.5
-180.0
-182.5
-185.0
-187.5
-190.0
-192.5
-195.0
-197.5
-200.0
-202.5
-205.0
-207.5
-210.0
274° 30'
274° 32'
274° 34'
274° 36'
274° 38'
274° 40'
274° 42'
274° 44'
28° 32'
28° 30'
28° 28'
28° 26'
28° 24'
28° 22'
Land

Figure 1

plt2

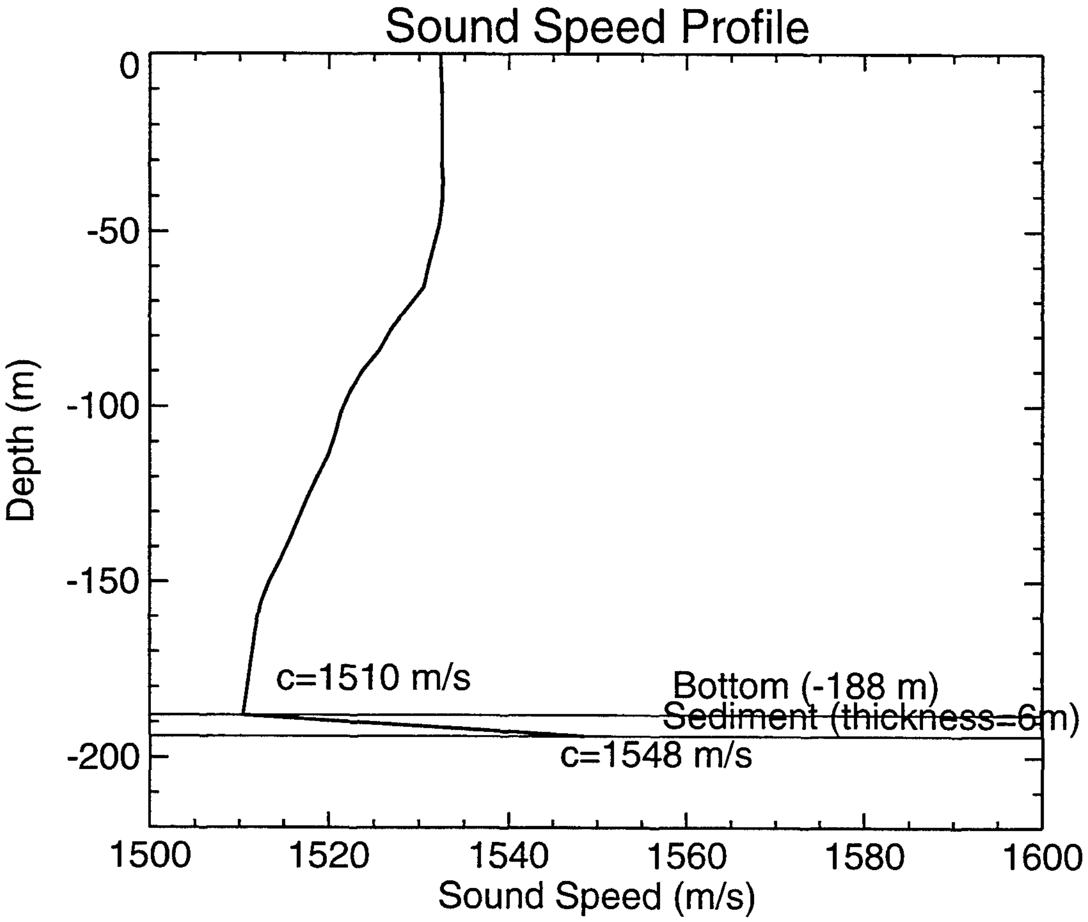

Figure 2.

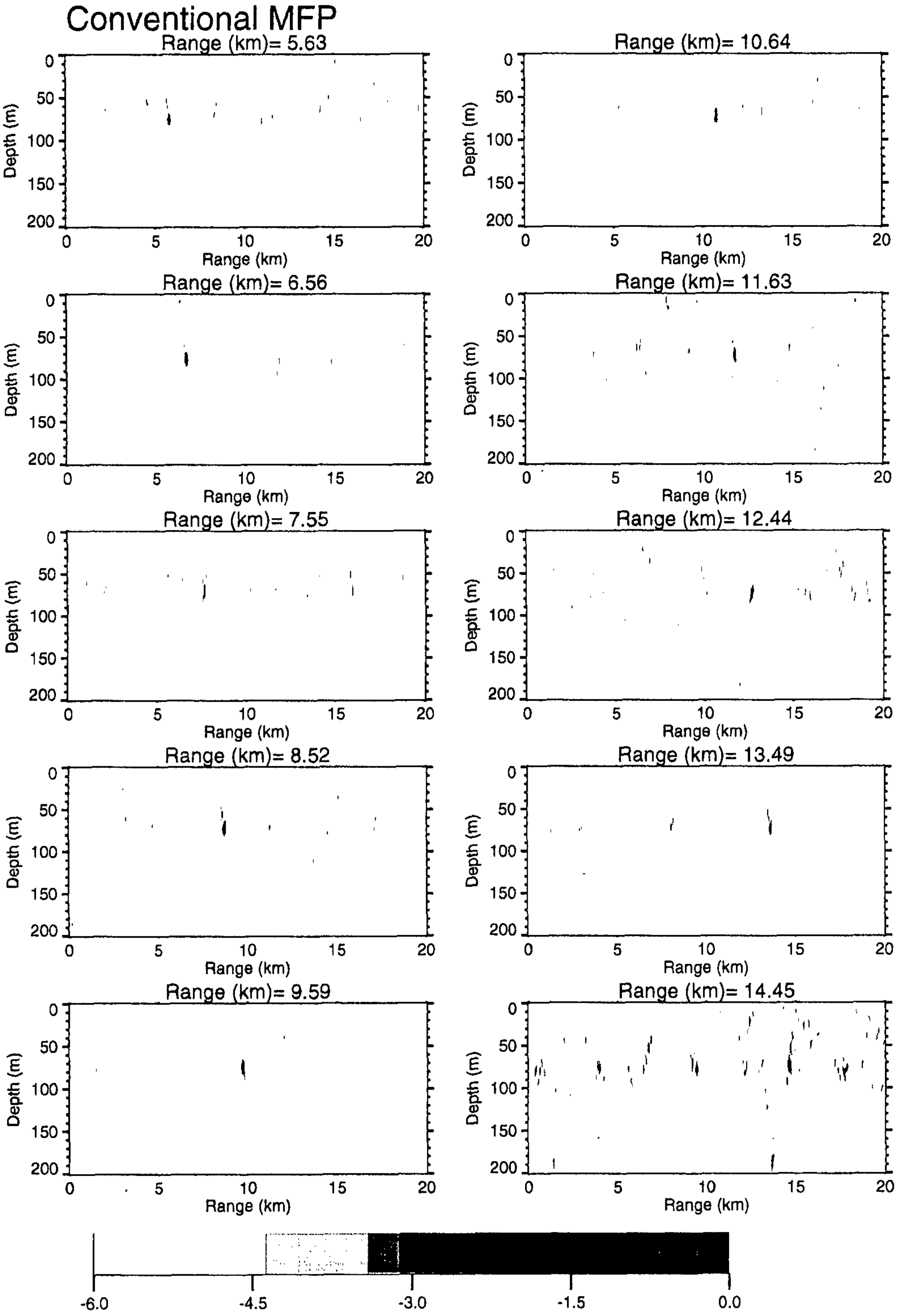
Conventional MFP
Range (km)= 5.63
Range (km)= 10.64
Range (km)= 6.56
Range (km)= 11.63
Range (km)= 7.55
Range (km)= 12.44
Range (km)= 8.52
Range (km)= 13.49
Range (km)= 9.59
Range (km)= 14.45
Depth (m)
0
50
100
150
200
Range (km)
0
5
10
15
20
-6.0
-4.5
-3.0
-1.5
0.0

Figure 3.

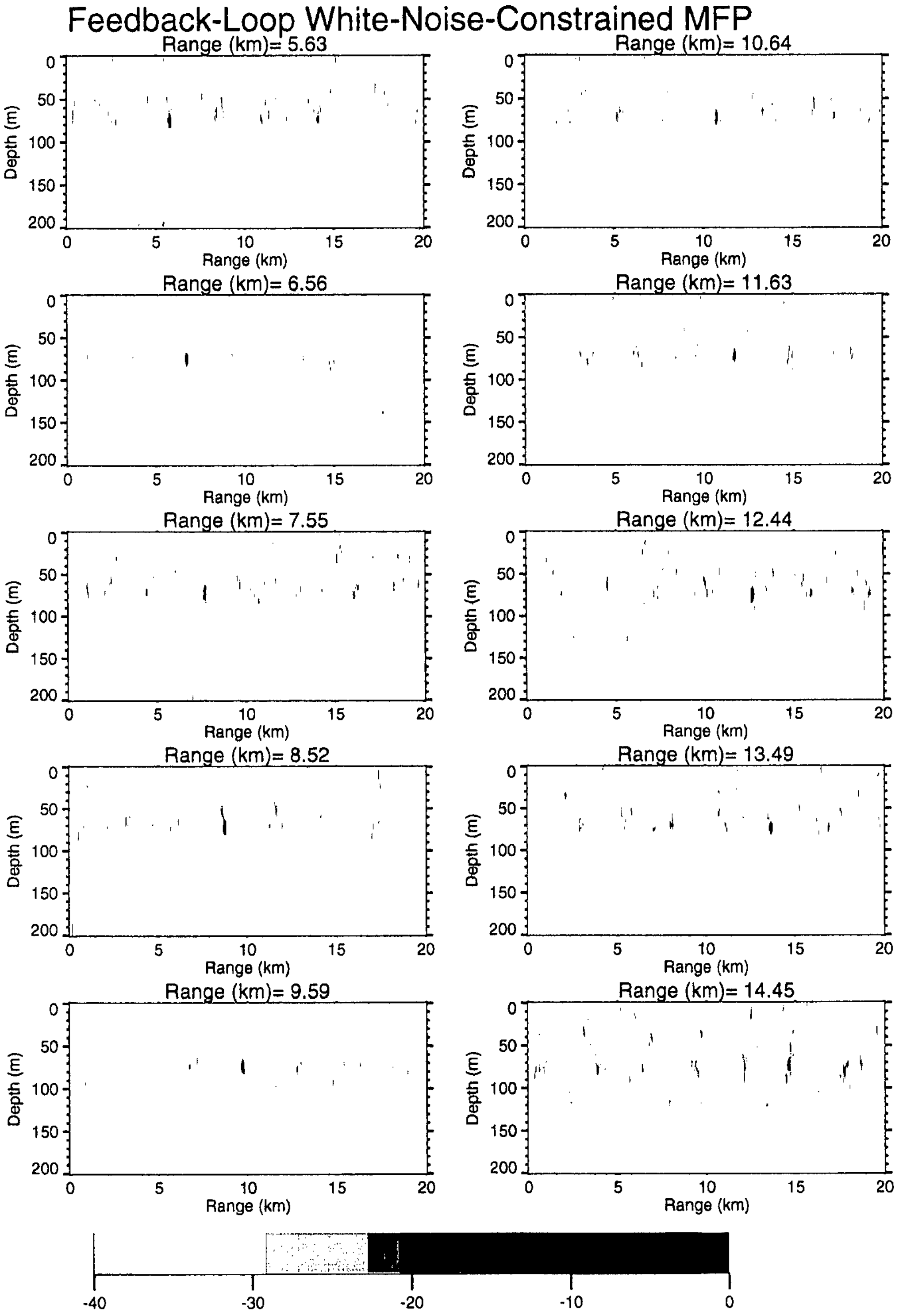
Feedback-Loop White-Noise-Constrained MFP
Range (km)= 5.63
Range (km)= 10.64
Range (km)= 6.56
Range (km)= 11.63
Range (km)= 7.55
Range (km)= 12.44
Range (km)= 8.52
Range (km)= 13.49
Range (km)= 9.59
Range (km)= 14.45
Depth (m)
0
50
100
150
200
Range (km)
0
5
10
15
20
-40
-30
-20
-10
0

Figure 4.

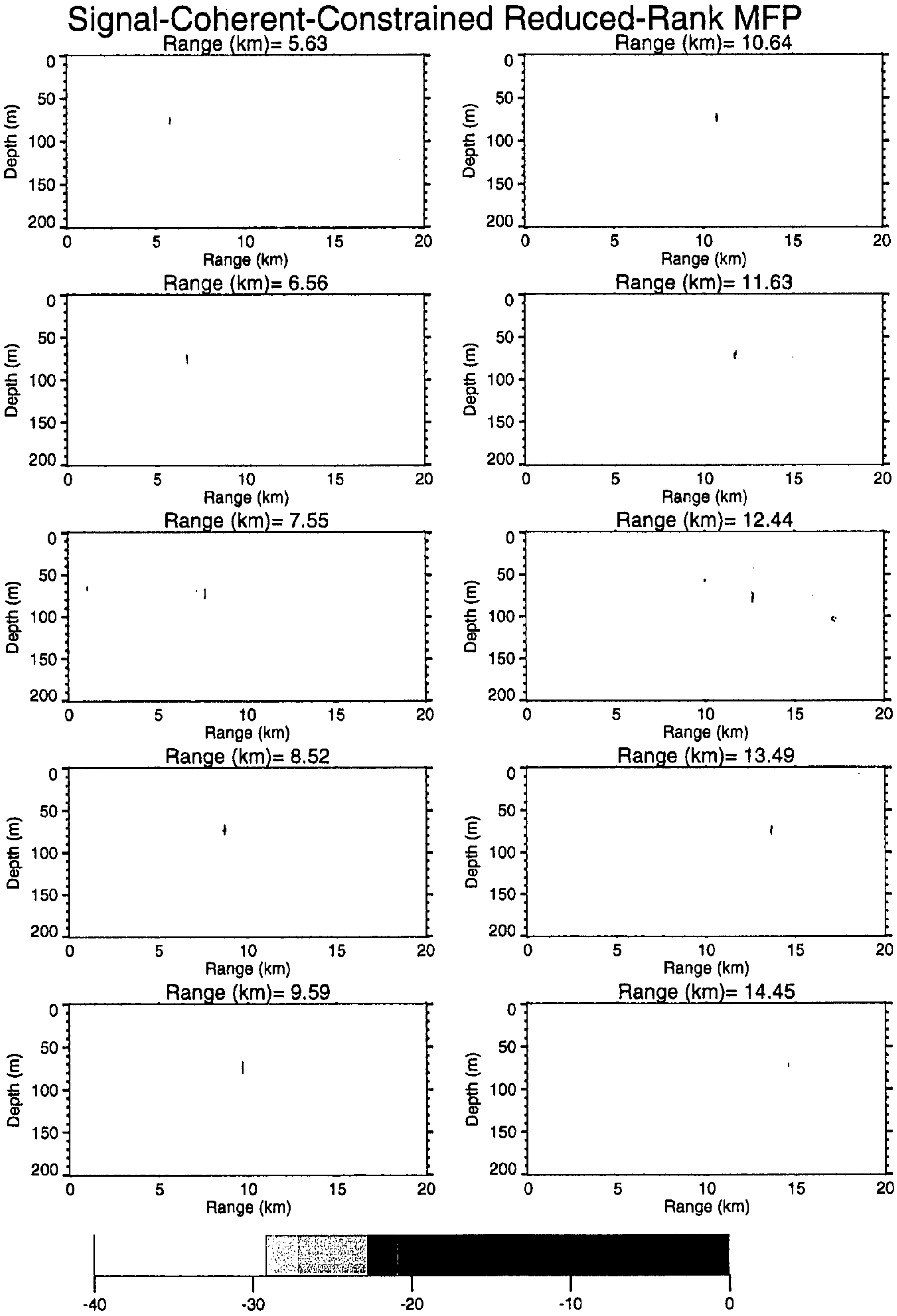
Signal-Coherent-Constrained Reduced-Rank MFP
Range (km)= 5.63
Range (km)= 10.64
Range (km)= 6.56
Range (km)= 11.63
Range (km)= 7.55
Range (km)= 12.44
Range (km)= 8.52
Range (km)= 13.49
Range (km)= 9.59
Range (km)= 14.45
Depth (m)
0
50
100
150
200
Range (km)
0
5
10
15
20
-40
-30
-20
-10
0

Figure 5.

plt324g

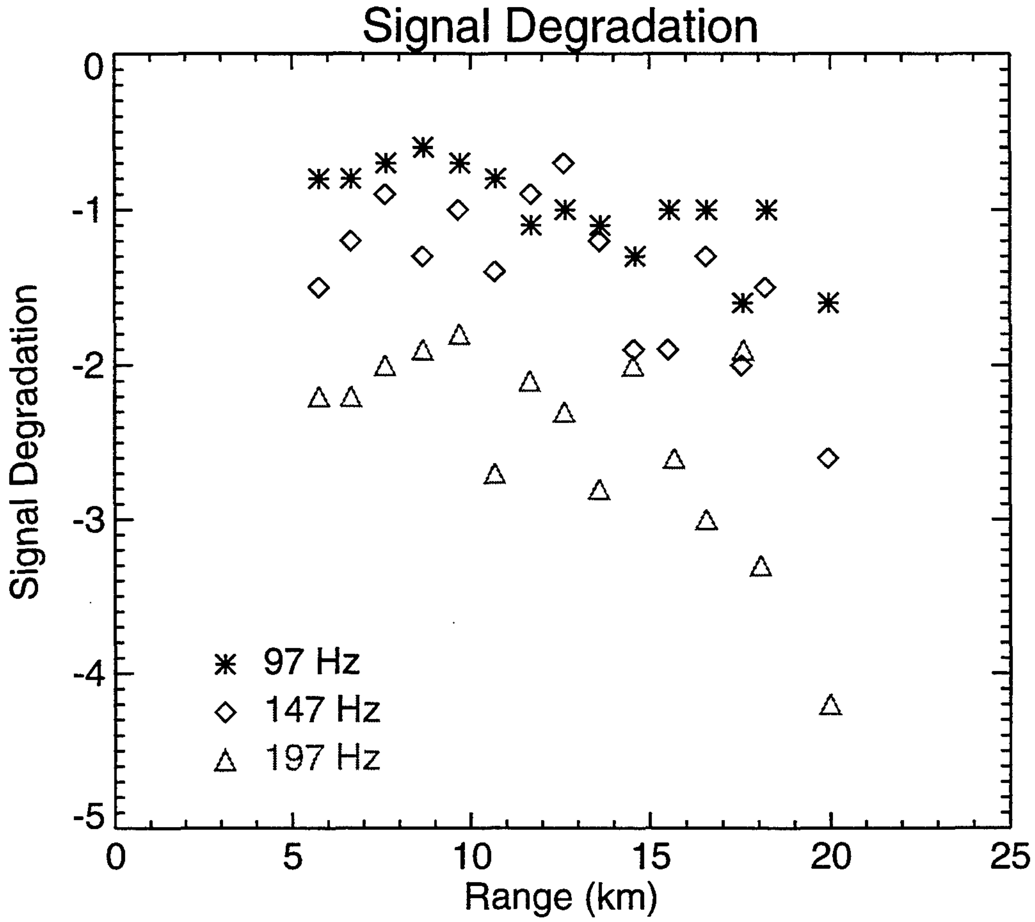

Figure 6.

plt324

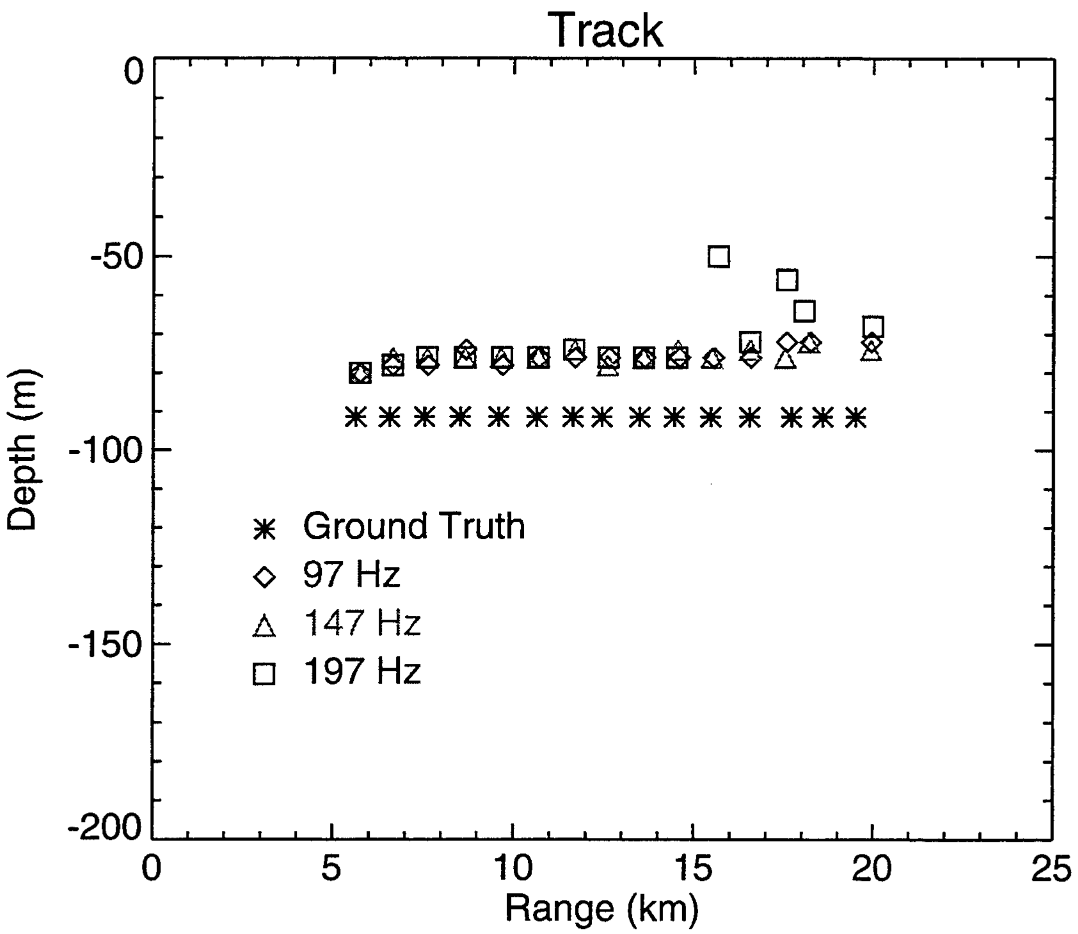

Figure 7.

Using Matched-Field Processing (MFP) Technique for Reverberation Characterization in Shallow Water.

Yung P. Lee
Science Applications International Corporation
1710 Goodridge Drive, M/S T1-3-5
McLean, VA 22102
yung@osg.saic.com

ABSTRACT

The goals of this research is to use MFP technique to map the spatial distribution of reverberation as a tool for understand the physics of ocean surface scattering. In a November 1995 experiment in the Gulf of Mexico, a vertical array was deployed in water 188 m deep and a CW source was placed on the bottom 760 m away from the array. The received energy was spectrally separated from the carrier to isolate the components scattered from the sea surface and then MFP was performed to examine its spatial distribution. A simulation was performed by generating time step realizations of an ocean surface with randomly distributed surface waves. A modified FEPE to include rough surface was used to propagate signals to a vertical array. In addition to the surface forward-scattered energy which is modeled in the simulation, bottom-back-scattered energy is also observed in the MFP data responses.

1. INTRODUCTION

MFP combines an acoustic propagation model with matched-filter processing to localize a source in three-dimensions. It has been shown to be effective in discriminating passive sources both in range and depth by exploiting the vertical structure of the signal. In active sonar systems, for frequencies below 1 kHz, most reverberation comes from the surface and bottom. MFP can discriminate in depth and should have potential to provide significant gain against active reverberation. In a numerical study, Dozier, et. al.(1) showed that it has the potential to yield gain against reverberation not far from the ideal array gain. We have applied MFP technique to map the forward-scattered signal around the active direct blast(2). MFP successfully maps the scattered energy near the surface in both real data and simulations.

In general, the active scattering problem should include two propagation paths: source to scatterer and scatterer to receiver. A scattering kernel is included to describe the scattering mechanism. In a stratified medium, the acoustic field scattered from a scatterer can be modeled as

$$P_{sc}(r,z)=\frac{\pi}{2k}\sum_{m,n}\frac{1}{\sqrt{k_m k_n \rho\rho_s}}e^{i(k_m\rho_s+k_n\rho)}\Psi_m(z_s)\,\Psi_m(z)\,S(\theta_m,\theta_n)\,\Psi_n(z)\,\Psi_n(z_r)$$

where Ψ_m are the mode functions and k_m are their associated wave numbers. S is the scattering kernel that describes how energy in one mode is re-distributed to other modes. In our study, we assume that the scatterer is illuminated by the source and "re-radiates" energy isotropically. In this case S=1, then

$$\begin{aligned} P_{sc}(r,z) &= \frac{\pi}{2k}\sum_m \frac{1}{\sqrt{k_m \rho_s}} e^{ik_m \rho_s} \Psi_m(z_s)\,\Psi_m(z) \sum_n \frac{1}{\sqrt{k_n \rho}} e^{ik_n \rho} \Psi_n(z)\,\Psi_n(z_r) \\ &= TL_{st}\sqrt{\frac{\pi}{2k}}\sum_n \frac{1}{\sqrt{k_n \rho}} e^{ik_n \rho} \Psi_n(z)\,\Psi_n(z_r) \end{aligned}$$

The propagation path from source to scatterer affects only the amplitude, but not the structure of the scattered signal. The scattered acoustic field received at a vertical array depends only on the propagation path from scatter to receiver. We then could use passive matched-field techniques to localize all the scatterers and characterize their spatial distribution.

To avoid the complication of long-range multiple bounces, in this paper we study MFP responses of one- and two-bounce scattered signals. The goal is to characterize the spatial distribution of the scattered field and to better understand the scattering mechanism in the temporally and spatially varying ocean environment.

In section 2, we will describe the setup of a 1995 shallow water experiment. In section 3, a simulation using a rough surface FEPE will be described. Results of real data and simulation will be presented in section 4 and a summary will be included in section 4.

2. EXPERIMENTAL SETUP

In November 1995, a test was conducted in the northeastern Gulf of Mexico. The objective of the test is to collect data for validating models for predicting reverberation distributions. One of the concept to be validated is how well MFP techniques can be used to study reverberation distribution in range and depth. The test site and season had been selected to minimize the complexity of acoustic modeling while still providing a wide range of sea conditions.

A vertical array was deployed in water 188 m deep. The array consisted of 32 hydrophones with the top hydrophone at a depth of 32 m; the upper 13 hydrophones were uniformly spaced at 8 m, and the lower 19 hydrophones were uniformly spaced at 3 m. Although the array was monitored by a transponder system, no array element location data are available at this time. So, the array was assumed to be perfectly vertical for this study. A CW source was placed on the bottom a short distance away from the vertical array. It broadcasted a 240.375 Hz CW with a source level of approximately 175 dB. The CW source was localized acoustically using MFP at 760 m from the vertical receiving array.

The plan was to turn the source on for 2 to 3 hours continuously 4 times a day for 5 consecutive days to sample various sea conditions. But due to the difficulty experienced during the experiment, only 10 minutes data were acquired for the short range measurement. The wind speed was about 10 knots and the significant wave height was about 2 feet. More than twenty sound speed profiles were collected, using XBTs and CTDs, within the two days proceeding the acoustic data collected. Figure 1 shows the average sound speed profile which is used in MFP processing. The sediment properties were modified from Knobles parameters(3) to best localize a towed source at various ranges.

3. SIMULATION

The finite-element parabolic equation (FEPE) method for acoustic propagation has been extended to handle a rough air-water interface treated as a series of stair steps(4). Because finer vertical spacing is needed to resolve the interface, finer vertical grids near the surface and coarser grids in the rest of the ocean are used. In our simulation, below 3 times of the maximum surface wave height a coarse spacing of 2.5 m is used, and above a finer spacing of 8 times denser is used.

A rough sea surface moving parallel to the source-receiver direction with a (20-knot) Pierson-Moskowitz spectrum was projected onto the surface of the 2D vertical plane containing the source and receiver. Simulation was done by generating correlated realizations, every half seconds, of an ocean surface with randomly distributed surface waves and using the modified rough surface FEPE to propagate signals to the array.

4. RESULTS

Phone spectra from data and simulation were calculated using an FFT with Hanning shading. Figure 2 shows the array average spectrum from data. We separated the Doppler spectrum into three bands, the Carrier, Down-Doppler, and Up-Doppler, and applied MFP using a range-independent normal mode code to each band. Figure 3 shows the range-depth responses of the Carrier frequency. The experimental results are shown in the top two panels and the corresponding simulation results are shown in the bottom two panels. The conventional MFP responses are shown on the left and the robust adaptive MFP responses(5) are shown on the right. The source was localized at 760 m on the bottom. The conventional MFP responses show high ambiguous sidelobes which depict the propagation paths outward from the source. It shows two paths reach the array: one path direct propagates to the array and the other path hits the surface and is refracted to the array. The robust adaptive MFP suppresses the sidelobes and shows an excellent localization of the source. Figure 4 shows the MFP responses of the down-Doppler energy and the Up-Doppler energy. The forward-scattered energy is localized near the place where the acoustic propagation paths reach the surface. The rough-surface FEPE simulated spatial distributions of the forward-scattered energy are consistent with the real data results. In additional to the forward-scattered energy other scattered-components which might be related to the bottom-back-scattered energy and volume-scattered-energy are observed in the MFP responses of the real data.

5. SUMMARY

In this study we have demonstrated that MFP technique can be used to study the range-depth spatial distribution of reverberation. More information can be obtained to better understand the physics of how the ocean surface is illuminated and re-radiates the energy.

REFERENCES:

1) Y. P. Lee, "Using Matched-Field Processing (MFP) Technique to Map The Forward-Scattered Signal," J. Acoust. Soc. Am. 97, 3424 (1995).

2) L. B. Dozier and H. A. Freese, "Active Matched Field Processing for Clutter Rejection," ***Ocean Reverberation***, D. D. Ellis et. al. (eds.) pp 313-318, Kluwer Academic Publishers, Netherlands, 1993.

3) D. P. Knobles and R. A. Koch, "A Time Series Analysis of Sound Propagation in a Strongly Multipath Shallow Water Environment with an Adiabatic Normal Mode Approach," IEEE J. Oceanic Eng., vol 21, pp 1-13, 1996.

4) A. P. Rosenberg and S. F. Magruder, "An accurate, efficient rough surface parabolic equation program," J. Acoust. Soc. Am. 97, 3314 (1995)

5) Y. P. Lee, P. Mikhalevsky, H. Freese, and J. Hanna, "Robust Adaptive Matched-Field Processing," Proc. of IEEE Oceans'93 Conference in November 1993, Vancouver, Canada.

plt2

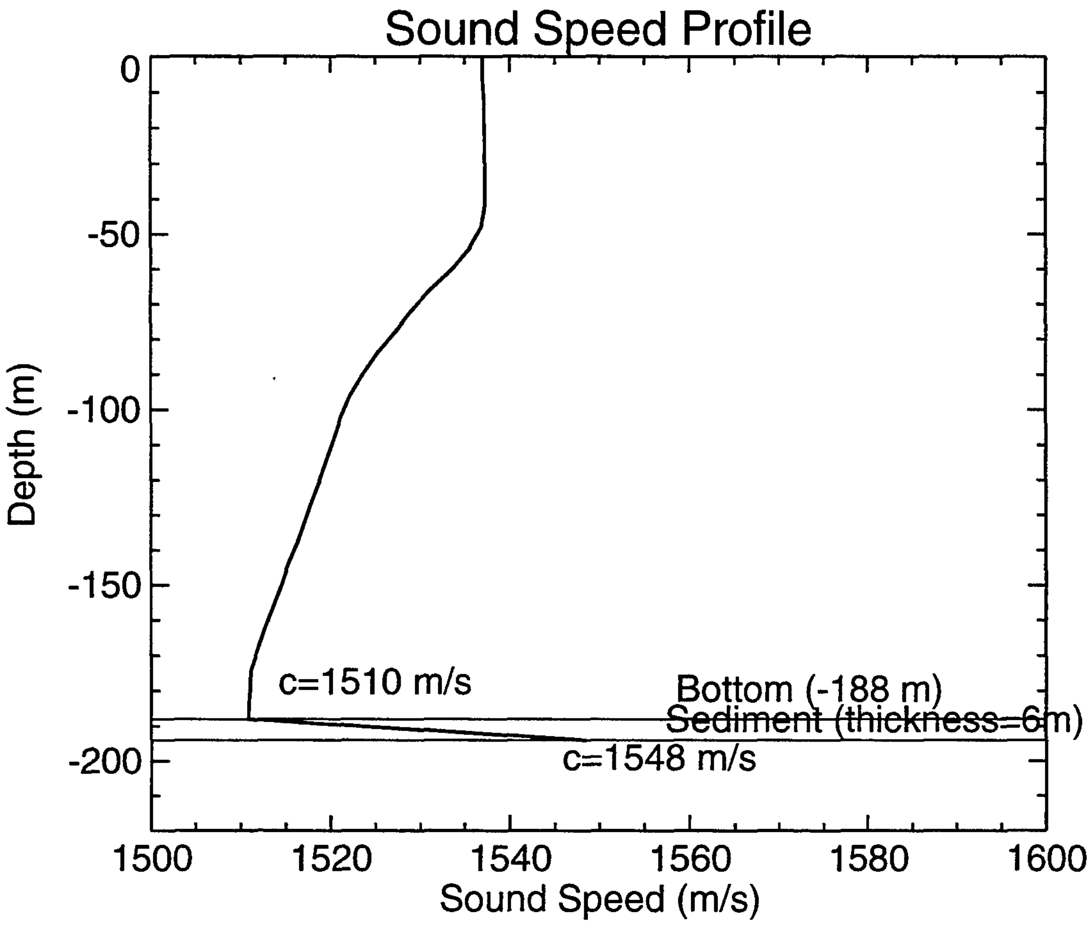

Figure 1.

pltbm1

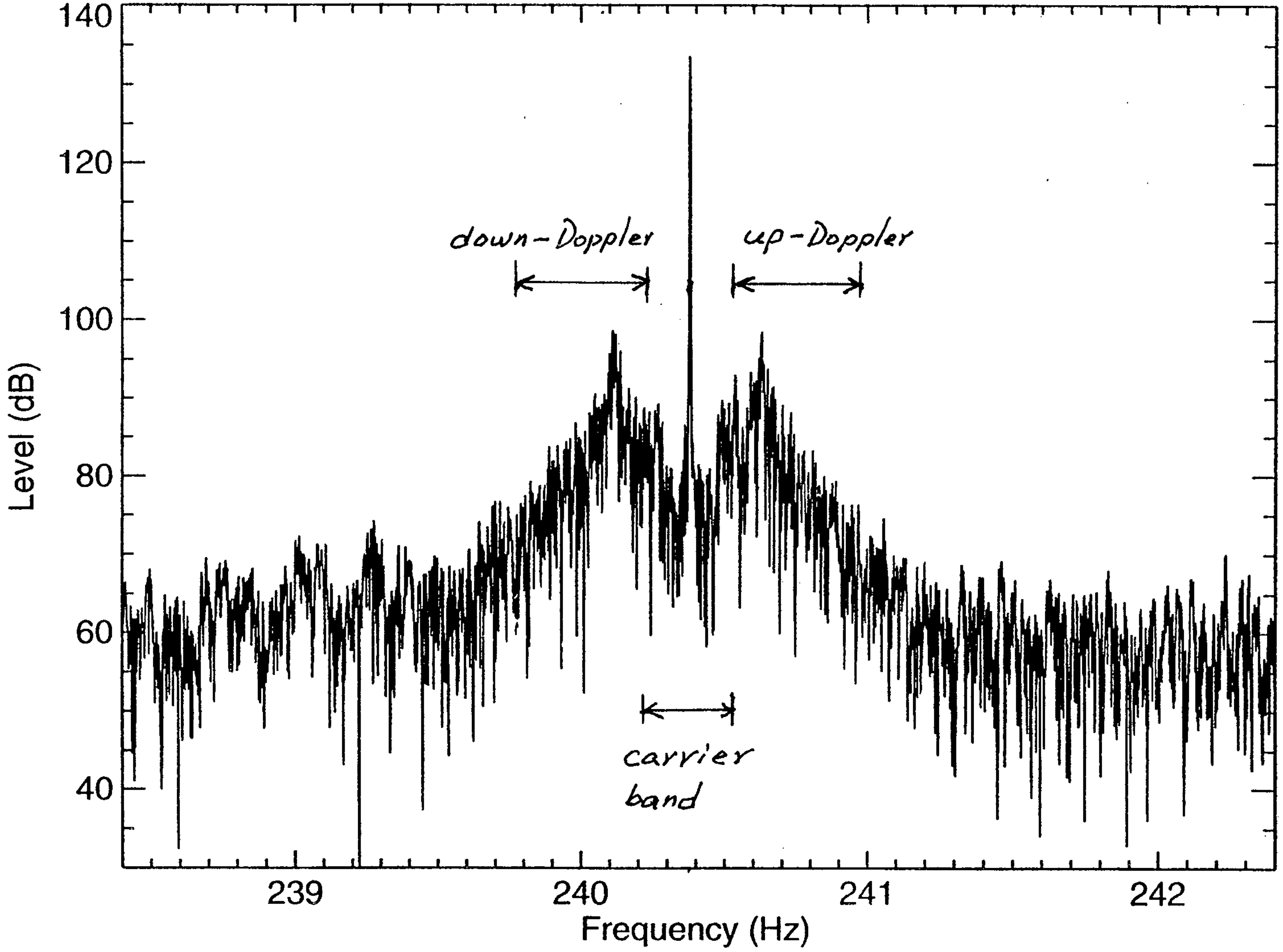

Figure 2.

Figure 3: MFP responses at Carrier (240-Hz, R=760m, Z=188m)

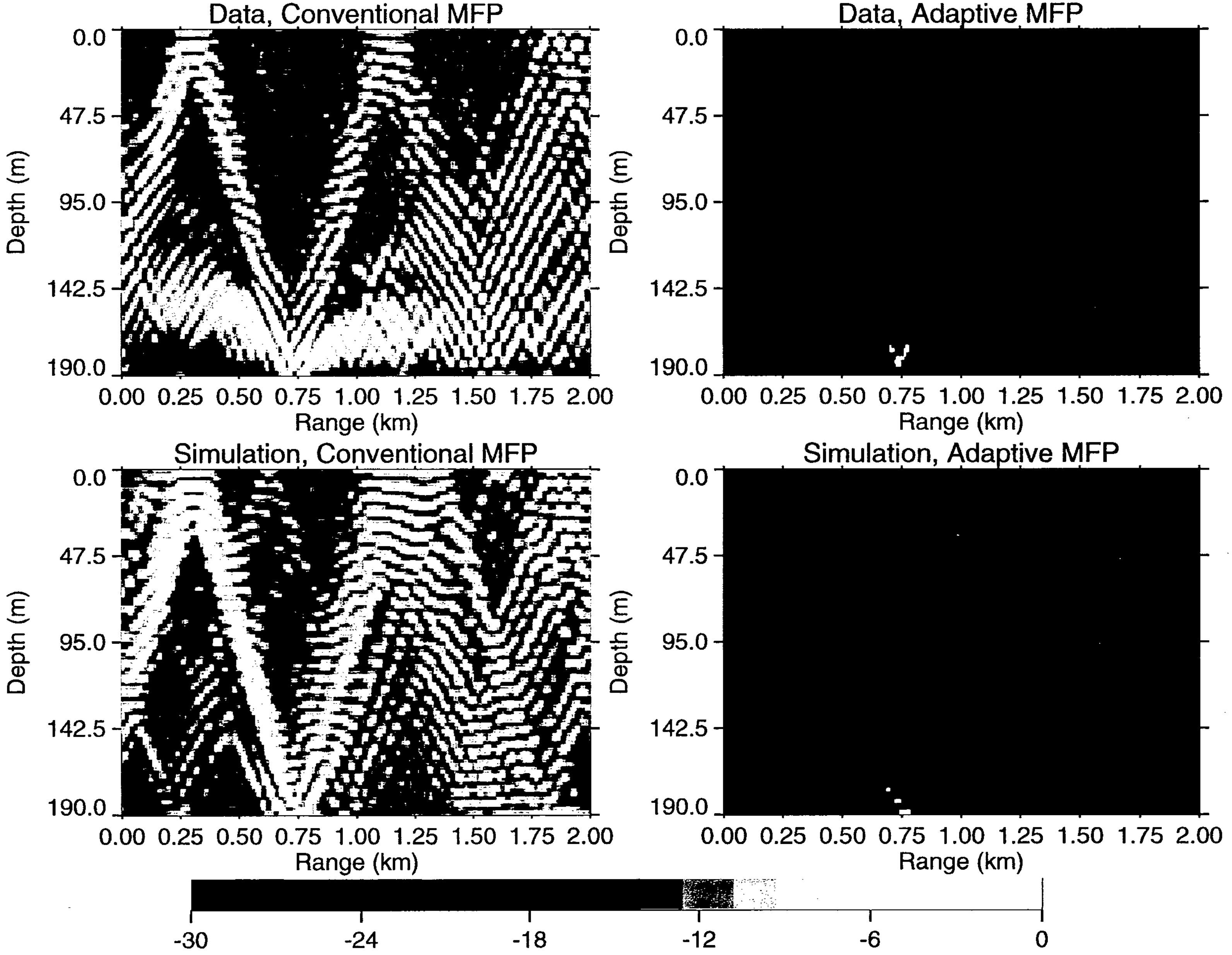

Figure 4: MFP responses of Scattered-Energy(Source @R=760m, Z=188m)

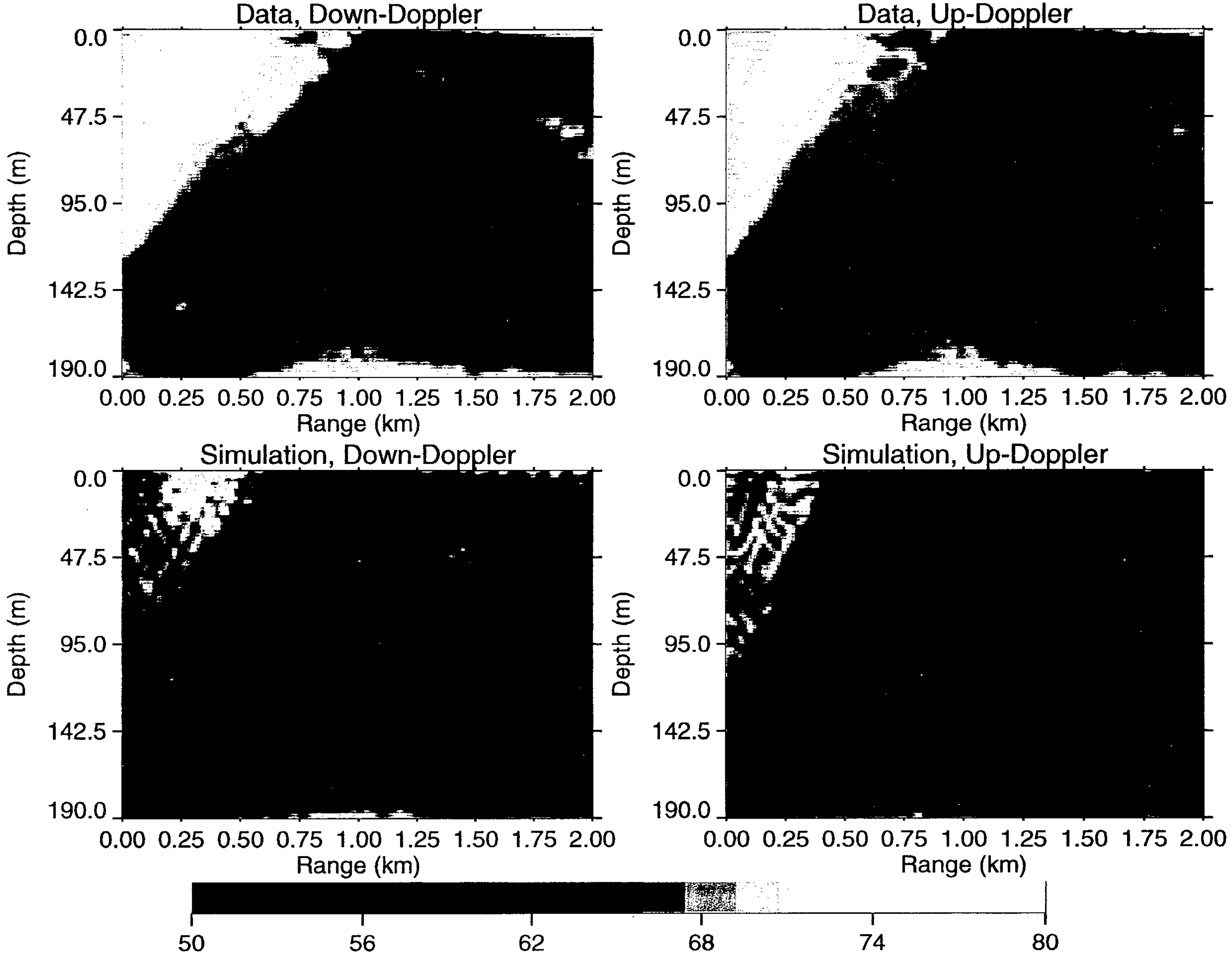

Modal Decomposition using Spectral Regularization Techniques

Cedric Zala and Alexander Timonov
Barrodale Computing Services Ltd.
Victoria, B.C., Canada
and
John Ozard
EDRD/DREA
Victoria, B.C., Canada
and
N. Ross Chapman and Stan Dosso
University of Victoria
Victoria, B.C., Canada

14 JULY 1996

Abstract

The effectiveness of novel regularization techniques for generating stable solutions to the ill-conditioned linear problem of modal decomposition was examined. These techniques were based on either a specific Tikhonov regularization scheme or one of several more general spectral regularizing algorithms. The model system for this simulation study consisted of an ideal waveguide and a vertical array spanning half the water column. It was verified that regularization was necessary to obtain a stable solution, and that the accuracy of estimation depended on the regularization scheme and the nature of the noise. When the noise was assumed to be known exactly (i.e., the deterministic case), spectral regularization gave the most accurate result. For the situation where only statistical knowledge of the noise was available, Tikhonov's scheme was somewhat more accurate than the spectral approach. The accuracy of the regularized solution was observed to depend strongly on the characteristics of the right-hand side of the system of linear equations as well as on the condition of the matrix. The most accurate solutions were obtained when the source depth was within the depth region spanned by the array.

I Modal Decomposition

Modal decomposition is an essential stage in the use of matched-mode processing (MMP) techniques for source detection and localization. MMP can be used in conjunction with a nearest neighbours algorithm to yield processing techniques which are substantially more efficient than matched-field processing. MMP first requires the estimation of the m complex mode amplitudes $\mathbf{x}$ from the measured fields $\mathbf{y}$ at the n sensors, by solving the $n \times m$ system of linear equations $\mathbf{A}\mathbf{x} = \mathbf{y}$, where $\mathbf{A}$ is the design matrix. We shall consider here only the case of vertical arrays, for which

$$\mathbf{A} = \begin{bmatrix} \phi_1(z_1) & \phi_2(z_1) & \dots & \phi_m(z_1) \\ \phi_1(z_2) & \phi_2(z_2) & \dots & \phi_m(z_2) \\ \phi_1(z_3) & \phi_2(z_3) & \dots & \phi_m(z_3) \\ \vdots & \vdots & \ddots & \vdots \\ \phi_1(z_n) & \phi_2(z_n) & \dots & \phi_m(z_n) \end{bmatrix},$$

where $\phi_j(z_k)$ is the mode function amplitude for the jth mode and the kth sensor and $\mathbf{x}$ is a vector of mode excitations at the source depth z_s; i.e.,

$$\mathbf{x} = [\phi_1(z_s)\frac{e^{ik_1 r}}{\sqrt{k_1 r}} \quad \phi_2(z_s)\frac{e^{ik_2 r}}{\sqrt{k_2 r}} \quad \dots \quad \phi_m(z_s)\frac{e^{ik_m r}}{\sqrt{k_m r}}]^*,$$

where $(^*)$ denotes the conjugate transpose.

II Inversion and Regularization

Given $\mathbf{A}$ and $\hat{\mathbf{y}}$, where the elements of $\hat{\mathbf{y}}$ are the noise-containing measured field values, the least-squares estimate of the mode amplitudes $\mathbf{x}$ is characterized by the normal equations:

$$\mathbf{A}^*\mathbf{A}\mathbf{x} = \mathbf{A}^*\hat{\mathbf{y}}.$$

Provided a unique solution exists, it can be conveniently expressed in terms of the eigendecomposition of $\mathbf{A}^*\mathbf{A}$; i.e.,

$$\begin{aligned} \mathbf{EDE}^*\mathbf{x} &= \mathbf{A}^*\hat{\mathbf{y}}, \qquad \text{from which} \\ \mathbf{x} &= \mathbf{ED}^{-1}\mathbf{E}^*\mathbf{A}^*\hat{\mathbf{y}}, \end{aligned}$$

where
$\mathbf{E}$ is a matrix of the eigenvectors of $\mathbf{A}^*\mathbf{A}$,
$\mathbf{D}$ is a diagonal matrix with diagonal elements λ_k,
$\mathbf{D}^{-1}$ is a diagonal matrix with diagonal elements $1/\lambda_k$, and
λ_k is the kth eigenvalue of $\mathbf{A}^*\mathbf{A}$.

For the case where the array spans only a portion of the water column, the matrix $\mathbf{A}^*\mathbf{A}$ can be very ill-conditioned. For example, for the case of an array spanning only the top half of a 100-m deep waveguide, the condition number of this matrix was found to increase from 10^6 to 5×10^{13} as the number of modes was increased from 5 to 10. This resulted in unstable and highly inaccurate estimates of $\mathbf{x}$ when the normal equations solution was computed.

The inversion (i.e., estimation of $\mathbf{x}$) may be stabilized through regularization. Regularizing operators R_δ provide a stabilized approximation to the inverse operator, and ensure that solutions obtained by inversion converge to the true solutions as errors in the measurements tend to zero. Design of suitable regularizing operators depends on the nature of the prior knowledge about the signal and noise characteristics. These operators can be expressed in spectral form in terms of the eigendecomposition above, where d_{kk}, the diagonal elements of the matrix $\mathbf{D}_\delta^{-1}$ (the regularized approximation to $\mathbf{D}^{-1}$), are

$$d_{kk} = \lambda_k/(\lambda_k^2 + q_\delta(\lambda_k)),$$

where $q_\delta(\lambda_k)$ is a nonnegative stabilizing function.

Standard **Tikhonov regularization** [1] is a global scheme which involves minimizing

$$||\mathbf{A}\mathbf{x}_\alpha - \hat{\mathbf{y}}||^2 + \alpha||\mathbf{x}||^2,$$

for which the form of the approximating operator is

$$R_\alpha = (\mathbf{A}^*\mathbf{A} + \alpha\mathbf{I})^{-1}\mathbf{A}^*. \tag{1}$$

We consider here the specific Tikhonov regularizing operator which is obtained by finding $\alpha = \alpha(\delta)$ and $\mathbf{x}_\alpha$ to satisfy the *discrepancy equation*:

$$G(\alpha) = ||\mathbf{A}\mathbf{x}_\alpha - \hat{\mathbf{y}}||^2 - \delta^2 = 0,$$

where δ^2 is a constant which depends on the noise level and model errors.

Spectral Regularization (SR) [2] is a more flexible form of regularization than the Tikhonov scheme. It may be expressed in the following form:

$$\begin{aligned} \mathbf{x} \approx R_\delta \hat{\mathbf{y}} &= \sum_k \frac{\lambda_k}{\lambda_k^2 + q_\delta(\lambda_k)}(\mathbf{e}_k^* \cdot \mathbf{A}^*\hat{\mathbf{y}})\mathbf{e}_k \\ &= \sum_k \frac{\lambda_k}{\lambda_k^2 + q_\delta(\lambda_k)}\hat{u}_k \mathbf{e}_k \\ &= \sum_k w_k \mathbf{e}_k, \end{aligned}$$

where
$\mathbf{e}_k$ is the kth eigenvector of $\mathbf{A}^*\mathbf{A}$,
$\hat{u}_k = (\mathbf{e}_k^* \cdot \mathbf{A}^*\hat{\mathbf{y}})$ is the kth component of the spectral decomposition of $\mathbf{A}^*\hat{\mathbf{y}}$, and
w_k is the kth spectral component of the solution $\mathbf{x}$.

We note that for the standard Tikhonov regularizing operator (Eq. 1), $q_\delta(\lambda_k) = \alpha$. Thus this operator is a simple form of spectral regularizing operator. However, in the following we shall restrict the use of the term "spectral regularization" to those forms described below.

In determining appropriate forms for q_δ and w, one approach is to assume that

$$|\hat{u}_k - u_k| \leq \sigma_k.$$

In this case it may be shown that the solution which minimizes $|w_k|$ is

$$w_k^0 = \begin{cases} 0 & \text{if } |\hat{u}_k| \leq \sigma_k \\ \frac{\hat{u}_k}{\lambda_k}(1 - \frac{\sigma_k}{|\hat{u}_k|}) & \text{if } |\hat{u}_k| > \sigma_k \end{cases}.$$

This form is termed the *initial solution.*

Once this initial solution has beed determined, the following expression may be iterated:

$$w_k^{n+1} = \frac{\lambda_k \hat{u}_k}{\lambda_k^2 + \frac{\sigma_k^2}{|\hat{w}_k^n|^2}}.$$

On convergence (i.e., when $n \to \infty$), this form is termed the *limit solution.*

Both forms require that an estimate of the spectral decomposition of the noise σ_k be provided for each spectral component k. This was done using one of two noise models: (1) *deterministic*, where the known noise values $\mathbf{n}$ at the sensors were used: i.e., set

$$\sigma_k = |(\mathbf{e}^*{}_k \cdot \mathbf{A}^*\mathbf{n})|,$$

and (2) *statistical*, where the RMS spectral decomposition of the noise was estimated for various realizations of noise $\mathbf{n}_j$ and scaled by a constant c: i.e., set

$$\sigma_k = c \times \sqrt{\frac{1}{P}\sum_{j=1}^{P} |(\mathbf{e}^*{}_k \cdot \mathbf{A}^*\mathbf{n}_j)|^2}.$$

Here, c was set to 2.0 (twice the RMS noise level); this value was chosen to suppress the effects of the larger random realizations of noise in the spectral components of the data. Thus, only when the signal+noise spectral level in the data was at least twice the estimated average noise level did the eigenvector corresponding to that spectral component contribute to the solution.

III Comparison of Regularization Schemes

The regularization schemes described above were compared in a series of simulations involving an ideal waveguide. The waveguide was 100 m deep, with a pressure-release surface and a rigid bottom. A vertical array was positioned so as to span the top or bottom half of the waveguide, and a source at a frequency between 15 and 75 Hz (giving between 2 and 10 modes) was modelled at a specified depth and range. The accuracy of the computed solution was expressed in terms of the relative sum of squares of deviations: i.e., $||\mathrm{x}_{\mathrm{estimated}} - \mathrm{x}_{\mathrm{true}}||^2/||\mathrm{x}_{\mathrm{true}}||^2$.

The following observations were made as a result of these simulations:

1. The SR scheme with deterministic noise was more accurate than the Tikhonov scheme (but this type of prior knowledge about the noise is not available in applications such as the present one, where the noise is random). The SR scheme with statistical noise, though realizable in practice, was somewhat less accurate than the Tikhonov scheme.
2. The initial form for SR was slightly more accurate than the limit form.
3. There was very little effect on accuracy of increasing the number of sensors in the array.
4. The accuracy tended to decrease rapidly as the number of modes was increased, but this decrease was not monotone.
5. The accuracy depended on range, but again the dependence was not monotone.
6. The accuracy depended on the depth at which the source was placed in the channel.

This last observation is illustrated in Figures 1 and 2, where the relative deviations of the solution were estimated as a function of the depth of the source. In these simulations, the frequency was 40 Hz (resulting in five modes) and the source-array range was 2000 m. Figure 1 shows the case for an array in the top half of the water column, and Figure 2 shows the results for an array in the lower half. It is evident that the most accurate solutions were obtained under conditions where the source depth was within the depth region spanned by the array.

This observation is also of theoretical interest, since under these conditions the matrix **A** for a particular array configuration is constant as the source depth varies. Therefore the accuracy of the solution is strongly influenced by the characteristics of the right-hand side of the system of equations as well as by the condition number. The physical explanation underlying this mathematical result is an area for future investigation.Φ

References

1. A. N. Tikhonov and V. Ya. Arsenin, *Methods of Solving Ill-Posed Problems*, Wiley, 1977.
2. V. Ya. Arsenin, Yu. A. Kriksin and A. A. Timonov, "On a spectral approach to the construction of local regularization algorithms," Soviet Math. Dokl. **39**, 86–90 (1989).

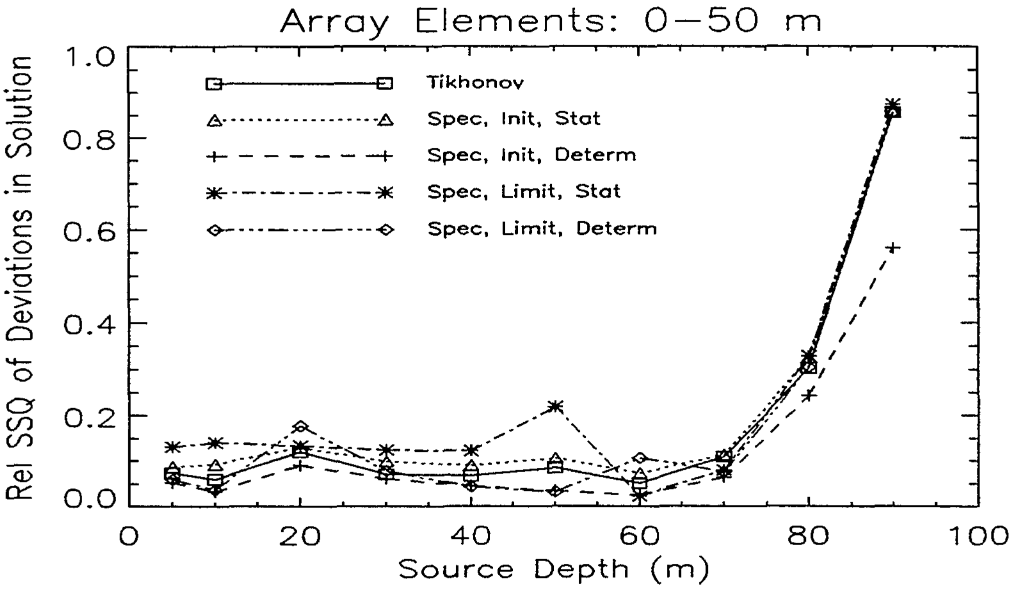

Figure 1: Relative sum-of-squares (SSQ) of deviations of regularized solutions as a function of source depth, for an array in the top half of the channel. These results were obtained for a 40-Hz source in a 100-m channel (5 modes) and a source-array range of 2000 m.

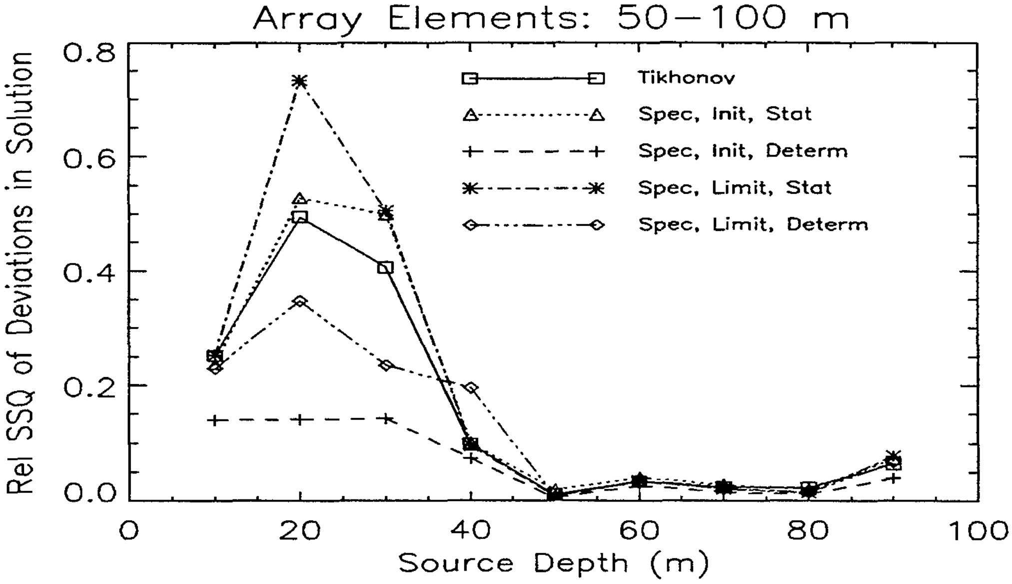

Figure 2: Relative sum-of-squares (SSQ) of deviations of regularized solutions as a function of source depth, for an array in the lower half of the channel. These results were obtained for a 40-Hz source in a 100-m channel (5 modes) and a source-array range of 2000 m.

Matched-field processing for multiple noise sources in an Arctic environment

S. E. Dosso,[1] M. V. Greening[2] and P. Zakarauskas[3]

[1]School of Earth and Ocean Sciences, University of Victoria, Victoria BC Canada V8W 3P6

[2]Datavision Computing Services Ltd., 203-1545 Pandora Ave.,Victoria BC Canada V8R 6R1

[3]Dept. of Opthamology, University of British Columbia, Vancouver BC Canada V5Z 3N9

Abstract

This paper applies the method of matched-field processing (MFP) to localize multiple sources in cases where the bathymetry is not well known. This is a practical problem, particularly in Arctic environments where the bathymetry is often poorly known and difficult to measure due to ice cover. A general approach to the problem of environmental mismatch in MFP was developed by Collins and Kuperman [1] based on generalizing the localization problem to include uncertain environmental parameters as well as source location in the search for an optimal match with the acoustic data. Dosso [2] applied this method to source localization in environments with uncertain bathymetry. Here, a broadband MFP algorithm is described which searches simultaneously for the location (range and bearing) and relative strength of multiple sources, and includes corrections to the bathymetry along the propagation path to each source in the inversion. The approach is illustrated with a synthetic example representing a distribution of active ice-ridge building events in the Arctic. The inversion is also applied to a set of Arctic ambient noise measurements collected in the Lincoln Sea.

1. Inversion Algorithm

The goal of MFP is to determine the location of one or more sources which minimize the mismatch between measured and modelled acoustic fields. For a broadband source, the mismatch E can be defined as

$$E = 1 - \left[\frac{\left| \sum_{p=1}^{H} \sum_{q=p+1}^{H} \sum_{f=f_l}^{f_u} R_{pq}(f)\, M_{pq}^{*}(f) \right|}{\left[\sum_{p=1}^{H} \sum_{q=p+1}^{H} \sum_{f=f_l}^{f_u} |R_{pq}(f)|^2 \right]^{1/2} \left[\sum_{p=1}^{H} \sum_{q=p+1}^{H} \sum_{f=f_l}^{f_u} |M_{pq}(f)|^2 \right]^{1/2}} \right], \qquad (1)$$

where H is the number of hydrophones, f_l and f_u are the lower and upper limits of the frequency band, and $R_{pq} = \langle R_p\, R_q^* \rangle$ and $M_{pq} = M_p\, M_q^*$ are the cross spectra of the measured and modelled acoustic fields R_p and M_p. Equation (1) is a multiple-frequency variant of the

Bartlett processor which omits the autospectra of the cross-spectral matrices. The Bartlett processor is used because it is less sensitive to environmental mismatch than high-resolution processors. Processing multiple frequencies decreases the number and amplitude of sidelobes, since these tend to occur at different ranges for different frequencies. The modelled acoustic field is determined by specifying pressure levels at the receiver as

$$M_q(f) = \sum_{i=1}^{S} \left[\frac{b_i(f)\; p(r_i, z_i, \theta_i, z_q, f)}{\left[\sum_{j=1}^{H} |p(r_i, z_i, \theta_i, z_j, f)|^2 \right]^{1/2}} \right], \tag{2}$$

where S is the number of sources and $b_i^2(f)$ is the total power received at the array for source i. The acoustic pressure p at receiver depth z_q due to a source at (r_i, z_i, θ_i) is calculated using an $N \times 2D$ adiabatic normal mode model

$$p(r_i, z_i, \theta_i, z_q) = \sum_{j=1}^{N} \phi_j[d(r_i, \theta_i), z_i]\; \phi_j[d(0,0), z_q]\; \frac{\exp(i \int_0^{r_i} k_j[d(r, \theta_i)]\, dr)}{\sqrt{\int_0^{r_i} k_j[d(r, \theta_i)]\, dr}}, \tag{3}$$

where N is the number of modes that propagate from source to receiver, $\phi_j[d(r,\theta), z]$ is the jth mode function at depth z for a water depth $d(r,\theta)$, and $k_j[d(r,\theta)]$ is the jth wavenumber. The mode functions and wavenumbers were pre-calculated for 20-m increments in water depth and stored in look-up tables for fast reference. Within the invesion algorithm, linear interpolation of the table entries was then used to determine modal values. This provides highly efficient computation of the matching fields. This is of key importance to the multi-dimensional inversion developed here, which requires the matching fields be modelled an extremely large number of times.

The matched-field localization algorithm searches simultaneously for the range, bearing and relative strength of a specified number of sources, together with corrections to the bathymetry model along the propagation path to each source. This requires an extremely large parameter space be examined to find the parameter set which minimizes the mismatch. The parameter search is carried out using the method of simulated annealing which provides an efficient stochastic search algorithm that avoids becoming trapped in unfavourable local minima [1, 2].

2. Synthetic Example

Inversion for multiple sources with uncertain bathymetry is investigated in this section using a synthetic example representing a distribution of active ice-ridge building events in an Arctic environment. The synthetic case is designed to simulate ambient noise measurements collected in the Lincoln Sea which are analyzed in Sec. 3. The environment and array geometry at the measurement site were adopted for the synthetic study and are summarized here. The hydrophone array was located in 430-m of water and consisted of vertical and horizontal sub-arrays of 24 and 7 sensors, respectively. The horizontal sub-array included one off-axis hydrophone to break the left-right symmetry. The sound-speed profile was measured at the array site and a number of experiments were carried out to measure the ocean-bottom

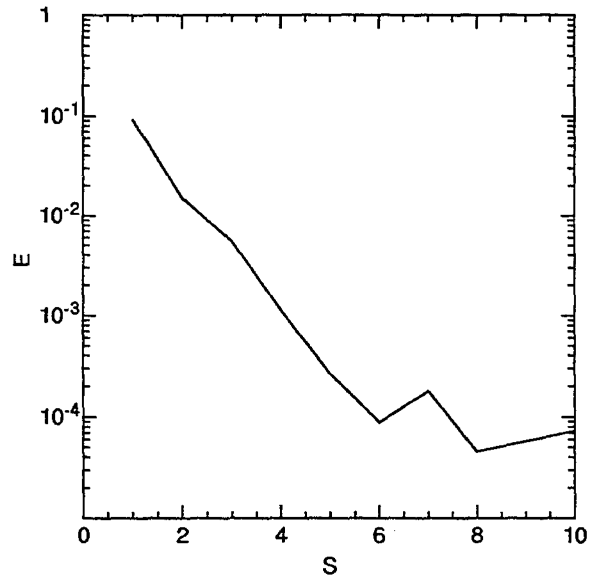

Fig. 1 Mismatch E vs. number of sources S for the synthetic example.

geoacoustic properties [3]. The bathymetry was taken from the chart of the Arctic basin published by the Naval Research Laboratory (NRL) [4]. This chart was digitized to 400-km range from the array site along radial paths every 1° in bearing. Synthetic acoustic data and matching fields were computed for the frequency band 10–30 Hz in 5-Hz increments using the adiabatic normal mode model. The applicability of the adiabatic approximation to this environment was investigated in a simulation study by Zala and Ozard [5], who found excellent agreement between an adiabatic normal mode model and a parabolic equation model at 20 Hz for slopes $< 3°$. The largest bottom slopes along radial paths from the array site are $< 2.4°$; hence, the adiabatic normal mode model should be applicable to this environment.

The number of sources contributing to the total acoustic field may be estimated by examining the mismatch E returned by the inversion algorithm as a function of the number of sources S sought in the inversion. Figure 1 shows E as a function of S when six sources were used as input to compute synthetic acoustic data (the source distribution is shown in Fig. 2a). The search interval for the bathymetry was ±50 m. In Fig. 1, the mismatch E decreases as the number of sources S increases to six. Increasing S beyond six does not significantly decrease E. Figure 2 shows the estimated source locations and relative levels determined by the inversion algorithm. When the number of sources is underestimated, the stronger sources are localized. When the correct number of sources is sought, excellent estimates of the source locations and levels are obtained. When the number of sources is overestimated, excellent estimates for the input sources are still obtained, with additional weak sources included to account for the required number. These additional sources do not contribute significantly to the acoustic field.

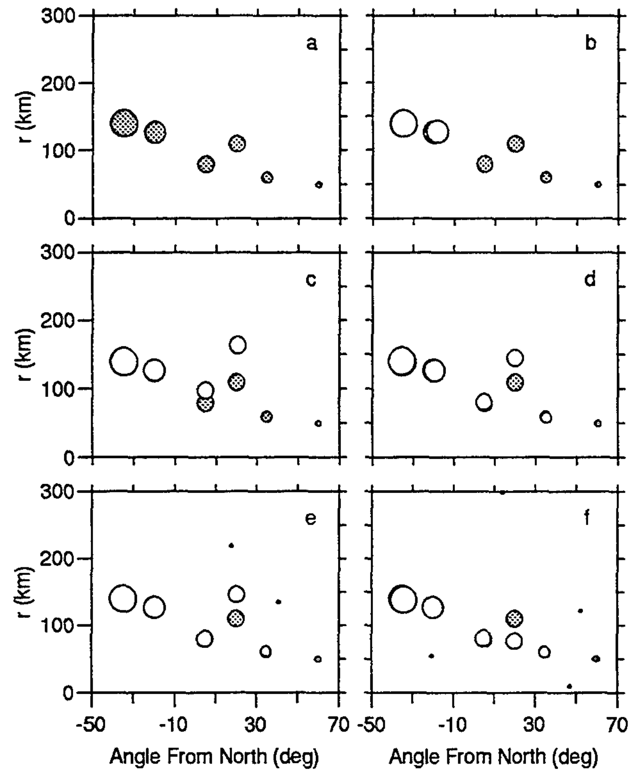

Fig. 2 True source distibution (a, shaded circles) and distributions determined by inversion for 2, 4, 6, 8 and 10 sources in (b)–(f). Circle size indicates relative source strength.

3. Arctic Ambient Noise Inversions

The measured data analyzed in this section consist of six two-minute samples of the ambient noise recorded in the Lincoln Sea. Five of the samples, denoted samples B–F, were dominated by distant ice-ridging noise. The sixth, sample A, was dominated by local thermal ice cracking and was included in the analysis for comparative purposes. Matching fields for the inversion were calculated using the adiabatic normal mode model (Eq. 3). An important factor influencing propagation in the Arctic is the scattering of acoustic energy at the rough under-side of the ice. In computing the matching fields, the Burke-Twersky ice-scattering model [6] was employed, which represents under-ice ridges by a random distribution of elliptical half-cylinders. The bathymetry was allowed to vary in the inversions by ±50 m from values from the NRL chart [3].

Figure 3 shows the mismatch E as a function of the number of sources S sought in the inversion for the six ambient noise samples. For the ice-ridging samples (B–F), E decreases rapidly as S increases to about 6–8, then decreases much more slowly. For seven sources $E < 0.01$ for each of these samples. The fit to the data is illustrated in Fig. 4, which

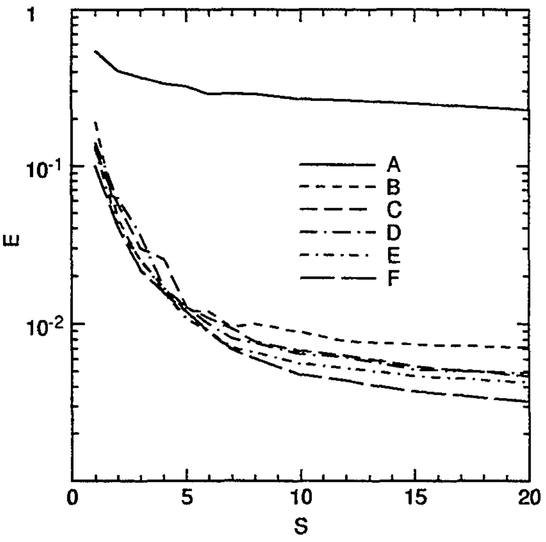

Fig. 3 Mismatch E vs. number of sources S for five ambient noise sampes.

shows the magnitude of the cross-spectral matrices for sample E and for the modelled source distribution with seven sources. All the major features of the measured cross spectra are reproduced by the modelled source distribution. Thus, 6–8 sources appear to be sufficient to model the ice-ridging noise samples used in this study. For sample A, the mismatch in Fig. 3 is much larger than for the ice-ridging samples and does not decrease significantly as the number of sources is increased up to 20. This indicates that the inversion method does not have so many degrees of freedom that it can simply reproduce any acoustic measurements, such as local (non-modal) ice-cracking noise.

Each of the inversions represented in Fig. 3 involved computing approximately 7×10^5 matching fields, and required ~2 hours CPU time on a DEC Alpha computer (computation speed: 20 Mflops). To verify that the parameter-space search was sufficient, several inversions were repeated with the number of matching fields increased by a factor of ten, with no appreciable change in the mismatch. To verify that the ±50 m search interval for the bathymetry was sufficient, several cases were repeated with a search interval of ±250 m, with no change in mismatch.

The source distributions determined by the inversions for seven sources are shown in Fig. 5. This figure also includes the results of broadband maximum-likelihood plane-wave beamforming applied to the acoustic data recorded on the horizontal array for the frequency band 10–30 Hz. The results suggest that sources located in the deep water to the north of

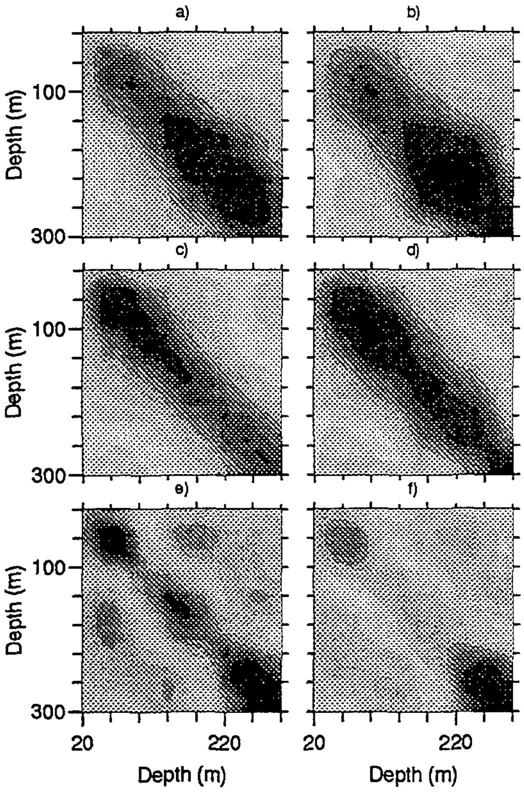

Fig. 4 Magnitude of cross-spectral matrices for measured (a, c, e) and modelled (b, d, f) fields. Frequencies are 10 Hz (a, b), 20 Hz (c, e) and 30 Hz (e, f).

the recording site dominate the ice-ridging samples B–F. The ice-cracking sample, sample A, has much flatter directivity than the ice-ridging samples, indicating an essentially isotropic distribution of sources.

Given that inverse problems are inherently non-unique, the good agreement between measured and modelled fields in Fig. 4 does not necessarily indicate that the sources are correctly localized. A test of the result is to obtain consistent source distributions for different initializations of the inversion algorithm. Unfortunately, this has not proved to be the case for the measured ambient noise data. Source ranges were found to be ambiguous, i.e., different initializations of the inversion lead to source distributions with similar mismatches that differed significantly in source ranges. However, source bearing estimates were found to be consistent with respect to different initialization of the inversion. In addition, re-initializing the inversion algorithm for different numbers of sources did not change the conclusion that 6–8 sources were required to model the ice-ridging noise.

There are a number of possible reasons for the ambiguity in range for the measured data. These include inadequacies of the ice-scattering model, mode coupling and three-dimensional propagation effects, errors in the location of the hydrophones, non-modal noise from other sources, and uncertainty in environmental parameters other than bathymetry.

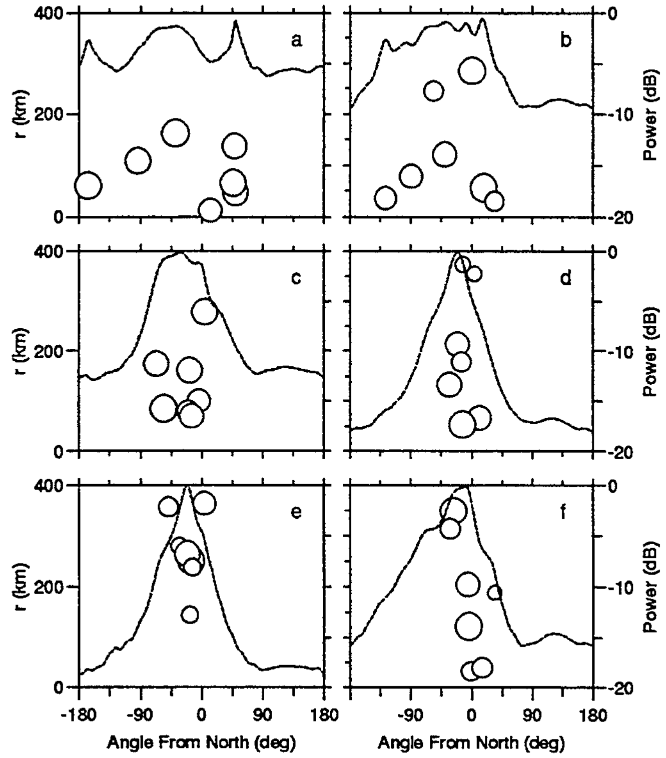

Fig. 5 Source distributions (circles) for samples A–F in (a)–(f), respectively. Dashed lines indicate beamforming results.

4. Summary

A matched-field inversion algorithm is described for localizing multiple sources with a limited knowledge of bathymetry. The method provides excellent results for synthetic examples representing a distribution of ice-ridging noise sources in the Arctic. Application to ambient noise measurements provided source distributions which reproduce the measured fields and are unambiguous in terms of the number and bearings of the sources; however, source ranges could not be estimated unambiguously.

References

[1] M. D. Collins and W. A. Kuperman, Focalization: environmental focusing and source localization, *J. Acoust. Soc. Am.*, **90**, 1410–1422 (1991).

[2] S. E. Dosso, Matched-field inversion for source localization with uncertain bathymetry, *J. Acoust. Soc. Am.*, **94**, 1160–1163 (1993).

[3] M. V. Greening and P. Zakarauskas, Spatial and source level distributions of ice

cracking in the Arctic Ocean, *J. Acoust. Soc. Am.*, **95**, 783–790 (1994).

[4] Naval Research Laboratory, Bathymetry of the Arctic Ocean, Map and chart series MC-56, Geological Society of America, Inc. Boulder, Colorado, U.S.A. (1986).

[5] C. A. Zala and J. M. Ozard, Comparison of parabolic equation and adiabatic mode propagation models for matched field processing in range-dependent environments, *Proceedings of the 6th IEEE workshop on statistical signal and array processing*, Victoria, Canada, 259–262 (1992).

[6] O. I. Diachok, Effects of sea-ice ridges on sound propagation in the Arctic Ocean, *J. Acoust. Soc. Am.*, **59**, 1110–1120 (1976).

Coherent Broadband Matched Field Processing for Geoacoustic Parameter Estimation

D. E. Hannay
JASCO Research Ltd.
Brentwood Bay, B.C., Canada

and
N. R. Chapman
University of Victoria
Victoria, B.C., Canada

13 August 1996

Abstract

Matched field processing of broadband SUS charge data was performed to evaluate a coherent broadband object function. This object function includes absolute phase and amplitude information at all frequencies, thereby matching the shapes and absolute timing of pressure waveforms measured on a vertical array. The coherent broadband object function is implemented together with the classical Bartlett object function, and an incoherent broadband function obtained by averaging the Bartlett function over frequency. All three functions are applied to determine their effectivenesses for inverting experimental geometry and ocean bottom parameters.

Introduction

Matched Field Processing (MFP) has been discussed in recent underwater acoustics literature. The method is applied as follows: certain characteristics of the pressure field measured on an array of hydrophones are matched with those predicted by a numerical model by varying the inputs to the model. The inputs causing the best match are taken as estimates of the corresponding parameters present in the vicinity of the experiment.

The inputs to the numerical model normally include the positions of the source and the receiver(s), and a set of parameters describing the geoacoustic environment. We refer to a specific set of inputs to the propagation model as an environmental model $\mathbf{m}$. It is denoted in bold to indicate that it represents the values of several parameters at once. An object function $E(\mathbf{m})$ is defined to indicate the degree of match for specific models. The problem then is to maximize the object function over a search space defined by the possible ranges for each of the components of $\mathbf{m}$.

The object or cost function dictates which information in the pressure field is matched. The following sections describe possible forms of the object function. The first type discussed is the single frequency Bartlett object function. Next, extension of the single frequency function to the incoherent broadband object function is described. Finally the coherent broadband object function is developed, and discussed in relation to the incoherent cases.

I Experiment

Experimental data was aquired by the Defence Research Establishment Pacific (DREP) during the Pacific Shelf sea trials in 1993 off the coast of Vancouver Island. The shot data processed for this work were recorded during a shot run in which a series of 0.82 kg SUS charges were dropped at increasing range from a vertical array which was stationary at approximately 49.02°N 126.86°W, where the water depth was approximately 400 m. The charges, set to detonate at 200 m, were dropped at ranges between 0.7 km and 12 km from the array, along a course which approximately paralleled the 400 m depth contour. The array consisted of 16 hydrophones equally spaced with 15 m separations, with the depth of the top hydrophone at 80 ± 5 m throughout the run. Hydrophone pressure was sampled continuously at a rate of 1500 samples per second on all hydrophones. These data were transmitted via a FM link from the array to a monitoring ship, where they were written directly to exabyte tape files.

II Object Functions

II.1 Incoherent object functions

The most common formulation of the object function in MFP is the single frequency classical Bartlett power function:

$$E(\mathbf{m}) = \frac{\left|\sum_{i=1}^{N} Q_i^*(\mathbf{m}) P_i\right|^2}{\sum_{i=1}^{N} |Q_i(\mathbf{m})|^2 \sum_{i=1}^{N} |P_i|^2}, \tag{1}$$

where N is the number of hydrophones, and $Q_i(\mathbf{m})$ and P_i are the predicted and measured complex Fourier components at one frequency on the i'th hydrophone, and $*$ represents complex conjugation. $E(\mathbf{m})$ ranges from 0 to +1, with +1 representing a perfect match. This occurs when $Q_i(\mathbf{m}) = \alpha P_i$ for all i, where α is any complex constant.

An incoherent broadband object function can be obtained from a weighted average of equation 1 over frequency. If M equally weighted frequencies are included the multiple frequency object function is

$$E = \frac{1}{M} \sum_{k=1}^{M} \frac{\left|\sum_{i=1}^{N} Q_i^*(\omega_k) P_i(\omega_k)\right|^2}{\sum_{i=1}^{N} |Q_i(\omega_k)|^2 \sum_{i=1}^{N} |P_i(\omega_k)|^2}. \tag{2}$$

II.2 Coherent Object Functions (Waveform matching)

A method for full field coherent broadband inversion was suggested by researchers in the geophysics field [1]. This method involves matching synthetic waveforms $q_i(t)$, referred to as synthetic seismograms, with measured waveforms $p_i(t)$. Prediction of the synthetic waveforms at each of N hydrophones requires knowledge of the source waveform $s(t)$, and the waveguide's impulse response functions $g_i(t)$, $i = 1...N$. Synthetic waveforms are obtained by convolving the source waveform by the impulse response functions:

$$q_i(t) = s(t) * g_i(t). \tag{3}$$

The convolution can usually be done more efficiently in the frequency domain. By the convolution theorem, the Fourier transform of equation 3 can be written.

$$Q_i(\omega) = S(\omega) G_i(\omega), \tag{4}$$

where $Q_i(\omega)$, $S(\omega)$, and $G_i(\omega)$ are the Fourier transforms of $q_i(t)$, $s(t)$, and $g_i(t)$ respectively. A numerical model is used to predict $G_i(\omega)$ for each environmental model $\mathbf{m}$. The procedure for calculating $q_i(t)$ then is to take the inverse Fourier transform of the right side of equation 4: $q_i(t) = \Im^{-1}\left(S(\omega)G_i(\omega)\right)$.

Because we wish to match waveforms, a good choice for the object function is the correlation between synthetic and measured waveforms. In order to be consistent with the previously described object functions, we define a new object function as the normalized sum over the hydrophones of the squared correlations of measured and predicted time pressure series:

$$E = \frac{\left[\sum\limits_{i=1}^{N} \int q_i(t)p_i(t)dt\right]^2}{\sum\limits_{i=1}^{N} \int q_i^2(t)dt \sum\limits_{i=1}^{N} \int p_i^2(t)dt}. \tag{5}$$

Application of equation 5 requires that the absolute timing of the measured waveforms, referred to the time of source radiation, be known. Absolute timing is unknown unless the source signal is monitored at the source location, and the absolute time reference between this and the signals recorded at the array is established. A method for treating this problem, when absolute timing is not available, is to search for the time delay τ which maximizes the correlation between $q_i(t+\tau)$ and $p_i(t)$. This is done by replacing the correlation coefficient in the numerator of equation 5 by the correlation function. The object function is then calculated from the maximum of the correlation function:

$$E = \frac{\left[\max_\tau \sum\limits_{i=1}^{N} \int q_i(t+\tau)p_i(t)dt\right]^2}{\sum\limits_{i=1}^{N} \int q_i^2(t)dt \sum\limits_{i=1}^{N} \int p_i^2(t)dt}. \tag{6}$$

The search for optimum time delay is performed outside of the summation over hydrophones because the same delay is common to all hydrophones. This object function can be calculated in the frequency domain making use of the correlation and Parseval's theorems:

$$E = \frac{\left[\max_\tau \left(\Re\left\{\sum\limits_{i=1}^{N} \int Q_i^*(\omega)P_i(\omega)e^{i\omega\tau}d\omega\right\}\right)\right]^2}{\sum\limits_{i=1}^{N} \int |Q_i(\omega)|^2 d\omega \sum\limits_{i=1}^{N} \int |P_i(\omega)|^2 d\omega}. \tag{7}$$

The integrals over continuous frequency can be replaced by summation over discrete frequencies if the source signal is band limited. Similarly, if the signal contains discreet tonals, the summations can be limited to those frequencies only. In either case, with M discrete frequencies, equation 7 becomes

$$E = \frac{\left[\max_\tau \left(\Re\left\{\sum\limits_{i=1}^{N} \sum\limits_{k=1}^{M} Q_i^*(\omega_k)P_i(\omega_k)e^{i\omega_k\tau}\right\}\right)\right]^2}{\sum\limits_{i=1}^{N} \sum\limits_{k=1}^{M} |Q_i(\omega_k)|^2 \sum\limits_{i=1}^{N} \sum\limits_{k=1}^{M} |P_i(\omega_k)|^2}. \tag{8}$$

An interesting special case of equation 8 is when there is only a single frequency ω_0. For this case, equation 8 reduces to

$$E = \frac{\left[\max_\tau \left(\Re\left\{\sum\limits_{i=1}^{N} Q_i^*(\omega_0)P_i(\omega_0)e^{i\omega_0\tau}\right\}\right)\right]^2}{\sum\limits_{i=1}^{N} |Q_i(\omega_0)|^2 \sum\limits_{i=1}^{N} |P_i(\omega_0)|^2}$$

$$= \frac{\left| \sum_{i=1}^{N} Q_i^*(\omega_0) P_i(\omega_0) \right|^2}{\sum_{i=1}^{N} |Q_i(\omega_0)|^2 \sum_{i=1}^{N} |P_i(\omega_0)|^2}, \tag{9}$$

which is exactly equivalent to the Bartlett object function of equation 1. The absolute time uncertainty which required searching over time delays does not affect this last expression.

III Application of MFP

III.1 Environment and geometry models

The sediment at the seafloor was fine to medium grain sand. A standard analysis of strong head wave arrivals present in the data indicated the existence of at least two sub-bottom layers having compressional speeds of 1890±30 m/s and 2070±30 m/s. The top of the first of these layers is at least 150 m beneath the seafloor, and the thickness of this layer is approximately 200 m. The geoacoustic environment chosen for inversion modeling purposes consisted of three homogeneous elastic ocean bottom layers. Several of the parameters describing these layers were fixed at values obtained by matching the above layer compressional speeds with those from similar sediments categorized in Hamilton's compilation of seafloor sediment properties [2]. In reference to Hamilton's work, the sediment types attributed to the three layers were sand, gravel and morain. The fixed parameter values assigned to these layers are given in table 1.

Models representing the geoacoustic and geometry information to be inverted for were described by: $\mathbf{m} = \{ d_s, d_r, r, D, t_1, t_2, c_1, c_2, c_3 \}$, where d_s is the source depth, d_r is the depth of the top hydrophone, r is the horizontal source to array range, D is the bottom depth, t_1 and t_2 are the thicknesses of the top two layers, and c_1, c_2, and c_3 are the compressional speeds in the layers. Additionally, the true measured ocean sound speed profile was used, and the measured array tilt angle was fixed at 5°.

III.2 Inversion

Because computational time is the major limiting factor for broadband propagation calculations, the normal mode model ORCA [3] was chosen as the forward model. ORCA efficiently calculates broadband waveguide transfer functions by tracking mode eigenvalues through a range of frequencies. Increasing the specified frequency resolution of the transfer function causes very little change in computation time. This characteristic made it possible and efficient to apply the object functions at a large number of frequencies. For our broadband trials, 136 equally spaced frequencies between 10 Hz and 60 Hz were used. The inversion was performed on data from a single shot at approximate range 3.2 km. Execution time was approximately 90 s per model on a 150 MHz R4000 Silicon Graphics workstation. However, this time included calculation of all ranges (r) at once.

The inversion was performed using a grid search in which the incoherent broadband object function (equation 2) and the coherent broadband object function (equation 8) were evaluated for a set models defined by discrete values within specified limits for each of the components of $\mathbf{m}$. Additionally, the single frequency object function (equation 1) was evaluated at a frequency of 50 Hz for this same set of models. The discrete parameter values for $\mathbf{m}$ are defined by the "Minimum", "Maximum", and "Num Steps" entries in table 2. On

Layer	Shear speed	Density	P-atten	S-atten
1	100 m/s	1.5 g/cm^3	0.8 dB/λ	2.0 dB/λ
2	200 m/s	1.6 g/cm^3	0.6 dB/λ	1.5 dB/λ
3	300 m/s	1.7 g/cm^3	0.4 dB/λ	1.0 dB/λ

Table 1: Fixed parameter values for bottom layers.

Parameter	Minimum	Maximum	Num Steps	Inversion Result
r	3.1 km	3.3 km	5	3.25 km
D	405 m	425 m	3	425 m
d_r	70 m	85 m	3	75 m
t_1	160 m	240 m	3	200 m
t_2	160 m	240 m	3	200 m
c_1	1500 m/s	1700 m/s	7	1600 m/s
c_2	1700 m/s	2000 m/s	4	1700 m/s
c_3	1900 m/s	2300 m/s	5	2000 m/s

Table 2: Parameter search ranges and coherent broadband results.

each iteration, ORCA generates the broadband output transfer function $G_i(\mathbf{m})$. A predicted field spectrum $Q_i(\mathbf{m})$ is calculated according to equation 4. The source spectrum $S(\omega)$, used for this calculation, was obtained from high resolution SUS charge recordings collected during a controlled experiment [4].

The model which produced the largest broadband coherent object function value was determined. The parameter values for this model are given in table 2. As mentioned in section II.2, application of the broadband coherent object function is equivalent to waveform matching. To demonstrate this, the measured waveforms and predicted waveforms based on the best model are shown together in figure 1.

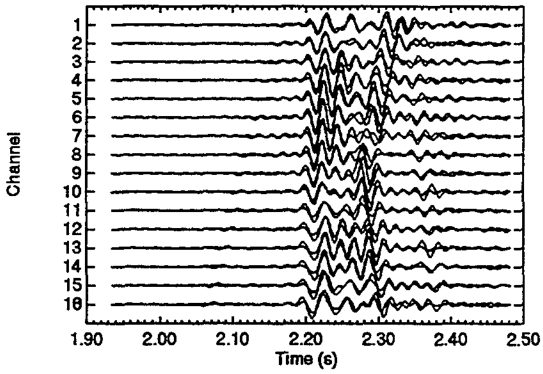

Figure 1: Modeled and predicted waveforms

III.3 Sensitivity Study

In order to obtain a measure of the robustness of the individual parameter estimates, we observed the amounts of change in the object functions' values as the parameters were varied through their respective search ranges. This was performed for all parameters of $\mathbf{m}$ with the exception of source depth, which was fixed at 196 m. When each parameter was varied, the remaining parameters were fixed at the optimal values given in table 2. The results of this study indicated that varying the parameters: source to receiver range, bottom depth, and array depth, causes significant change in all object functions. The broadband functions are particularly sensitive to the upper layer compressional speed, in contrast to the single frequency object function which is fairly insensitive to this parameter, and shows two local maxima over its search range. All three object functions are very insensitive to the remainder of the ocean bottom parameters. An interesting feature is that the single frequency and broadband incoherent functions have consistently and significantly higher values than the broadband coherent function. The reason for this feature is unknown.

III.4 Source Localization Problem

The sensitivity study indicated that all three object functions were relatively insensitive to the geoacoustic parameters of the lower two subbottom layers, but that they were sensitive to experimental geometry. Consequently, the methods are expected to perform well for the common problem of localizing a source. A test of MFP source localization was performed by fixing all geoacoustic parameters at the optimal values shown in table 2. The object functions were evaluated as a function of source depth and range from the array. The localizations tested a grid of 81 ranges, between 2.0 km and 4.0 km, by 41 depths, between 10 m, and 410 m. Contour plots of object function versus source range and depth are referred to as ambiguity surfaces. Figures 2, 3, and 4 show the ambiguity surfaces respectively for the single frequency, incoherent broadband and coherent broadband object functions. All three processors give very good results, with strong peaks at the source position: 3.25 km range and 196 m depth. The single frequency object function performs suprisingly well even though it uses significantly less acoustic field information. In fact, the peak at the source location is even sharper than that of both broadband functions. This is likely due to the fact that the broadband object functions included lower frequencies for which there is significant energy in the source spectrum. These lower frequencies have broader main lobes in the ambiguity surface.

Secondary lobes for the single frequency processor are distributed fairly evenly over the ambiguity surface. Both the broadband coherent and broadband incoherent processors have fewer, and smaller secondary lobes than the single frequency processor. Additionally, these lobes are elongated, showing some coupling between the range and depth parameters.

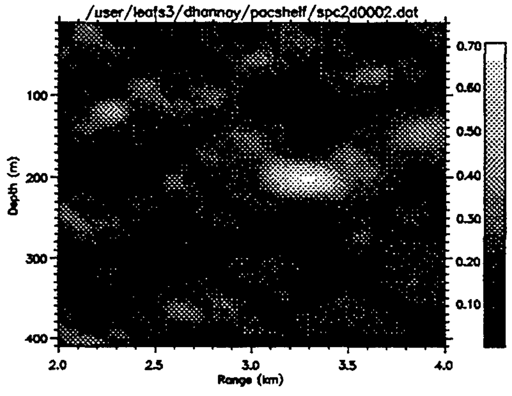

Figure 2: Single frequency Bartlett ambiguity surface

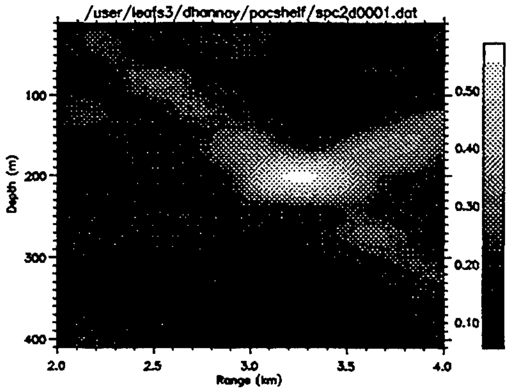

Figure 3: Incoherent Broadband ambiguity surface

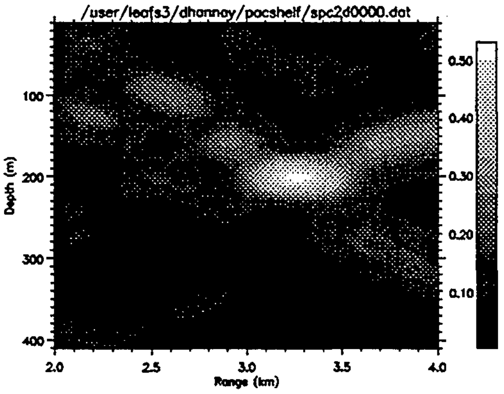

Figure 4: Coherent Broadband ambiguity surface

Conclusions

Matched Field Processing of transient SUS charge data was used to evaluate and compare coherent broadband, incoherent broadband, and single frequency object functions for the problem of geoacoustic parameter inversion. The evaluations were performed on data from a charge at 3.2 km, in a frequency band between 10 Hz and 60 Hz for the broadband processors, and at 50 Hz for the single frequency processor. The results of these evaluations indicate that all three processors are sensitive to experimental geometry, but none was found to be sensitive to the geoacoustic parameters for the second and third bottom layers. Only the broadband processors are sensitive to the compressional speed in the top ocean bottom layer.

An important feature of the coherent broadband processor, applied in this evaluation, is that it required searching over time delays. This step was necessary because the absolute timing of the measured signals with respect to source detonation was unavailable. If the source had been monitored and recorded with an absolute time reference to the signals on the array, searching over time delay would not be necessary and calculation of the full correlation function would not be required. More importantly, absolute propagation times as well as hydrophone to hydrophone differential times for all acoustic paths would be matched. Greater sensitivity to parameters affecting absolute propagation times, such as: range, ocean depth, and bottom layer thickness to layer speed ratios, would be expected.

References

[1] SEN, M. K., AND STOFFA, P. L. *Nonlinear One-Dimensional Seismic Waveform Inversion Using Simulated Annealing,* Geophysics **56**, No. 10, 1624-1638, (1991)

[2] HAMILTON, E. L. *Geoacoustic Modeling of the sea floor,* J. Acoust. Soc. Am. **62**, 1313-1340, (1980)

[3] WESTWOOD, E. K., TINDLE, C. T., AND CHAPMAN, N. R. *A Normal Mode Model for Acousto-Elastic Ocean Environments,* J. Acoust. Soc. Am. **95**, 2909 (1994)

[4] CHAPMAN, N. R. *Source levels of shallow explosive charges,* J. Acoust. Soc. Am. **84**, 679-802, (1988)

Successes and failures using MFP for the estimation of shallow water bottom properties

A. Tolstoy
Integrated Performance Decisions, Inc.
Honolulu HI 96816

14 JULY 1996

Abstract

The determination of shallow water bottom properties can be extremely difficult, but among the most promising methods are remote sensing techniques which exploit the sensitivity of propagating acoustic fields to such properties. In particular, there are the Matched Field Processing (MFP) based inverse techniques which consider both the acoustic phases and amplitudes in their hunt for estimates of such environmental properties as sediment layer thicknesses, densities, and sound-speeds. This paper focusses primarily on recent efforts by the author to estimate such parameters for two experimental data sets (Mediterranean Sea north of Elba and Hudson Canyon). However, an important but unresolved issue for *all* the inverse techniques (not just the MFP based ones) remains that of uniquely determining the "true" or "solution" set of parameter values.

Introduction

Matched Field Processing (MFP) has recently been the explicit basis for a variety of methods for the estimation of shallow water bottom properties. The particular MFP approach to be discussed here is similar to the MFP tomographic method used for the estimation of deep ocean sound-speed profiles, except that now more parameters need to be determined (four to six per sediment layer excluding elasticity considerations), the frequencies to be processed need to be higher (50 to 500Hz), the source to array ranges are much shorter (less than 20km), and the field sensitivities to the individual parameters vary by scenario.

In this paper we process and analyze *experimental* test data from two shallow water scenarios: one in the Mediterranean Sea north of Elba and one in the Hudson Canyon off the New Jersey Continental shelf. For each we assume no range or azimuthal variability, a single source, and a single nearly vertical array. We use the KRAKEN normal mode model[2] and concentrate on the performance of the Minimum Variance (MV) processor[4].

I Discussion

The Mediterranean Sea data involved shot sources which produced a broadband of frequencies (from 60-420Hz) displaying strong components for frequencies around 100Hz over the entire array (we selected a uniform subarray of 9 phones at 8m spacings with the top phone nominally at 35m depth). The processing and inversion were performed at 100.6Hz and eventually assumed two sediment layers over a half-space (for a total of eight environmental parameters to be determined). This resulted in several very good MV peak values (approximately 0.5 out of a maximum possible of 1.0) near the "known" source location (additionally refined by the processing). The MV based method was seen to be quite sensitive to phone location errors, and so, an iterative algorithm was introduced to allow for the inclusion of phone coordinates as parameters.

Subsequently, phone range displacements of less than 1.0m resulted in improved MV peak values up to 0.7. Complete details can be found in Tolstoy (1996). Unfortunately, these new parameters do not result in such strong MFP values at neighboring frequencies, suggesting that the "true" set of values has yet to be determined. It should be noted that the Linear processor peaks were frequently near the maximum value 1.0. The to-be-expected tradeoff is that while an MV based method is far more sensitive to measurement errors, it can more easilty suppress sidelobe solutions. It seems that the Linear processor has such an easy time finding peaks near 1.0 that only a high resolution method may have sufficient sidelobe suppression to find a "true" solution. Perhaps we can generally conclude that if an inversion method produces estimates which do *not* result in strong MV peak values, then we have a good indication of the presence of some kind of unknown mismatch, and the inversion results should be suspect.

Some of the Hudson Canyon data have also been processed through the MFP MV inversion software where these data were selected because they are extremely well documented[1], because they are readily available by anonymous ftp, and because earlier inversion efforts have already made excellent progress in the broadband processing of those data for the purposes of source tracking[3]. For our processing we used a uniform subarray (an 8 phone subset at 7.5m spacings with the top phone at 19.95m) and selected the 50Hz CW signal at a nominal range of 4.58km. After the inversion, we arrived at a six parameter set (single sediment layer over a half space) which produced an MV peak value of 0.76 (and a number of sets producing values near 0.7 with Linear processor peaks at 1.00). After including iterations for phone displacement we finally arrived at a top MV peak value of 0.83. More details can be found in Tolstoy and Michalopoulou (1996). Additional frequencies remain to be examined. However, it is not likely that we have yet found the "true" solution set for these data.

At this point it seemed like a good idea to pause rather than blindly continue the searches for more parameter sets. The MV based MFP method discussed here requires progressive searching through parameter spaces which are enormous (4 to 6 parameters per layer each with dozens to hundreds of possible discrete values, plus simultaneous refinements for source range and depth, and iterative refinements for array phone coordinates). Moreover, the spaces are very non-convex making the search for a global maximum exceedingly difficult. Unfortunately, even for these very large search spaces, one major uncertainty (for both these data sets) remains: have we modeled each situation appropriately, i.e., does each search space encompass the "true" environment? Or do we need to:

- search over *larger* intervals for our parameter values?
- introduce *more* environmental variables, e.g., more sediment layers?
- consider more errors, e.g., in the assumed water column sound-speed profile?
- consider range dependence?

Conclusions

When applied to the two sets of experimental test data discussed above, an important result of the *single* frequency inversion is:

- strong processing power peaks for the highly sensitive MV processor, i.e., peaks greater than 0.5.

The additional considerations of refined source location plus array deformation (non-uniform range shifts) result in even larger MV processing peaks. The corresponding Linear processor showed MFP peak values of 1.00. However, the strong MV peaks did not generalize across neighboring frequencies suggesting that the "true" parameters have not yet been found.

A number of critical issues remain unresolved. In particular:

- How realistic are the environmental parameters estimated by this (or any) MFP technique? How close are they to the "true" values?

- No measurement technique offers sufficient resolution of the bottom parameter values with respect to the MV MFP method discussed here. So, *how* do we validate the inversion results? Will it be necessary and/or sufficient to achieve results with high MV peak values (greater than 0.5 out of a maxmimum of 1.0) over a range of frequencies?
- How valid are the suggested array deformations? Simulations under ideal conditions converge to "true" array shapes, but this is not the case when errors (such as those due to environmental mismatch) are present.
- When do we stop the search?

References

[1] CAREY, W.M., DOUTT, J., EVANS, R.B., AND DILLMAN, L.M. Shallow-water sound transmission measurements on the New Jersey continental shelf *IEEE J. Oceanic Eng. 20* (1995), 321–336.

[2] JENSEN, F.B., KUPERMAN, W.A., PORTER, M.B., AND SCHMIDT, H. *Computational Ocean Acoustics*. Am. Inst. Physics, 1994.

[3] MICHALOPOULOU, Z-H., AND PORTER, M.B. Source tracking in the Hudson Canyon *J. Computat. Acoust. 1* (1996), to appear.

[4] TOLSTOY, A. *Matched Field Processing for Underwater Acoustics*. World Scientific Pub., 1993.

[5] TOLSTOY, A. Using matched field processing to estimate shallow water bottom properties from shot data taken in the Mediterranean Sea. *IEEE J. Oceanic Eng.* (1996), to appear.

[6] TOLSTOY, A. AND MICHALOPOULOU, Z-H. Shallow water bottom properties via MFP on a vertical array. *Proceedings of the 3rd European Conference on Underwater Acoustics*. ed. J. Papadakis, Crete University Pr., 1996.

Matched Field Inversion for Array Shape Estimation

W.S. Hodgkiss, D.E. Ensberg, J.J. Murray, and G.L. D'Spain

Marine Physical Laboratory
Scripps Institution of Oceanography
La Jolla, CA 92093-0701

N.O. Booth and P.W. Schey

Ocean and Atmospheric Sciences Division
NCCOSC RDTE Div. Code 881
San Diego, CA 92152-5001

Abstract

Accurate knowledge of array shape is essential for carrying out full wavefield (matched field) processing. Direct approaches to array element localization (AEL) include both non-acoustic (tilt-heading sensors) and acoustic (high frequency, transponder-based navigation) methods. The low frequency signature emitted from a distant source also can be used in an inversion approach to determine array shape. The focus of this paper is on a comparison of the array shape results from these three different methods using data from a 120 m aperture vertical array deployed during SWellEx-3 (Shallow Water evaluation cell Experiment #3). Located 2 m above the shallowest array element was a self-recording package equipped with depth, tilt, and direction-of-tilt sensors, thereby permitting AEL to be performed non-acoustically. Direct AEL also was performed acoustically by making use of transponder pings (in the vicinity of 12 kHz) received by high frequency hydrophones spaced every 7.5 m along the vertical array. In addition to these direct approaches, AEL was carred out using an inversion technique where matched-field processing was performed on a multi-tone (50-200 Hz), acoustic source at various ranges and azimuths from the array. As shown, the time-evolving array shape estimates generated by all three AEL methods provide a consistent picture of array motion throughout the 6 hour period analyzed.

[Work supported by ONR, Code 321US.]

Matched Field Inversion for Array Shape Estimation

W.S. Hodgkiss

D.E. Ensberg

J.J. Murray

G.L. D'Spain

Marine Physical Laboratory
Scripps Institution of Oceanography
La Jolla, CA 92093-0701

N.O. Booth

P.W. Schey

Ocean and Atmospheric Sciences Division
NCCOSC RDTE Div. Code 881
San Diego, CA 92152-5001

14 June 1996

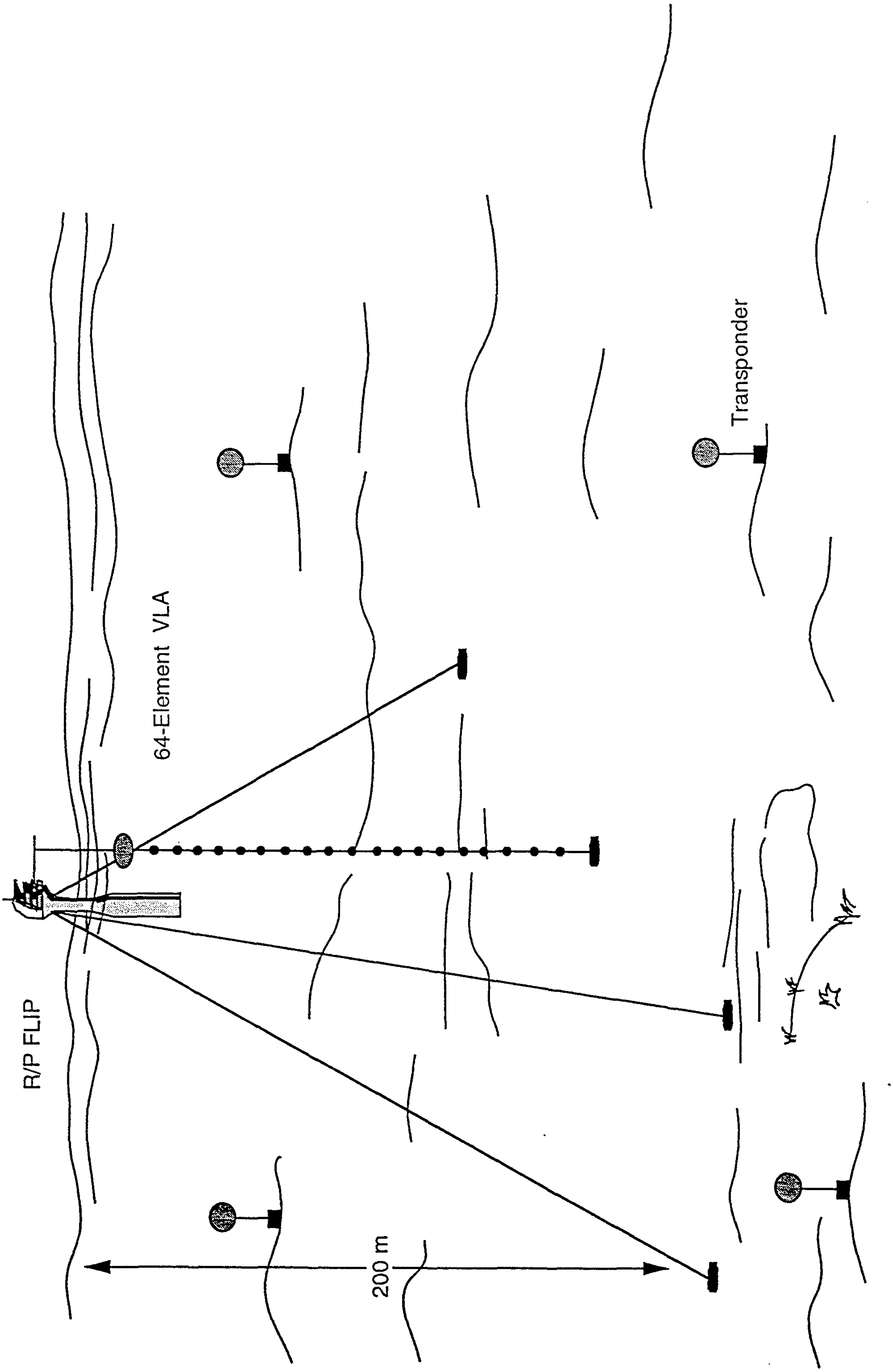
R/P FLIP
64-Element VLA
Transponder
200 m

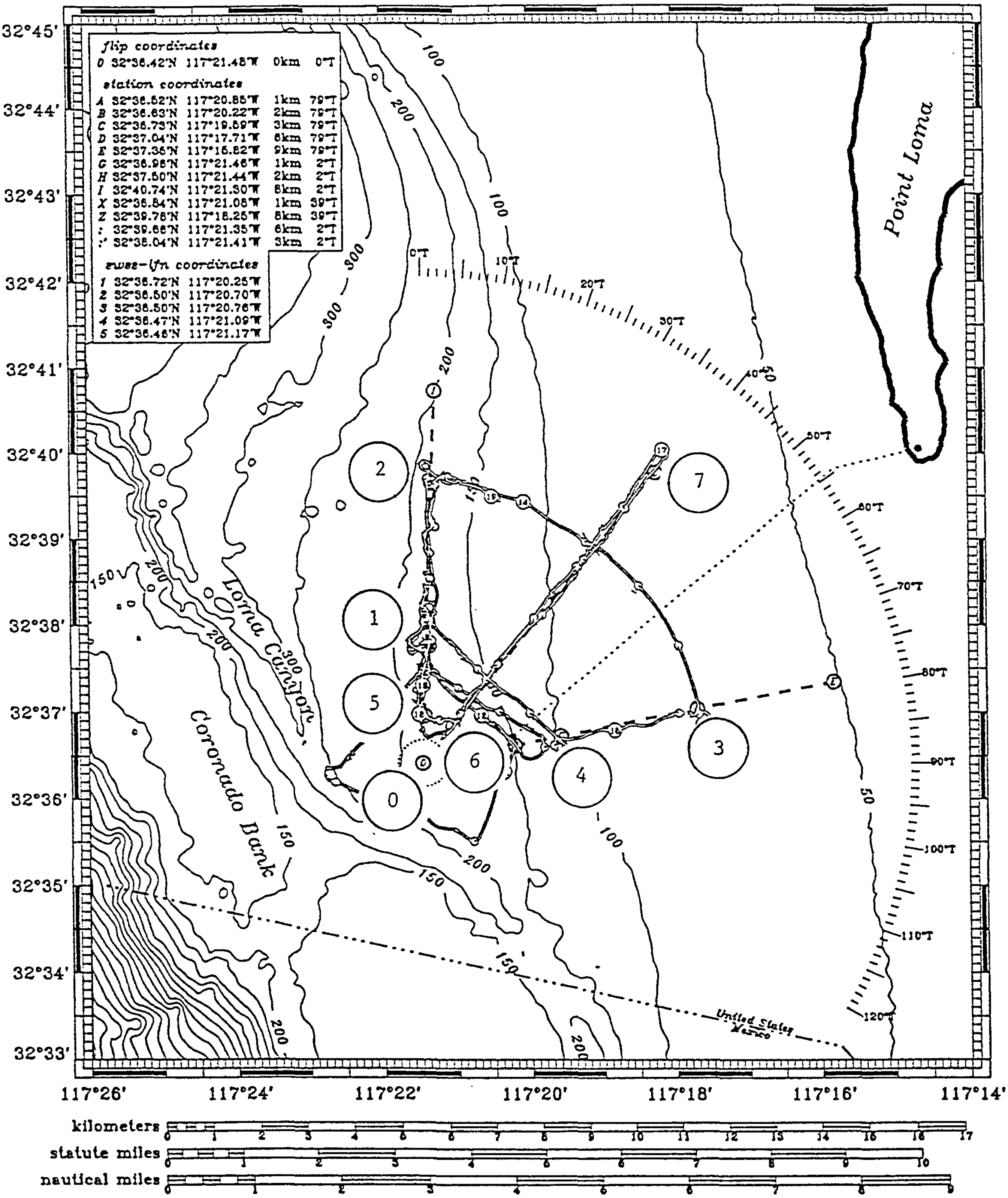

flip coordinates

0	32°36.42'N	117°21.48'W	0km	0°T

station coordinates

A	32°36.52'N	117°20.86'W	1km	79°T
B	32°36.63'N	117°20.22'W	2km	79°T
C	32°36.73'N	117°19.59'W	3km	79°T
D	32°37.04'N	117°17.71'W	6km	79°T
E	32°37.36'N	117°16.82'W	9km	79°T
G	32°36.96'N	117°21.46'W	1km	2°T
H	32°37.50'N	117°21.44'W	2km	2°T
I	32°40.74'N	117°21.30'W	8km	2°T
X	32°36.84'N	117°21.08'W	1km	39°T
Z	32°39.78'N	117°18.25'W	8km	39°T
:	32°39.66'N	117°21.35'W	6km	2°T
:'	32°38.04'N	117°21.41'W	3km	2°T

swss-lfn coordinates

1	32°36.72'N	117°20.25'W
2	32°36.50'N	117°20.70'W
3	32°36.50'N	117°20.76'W
4	32°36.47'N	117°21.09'W
5	32°36.46'N	117°21.17'W

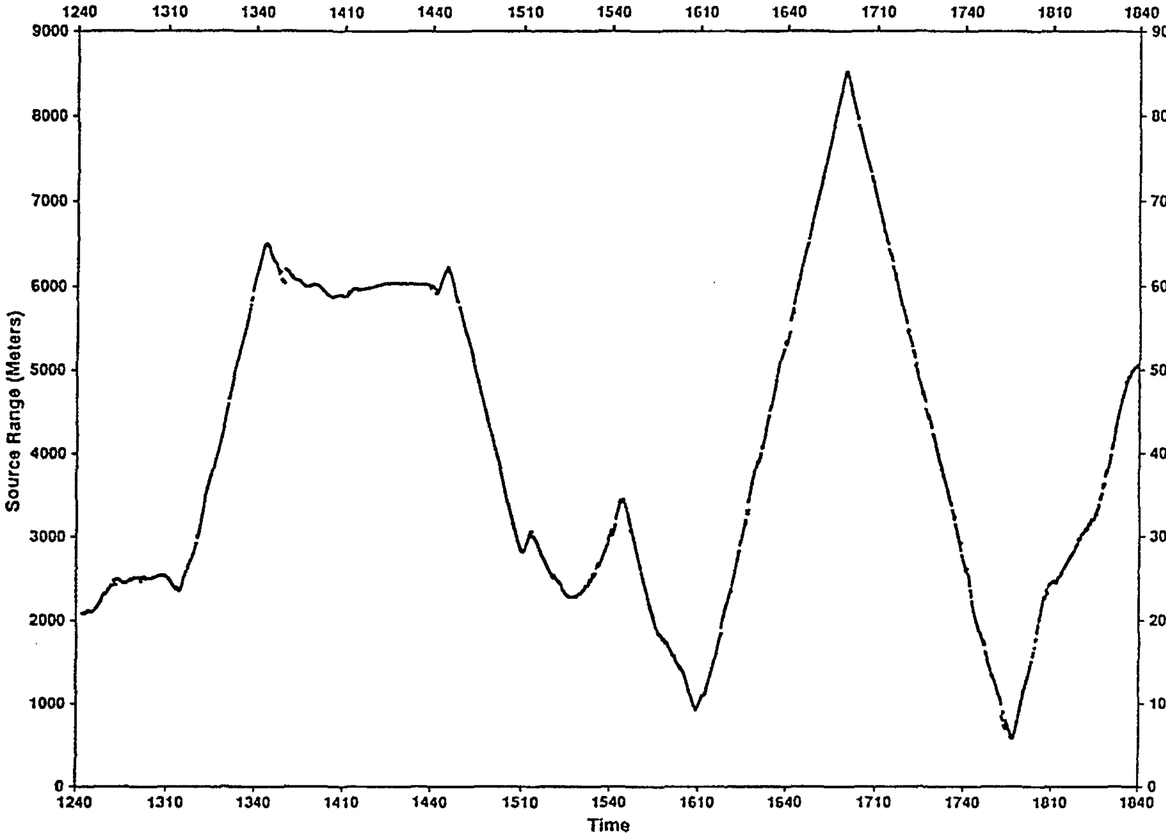
1240
1310
1340
1410
1440
1510
1540
1610
1640
1710
1740
1810
1840
9000
8000
7000
6000
5000
4000
3000
2000
1000
0
Source Range (Meters)
Time

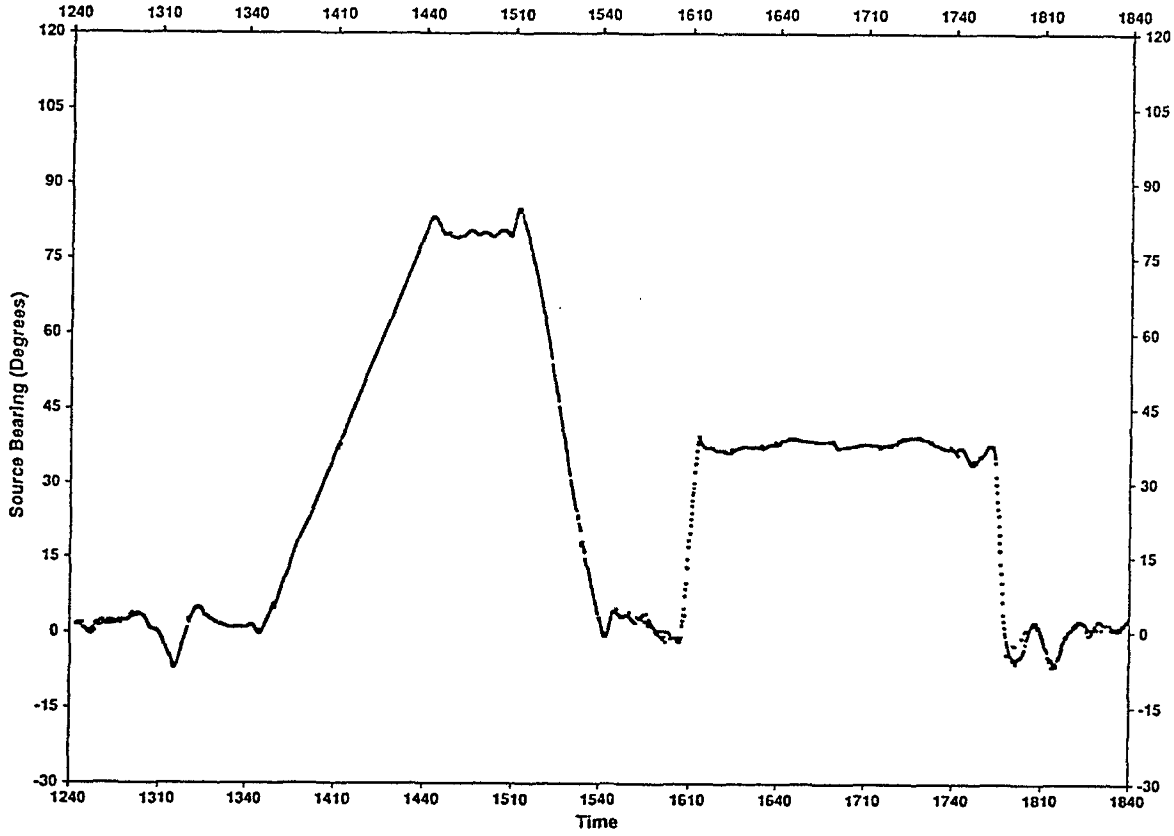
1240
1310
1340
1410
1440
1510
1540
1610
1640
1710
1740
1810
1840
120
105
90
75
60
45
30
15
0
-15
-30
Source Bearing (Degrees)
Time

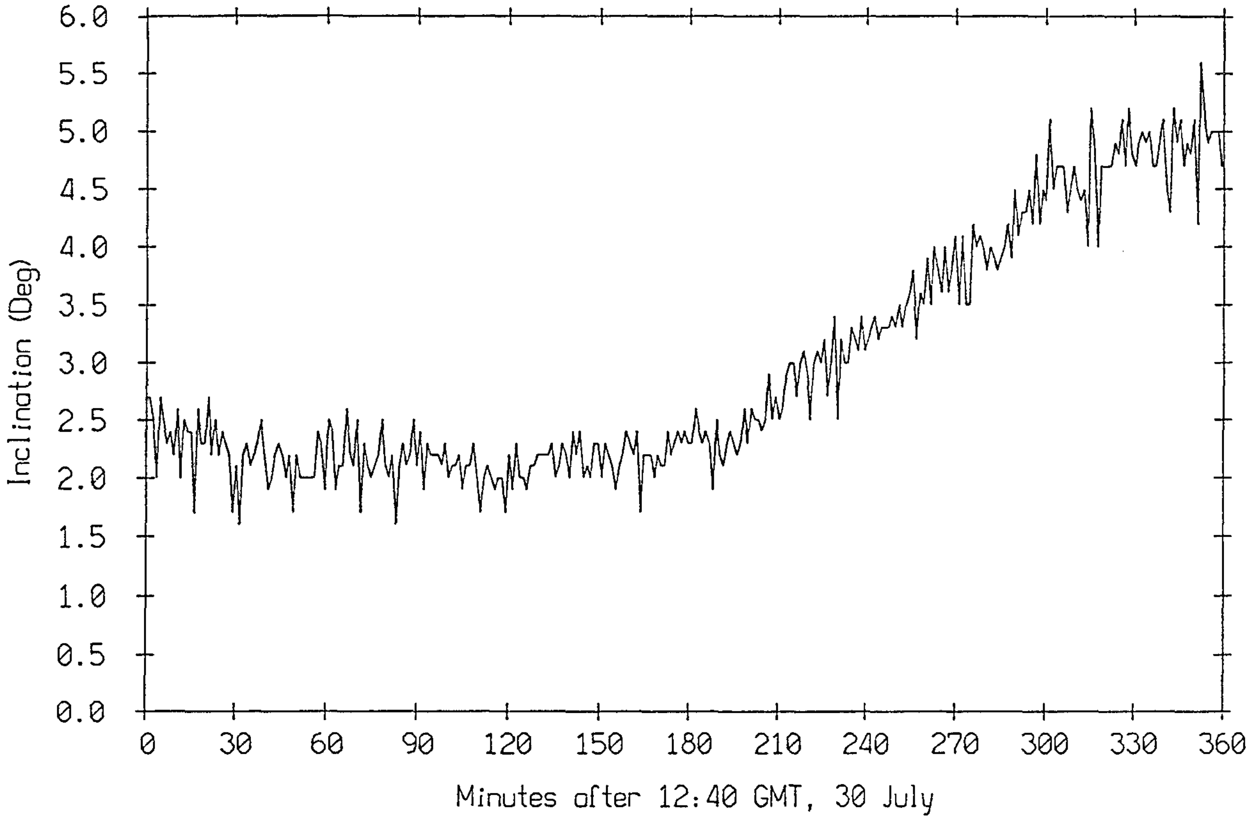
6.0
5.5
5.0
4.5
4.0
3.5
3.0
2.5
2.0
1.5
1.0
0.5
0.0
Inclination (Deg)
0
30
60
90
120
150
180
210
240
270
300
330
360
Minutes after 12:40 GMT, 30 July

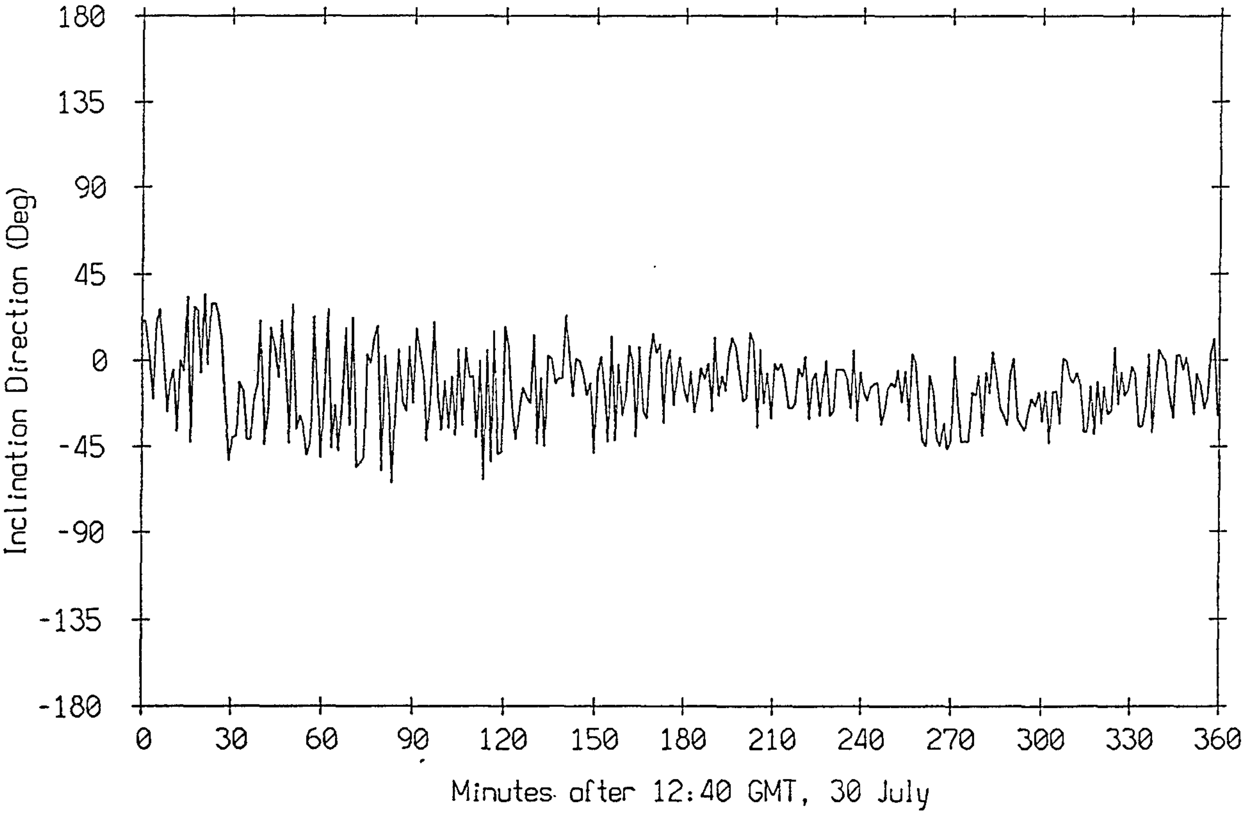
180
135
90
45
0
-45
-90
-135
-180
Inclination Direction (Deg)
0
30
60
90
120
150
180
210
240
270
300
330
360
Minutes after 12:40 GMT, 30 July

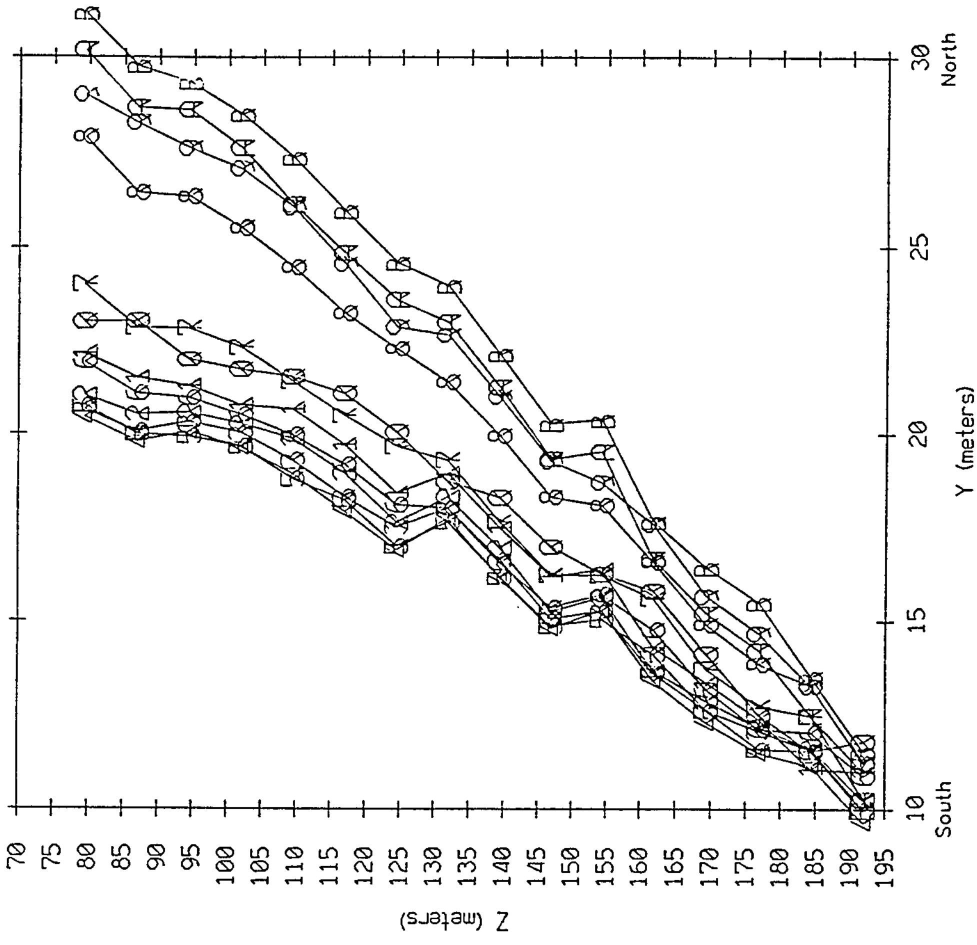
Z (meters)
70
75
80
85
90
95
100
105
110
115
120
125
130
135
140
145
150
155
160
165
170
175
180
185
190
195
Y (meters)
10
South
15
20
25
30
North

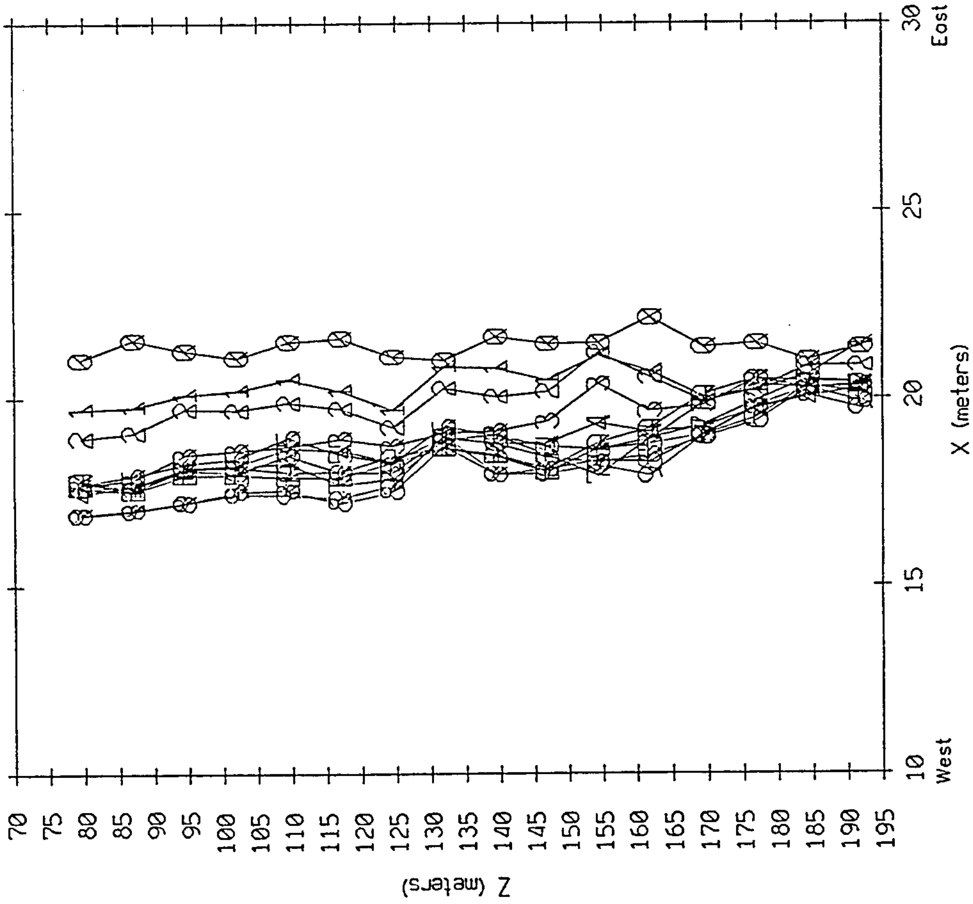
Z (meters)
70
75
80
85
90
95
100
105
110
115
120
125
130
135
140
145
150
155
160
165
170
175
180
185
190
195
X (meters)
10
West
15
20
25
30
East

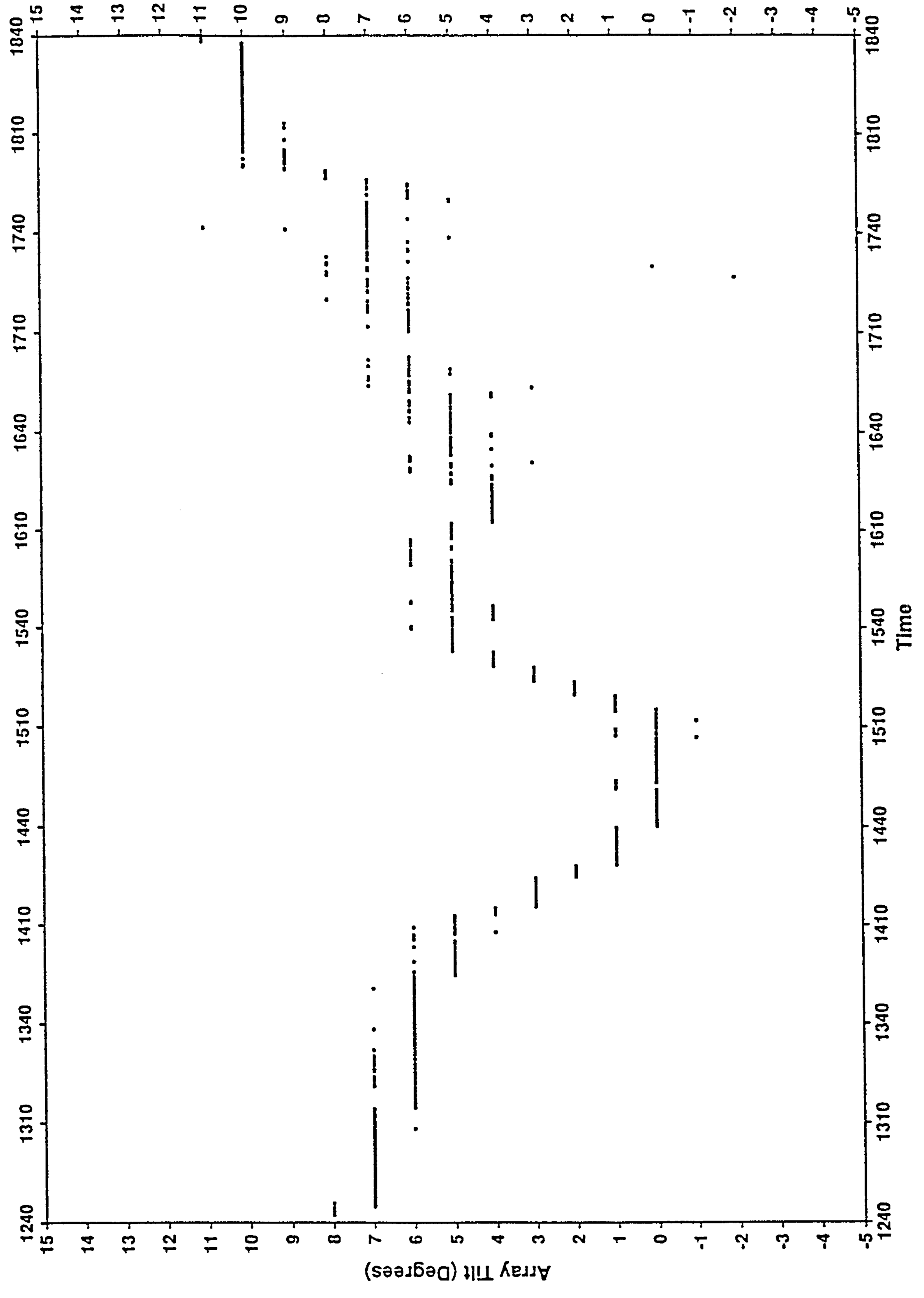
Array Tilt (Degrees)
Time
1240
1310
1340
1410
1440
1510
1540
1610
1640
1710
1740
1810
1840
-5
-4
-3
-2
-1
0
1
2
3
4
5
6
7
8
9
10
11
12
13
14
15

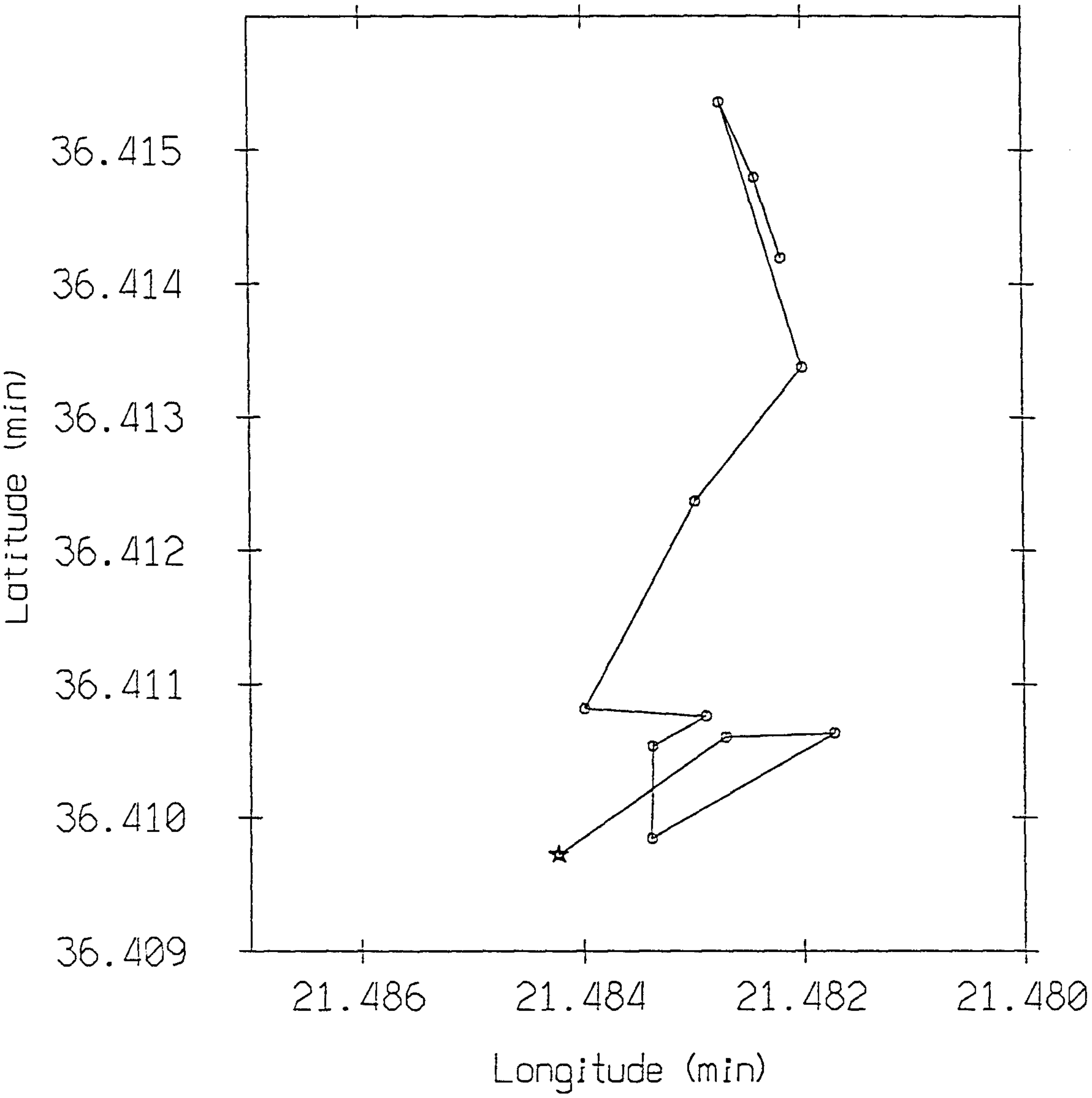

36.415
36.414
36.413
36.412
36.411
36.410
36.409
Latitude (min)
21.486
21.484
21.482
21.480
Longitude (min)

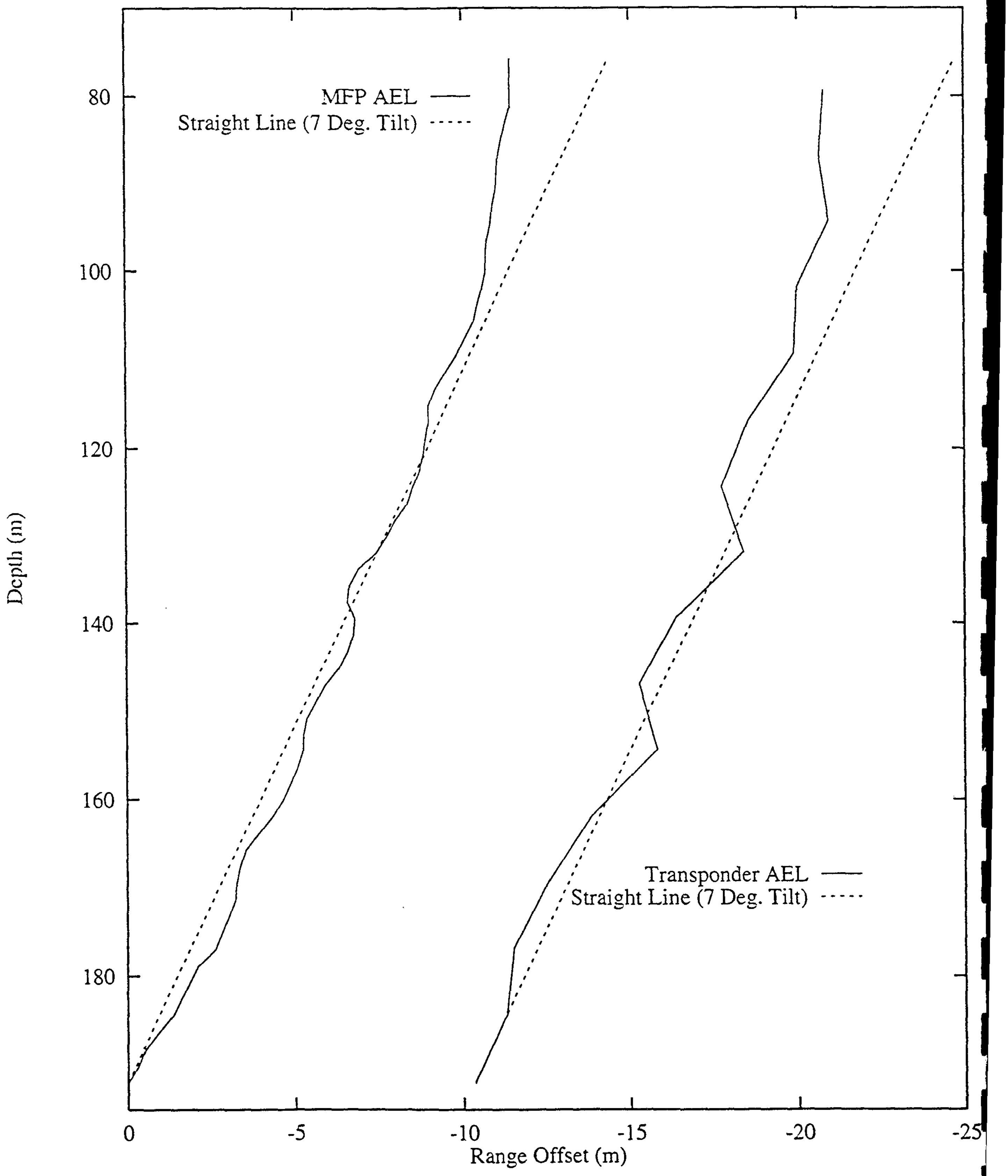

MFP AEL
Straight Line (7 Deg. Tilt)
Transponder AEL
Straight Line (7 Deg. Tilt)
Depth (m)
80
100
120
140
160
180
0
-5
-10
-15
-20
-25
Range Offset (m)

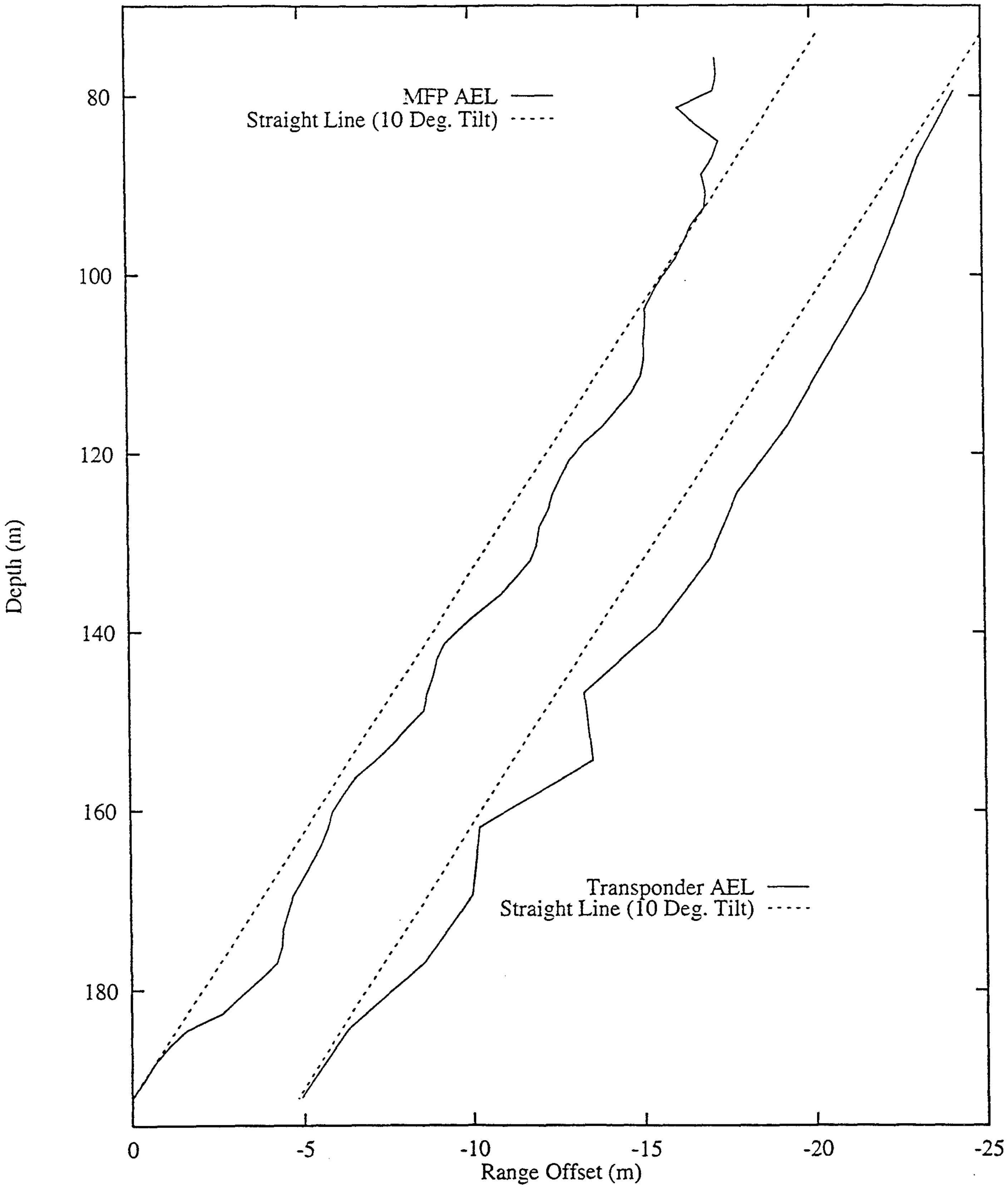
MFP AEL
Straight Line (10 Deg. Tilt)
Transponder AEL
Straight Line (10 Deg. Tilt)
Depth (m)
80
100
120
140
160
180
Range Offset (m)
0
-5
-10
-15
-20
-25

Algorithms for Matched-Field Inversion: Comparison and Performance

Cedric Zala
Barrodale Computing Services Ltd.
Victoria, B.C., Canada
and
John Ozard
EDRD/DREA
Victoria, B.C., Canada

14 JULY 1996

Abstract

This simulation study examined several optimization-based approaches to inversion for geoacoustic parameters. Using the program Orca to compute normal mode models for realistic range-independent waveguides, the sensitivities of and the dependencies between several of the geoacoustic parameters were examined. Two-dimensional plots of the normalized Bartlett processor as a function of parameter pairs were often multimodal and of complex structure, and certain parameter pairs exhibited interdependence. Using a rapidly evaluated model function with similar overall characteristics (i.e., multiple local optima, different parameter sensitivities, and parameter interdependence), a comparison of inversion algorithms was done; these included simulated annealing, a genetic algorithm, and a combined random search/local optimization approach. The performance of several local optimization algorithms was also compared using this model function. Based on the results, a strategy was adopted which consisted of an initial random search stage followed by local optimization (using a quasi-Newton optimizer) of those best matches found during the search. This two-stage technique was implemented in an MFP/MFI software system written in IDL.

I Introduction

Successful MFP requires a knowledge of the bathymetry and the existence of a suitable geoacoustic model for the sound speed profile and the bottom characteristics. In practice, these parameters are known only approximately, and it is desirable to obtain more accurate estimates to improve the effectiveness of MFP. This aim may be achieved through matched-field inversion (MFI) of data obtained using a source at a series of known locations in the environment. Development of effective inversion procedures requires the use of appropriate numerical optimization techniques suited to the nature of the multimodal multidimensional matching functional, or ambiguity surface, to be optimized.

II Pairwise Plots

Using a vertical 20-element array, and the normal mode program Orca [1] to model the acoustic fields, the relations between various parameter pairs of geoacoustic models typical of the Pacific and Arctic continental shelves were examined. An example of these results, showing the normalized Bartlett processor output as a function of channel depth and compressional sound speed in the sediment layer, is shown in Figure 1. This and other plots indicated the multimodal nature of the function to be optimized, the wide range of sensitivities of the various parameters, and the existence of complex interdependencies between certain parameters.

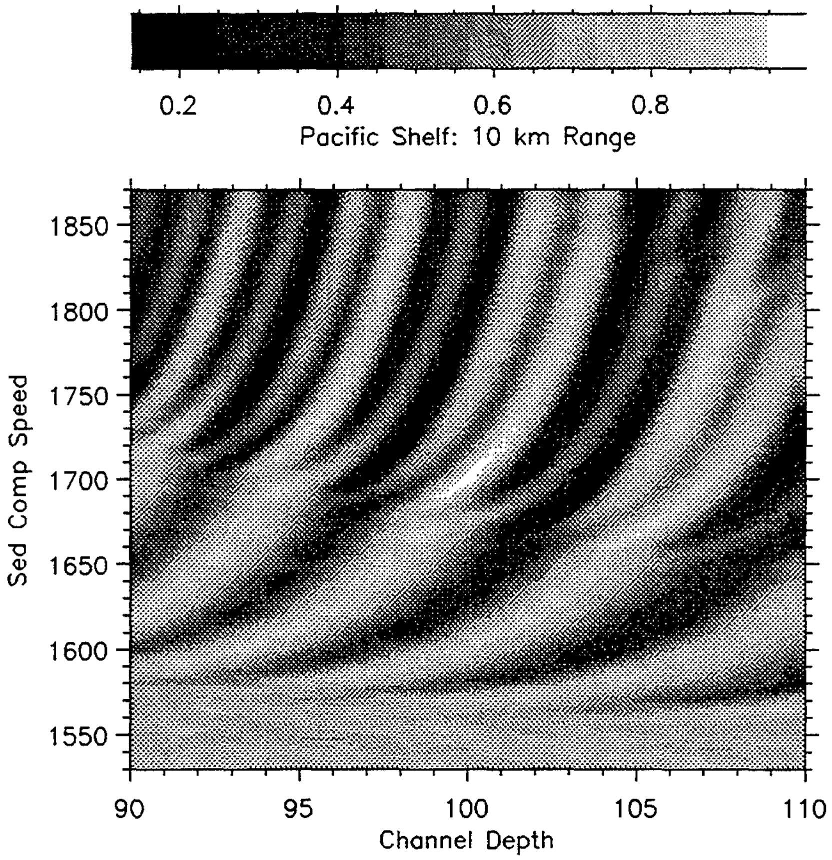

Figure 1: 2-D plot of normalized Bartlett processor output as a function of channel depth and compressional sound speed. The true values (100 m and 1700 m/s) are in the centre of the plot.

III Comparison of Optimization Techniques using Model Functions

To fully compare the performance of various algorithms for inversion using a geoacoustic modelling program would be extremely time-consuming. Instead, a model function with the properties described above was designed for use in this comparison. The form of this function was

$$F(\mathbf{x}) = \frac{1}{K}\sum_{k=1}^{K}\cos^2[2\pi\{(\mathbf{L}(\mathbf{x}-\mathbf{x}_0)\cdot\mathbf{f}_k)\}],$$

where
$\mathbf{x}$ is an n-element vector of parameters,

$\mathbf{x}_0$ is a vector of true values for the n parameters,
K is the number of cosine terms,
$\mathbf{f}_k$ is the kth vector of frequencies, with one element of $\mathbf{f}_k$ per parameter, and
$\mathbf{L}$ is the lower triangle of the Cholesky decomposition of a *parameter interdependency matrix* $\mathbf{R}$, with

$$\mathbf{R} = \begin{bmatrix} 1 & \rho_{12} & \rho_{13} & \cdots & \rho_{1n} \\ \rho_{12} & 1 & \rho_{23} & \cdots & \rho_{2n} \\ \rho_{13} & \rho_{23} & 1 & \cdots & \rho_{3n} \\ \vdots & \vdots & \vdots & \ddots & \vdots \\ \rho_{1n} & \rho_{2n} & \rho_{3n} & \cdots & 1 \end{bmatrix}.$$

This function has a global maximum of 1.0 when $\mathbf{x} = \mathbf{x}_0$. Parameter sensitivity was simulated in each run by taking the frequency values f_{kj} corresponding to the jth parameter as realizations from a uniform distribution on $[-u_j, +u_j]$. Increasing u_j results in an increase in sensitivity. Typically, four to six parameters were used, with a factor of two or three between the successive values of u_j, to give a wide range of sensitivities. The bounds for the parameters were set to give approximately 10–20 peaks in the 2-D surfaces computed for the two most sensitive parameters.

Using a large number of realizations of this functional form (i.e., a different set of values of the $\mathbf{f}_k$ for each run), simulated annealing [2] and a genetic algorithm [3] were compared for their rate of reduction in the function value, convergence of the parameters, and success in localizing the parameters to the region of the true global optimum. It was found that the performance of simulated annealing and the genetic algorithm was quite similar, but their rates of convergence were very slow. Furthermore, their success in identifying a point in the region of the true optimum was less than that of a simple random search.

In practice, function evaluations (especially those based on PE) are time-consuming, and it is essential to develop a strategy which will have a rapid rate of convergence, as well as a high likelihood of identifying the global optimum. In view of the above results, a two-stage procedure was examined, in which the first stage involved a random search, and the second stage involved a number of local optimizations, each starting from one of the best matches found during the search stage. This two-stage approach had the advantages of: (1) the most thorough sampling of the parameter space, with the resulting highest probability of identifying a point in the region of the true optimum; (2) rapid convergence of the local optimization technique; and (3) redundancy, when several different starting points are observed to converge to the same optimum.

Two local optimization algorithms were examined for their effectiveness in this application: the Powell direction set method and the quasi-Newton technique [4]. It was found that for independent parameters (i.e., $\rho_{ij} = 0$ for $i \neq j$), the direction set method converged slightly faster, but when the parameters were strongly interdependent, the quasi-Newton procedure gave much faster convergence.

The overall result of these experiments, using realizations of the model function above, was the adoption of a two-stage strategy involving a random search followed by applying the quasi-Newton technique to optimize the best matches found during the search.

IV Effectiveness of Two-Stage Approach in Geoacoustic Inversion

An example of the performance of this two-stage approach is shown in Figures 2 and 3. Here Orca was used to compute normal mode models for an Arctic 650-m deep channel at 25 Hz; the true values and the bounds on the parameters to be optimized are shown in Table 1.

The two-stage approach was applied to estimate these geoacoustic parameters. In the first stage, 500 function evaluations were performed, with parameter values independently randomly distributed between the bounds specified in Table 1. In the second stage, the sets of parameters corresponding to the 10 best matches (lowest function values) were used as starting points for optimization.

Table 1: Geoacoustic parameters (true values and bounds for inversion) for the Arctic environment used for the parameter inversion illustrated in Figures 2 and 3.

Parameter varied	True	Bounds
Source-array range (km)	5	4.9 - 5.1
Water depth (m)	650	580 - 720
Sediment compressional speed (m/s)	1800	1620 - 1980
Sediment shear speed (m/s)	300	270 - 330
Sediment compressional atten (dB/wl)	0.1	0.07 - 0.13
Sediment shear atten (dB/wl)	0.1	0.07 - 0.13
Sediment thickness (m)	10	5 - 15
Basement compressional speed (m/s)	2250	2025 - 2475
Basement shear speed (m/s)	800	720 - 880
Basement compressional atten (dB/wl)	0.05	0.03 - 0.07
Basement shear atten (dB/wl)	0.20	0.15 - 0.25
Array tilt (°)	0	−5 - 5

The results in Figure 2 show that for 6 of the 10 best starting estimates, the function values rapidly converged to zero during the optimization. For these cases, essentially perfect matches were obtained at a computational cost of 20–30 function evaluations per parameter during each optimization stage.

The results in Figure 3 show the evolution of the 12 individual parameters listed in Table 1 during optimization (within each plot, the line types correspond to those in Figure 2). It is evident that there was a wide range of sensitivities among the parameters, with range, depth, sediment thickness, basement compressional speed, and array tilt being most sensitive under these conditions, and the others being almost invariant as optimization proceeded. For the sensitive parameters, multiple instances of convergence of the different starting estimates to (approximately) the same final values were apparent; these corresponded to the convergences of the function values to zero as observed in Figure 2.

Within the sensitive parameters, different convergence properties were also observed. For example, array tilt converged rapidly to the true value in all cases, while range converged more slowly and only approached the true value in 7 of the 10 cases. In practice, the combination of multiple convergences of the sensitive parameters to similar values, combined with low function values under these conditions, should provide an effective means of identifying the most appropriate estimates for these parameters.

These results confirm the effectiveness of the two-stage strategy (i.e., random search followed by optimization of best matches) for geoacoustic parameter inversion.

References

1. E. K. Westwood, C. T. Tindle and N. R. Chapman, "A normal mode model for acoustoelastic ocean environments," (submitted to J. Acoust. Soc. Am.).

2. M. D. Collins and W. A. Kuperman, "Focalization: Environmental focusing and source localization," J. Acoust. Soc. Am. **90**, 1410–1422 (1991).

3. P. Gerstoft, "Inversion of seismoacoustic data using genetic algorithms and *a posteriori* probability distributions", J. Acoust. Soc. Am. **95**, 770–782 (1994).

4. W. H. Press, B. P. Flannery, S. A. Teukolsky and W. T. Vetterling, *Numerical Recipes: The Art of Scientific Computing,* Cambridge Unversity Press, Cambridge, 1989.

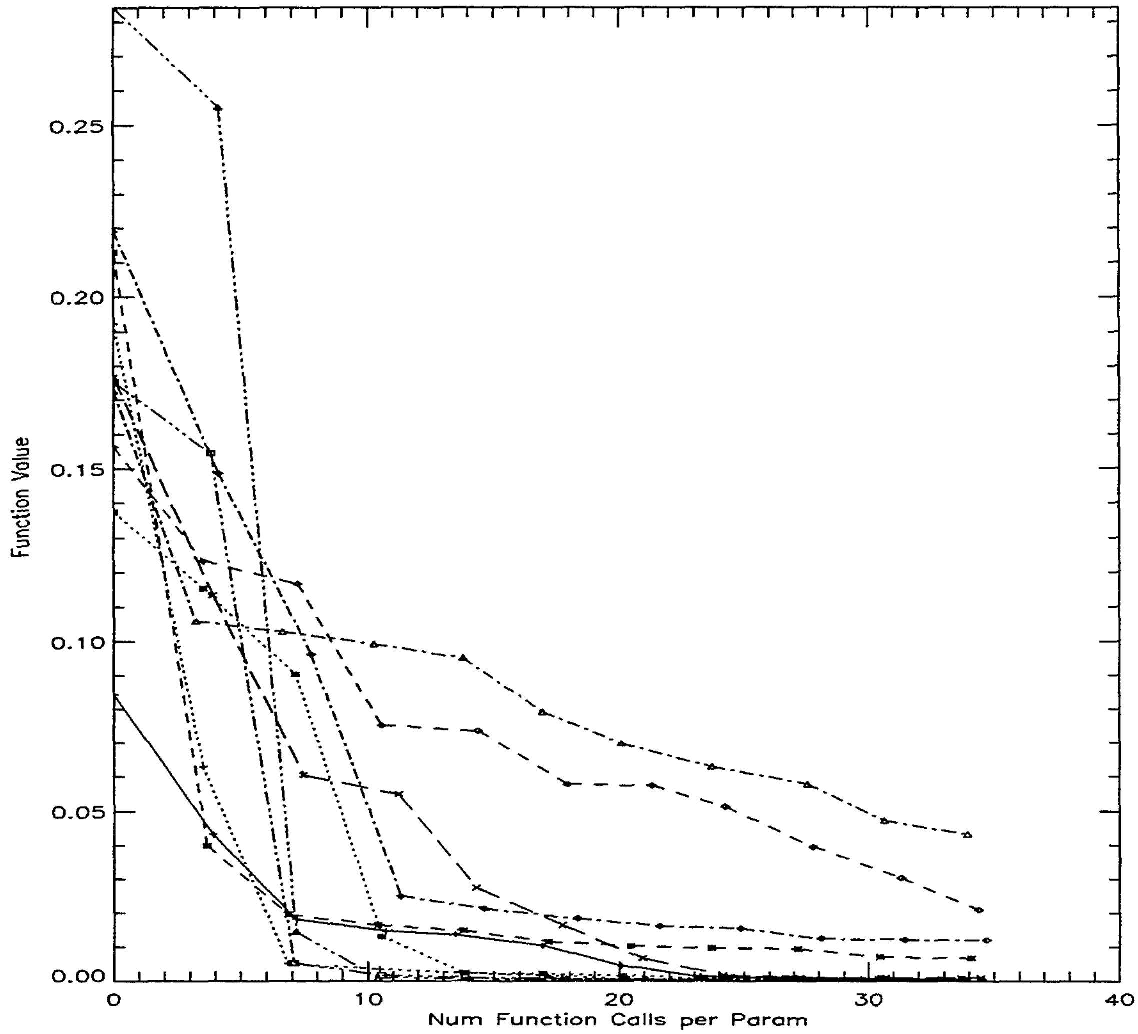

Figure 2: Decrease in function values during local optimization of 10 best matches.

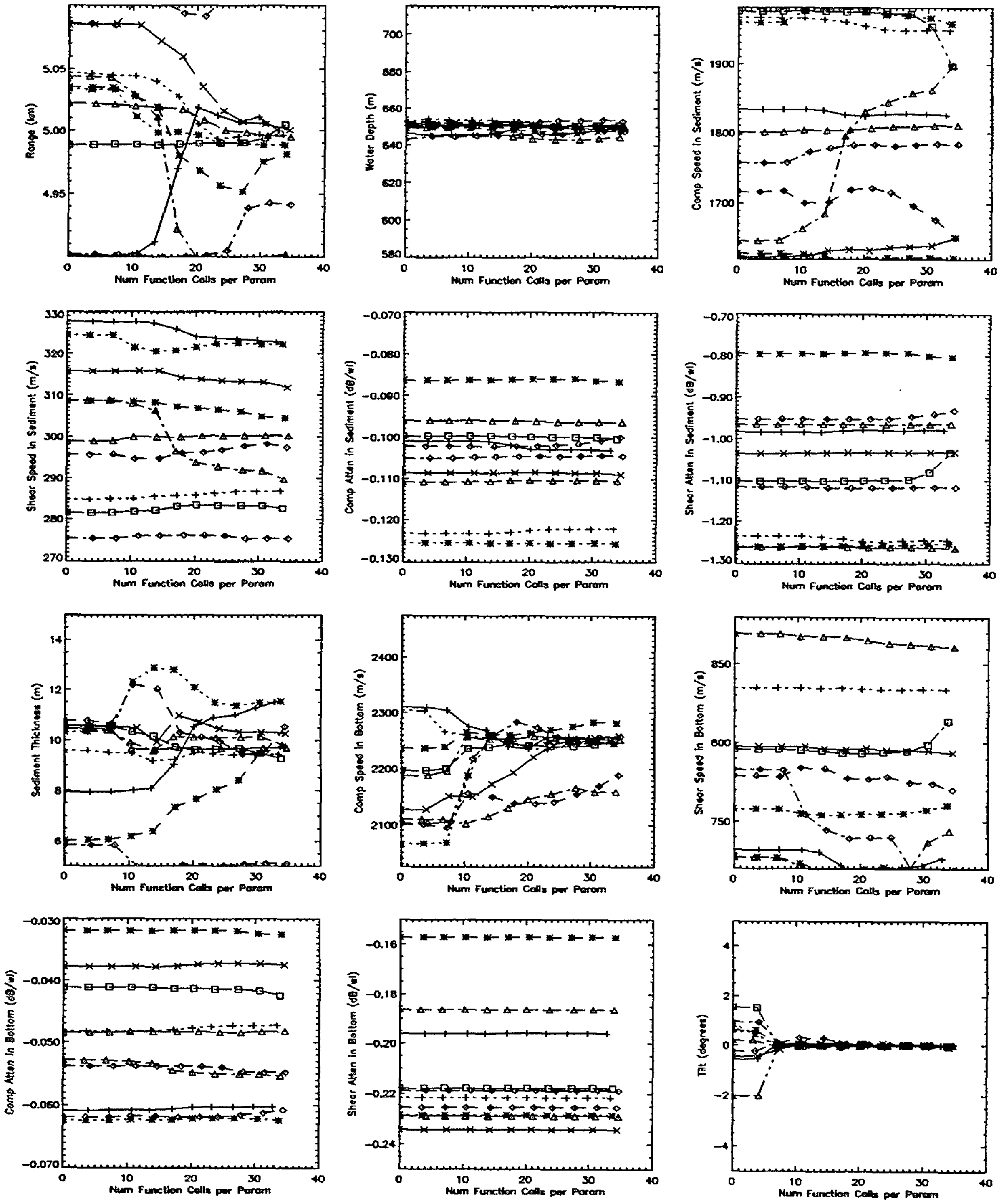

Figure 3: Convergence of parameters during local optimization of 10 best matches.

Beamforming inversion

Patrick PIGNOT

Centre d'Etude des PHénomènes Aléatoires et Géophysiques de Grenoble
(URA CNRS 346), BP46
38402 Saint Martin d'Hères FRANCE
e-mail : pignot@cephag.observ-gr.fr

Abstract

This study aims at the identification of sound speed fields in Mediterranean sea with multisensor analysis by using the modal theory. In Ocean Acoustic Tomography, the use of only one receiver does not always allow an inversion with a good accuracy. Therefore a large vertical array receiver is used. We propose here to realise a Matched Field Inversion by using the beamforming patterns. The principle of this inversion is to re-establish the link between the horizontal group velocity and phase velocity from the beamforming patterns. The mean sound speed profile is reconstructed by using an adaptative inversion algorithm. At first, we present the principle of this Matched Field Inversion, and then, we use it to process experimental data obtained during the 1994 THETIS 2 campaign.

1 Introduction

Matched-field beamforming is generally used to determine range/depth localization of underwater acoustic source. In Ocean Acoustic Tomography, such a method can be used to reconstruct geoacoustic properties of the medium and especially the sound speed profile. In this study, we suppose that the source position is well known. We will only consider a range-independent environment and we will try to reconstruct the mean sound speed profile of the medium. Generally, the modal inversion schemes are based on modal-travel time approaches [1]. We consider here a new approach to process the inverse problem based on the beamforming patterns. We will see that the modal horizontal group velocity and phase velocity are directly linked to the beamforming pattern. Using the *group velocity - phase velocity* relation, the inversion algorithm is introduced. A Matched-Field method is then used to reconstruct the mean sound field by minimizing the mean square error between the experimental and theoritical signal. The proposed method allows to process directly experimental data.

2 Modal approach

Consider a source at depth z_s, which emits a wideband signal. The acoustic modal pressure at detph z from a distant source at range r can be expressed as a sum of four planes waves [5]:

$$P(r,z,t) = A_m e^{j(\omega t - k_{m,r} r)} \left(e^{jk_{m,z}(z+z_s)} + \alpha e^{-jk_{m,z}(z+z_s)} + \beta e^{jk_{m,z}(z-z_s)} + \gamma e^{-jk_{m,z}(z-z_s)} \right) \quad (1)$$

where each mode m is characterized by the emission angle θ_m which satisfies :

$$\left\{ \begin{array}{l} k_{m,r} = k_o cos\theta_m \\ k_{m,z} = k_o sin\theta_m \end{array} \right. \text{with } k_o = \frac{\omega}{c_o} \quad (2)$$

2.1 Group and phase velocities

The phase velocity corresponding to the m-th mode is defined as $v_{\phi,m} = \frac{\omega}{k_{m,r}}$ and in the case of a wideband emission signal, centered around the angular frequency ω_o, the horizontal and vertical group velocities are respectively defined as $v^h_{gr,m} = \left.\frac{\partial \omega}{\partial k_{m,r}}\right|_{\omega=\omega_o}$ and $v^v_{gr,m} = \pm \left.\frac{\partial \omega}{\partial k_{m,z}}\right|_{\omega=\omega_o}$. The group velocity corresponds to the velocity of the wavetrain in the medium ; the velocity along the depth for the vertical group velocity, and along the range for the horizontal group velocity. Each mode is propagated through a waveguide whose thickness h_m satisfies $c(z) \leq v_{\phi,m}$. The different types of propagation can be classified according to their interaction with the top and bottom boundaries [2] (figure 1). Consider the ray/mode duality [3] and by analogy with the rays theory, the modal caustics are located at depth of the rays turning points. A ray, emitted with an incidence angle θ_m^S (at source depth), will have a turning point at depth z_m such that $c(z_m) = \frac{c_S}{cos\theta_m^S}$, where c_S is the sound velocity at source depth. Consider the phase velocity of the m-mode, we have :

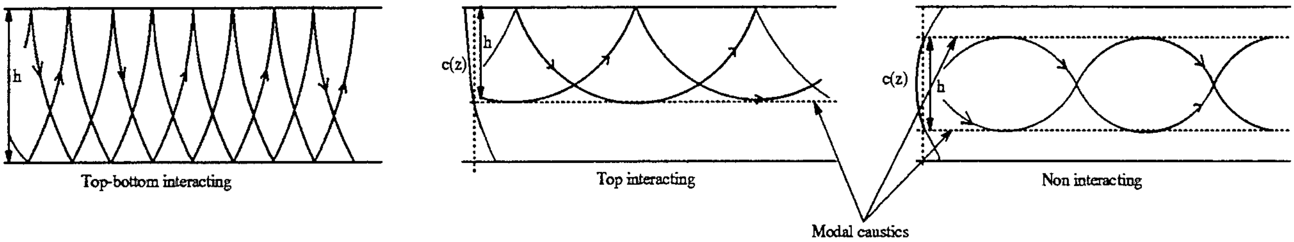

Figure 1: Mode types according to their interaction

$$v_{\phi,m} = \frac{\omega}{k_{m,r}} = \frac{c_S}{cos\theta_m^S} = c(z_m) \tag{3}$$

On a given receiver, the received modal angles θ_m^R verify equation (3). It follows :

$$v_{\phi,m} = \frac{c_S}{cos\theta_m^S} = \frac{c_R}{cos\theta_m^R} = c(z_m) \tag{4}$$

where c_R is the sound velocity at receiver depth.

2.2 Propagation time

The modal travel time is obtained via the horizontal and vertical group velocities. At depth z and range r, it can be expressed as :

$$t_m(\varepsilon_1, \varepsilon_2) = \frac{r}{v_{gr,m}^h} + \frac{z + \varepsilon_2 z_s}{v_{gr,m}^v(\varepsilon_1)} \quad \text{with } v_{gr,m}^v(\varepsilon_1) = \varepsilon_1 \frac{\partial \omega}{\partial k_{m,z}}\bigg|_{\omega=\omega_o} \tag{5}$$

where $\varepsilon_1 = \pm 1$ and $\varepsilon_2 = \pm 1$.
The propagation time of each mode depends on the values of ε_1 and ε_2. According to equation (5), four propagation times correspond to each mode.

2.3 Maxima of energy and *group velocity - phase velocity* relation

The modal positions of the maxima of energy of the received signals are obtained when the phase difference between two consecutive modes is a multiple of 2π. This condition may be expressed as :

$$k_o[Rcos\theta_m^R + \varepsilon_1 sin\theta_m^R(z + \varepsilon_2 z_s)] - k_o[Rcos\theta_{m+1}^R + \varepsilon_1 sin\theta_{m+1}^R(z + \varepsilon_2 z_s)] = 2p\pi \tag{6}$$

where $p = 0, 1, 2, \ldots$.
An illustration of different p values is given in figure 2.
Each p value gives four modal solutions for m noted $m_p(\varepsilon_1, \varepsilon_2)$. We define the *mean* value M_p of these four modes as :

$$k_o R(cos\theta_{M_p}^R - cos\theta_{M_p+1}^R) = 2p\pi \tag{7}$$

By using equations (4) and (5), the propagation times and arrival angles of the received maxima of energy are then written :

$$\begin{cases} cos\theta_{m_p(\varepsilon_1,\varepsilon_2)}^R = \frac{c_R}{c(z_{m_p(\varepsilon_1,\varepsilon_2)})} \\ t_{m_p(\varepsilon_1,\varepsilon_2)}(\varepsilon_1, \varepsilon_2) = \frac{r}{v_{gr,m_p(\varepsilon_1,\varepsilon_2)}^h} + \frac{z+\varepsilon_2 z_s}{v_{gr,m_p(\varepsilon_1,\varepsilon_2)}^v(\varepsilon_1)} \end{cases} \tag{8}$$

For a given p value, the four modes (satisfying equation (6)), associated with the four maxima of energy, are neighbouring and have approximately the same physical properties. We can consider, in first approximation, that the vertical group velocity is constant in the vicinity of these four modes, so that the *mean* value of the second term of the propagation time is equal to zero. The mean propagation time of these four maxima of energy can be then written :

$$t_{M_p} = \frac{r}{v^h_{gr,M_p}} \tag{9}$$

This travel time only depends on the horizontal group velocity. According now to equation (4), the *mean* received angles of the four maxima of energy can be expressed as a function of the phase velocity, we have :

$$cos\theta^R_{M_p} = \frac{c_R}{v_{\phi,M_p}} \tag{10}$$

From equations (9) and (10), we can directly compare the *spatio-temporal* representation to the *horizontal group velocity - phase velocity* relation. The set $(\mathcal{E})$ of points $\left(\frac{r}{t_{M_p}}, \frac{c_R}{cos\theta^R_{M_p}}\right)$ is a member of the *horizontal group velocity - phase velocity* curve, so that, the different positions (in the spatio-temporal representation) of the maxima of energy of the received signal allow to reconstruct the link between the horizontal group velocity and the phase velocity. This can be obtained by using the following equations :

$$\left\{ \begin{array}{l} v_{gr,n} = \frac{r}{t_n} \\ v_{\phi,n} = \frac{c_R}{cos\theta^R_n} \end{array} \right. \tag{11}$$

where $n = 1, 2, ..., N$ (N is the number of maxima). (t_n, θ^R_n) are the spatio-temporal positions of the maxima of energy at the receiver.

In other respects, W. Munk and C. Wunch [3] have shown, by using the WKBJ approximation, that the relation linking the horizontal group velocity to the phase velocity is independent of the angular frequency ω and only depends on the sound speed profile. This group and phase velocity reconstruction is allowed for any type of signal then. The result is totally independent of the emitted signal frequency.

2.4 Simulations

In practice, the spatio-temporal representation is obtained via a large vertical array by beamforming. In this case, the c_R sound speed at receiver depth will be the *mean* sound speed measured on the whole array.

In order to illustrate the group and phase velocity reconstruction from a beamforming pattern, figure 2 represents a beamforming in the case of a homogeneous medium (isovelocity problem $c = 1500\ m/s$). We superimpose on this picture the set $(\mathcal{D})$ of points $\left(\frac{r}{v^h_{gr,m}}, \pm\ arccos\left(\frac{c_R}{v_{\phi,m}}\right)\right)$ represented by crosses. The considered medium is 1000 m depth, with a perfectly reflecting bottom. The source is placed at 200 meters depth, the receiving array between 300 meters and 500 meters made of 21 sensors. The pulsed source has a 300 Hz central frequency, 200 Hz bandwidth and gaussian shape. The propagation length is 50 km.

From the beamforming pattern, if the mean sound speed c_R along the vertical array and the propagation length are known, the *spatio-temporal* positions of the maxima of energy allow to reconstruct the *group velocity - phase velocity* relation (set $(\mathcal{E})$). In the case of the isovelocity problem, the vertical group velocity is infinite so that the set $(\mathcal{E})$ is a member of the theoretical *group velocity - phase velocity* relation (see figure 3, [5]).

In the general case, the vertical group velocity introduces a spatio-temporal shift of the maxima of energy. The reconstruction of group and phase velocities is obtained by using equation (11). It is then possible to restore the *horizontal group velocity - phase velocity* relation by computing the *mean* position of the maxima of energy for each p value. As an example, we refer to the linear sound speed profile. Figure 4 shows the *horizontal group velocity - phase velocity* reconstruction from a beamforming pattern. Figure 4 shows clearly that the set of mean reconstructed points $(\mathcal{E})$ is member to the theoretical *horizontal group velocity - phase velocity* curve.

3 Inversion scheme

Consider the *horizontal group velocity - phase velocity* relation $v_\phi = f(v_{gr})$. The characteristics of this curve only depend on the sound speed profile (supposed to be range-independent). For a given sound speed profile, one function f

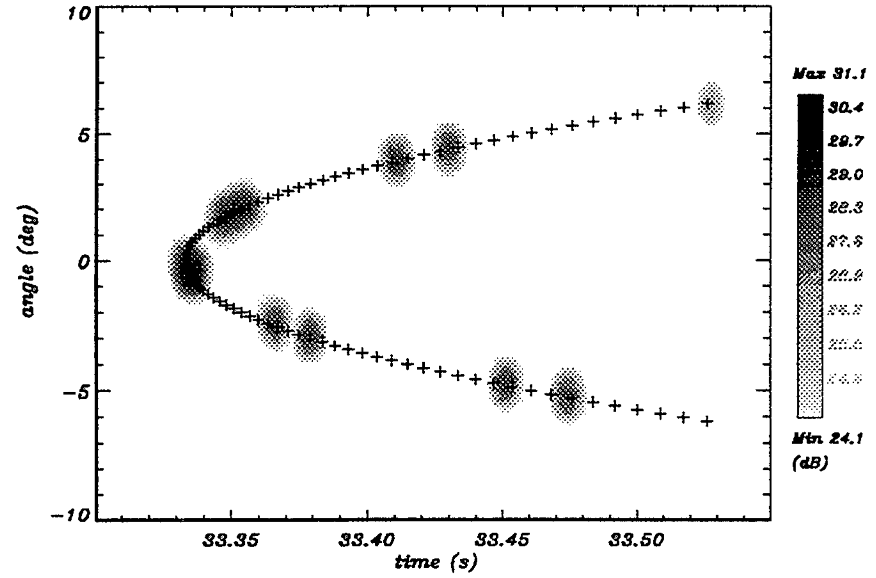

Figure 2: Beamforming pattern : case of the homogeneous medium.

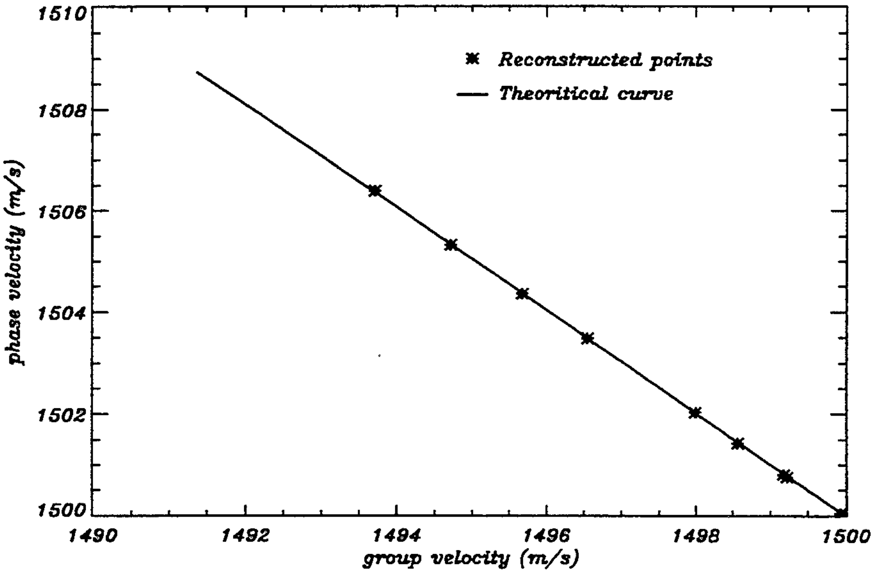

Figure 3: Group and phase velocity relation : case of the homogeneous medium

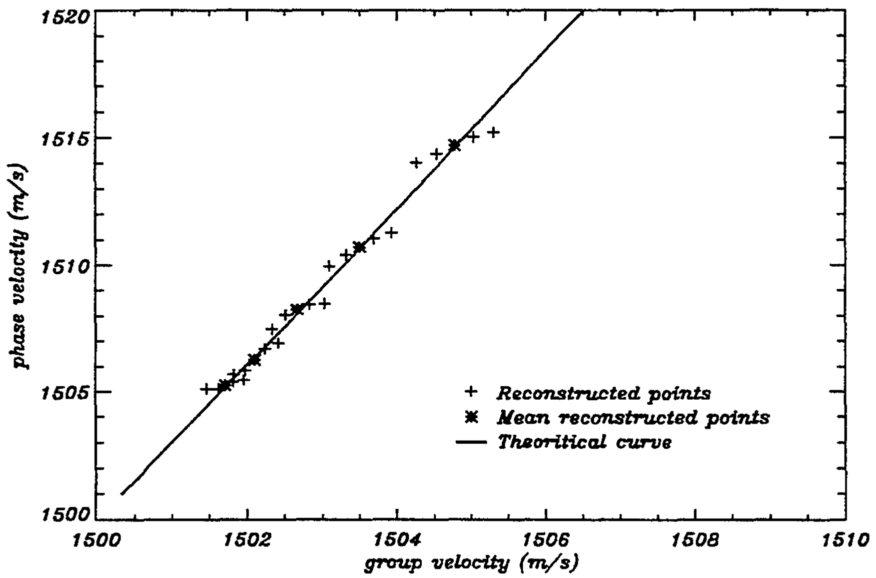

Figure 4: Group and phase velocity relation : linear profile case. The stars represent the set $(\mathcal{E})$.

exists which satisfies $v_\phi = f(v_{gr})$. Unfortunately, the converse is false. Actually, the *horizontal group velocity - phase velocity* relation depends on the different thicknesses of the modal waveguides, so that, many sound speed profiles can have the same *horizontal group velocity - phase velocity* characteristics, and then the same function f : any similarity along the depth of the sound speed profile does not change the *horizontal group velocity - phase velocity* curve. If the sound speed profile is a monotonous function (it is the case in winter in the Mediterranean sea), the thickness of the modal waveguides corresponds to the sound speed profile. In other cases (presence of a SOFAR), the thickness of the modal waveguides is not sufficient to reconstruct the sound speed profile.

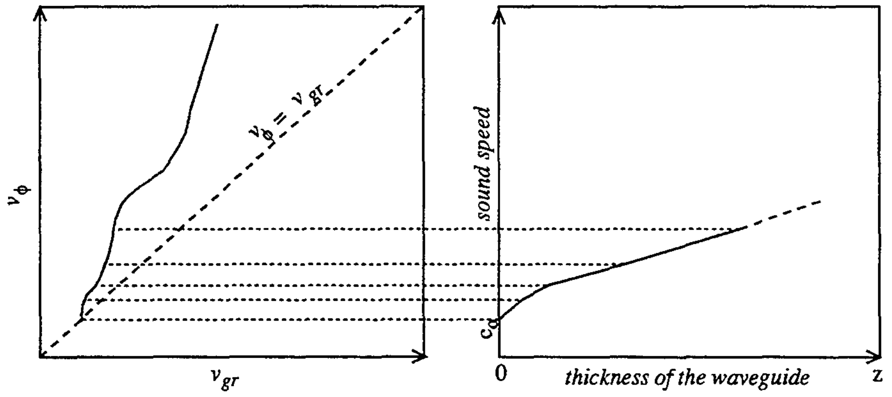

Figure 5: $v_\phi = f(v_{gr})$ curve and relation between the sound speed and the thickness of the waveguides

3.1 Algorithm

We developed a recursive algorithm allowing to reconstruct the relation between the sound speed and the thickness of the waveguides. The first step consists in discretising the phase velocity v_ϕ^i, $i = 0, 1, 2, \ldots$, where $v_\phi^0 = c_o$ corresponds to the minimum value. For each value of i, the algorithm calculates the thickness of the waveguide (which satisfies $c(z) \leq v_\phi^i$) in order to obtain the same *horizontal group velocity - phase velocity* relation. The phase and group velocities are calculated with the KRAKEN program.

3.2 Inversion conditions

The accuracy of the inversion depends on the knowledge of three parameters : the sound speed c_R at receiver depth, the minimum sound speed c_o and a particular point P of the sound speed profile (in order to know the homothety ratio). These three parameters are generally unknown, especially the c_R and c_o parameters. The particular point P can be chosen at great depth, where the temperature and salinity of the medium are almost the same throughout the year at a given depth. It is then possible to reduce the number of unknowns to two parameters : c_R and c_o. In order to estimate the different unknowns, a Matched Field Processing method is used. The principle consists in minimizing the Mean Square Error (MSE) [6] between the experimental and theoretical time signal, we have :

$$\epsilon(c_o, c_R, P) = \frac{1}{N} \sum_{n=1}^{N} \frac{1}{T} \int_T \| x_{exp,n}(t) - x_{th,n}(t, c_o, c_R, P) \|^2 dt \qquad (12)$$

where N is the number of sensors on the array.

3.3 Simulations

Two simulations are presented corresponding to two different *background* sound speed profiles. The results are presented figure on 7 and 8. We consider a wideband signal centered arround the central frequency 400 Hz, 100 Hz bandwidth and gaussian shape. The propagation length is 150 km. The source is placed at 100 m depth, the receiving array between 0 and 200 m. The results are presented in the case where the parameters c_o, c_R and P are known. From the background profiles ((c), dashed line), we calculate the beamforming pattern (a) and the theoritical curve *horizontal group velocity - phase velocity* ((b), solid line). We now try to solve the inverse problem. From the beamforming pattern, we directly reconstruct the set of points ($\mathcal{E}$)) by using equation (11). The reconstructed points are represented by stars (b). The inversion algorithm allows to reconstruct the sound speed profile ((c), solid line). A comparison of both simulations shows that the inversion accuracy is very satisfying. In the case where parameters c_o, c_R and P are known, the calculation cost is low (less than 5 minutes). In other cases, we use the method described in the previous section. The calculation cost is far bigger then, but the inversion accuracy is the same (in simulations). This inversion method allows to reconstruct the sound speed profile without any *a priori* information and can be directly applied to experimental data.

3.4 Experimental data processing

We applied this inversion method to experimental data obtained during the 1994 THETIS 2 campaign. We consider here the propagation between a mooring (W5) situated close to the Corse coast and a reception array made of 16 sensors, situated close to the French coast (Cap Ferrat). We processed here only one record dated the 28th of September 1994 at 11h28 UTC. The array characteristics are as follows : the first hydrophon is situated at depth 145.8 m and the last one at 184.2 m, the 14 others are vertically distributed between these two depths. At the record date, the source depth (W5) is 125.5 m, and the propagation length, calculated with the Andoyer's formula, is 153.427 km. The emited signal is a series of 15 or 30 sequences of 5.11 seconds BPSK. In this propagation configuration, we try to determine the mean sound speed field between W5 and the vertical array. Unfortunately, the used vertical array is too short : we have no information between 0 m and 145 m, and especially at the SOFAR depth (around 100 m depth), so that it is almost impossible to reconstruct the sound speed between the surface and the SOFAR depth.

By using the inversion scheme and by minimizing the Mean Square Error defined by equation (12), it has been possible to reconstruct the sound speed field for only deep water (from 100 m to 2000 m). The first 100 m were reconstructed by using experimental measurements obtained in october 1994, 50 km from the array. The beamforming pattern and the inversion result are presented in figure 9. The recorded and predicted arrival patterns are compared (for the central receiver).

4 Source or receiver detph estimation

It is possible to estimate the depth of one sensor (transmitter or receiver) by using a group of four maxima of energy. The group velocity corresponding to a maximum of energy is given by :

$$\left|v_{gr}^{v}(\varepsilon_1,\varepsilon_2)\right| = \frac{\varepsilon_1(z+\varepsilon_2 z_s)}{t(\varepsilon_1,\varepsilon_2)}. \tag{13}$$

Using the approximation that the vertical group velocity is approximatively the same around the four maxima, we have :

$$v_{gr}^{v}(\varepsilon_1,\varepsilon_2) \simeq v_{gr}^{v} \tag{14}$$

It is then possible to express the depth of an instrument with respect to another. By using the four propagation times $t(\varepsilon_1,\varepsilon_2)$, the source depth according to the receiver depth is :

$$z_s = z_R \frac{[t(1,1)-t(-1,1)]-[t(1,-1)-t(-1,-1)]}{[t(1,1)-t(-1,1)]+[t(1,-1)-t(-1,-1)]}, \tag{15}$$

and we can express the receiver depth according to the source depth by :

$$z_R = z_s \frac{[t(1,1)-t(-1,1)]+[t(1,-1)-t(-1,-1)]}{[t(1,1)-t(-1,1)]-[t(1,-1)-t(-1,-1)]}. \tag{16}$$

In order to apply this processing to experimental data, we do not use the absolute propagation times, but only the relative propagation times. The result is totally independent of the propagation length r. If the propagation times are known to within 1 ms, the estimation error is less than 1 %. Such a method may be used to estimate the source depth or the receiver depth (for example when a synthetic array is used) [5].

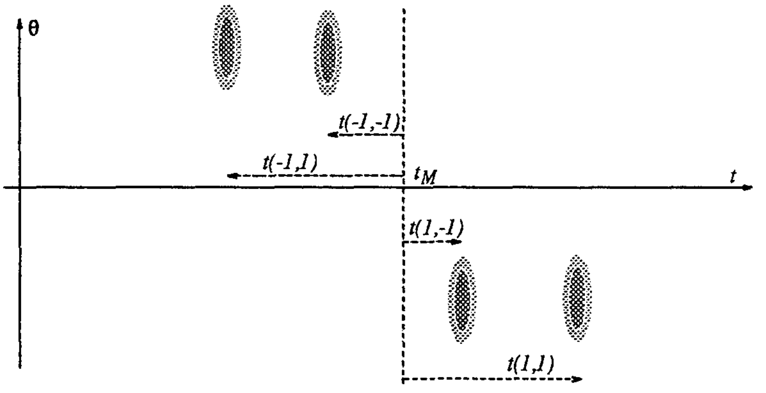

Figure 6: representation of a group of four maxima of energy

5 Conclusion

In this study, we have seen that the beamforming pattern allows to reconstruct the *horizontal group velocity -phase velocity* relation. The main application of such a processing is the estimation of the sound speed profile. The Matched Field Processing method, presented in chapter 3.2, is then used. This inversion method may be directly used to process experimental data and allows to reconstruct the sound speed profile without any *a priori* information. The inversion accuracy depends on the number of sensors and the length of the vertical array. In the Mediterranean basin, we can hope a very good inversion accuracy by using a 200 m high array from the surface to 200 m depth. Unfortunately, it was not the case in our experimetal data. Another application is the source or receiver depth estimation presented in chapter 4. In the future, we will try to estimate geoproperties of the bottom by using the *horizontal group velocity - phase velocity* reconstruction and the inversion by Matched Field Processing.

Acknowledgements

This study is part of the 1994 THETIS 2 campaign (MAST program) in collaboration with the CTSN (Centre Technique des Systèmes Navals). The experimental data come from the CMO (Centre Militaire d'Océanographie).

References

[1] Taroudakis M. and Papadakis J., *A modal inversion scheme for ocean acoustic tomography*, Journal of Computational Acoustics, Vol 1, No. 4, 395 - 421, 1993.

[2] Kamel A. and L.B. Felsen, *On the ray equivalent of a group of modes* , JASA 71(6), June 1982.

[3] Munk W. and Wunsch C., *Ocean acoustic tomography : Rays and modes*, Rev. Geophys. Space Phys. 21, 777-793, 1983.

[4] Munk W., Worcester P. and Wunsch C., *Ocean Acoustic Tomography*, Cambridge university press, 1995.

[5] Pignot P., *Caractérisation spatio-temporelle de la propagation acoustique sous-marine : reconstruction des vitesses de groupe et de phase*, submitted to the french revue *Traitement du Signal*, july 1996.

[6] Pignot P. and Faure B., *Marin media identification*, 3^{rd} European Conference on Underwater Acoustics, Heraklion, 24-28 june 1996.

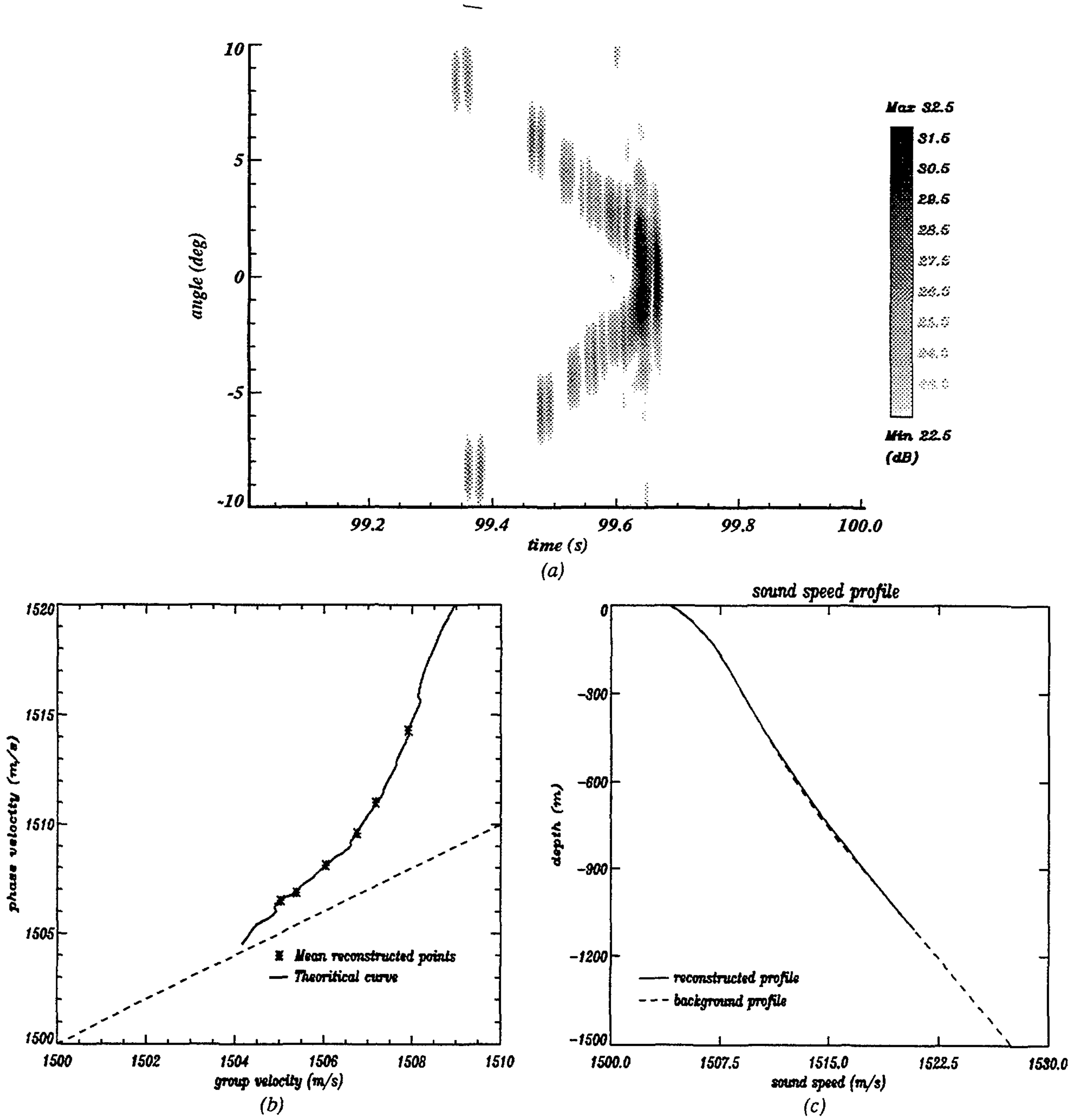

(a)

(b)

(c)

Figure 7: (top) beamforming pattern obtained with the background profile. (Down left) Group and phase velocities reconstruction (the dashed line corresponds to the line $v_\phi = v_{gr}$). (Down right) Inversion result.

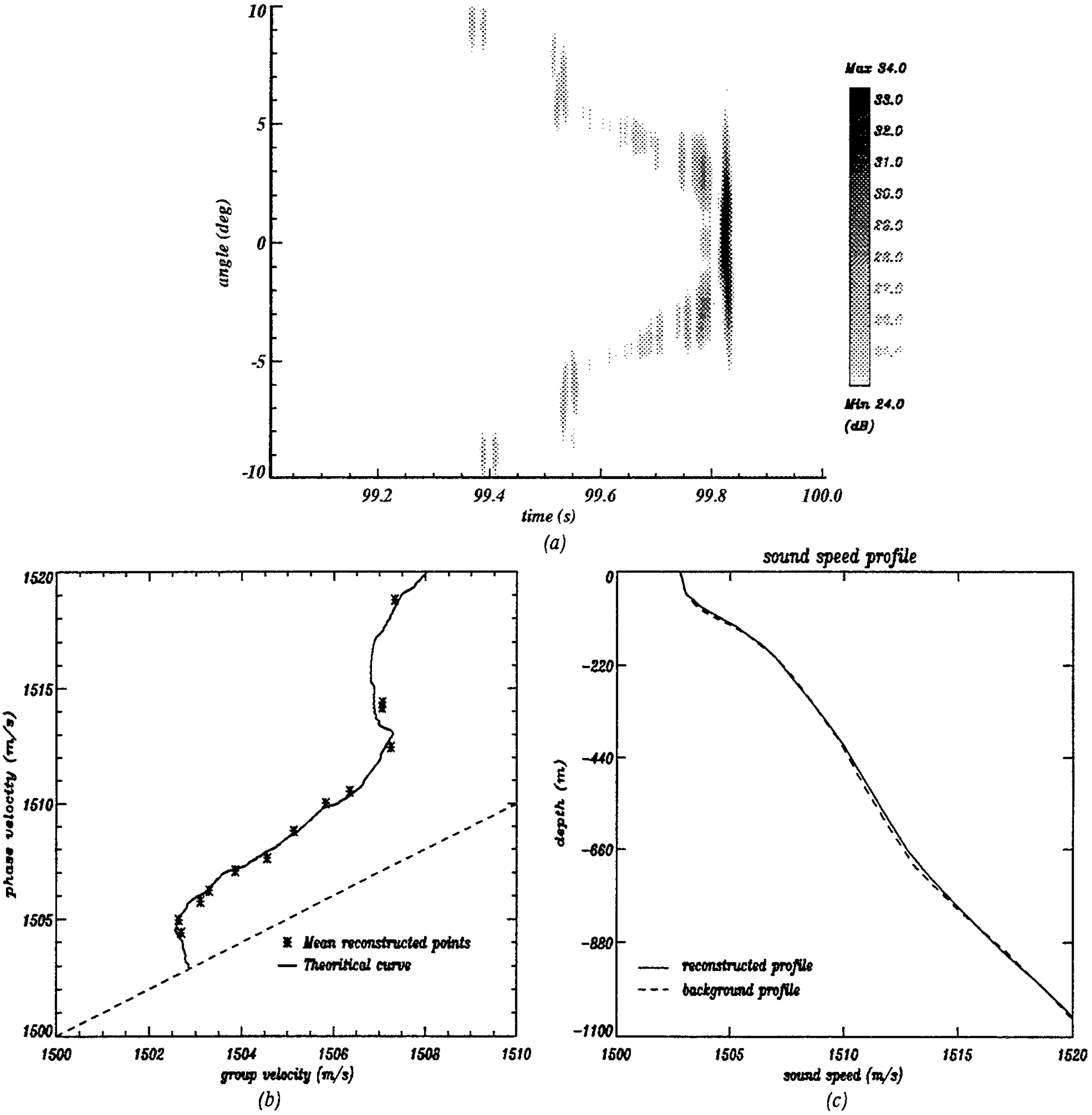

Figure 8: (top) beamforming pattern obtained with the background profile. (Down left) Group and phase velocities reconstruction (the dashed line corresponds to the line $v_\phi = v_{gr}$). (Down right) Inversion result.

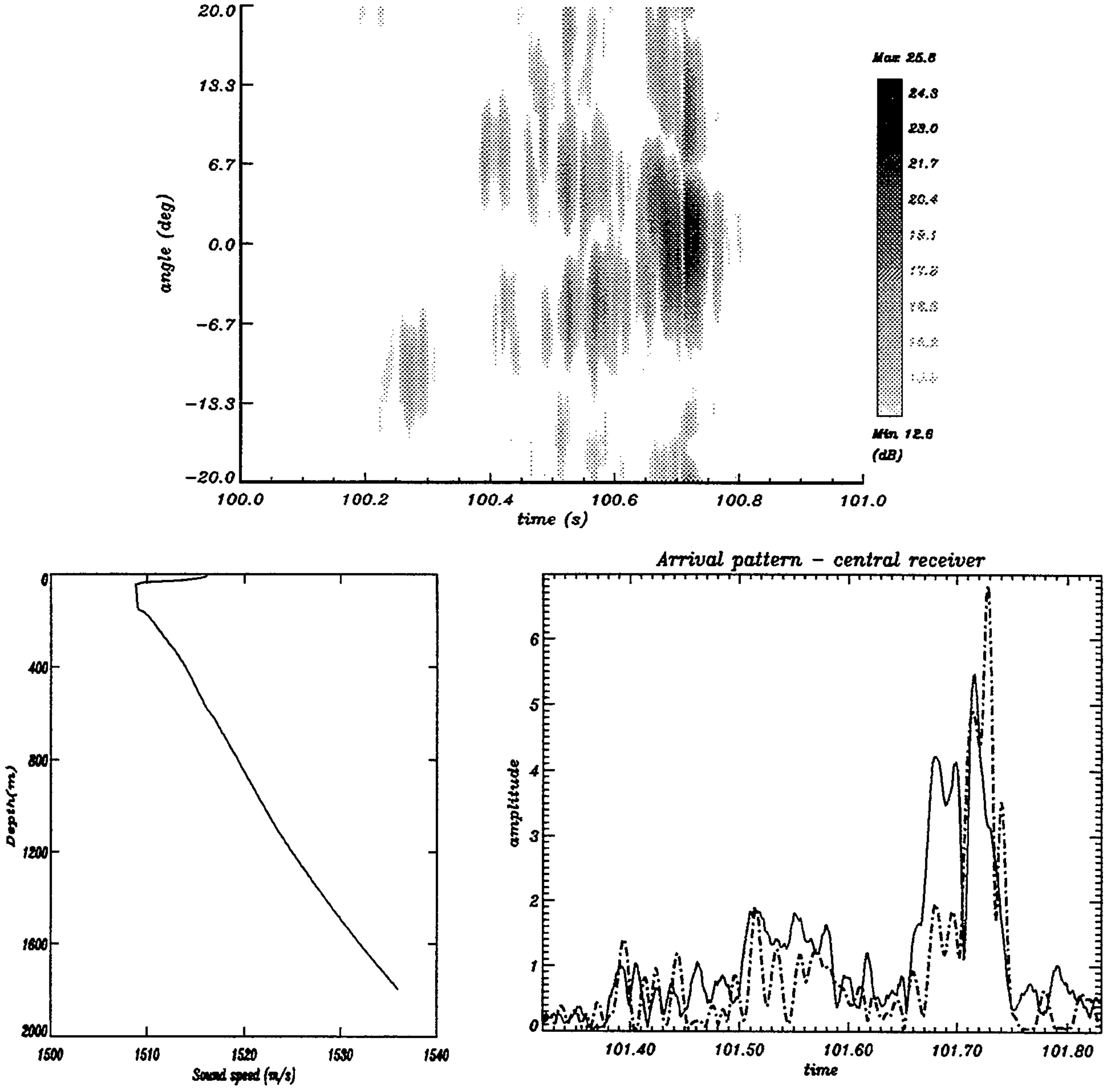

Figure 9: (top) beamforming pattern - (down left) reconstructed sound speed profile - (down right) experimental signal (solid line), reconstructed signal (dash dot)

A Rapid Development Tool For MFP

J.M. Ozard, D.J. Thomson, G.R. Ebbeson and M.L. Yeremy
Esquimalt Defence Research Detachment/Defence Research Establishment Atlantic,
FMO Victoria, B.C., Canada V0S 1B0

and
M.J. Wilmut
Royal Military College,
Kingston, Ontario, Canada K7K 5L0

31 July 1996

Abstract

For over a decade, advanced signal processing techniques based on Matched-Field, Matched-Mode or Model-Based Processing (MFP/MMP/MBP) concepts have been developed for improving the capability of passive and active sonar systems. Studies carried out at various laboratories have shown that MFP/MMP/MBP techniques can provide increased performance over conventional beamforming schemes for detecting and localizing underwater targets. At the Esquimalt Defence Research Detachment, a second generation of MFP/MMP based software called the Advanced Acoustic Signal Processor (AASP) is currently being developed in collaboration with contractors and researchers at universities. The basic components of the AASP system consist of data preconditioning, an environmental database, a propagation model, a matcher and a tracker. An inversion algorithm is also included for updating the environmental parameters. Hydrophone signals received from a surveillance or tactical array are correlated with replica fields generated using a propagation model to cover the search region. This matching is carried out for many candidate target locations to form an ambiguity surface whose values reflect the likelihood that the source is at the positions in the search region. A sequence of such ambiguity surfaces in time is processed by a detect-after-track algorithm. Uncertainties in the knowledge of the environmental parameters can degrade the matching between the measurements and the replicas: these can be mitigated by the tracker or reduced by using geoacoustic inversion methods to focus the ambiguity surfaces. The AASP is being designed to run on shared-memory and distributed processors connected by a local area network and will incorporate the lessons learned from the previous generation of MFP/MMP systems into an end-to-end research tool for the development, testing and evaluation of individual processor components. In this paper, the nature of the processor components and their integration into the AASP will be discussed.

Introduction

The objective in developing the Advanced Acoustic Signal Processor (AASP) is to produce portable software for research and development of Matched-Field Processing (MFP). This is to be achieved through a collaborative effort that involves the Department of National Defence (DND), the private sector and universities. The funding from DND is subsidized by reduced rates from the prime contractor and makes use of expertise existing among the subcontractors. Economy is also achieved through reuse of existing code held at the Esquimalt Defence Research Detachment, a division of Defence Research Establishment Atlantic (DREA) and at DREA.

Previously our Matched-Field Processing (MFP) has been carried out in stages with significant operator intervention. The development of an end-to-end AASP software package will enable analysis of data with less skilled manpower. This is possible on account of the more advanced state of MFP and software development environments and is a natural step in the development of a prototype on the route to an operational system.

The software is being developed in a modular form to enable subsequent enhancements to a variety of applications. The first priority, that is anticipated will take two years to complete, is the development of surveillance oriented software for a fixed array. It is planned that subsequent enhancements to the software for data from sonobuoys, geobuoys and towed arrays will follow.

The research on which the AASP is based is documented in numerous papers and is broadly supported by the MFP literature. Recently, the emphasis at EDRD has been to investigate those aspects necessary for the development of an operational system. Results from data analysis obtained during the past two years indicate that it is now appropriate to develop a prototype. Such a prototype will allow the timely evaluation and demonstration of end-to-end MFP software for R&D that is the last step before developing an experimental development model.

The remainder of this paper describes the environmental database, propagation modelling, matching, tracking and inversion components, and gives the reasoning behind the choices made. This is followed by a description of the implementation of the rapid prototype and its capabilities. Some details of the propagation modelling will be included while such details for other components may be found in the references cited.

System components

Overview

MFP consists of matching acoustic data with predictions of the data for all possible source positions to find the matching source range, depth and bearing. This leads to improved array gain and a better determination of the source position than plane wave, bearings-only, beamforming. In the first step in MFP, acoustic data is windowed and Fourier transformed prior to MFP in a similar manner to that used in plane wave beamforming. Replica vectors, predictions of the received data, for all source positions in the search region are then calculated from the propagation model using an estimate of the environment drawn from the database. Each of these replicas is compared to a measured data vector to form points on an ambiguity 'surface'. A sequence of data vectors results in a sequence of ambiguity surfaces. In our implementation, linear or circular tracks are formed through the largest peaks on the sequence of ambiguity surfaces to determine the track with the highest signal-to-noise ratio and therefore the most likely track.

MFP-based processing on sparse environmental data has demonstrated detection of weak sources and the determination of their range, depth and bearing. Further improvement in performance can be expected when a better model of the environment is available. MFP inversion for estimating the environmental properties can be carried out on a continuing basis for this purpose.

Environmental database

We have employed files to store environmental data for propagation modelling in the past with the user entering data for each application. This has been a laborious process that has been repeated for each application with little use being made of existing databases because of the large initial cost. A more efficient method of storing and retrieving environmental data is desirable now that repeated database use is likely. A high performance object-relational spatial database management system called ILLUSTRA has been chosen for the development of such a database. Because ILLUSTRA is a spatial database, it is efficient in two and three dimensional searches of environmental data required by the AASP. Subsequent development to provide a database for all the MFP data files may also be carried out with ILLUSTRA.

Initially, the Environmental DataBase (EDB) is to include both environmental data and geometric data pertaining to the array position. Included in the environmental data are bathymetry as well as sound speed(s) and attenuations in the water, bottom and ice. Additional parameters such as boundary roughness could be added later.

The EDB has a layered modular design [1, 2]. There are three modules, a data visualization module, an interpolation module and the ILLUSTRA module itself. The interpolation module carries out the two and three dimensional interpolation to provide the data files required by the propagation model. Data visualization is used to check on features of the data stored in the database or for presentation of the data. This is particularly useful when new data has been entered into the database and some check of the success of the process is required.

Propagation model

Numerical PE predictions are routinely used to model underwater sound propagation. The main rationale for this is that accurate full-wave solutions to the PE can be computed efficiently using marching algorithms for both depth- and range-dependent inhomogeneous media [3]. The development of the PE method has reached the point where finite-difference implementations derived from Padé series expansions can provide accurate solutions to one-way wave propagation for realistic geoacoustic conditions, including variable-depth bathymetry. Moreover, with the introduction of both exact and approximate PE procedures for handling elastic media, the physics of shear wave propagation can be incorporated in a straightforward way.

In two dimensions, range r and depth z with positive down, let the region $0 < z < z_b$ below the ocean surface ($z = 0$) be occupied by a fluid with density $\rho(r,z)$, compressional sound speed $c(r,z)$ and compressional absorption $\alpha(r,z)$. For $z > z_b$, these material properties are assumed to have the constant values ρ_b, c_b and α_b, respectively. In the case of a solid medium, the shear speed c_s and shear absorption α_s must also be specified. It is convenient to define $N = n(1 + i\alpha)$ where $n = c_0/c$ is the usual acoustic refractive index, and $k_0 = \omega/c_0$ is a reference wavenumber.

For $r > 0$, the outgoing component of the spatial pressure field $p(r,z) = \psi(r,z)\exp(ik_0 r)/\sqrt{r}$ produced by a harmonic $\exp(-i\omega t)$ point source located at $(r,z) = (0, z_s)$ can be recovered from the step-by-step numerical solution of the higher-order Padé PE

$$\frac{\partial\psi}{\partial r} = ik_0(Q-1)\psi \approx \sum_{j=1}^{J} \frac{a_{j,J}(Q^2-1)}{1 + b_{j,J}(Q^2-1)}\psi, \tag{1}$$

where the Padé coefficients $a_{j,J}$, $b_{j,J}$ and the operator Q^2 are defined by [4]

$$a_{j,J} = \frac{2j}{2J+1}\sin^2\frac{\pi j}{2J+1}, \qquad b_{j,J} = \cos^2\frac{\pi j}{2J+1}, \qquad Q^2 = N^2 + k_0^{-2}\rho\frac{\partial}{\partial z}\left(\rho^{-1}\frac{\partial}{\partial z}\right). \tag{2}$$

Equation (1) can be solved for the field at $r + \Delta r$ in terms of the field at r as a sequence of J systems of equations, where the jth system is given by

$$\left[1 + c_{j,J}^{-}\left(Q^2 - 1\right)\right]\psi(r + \frac{j}{J}\Delta r, z) = \left[1 + c_{j,J}^{+}\left(Q^2 - 1\right)\right]\psi(r + \frac{j-1}{J}\Delta r, z), \tag{3}$$

and where we have set $c_{j,J}^{\pm} = b_{j,J} \pm \frac{1}{2}ik_0\Delta r a_{j,J}$. If $\left(Q^2 - 1\right)\psi(r,z)$ is evaluated in the heterogeneous approximation [5] at each point z on the depth grid, namely

$$\left(Q^2 - 1\right)\psi(r,z) \approx \left(N^2 - 1\right)\psi(r,z) + \frac{\rho_-\psi(r, z-\Delta z) - \rho_0\psi(r,z) + \rho_+\psi(r, z+\Delta z)}{k_0^2\Delta z^2}, \tag{4}$$

where $\rho_\pm$ and ρ_0 denote the density combinations

$$\rho_\pm = \frac{2\rho(r,z)}{\rho(r,z) + \rho(r, z\pm\Delta z)}, \qquad \rho_0 = \rho_- + \rho_+, \tag{5}$$

then Eq. (3) becomes a tri-diagonal system of equations that can be efficiently solved by double recursion. A simple analytic starter is used to specify an initial field at $r = 0$. The radiation condition at $z \to \infty$ is approximated by appending an absorbing layer to the computational grid and applying a pressure-release boundary condition at the base of this layer.

Two aspects of the above implementation deserve comment. First, it is convenient in some applications to replace the real coefficients $a_{j,J}$ and $b_{j,J}$ in Eq. (2) with complex ones. For $j \leq 8$, suitable values have been determined numerically and tabulated [6]. Second, although a PE formalism exists for solving the elastic PE [3, 6, 7], it is more efficient to make use of an equivalent fluid approximation developed by Zhang and Tindle [8]. In this case, the (real) density ρ of an elastic medium is simply replaced by a complex density ρ^* that is determined from the shear properties of the medium according to

$$\rho^*(r,z) \approx \rho(r,z)\left[\left(1-\frac{2}{N_s^2(r,z)}\right)^2+\frac{4\sqrt{N^2(r,z)-1}\sqrt{N_s^2(r,z)-1}}{N_s^4(r,z)}\right], \tag{6}$$

where $N_s \equiv (c_0/c_s)(1+i\alpha_s)$.

Matching

The matcher is a critical component in the determination of the robustness of the MFP software. As with all components, the simplest matcher that provides the detection and localization capability required was selected. For low Signal-to-Noise ratios (SNR's) in spatially uncorrelated noise whose amplitudes are Gaussian distributed, the Bartlett matcher represents an optimum matcher. Since this is simply an inner product of the Fourier transformed data vector and the replica vectors, it is also easy to implement. Such a choice implies that the data needs to be prewhitened for the prevailing noise. It would also be desirable to remove impulses in the noise in order to satisfy the assumption that the noise amplitudes are Gaussian distributed. Lastly, the replicas are normalized to have unit norm to ensure that in spatially white noise the ambiguity surfaces are flat.

Since the computational load of matching would limit the applicability of MFP, schemes have been investigated for reducing the load without incurring an unacceptable performance degradation. The performance enhancements to be expected at high signal to noise ratios are substantial [9]. At low SNR's the computational load can be reduced by an order of magnitude at a cost of a 1-dB SNR penalty [10, 11]

Tracking

At high SNR's, and when the environmental parameters are sufficiently well known, the largest peak in an ambiguity surface will occur at the true source position with sidelobes at a lower level. The position of these sidelobes will depend on the source position and the scenario. At low SNR's, or when the environment is poorly known, the largest peak may not occur at the true source position. On average the largest peak will be found most frequently at the source position. If the source is moving, the sidelobes will vary in their position relative to the source position. Thus integrating the Bartlett statistic on successive ambiguity surfaces along all possible source tracks would allow one to recover the source track, as it would have the highest integral. In practice this takes too long because of the enormous number of possible source tracks. Our solution is to integrate along linear tracks which pass through the largest peaks on pairs of ambiguity surfaces [12, 13, 14]. This reduces the computation time about seven orders of magnitude for search regions of interest. Our efficient tracking algorithm also determines the track segment over which a source appears to be present. The present version of the tracking algorithms search for linear or circular track segments. These are then concatinated to determine the overall track shape. This efficient algorithm incurs only a small performance loss compared to an exhaustive search and yet can be implemented in a real time system.

Inversion

Inversion consists of finding the set of environmental and geometric parameters that provide a replica that best matches the data. As with tracking, this can be computationally prohibitive. Restricting the number of environmental parameters to those that most affect the match reduces the computational load. Synthetic anealing and genetic algorithms have been widely reported on for the purpose. Recently, a two-step method has been investigated. In the first step, candidates for the optimum parameter set are found through a random search. This is followed by a gradient search to find optimum values. This two-step algorithm has been compared favorably to the synthetic anealing and genetic algorithms in that it finds the optimum parameter set more efficiently and more consistently in simulations [15]. The gradient search also has the advantage of requiring no user specified parameters. Synthetic anealing, genetic and two-stage searches will be investigated more fully with the prototype.

Implementation and system capabilities

Implementation

In order to minimize programming cost and yet provide a user-friendly software package, the software was and is being written in Research Systems Interactive Data Language (IDL). This allows efficient development of widget-driven software that minimizes the need for an extensive users guide for a novice operator. This software approach also minimizes data entry and makes use of a point and click approach for efficiency of use. IDL code may be executed on a wide range of single CPU platforms and can provide a good graphical output at a reasonable programming cost. Furthermore code written in IDL is more easily maintained by a mixed group of defence scientists and contractors at separate locations. For the protyping of any component, it was also considered too time consuming to write code in a language such as FORTRAN. Instead, it was decided to implement all code directly in IDL. Where necessary existing components in other languages could be accommodated and resources permitting other more computationally efficient codes would be used for the kernels in an experimental demonstration model. Our code has been tested under Unix on HP, Sun and SGI work stations as well as under Windows on PCs and MacOs on the Power Macintosh.

System capabilities

At present, a rapid prototype exists that allows simulation and analysis of data for a vertical array. Simulation includes the addition of spatially white noise to the signal obtained from the propagation model while analysis includes matching, tracking and inversion for environmental properties. The propagation model assumes a range-independent environment and the propagation modelling is N by 2-D. The matching is exhaustive while the tracking assumes a source moving along a straight line or circle in three dimensions. Enhancements planned include 3-D propagation modelling, the replacement of the file-based database with the ILLUSTRA-based database, efficient matching, and the development of a version for a multi-CPU platform. The intention is that the prototype enable the efficient evaluation of these and other enhancements.

Concluding remarks

Experience to date with the preliminary version of the software shows that it has proven portable, to have a shorter learning curve for its use, to have relatively trouble-free execution and is easy to modify. It has the look and feel of recently developed userfriendly code. As expected it executes more slowly than code written in FORTRAN. This is an acceptable tradeoff for a development prototype. The present version took about one man year to produce and contains many of the features planned for the final system. Three dimensional propagation modelling, a true database and a multiprocessor capability are the principle developments planned in the next phase.

References

[1] LAKE R. AND J. SIEGEL, A Study of Database Technology for the Environment Database Associated with DREP's Advanced Acoustic Signal Processor, *DREP Contractor Report 94-07, pp. 77, January 1994.*

[2] LAKE R., A Matched Field Processing Environmental Database: Database vs. Flatfile Implementation, *DREA Contractor Report CR/96/404SPK, December 1995.*

[3] JENSEN, F.B., KUPERMAN, W.A., PORTER, M.B., AND H. SCHMIDT, *Computational Ocean Acoustics*. AIP Press, New York, 1994.

[4] COLLINS, M.D., Benchmark calculations for higher-order parabolic equations, *J. Acoust. Soc. Am. 87* (1990), 1535–1538.

[5] THOMSON, D.J., Wide-angle parabolic equation solutions to two range-dependent benchmark problems, *J. Acoust. Soc. Am. 87* (1990), 1514–1520.

[6] COLLINS, M.D., Higher-order Padé approximations for accurate and stable elastic parabolic equations with application to interface wave propagation, *J. Acoust. Soc. Am. 89* (1991), 1050–1057.

[7] WETTON, B.T.R. AND G.H. BROOKE, One-way wave equations for seismoacoustic propagation in elastic waveguides, *J. Acoust. Soc. Am. 87* (1990), 624–632.

[8] ZHANG, Z.Y. AND C.T. TINDLE, Improved equivalent fluid approximations for a low shear speed ocean bottom, *J. Acoust. Soc. Am. 98* (1995), 3391-3396.

[9] ZAKARAUSKAS P. AND J. M. OZARD, Complexity analysis for a fast nearest neighbor search, *In press, Transactions on Pattern Analysis and Machine Intelligence.*

[10] OZARD J.M., WILMUT M.J., BERRYMAN D.G. AND P. ZAKARAUSKAS, Anearest neighbors algorithm for fast matched-field processing with a vertical line array, *Special Issue on Detection and Estimation in Matched-Field Processing, IEEE Journal of Oceanic Engineering 18, 265-270, 1993.*

[11] RACCA R., MENG Z., OZARD J.M. AND M.J. WILMUT, Evaluation of Massively Parallel Computing for Exhaustive and Clustered Matched-Field Processing, *To appear in June issue of J. Comp. Acoust. 1996.*

[12] WILMUT M.J., OZARD J.M. AND B. WOODS, An Efficient Target Tracking Algorithm for Matched Field Processing *OCEANS 93, Vol III,81-85, 1993.*

[13] WILMUT M.J. AND J.M. OZARD, Detection Performance of Two Efficient Source Tracking Algorithms for Matched Field Processing, *submitted to J. Acoust. Soc. Am..*

[14] ZALA C.A., WILMUT M.J., OZARD J.M. AND B. WOODS, Detection Performance of Two Efficient Source Tracking Algorithms for Matched Field Processing, *To Appear in Matched-Field Processing Workshop Proceedings held at Esquimalt Defence Research Detachment at Victoria B.C. Canada.*

[15] ZALA C.A. AND J.M. OZARD, Algorithms for Matched-Field Inversion: Comparison and Performance, *To Appear in Matched-Field Processing Workshop Proceedings held at Esquimalt Defence Research Detachment at Victoria B.C. Canada.*

REPORT DOCUMENTATION PAGE

Form Approved
OMB No. 0704-0188

1. AGENCY USE ONLY *(Leave blank)*

2. REPORT DATE
October 1996

3. REPORT TYPE AND DATES COVERED
Final: 12–14 June 1996

4. TITLE AND SUBTITLE
PROCEEDINGS OF THE 8TH MATCHED-FIELD PROCESSING WORKSHOP 12–14 JUNE 1996

5. FUNDING NUMBERS
PE: 0602435

6. AUTHOR(S)
Compiled by Dr. B. Sotirin and Ms. S. Hall

7. PERFORMING ORGANIZATION NAME(S) AND ADDRESS(ES)
Naval Command, Control and Ocean Surveillance Center (NCCOSC)
RDT&E Division
San Diego, CA 92152–5001

8. PERFORMING ORGANIZATION REPORT NUMBER

9. SPONSORING/MONITORING AGENCY NAME(S) AND ADDRESS(ES)

Esquimalt Defence Research
Detachment (EDRD)
FMO Victoria, Bldg. 199
Victoria, BC, CANADA V0S 1B0

Naval Command, Control and Ocean
Surveillance Center (NCCOSC)
RDT&E Division
San Diego, CA 92152–5001

10. SPONSORING/MONITORING AGENCY REPORT NUMBER
NRaD TD 2932

11. SUPPLEMENTARY NOTES

12a. DISTRIBUTION/AVAILABILITY STATEMENT
Approved for public release; distribution is unlimited.

12b. DISTRIBUTION CODE

13. ABSTRACT *(Maximum 200 words)*

This document is a compilation of work presented at the 8th Matched-Field Processing Workshop, 12–14 June 1996, Victoria, BC, Canada.

14. SUBJECT TERMS
acoustics
signal processing
matched-field processing
submarine detection

15. NUMBER OF PAGES
201

16. PRICE CODE

17. SECURITY CLASSIFICATION OF REPORT
UNCLASSIFIED

18. SECURITY CLASSIFICATION OF THIS PAGE
UNCLASSIFIED

19. SECURITY CLASSIFICATION OF ABSTRACT
UNCLASSIFIED

20. LIMITATION OF ABSTRACT
SAME AS REPORT

21a. NAME OF RESPONSIBLE INDIVIDUAL Dr. B. Sotirin	21b. TELEPHONE *(include Area Code)* (619) 553–3104 sotirin@nosc.mil	21c. OFFICE SYMBOL Code D881

INITIAL DISTRIBUTION

Code D0012	Patent Counsel	(1)
Code D0271	Archive/Stock	(6)
Code D0274	Library	(2)
Code D0271	D. Richter	(1)
Code D881	B. Sotirin	(13)

Defense Technical Information Center
Fort Belvoir, VA 22060–6218 (4)

NCCOSC Washington Liaison Office
Arlington, VA 22245–5200

Center for Naval Analyses
Alexandria, VA 22302–0268

Navy Acquisition, Research & Development
Information Center (NARDIC)
Arlington, VA 22244–5114

GIDEP Operations Center
Corona, CA 91718–8000

Scripps Institution of Oceanography (MPL)
San Diego, CA 92106 (6)

Esquimalt Defence Research Establishment
(EDRD)
FMO Victoria,
Victoria B.C. VOS 1B0, Canada (20)

Office of Naval Research
Arlington, VA 22217–5660

New Jersey Institute of Technology
Newark, NJ 07102 (2)

TNO Physics and Electronics Laboratory
The Hague, The Netherlands (2)

Naval Undersea Warfare Center
Newport, RI 02841

The University of Rhode Island
Kingston, RI 02881 (2)

Science Applications International
Corporation
McLean, VA 22102

Integrated Performance Decision, Inc.
Honolulu, HI 96816

Centre d'Etude des Phenomenes Aleatoires
et Geophysiques de Grenoble
38402 Saint Martin d'Heres, France